



**HAL**  
open science

**metallic nanowire networks: silver nanowire network  
stability enhancement using metal oxide coatings,  
Percolation onset of nano-object network**

Sara Aghazadehchors

► **To cite this version:**

Sara Aghazadehchors. metallic nanowire networks: silver nanowire network stability enhancement using metal oxide coatings, Percolation onset of nano-object network. Chemical and Process Engineering. Université Grenoble Alpes [2020-..]; Université de Liège, 2021. English. NNT : 2021GRALI044 . tel-03628360

**HAL Id: tel-03628360**

**<https://theses.hal.science/tel-03628360>**

Submitted on 2 Apr 2022

**HAL** is a multi-disciplinary open access archive for the deposit and dissemination of scientific research documents, whether they are published or not. The documents may come from teaching and research institutions in France or abroad, or from public or private research centers.

L'archive ouverte pluridisciplinaire **HAL**, est destinée au dépôt et à la diffusion de documents scientifiques de niveau recherche, publiés ou non, émanant des établissements d'enseignement et de recherche français ou étrangers, des laboratoires publics ou privés.

## THÈSE

Pour obtenir le grade de

**DOCTEUR DE L'UNIVERSITÉ GRENOBLE ALPES**

Spécialité : **Matériaux, Mécanique, Génie Civil, Electrochimie**

Arrêté ministériel : 25 mai 2016

Présentée par

**Sara AGHAZADEHCHORS**

Thèse dirigée par **Daniel BELLET** et **Ngoc Duy NGUYEN**

Co-encadrée par **David MUÑOZ-ROJAS**

Préparée au sein du **Laboratoire des Matériaux et du génie Physique (LMGP)** et du **Physique du solide, interfaces et nanostructures (SPIN)**

Dans l'**École Doctorale I-MEP**, l'**École Doctorale en Sciences et European Joint Doctorate in Functional Materials Research**

**Réseaux de nanofils métalliques : amélioration de la stabilité des réseaux de nanofils d'argent grâce à des revêtements d'oxydes métalliques, étude des seuils de percolation de réseaux de nano-objets**

**Metallic nanowire networks: silver nanowire network stability enhancement using metal oxide coatings, Percolation onset of nano-object network**

Thèse soutenue publiquement le 29 Mars 2021

devant le jury composé de :

**Mme. Mona Treguer-Delapierre**

Professeur des universités, Université de Bordeaux, Rapporteur

**Mr. Philippe Poulin**

Directeur de recherche, Université de Bordeaux, Rapporteur

**Mr. Noël Jakse**

Professeur des universités, UGA, Président du Jury

**Mr. Jean-Yves Raty**

Maîtres de recherches, Université de Liège, Examineur

**Mr. Jean-Pierre Simonato**

Directeur de recherches, CEA LITEN, Examineur

**Mr. Matthias Pauly**

Maître de conférences, Université de Strasbourg, Examineur



## Abstract:

This study is focused on the fabrication and optimization of Transparent Electrodes (TEs) based on silver Nanowires (AgNW) networks. The TEs are one of the main components of many modern devices such as solar cells, Light Emitting Diodes, smart windows, transparent heaters and, display panels. These devices require high optical transmittance (above 90%), low electrical resistance, and in some cases, high mechanical flexibility. Currently, the most commercialized material for TEs is Transparent Conductive Oxides (TCOs) and Indium-doped tin oxide (ITO) is the leading TCO in the TEs market. Despite the great electro-optical properties of ITO, there are drawbacks associated with it including the scarcity of indium resources, expensive and vacuum-required deposition techniques, a high amount of required indium, and poor mechanical flexibility. Percolative networks composed of high-aspect-ratio Metallic Nanowires (MNWs), mainly AgNWs, are promising candidates among emerging materials to substitute ITO based electrodes.

Using the air-brush spray procedure described in this thesis, AgNW networks were deposited on Corning glass, with a sheet resistance of  $5.9 \Omega\text{sq}^{-1}$  and optical transmittance at 500 nm (without subtracting the substrate contribution) of 84.3%. However, despite such excellent electro-optical properties, there are drawbacks associated with AgNW based TEs. Lack of sufficient thermal and electrical stability, the tendency of MNWs to oxidation or sulphidation, high surface roughness, and poor adhesion of MNWs to the substrates are among major disadvantages. Addressing the lack of efficient stability, was the main focus of experimental studies in the scope of this thesis. We have chosen thin coatings of metal oxides (a few tens of nanometers) to enhance the stability of AgNW based TEs. AP-SALD was used to deposit high-quality coatings of ZnO and  $\text{Al}_2\text{O}_3$ . We have confirmed that the coatings of ZnO and  $\text{Al}_2\text{O}_3$  can dramatically improve the electrical, thermal, and aging stability of AgNW networks, the higher the oxide thickness, the higher the stability. Furthermore, to find a trade-off between the reproducibility of ZnO-coated AgNW networks and the high optical performance of  $\text{Al}_2\text{O}_3$ -coated ones, bilayer coatings of ZnO/  $\text{Al}_2\text{O}_3$  has been proposed and tested.  $\text{Al}_2\text{O}_3$  coating has been used as an anti-reflective coating over ZnO films. Samples of bilayer ZnO/  $\text{Al}_2\text{O}_3$  coatings showed excellent stability after 6 cycles of annealing from room temperature to 450 °C. Finally, the mechanical flexibility of bare, ZnO and bilayer ZnO/  $\text{Al}_2\text{O}_3$ -coated AgNW networks was measured and showed significant superiority compared to reference ITO electrodes. The results presented in this work indicate a path to low-cost, highly stable, and transparent composite electrodes based on AgNWs and oxide coatings.

Also, we have used Monte Carlo simulations to investigate the percolation behavior of networks composed of random nano-objects with different orders of symmetry to find the elemental shapes with the lowest possible

percolation threshold. We observed that considering an optimum order of symmetry of nano-objects, like branched NWs and nano-stars, can lead to a decrease in material areal density down to 50% compare to similar networks composed of sticks. These findings can be used as a guideline for chemists to synthesize new shapes of nano-objects. Finally, we focused on the collection efficiency of MNW based TEs for solar cells studying the effect of parameters such as MNW network density, NW length, and Diffusion lengths of photo-generated charge carriers in the active material. Our findings indicate for each type of solar cells and NW length, what would be the ideal network density to optimize the performance of electrodes. We believe that improving our model can provide a reliable guideline to design a TE for a targeted solar cell application from the NW geometry to network properties level.

## Résumé:

Cette étude est axée sur l'élaboration et l'optimisation d'électrodes transparentes (TE) basées sur des réseaux de nanofils d'argent (AgNW). Les TE constituent l'un des principaux composants de nombreux dispositifs modernes tels que les cellules solaires, les diodes électroluminescentes, les fenêtres intelligentes, les films chauffants transparents et les panneaux d'affichage. Ces dispositifs exigent une transmission optique élevée ( $> 90\%$ ), une faible résistance électrique et, dans certains cas, une grande souplesse mécanique. Actuellement, le matériau le plus commercialisé pour les TE est la famille des oxydes conducteurs transparents (TCO) et l'oxyde d'indium dopé à l'étain (ITO) est le TCO leader sur le marché des TE. Malgré les très bonnes propriétés électro-optiques de l'ITO, il présente des inconvénients, notamment la rareté des ressources en indium, les techniques de dépôt sous vide et coûteuses, la grande quantité d'indium nécessaire et enfin la faible flexibilité mécanique. Les réseaux percolants composés de nanofils métalliques (MNW) à fort rapport d'aspect, principalement des AgNW, sont des candidats prometteurs parmi les matériaux émergents pour remplacer les électrodes à base d'ITO.

En utilisant la méthode de spray, des réseaux AgNW ont été déposés sur du verre, avec une résistance de feuille de  $5,9 \Omega\text{sq}^{-1}$  et une transmission optique à 500 nm de 84,3%. Cependant, l'absence de stabilité thermique et électrique suffisante, la tendance des MNW à l'oxydation ou à la sulfuration, la rugosité de surface élevée et la mauvaise adhérence des MNW aux substrats sont parmi les principaux inconvénients. L'amélioration de la stabilité a été le principal objectif des études expérimentales dans le cadre de cette thèse. Nous avons choisi des couches minces d'oxydes métalliques (quelques dizaines de nanomètres) pour améliorer la stabilité des TE à base d'AgNW. L'AP-SALD a été utilisée pour déposer des revêtements de haute qualité de ZnO et  $\text{Al}_2\text{O}_3$ . Nous avons confirmé que les revêtements de ZnO et d' $\text{Al}_2\text{O}_3$  peuvent améliorer considérablement la stabilité électrique, thermique et de vieillissement des réseaux AgNW ; plus l'épaisseur de l'oxyde est importante, plus la stabilité est élevée. Des revêtements bicouches de ZnO/ $\text{Al}_2\text{O}_3$  ont été proposés et testés. Le revêtement  $\text{Al}_2\text{O}_3$  a été utilisé comme revêtement anti-reflet sur les films ZnO. Enfin, la flexibilité mécanique des réseaux AgNW nus, revêtus de ZnO et de ZnO/ $\text{Al}_2\text{O}_3$  bicouches a été mesurée et a montré une supériorité significative par rapport aux électrodes ITO de référence.

Nous avons également utilisé des simulations de Monte Carlo pour étudier la percolation des réseaux composés de nano-objets aléatoires avec différents ordres de symétrie afin de trouver les formes élémentaires ayant le seuil de percolation le plus bas possible. Nous avons observé que la prise en compte d'un ordre de symétrie optimal des nano-objets, tels que les nano-étoiles, peut entraîner une diminution de la densité surfacique de matière jusqu'à 50

% par rapport à des réseaux similaires composés de nanofils. Ces résultats peuvent être utilisés comme guide pour les chimistes afin de synthétiser de nouvelles formes de nano-objets. Enfin, nous nous sommes concentrés sur l'efficacité de collecte des TE basées sur les MNW pour les cellules solaires en étudiant l'effet de paramètres tels que la densité du réseau MNW, la longueur NW et les longueurs de diffusion des porteurs de charge photo-générés dans le matériau actif. Nos résultats indiquent, pour chaque type de cellules solaires et longueur des NW, quelle serait la densité de réseau idéale pour optimiser la performance des électrodes. Nous pensons que l'amélioration de notre modèle peut fournir une ligne directrice fiable pour concevoir une TE pour une application ciblée de cellules solaires, de la géométrie NW au niveau des propriétés du réseau.

# Contents

<b>Introduction</b> .....	1
<b>References:</b> .....	10
<b>Chapter 1: Transparent electrodes based on silver nanowire networks, synthesis of nanowires, properties of networks and applications in opto-electronic devices</b> .....	17
<b>1.1. Transparent Conductive Materials</b> .....	19
<b>1.2. AgNWs: synthesis and properties of single NWs</b> .....	20
<b>1.2.1. Synthesis of AgNWs: polyol process</b> .....	21
<b>1.2.2. The electrical conductivity of an individual silver NW</b> .....	22
<b>1.2.3. Sintering junctions between adjacent AgNWs to form conductive networks</b> .....	23
<b>1.3. Properties of networks consisted of AgNWs: the study of electro-optical properties and figure of merit versus network density</b> .....	26
<b>1.3.1. Electrical resistance of AgNW networks</b> .....	26
<b>1.3.2. Optical properties of AgNW networks</b> .....	27
<i>1.3.2.1.Total Transmittance</i> .....	27
<i>1.3.2.2.Diffuse transmittance and haze factor</i> .....	29
<b>1.3.3. Figure of Merit</b> .....	30
<b>1.4. Applications of AgNWs in opto-electronic devices</b> .....	31
<b>1.4.1. AgNW networks in solar cells</b> .....	31
<b>1.4.2. AgNW networks in Light Emitting Diodes</b> .....	33
<b>1.4.3. AgNW networks in transparent heaters</b> .....	35
<b>1.5. Closing remarks</b> .....	38

<b>References:</b> .....	40
<b>Chapter 2: Experimental methods related to deposition and characterization along with preliminary results of bare AgNW networks</b> .....	47
<b>2.1. Introduction</b> .....	49
<b>2.2. Deposition of AgNW networks</b> .....	40
<b>2.2.1. Spin coating of AgNWs</b> .....	50
<b>2.2.2. Air-brush spray coating of AgNWs</b> .....	53
<b>2.2.3. Silver contacts deposited by evaporation</b> .....	55
<b>2.3. Characterization of AgNW based transparent electrodes: electrical, morphological and optical properties, the effect of bending on the electrical resistance</b> .....	57
<b>2.3.1. Four-point probe method for measuring the sheet resistance</b> .....	57
<b>2.3.2. Scanning Electron Microscopy (SEM)</b> .....	57
<b>2.3.3. Transmission Electron Microscopy (TEM)</b> .....	58
<b>2.3.4. UV-Visible-IR spectrophotometer for optical measurements</b> .....	58
<b>2.3.5. Mechanical bending measurement setup</b> .....	59
<b>2.4. Post deposition treatments, main focus on the rmal annealing</b> .....	60
<b>2.4.1. Ramped thermal annealing of AgNW networks</b> .....	60
<b>2.4.2. Isothermal annealing</b> .....	63
<b>2.5. Conclusions</b> .....	64
<b>References:</b> .....	65
<b>Chapter 3: Enhancing the stability of AgNW networks thanks to conformal metal oxide coatings deposited by AP-SALD</b> .....	67
<b>3.1. Introduction</b> .....	69
<b>3.2. Lack of sufficient stability as a major drawback of AgNW networks</b> .....	69
<b>3.2.1. Plateau-Rayleigh instability</b> .....	69



3.2.2. Breakdown of silver NWs as a result of high electrical current and electromigration .....	71
3.2.3. Sulphidation or oxidation of silver NWs .....	72
3.3. AP-SALD as a novel technique to coat AgNWs and its advantages over spin coating, ALD or sputtering .....	74
3.4. ZnO coating of the AgNW network with AP-SALD .....	75
3.4.1. Effect of ZnO coating on the adhesion of AgNWs on the glass substrate .....	76
3.4.2. Effect of ZnO coating thickness on the optical transmittance and haze factor of AgNW networks .....	78
3.4.3. Effect of ZnO coatings on the ageing process of AgNW networks .....	80
3.4.4. Effect of ZnO coatings on the electrical stability of AgNW networks .....	82
3.4.5. Formulation of the effect of the ZnO coating on the stability of AgNW networks .....	83
3.4.6. Effect of the ZnO coating on the thermal stability of AgNW networks .....	86
3.5. Al <sub>2</sub> O <sub>3</sub> Coating of the AgNW network with AP-SALD.....	88
3.5.1. Effect of Al <sub>2</sub> O <sub>3</sub> coating on the optical transmittance of AgNW networks .....	89
3.5.2. Effect of Al <sub>2</sub> O <sub>3</sub> coating on the thermal stability of AgNW networks .....	91
3.5.3. Delamination of Al <sub>2</sub> O <sub>3</sub> coated AgNW networks at elevated temperatures .....	92
3.6. Bilayer metal oxide coatings on AgNW networks .....	93
3.6.1. Anti-reflective bilayer coatings based on ZnO/ Al <sub>2</sub> O <sub>3</sub> films on AgNW networks .....	93
3.6.2. Thermal stability of bilayer metal oxide coated AgNW networks .....	100
3.7. The flexibility of bare, ZnO and ZnO/ Al <sub>2</sub> O <sub>3</sub> coated AgNW networks.....	102
3.8. Summary and Conclusions.....	106
References: .....	107
Chapter 4: Monte Carlo simulations to find critical network density ( $n_c$ ) and its effect on the properties of the networks .....	115
4.1. Determination of the critical density $n_c$ by Monte Carlo simulations and study of its effect on the properties of networks .....	118

4.2.	<b>Nano-objects beyond sticks, experimental examples</b> .....	120
4.3.	<b>Tree-based algorithm to find the percolation threshold</b> .....	121
4.4.	<b>Introduction of the constant <math>\eta</math> and effect of the nano-object size</b> .....	124
4.5.	<b>Effects of the symmetry of nano-objects on the percolation onset</b> .....	128
4.5.1.	<b>Effect of order of symmetry on percolation threshold, m-fold periodic stick arrangements and polygons/ circles</b> .....	129
4.5.2.	<b>Morphological imperfections of network components and heterogeneous network compositions: effects on the percolation threshold</b> .....	131
4.5.2.1.	<i>Angular distribution in 2-and 3-fold periodic stick arrangement</i> .....	131
4.5.2.2.	<i>Mixtures of sticks and circles, mixtures of sticks and 3-fold periodic stick arrangements</i> .....	133
4.5.3.	<b>Percolation threshold for random networks of finite-size regular grids</b> .....	136
4.5.4.	<b>Percolation threshold for random networks of non-regular finite-size grids</b> .....	138
4.5.5.	<b>Effect of compactness of elemental objects on the percolation threshold</b> .....	140
4.5.6.	<b>Percolation threshold for non-randomly oriented nanowires</b> .....	143
4.5.7.	<b>Conclusion over the effect of symmetries on the percolation onset of random nanoscale networks</b>	145
4.6.	<b>Collection efficiency of MNW based TEs for solar cell applications</b> .....	146
4.6.1.	<b>Obtaining collection efficiency maps for MNW based solar cells</b> .....	148
4.6.2.	<b>Collection efficiency maps for changing network density and Diffusion length</b> .....	149
4.6.3.	<b>Estimation of collection efficiency based on the sum of areas method</b> .....	152
4.6.4.	<b>A new definition for the Figure of Merit (<i>FoM</i>)</b> .....	153
4.6.5.	<b>Conclusion over collection efficiency of MNW based TEs in solar cells applications</b> .....	154
	<b>References:</b> .....	155
	<b>Conclusions and future work :</b> .....	163
	<b>References:</b> .....	171

# **Introduction**



A wide range of modern devices, including flat panel displays, solar cells, Light Emitting Diodes (LEDs), smart windows, touch screen panels, and transparent heaters require a transparent electrode (TE) for their proper operation.[1], [2] TE should meet the required electro-optical properties for each device. Although optical transmittance above 90% is essential for many of these devices, the required electrical resistance strongly depends on the application.[3], [4] For example, touch screens can be functional with TE associated with sheet resistance ( $R_{sh}$ ) of few hundreds  $\Omega\text{sq}^{-1}$ , while a solar cell device would need much lower  $R_{sh}$  values, below  $10 \Omega\text{sq}^{-1}$ , to be efficiently functional. [5], [6] Mechanical flexibility is another feature that is essential in some modern devices, as in wearable electronics for example. Moreover, sustainability, along with cost-efficiency both in the chosen materials and also for the chosen materials deposition method, are critical aspects which should be considered if a TE material is to be commercialized and integrated into devices at large scale. Cost efficiency leads to fabrication processes that are easily scalable and preferably easily adapted to roll-to-roll techniques for instance. Finally, the reliability of many devices depends on their long-term performance. Degradation of physical properties of a TE in the long-term is also an obstacle to be considered. Taking into account all of these factors, explains why despite high electro-optical properties, along with high thermal/ electrical stability of TEs based on Transparent Conductive Oxides (TCOs) there is an intense effort to replace them with substitutional materials.[7]

Currently, most commercialized material for TE is TCOs including Indium doped Tin Oxide (ITO), [8], [9] Fluorine doped Tin Oxide (FTO), [10] Aluminum doped Zinc Oxide (Al:ZnO). [11], [12] TEs based on ITO are the leading material in the market due to the low electrical resistance (as low as  $10 \Omega\text{sq}^{-1}$ ) and high optical transmittance (above 90%) of these films.[8], [9] Despite the great potential of ITO to meet requirements as a TE in many devices, it suffers from some drawbacks in the main features which motivate the search for alternative materials. The main issues regarding TEs based on ITO include the scarcity of indium resources,[13] rather expensive and vacuum-required deposition techniques to fabricate the ITO thin films (mainly DC and RF magnetron sputtering), [14] high amount of required indium to reach desired electro-optical properties, [2] and poor mechanical flexibility.[15] Different substitutional materials have so far been suggested to replace ITO[7]: random networks of metallic nanowires (MNWs), metallic grids,[16], [17] conductive polymers,[12][13] carbon-based materials like carbon nano tubes (CNTs) or graphene.[7], [20]

Percolative networks composed of high-aspect-ratio MNWs are promising candidates among these emerging materials,[1], [2], [5], [21]–[24] since they exhibit excellent electro-optical properties comparable to ITO, along with high mechanical flexibility.[25]–[28] TEs based on MNWs with sheet resistance of less than  $10 \Omega\text{sq}^{-1}$  and

optical transmittance above 90% have been reported by many research groups so far.[25] To date, silver nanowires (AgNW) based TEs are the most widely studied type of TEs based on MNWs. One reason behind this is that large-volume synthesis of silver nanowires of controlled diameters (typically few tens to few hundreds of nanometres) and lengths (few tens to few hundreds of micrometres) is well mastered in research and industry.[29]–[31] The high electrical conductivity of silver among all materials at room temperature, high mechanical flexibility, [25], [32], [33] chemical stability, and having antibacterial activity[34]–[36] effects of AgNWs are among other reasons behind the attraction of AgNW based TEs.

Here we will have a closer look at some of the applications of TEs and explore first, the significance of each application and second, the reason why AgNW networks can appear as an interesting candidate to replace ITO based transparent electrodes. One of the major applications concerns the field of energy. Today's demanding growth for energy, along with increased awareness from both among nations and governments about CO<sub>2</sub> emission level and global pollution, promotes further investments in clean and reliable energy resources. Solar cells are one example of promising and sustainable solutions based on renewable energy resources. TEs are one of the indispensable components of solar cells to allow maximum absorption of light in the active layer while collecting the photo-generated carriers (at least for the front electrode). There has been an average of 50% annual growth in the U.S. solar sector, and at the same time, solar cell installation costs have dropped by over 70% from the beginning of 2010 up to date.[37]

Another rapidly growing application for TEs is LED devices, which have recently entered the mainstream lighting sector. In 2019, nearly 50% of all lighting sales worldwide were LED-based devices, while its share was only 5% of global market in 2013.[38] LEDs bear similarities to solar cell devices and require a TE in the front layer to enable emission of light. Currently, ITO-based electrodes are the most commonly used TEs in both solar cells and LED devices.[39] AgNW network based TE appears as an interesting candidate to replace ITO in these devices for several reasons. First, the deposition method of AgNWs is low-temperature and easily adapted to roll-to-roll device fabrication process.[40]–[43] Secondly, the amount of required silver is very low (100-200 mg m<sup>-2</sup>) compared to the required indium in ITO films (750–1050 mg m<sup>-2</sup>) to reach similar electro-optical properties.[2] Therefore, the limited resources of indium along with its geopolitical limitations, cannot provide enough material for the growing demand for cheap solar panels and LED devices. Eventually, electrodes based on AgNWs offer much superior mechanical flexibility when compared to ITO-based electrodes.[44] Therefore, AgNW-based TEs may prove to be compatible with components of cheap and flexible Organic solar cells,[45], [46] Organic LEDs (OLEDs) and polymer-based LED panels.[47]

Wearable electronics, mainly wrist wearables, are another rapidly growing potential market for TEs. The global market of wearable wrist devices alone was around 100 million units in 2019.[48] AgNW networks are excellent candidates for wearable electronic devices due to their outstanding mechanical flexibility. Furthermore, AgNWs have the potential to be integrated into mobile devices, large-area screen displays and in automotive lighting. High-quality electrodes of AgNWs can be deposited on light and flexible polymeric substrates, thereby decrease the weight and the overall cost of display panels.

Transparent heaters (THs) are another example where there is a potential market growth for AgNW based TEs. [49] THs are required for the proper performance of a wide range of modern devices. Defrosting windows of cockpits and automobiles, heating display panels of gadgets such as handheld scanners, security cameras, outdoor LCD panels, copy machines, refrigeration equipment are among some of the major applications. There are several essential criteria that a functional TH is required to meet. Ease of installation and fabrication on various surfaces, fast thermal response, accurate control over the temperature, homogenous heating pattern over the heating area, long term stability and high visibility are among these criteria. [50] Extensive research concerning AgNW based THs has confirmed that these coatings have great potential to perform as an easily scalable and installable, reliable and fast film on various range of substrates. [51]–[53]

Considered together, there is a motivation for further investigations into AgNW networks to gain a deeper understanding of their electrical, optical, and mechanical properties; as well as optimizing their properties and stability. In LMGP several PhD theses have already been dedicated to the investigation of transparent electrodes based on AgNWs. In 2014, Daniel Langley finished his PhD Thesis between LMGP and SPIN at University of Liège under the supervision of Daniel Bellet and Ngoc Duy Nguyen. His work was dedicated to a comprehensive simulation study on the percolation behaviour of random AgNW networks and confirmation of the findings by experimental observations.[54], [55] Langley mainly studied the effect of parameters such as length distribution, angular anisotropy, and curvature of AgNWs on the percolation threshold and electrical resistance of following percolating networks.[55] Also, the effect of thermal annealing as an efficient method to improve the electrical properties of AgNW networks under different annealing conditions was studied.[56] Following this work, Mélanie Lagrange also completed a PhD dedicated to AgNW based TEs in LMGP in October 2015 under the supervision of Daniel Bellet and Yves Bréchet. Her work was mainly focused on the optimization of AgNW networks (both in electrical and optical) properties, considering the effect of different parameters such as network density and NW size (diameter and length) to optimize the performance of these networks. [57], [58] Significant work was also dedicated to the optimization of THs made of AgNW networks and their failure mechanisms.[59] Moreover, Thomas Sannicolo finished his thesis under the supervision of Jean-Pierre Simonato at CEA-LITEN and Daniel

Bellet at LMGP on AgNW networks in October 2017. This work was mainly dedicated to studying “electrical percolation” (the electrical distribution in the percolating network) and electrical failure of AgNW networks. Using Lock-in Thermography (LiT) they observed an activation process of AgNW networks (as a result of thermal/ current annealing) and the occurrence of degradation in the AgNW network while the electrical stress increases. They also discussed the impact of parameters such as network density, NW-to-NW junction efficiency, and electrical instabilities on the electrical distribution of standard AgNW networks.[60], [61] Viet Huong Nguyen finished his thesis under the supervision of David Muñoz-Rojas and Daniel Bellet in LMGP and Delfina Muñoz at LHET in CEA, in October 2018. This work was mainly contributed to Atmospheric Pressure- Spatial Atomic Layer Deposition (AP-SALD) and development of low-cost TEs for solar cell devices.[62], [63] They used composite electrodes made of AgNWs and thin coatings (less than 100 nm) of AP-SALD coated ZnO films and confirmed the enhancement of electrical and thermal stability of composite electrodes compared to solely AgNW ones. They also confirmed the effect of Al: ZnO coating on AgNW networks, confirming that such composites can have prominent electro-optical properties (sheet resistance of  $7 \Omega\text{sq}^{-1}$  and optical transmittance around 83%).[62] Finally, in December 2020, Dorina (Theodora) Papanastasiou completed her thesis under the supervision of Daniel Bellet and David Muñoz-Rojas and in LMGP. This work had mainly focused on understanding the failure of AgNWs under electrical and/or thermal stresses. A further step was also taken to integrate AgNW based TEs into functional devices including transparent heaters for bio-chips, energy harvesting, and cold emission electron devices. [64]

These studies were invaluable in providing a comprehensive understanding of the physical properties of networks composed of AgNWs. However, there are still limitations regarding the successful integration of AgNWs in industrial devices, which need further effort from researchers. One of the major issues which will be tackled during this thesis is the fragility of AgNW networks when exposed to high thermal (typically above 300 °C) or electrical stress. For instance, AgNW networks may not be able to undergo some of the fabrication steps of thin-film devices, e.g. thin-film solar cells. Another example of the failure of NWs is when integrated into THs as Lagrange et al. studied.[59] Long-term storage of AgNWs in atmospheric conditions might also cause changes in the surface chemistry of NWs and lead to the appearance of Ag<sub>2</sub>S nanoparticles as a result of the sulphidation of silver. These factors can each contribute to a degradation in the electrical performance of AgNW networks in the long-term. Therefore, tackling this lack of stability (be it thermal, electrical, or environmental) is one of the main themes of this thesis.

The current document is divided into four specific chapters. We begin with a “state-of-the-art” review, presented in **Chapter 1**, which covers a general introduction of Transparent Conductive Materials (TCMs), followed by synthesis process of AgNWs, electrical properties of single NWs, junctions between NWs and the wider network,



and optical properties of AgNW networks. This chapter also introduces the Figure of Merit (*FoM*) as a tool to evaluate networks performance in terms of electro-optical properties. Finally, several examples of successful integration of AgNW networks into functional devices are presented.

**Chapter 2**, mainly deals with experimental conditions regarding the fabrication and characterization of AgNW networks. Spin-coating and more recent air-brush spray coating techniques are examined for the formation of random, large-area AgNW networks. Details about the morphological, electrical, optical, and mechanical characterization of AgNW networks along with some preliminary results are presented in this chapter. The main experimental findings of this thesis are presented in **Chapter 3**, where we deal with the lack of stability of AgNW networks. We have confirmed the efficiency of a novel deposition technique, AP-SALD, thanks to conformal and homogenous coatings of ZnO and Al<sub>2</sub>O<sub>3</sub> over AgNW networks with controlled thicknesses of a few tens of nanometres. These coatings were compared based on their stability-enhancement and their loss of optical transmittance, to find the optimum metal oxide composition and thickness. One should consider that the optimum coating strongly depends on the final application. Finally, we introduced a bilayer coating of ZnO/ Al<sub>2</sub>O<sub>3</sub>, which dramatically enhances the stability of AgNW networks, while demonstrating an anti-reflection effect of Al<sub>2</sub>O<sub>3</sub> over ZnO coating and causing a milder impact on the optical transmittance of AgNW networks compared to solely ZnO-coated networks.

In this study, using spin-coating and spray coating techniques AgNW networks with sheet resistance values of 9.2  $\Omega \text{sq}^{-1}$  and 5.9  $\Omega \text{sq}^{-1}$  and optical transmittances at 500 nm of 84% and 84.3%, were respectively fabricated. Lack of stability in bare AgNW networks was refined by bilayer coatings consisting of 70 nm ZnO/ 70 nm Al<sub>2</sub>O<sub>3</sub>. The achieved composites were stable after 6 cycles of annealing in the air from room temperature to 450 °C. A further step in the study of stability can be investigating a wide range of other metal oxides that can be also deposited by AP-SALD. Titanium dioxide (TiO<sub>2</sub>), Silicon dioxide (SiO<sub>2</sub>), Molybdenum trioxide (MoO<sub>3</sub>), are among the few candidates which can be used as coating layers on AgNWs. Selective coating of AgNW networks (and leaving the beneath substrate un-coated) is another approach which can be used to enhance the stability of AgNW networks while preserving high optical performances. Electrodeposition is an example of such approaches that are not taken during this study but will be out of interest for future investigation.[65]

As mentioned above, AgNWs are the most widely studied type of TEs based on randomly deposited metallic nano-objects. However, nanowires are not the only metallic nano-objects that can be synthesized using solution-based techniques. Branched silver NWs and shapes like nano-stars [72], [73], nano-cubes, and nano-rods [74], [75] of silver and gold have been already successfully synthesized. However, the sizes of these nano-objects are much

smaller compared to commercialized AgNWs, few tens of nanometres for gold nano-stars [76] and few micrometres for branched silver NWs.[77] The question treated in this work is whether or not the introduction of symmetry in these nano-objects (i.e. using nano-stars instead of nanowires) can lower the percolation threshold of formed networks. This question is critical, since reducing the percolation threshold leads to the lower material consumption in TEs and is also expected to result in higher optical transparency. To investigate this question, **Chapter 4** describes a comprehensive study on the effect of symmetry on the percolation onset of nano-objects using Monte-Carlo simulations. In our simulations, we used the algorithm initially developed by Daniel Langley, which as mentioned above focused on stick percolation only. Using the framework of algorithms for sticks, we developed algorithms to predict the percolation onset of random networks composed of different nano-objects such as m-fold periodic stick arrangement or regular polygons of m-edges. Furthermore, we aimed to evaluate the effect of imperfections of symmetric nano-objects on the network percolation threshold. We confirmed the validity of our simulations by comparing our results to the percolation onset of geometries, which have been already reported in the literature. [78] Our study confirmed that networks composed of symmetric nano-objects (e.g. m-fold periodic stick arrangements, or polygonal shapes, or finite-size regular grids) can decrease the total length of material areal density down to 50% compared to similar networks composed of sticks.

Finally, a second simulation attempt has been devoted to predicting the performance of MNW-based TEs in solar cells. The model of photo-generated charge carriers diffusion length was developed by Gonzalez-Vazquez et al. [79] Monte Carlo simulations using charge carriers diffusion length, enable us to estimate the collection efficiency ( $\eta$  in %) of MNWs as front electrodes in solar cells. In this section, we have studied the dependence of collection efficiency of photo-generated charge carriers (which correlates with the efficiency of power conversion in the final device) on parameters such as network density, average areal density of MNWs, MNW length, and electron diffusion length in the active layer of solar cells. One can anticipate using our simulations, that increasing the density of MNW networks increases  $\eta\%$ , while increasing the ratio of NW length to Diffusion lengths decreases  $\eta\%$ . We believe that improving models that were used in our simulations, can enrich our understanding of different physical properties of TEs based on random metallic nano-objects. Eventually, proposed models can be used as a guideline to choose the best geometry and network properties of metallic nano-objects to meet the requirements of TEs in diverse applications.



## References:

- [1] D. Bellet *et al.*, *Smart Nanosystems for Biomedicine, Optoelectronics and Catalysis*. intechopen. 2019. doi: 10.5772/intechopen.89281.
- [2] T. Sannicolo, M. Lagrange, A. Cabos, C. Celle, J.-P. Simonato, and D. Bellet, “Metallic Nanowire-Based Transparent Electrodes for Next Generation Flexible Devices: a Review,” *Small*, vol. 12, no. 44, pp. 6052–6075, Nov. 2016, doi: 10.1002/sml.201602581.
- [3] S. Bae, S. J. Kim, D. Shin, J.-H. Ahn, and B. H. Hong, “Towards industrial applications of graphene electrodes,” *Phys. Scr.*, vol. 2012, no. T146, p. 014024, Jan. 2012, doi: 10.1088/0031-8949/2012/T146/014024.
- [4] P. Yi, Y. Zhu, and Y. Deng, “Fabrication and Applications of Flexible Transparent Electrodes Based on Silver Nanowires,” *Flexible Electronics*, Nov. 2018, doi: 10.5772/intechopen.77506.
- [5] H. G. Manning, C. G. da Rocha, C. O. Callaghan, M. S. Ferreira, and J. J. Boland, “The Electro-Optical Performance of Silver Nanowire Networks,” *Sci Rep*, vol. 9, no. 1, pp. 1–9, Aug. 2019, doi: 10.1038/s41598-019-47777-2.
- [6] M. Morales-Masis, S. De Wolf, R. Woods-Robinson, J. W. Ager, and C. Ballif, “Transparent Electrodes for Efficient Optoelectronics,” *Advanced Electronic Materials*, vol. 3, no. 5, p. 1600529, May 2017, doi: 10.1002/aelm.201600529.
- [7] D. S. Hecht, L. Hu, and G. Irvin, “Emerging transparent electrodes based on thin films of carbon nanotubes, graphene, and metallic nanostructures,” *Advanced Materials*, vol. 23, no. 13, pp. 1482–1513, 2011, doi: 10.1002/adma.201003188.
- [8] F. O. Adurodija, L. Semple, and R. Brünig, “Crystallization process and electro-optical properties of  $\text{In}_2\text{O}_3$  and ITO thin films,” *J Mater Sci*, vol. 41, no. 21, pp. 7096–7102, Nov. 2006, doi: 10.1007/s10853-006-0038-3.
- [9] M. Gulen, G. Yildirim, S. Bal, A. Varilci, I. Belenli, and M. Oz, “Role of annealing temperature on microstructural and electro-optical properties of ITO films produced by sputtering,” *J Mater Sci: Mater Electron*, vol. 24, no. 2, pp. 467–474, Feb. 2013, doi: 10.1007/s10854-012-0768-8.
- [10] G. Rey, C. TERNON, M. Modreanu, X. Mescot, V. Consonni, and D. Bellet, “Electron scattering mechanisms in fluorine-doped  $\text{SnO}_2$  thin films,” *Journal of Applied Physics*, vol. 114, no. 18, p. 183713, Nov. 2013, doi: 10.1063/1.4829672.
- [11] E. Fortunato, D. Ginley, H. Hosono, and D. C. Paine, “Transparent conducting oxides for photovoltaics,” *MRS Bulletin*, vol. 32, no. 03, pp. 242–247, 2007, doi: 10.1557/mrs2007.29.
- [12] R. G. Gordon, “Criteria for choosing transparent conductors,” *MRS Bulletin*, vol. 25, no. 08, pp. 52–57, Aug. 2000, doi: 10.1557/mrs2000.151.
- [13] “<https://www.usgs.gov/centers/nmic/indium-statistics-and-information>.” .

- [14] O. Tuna, Y. Selamat, G. Aygun, and L. Ozyuzer, “High quality ITO thin films grown by dc and RF sputtering without oxygen,” *J. Phys. D-Appl. Phys.*, vol. 43, no. 5, p. 055402, Feb. 2010, doi: 10.1088/0022-3727/43/5/055402.
- [15] K. Alzoubi, M. M. Hamasha, S. Lu, and B. Sammakia, “Bending Fatigue Study of Sputtered ITO on Flexible Substrate,” *Journal of Display Technology*, vol. 7, no. 11, pp. 593–600, Nov. 2011, doi: 10.1109/JDT.2011.2151830.
- [16] S. Hong *et al.*, “Nonvacuum, Maskless Fabrication of a Flexible Metal Grid Transparent Conductor by Low-Temperature Selective Laser Sintering of Nanoparticle Ink,” *ACS Nano*, vol. 7, no. 6, pp. 5024–5031, Jun. 2013, doi: 10.1021/nn400432z.
- [17] J. H. Park *et al.*, “Flexible and Transparent Metallic Grid Electrodes Prepared by Evaporative Assembly,” *ACS Appl. Mater. Interfaces*, vol. 6, no. 15, pp. 12380–12387, Aug. 2014, doi: 10.1021/am502233y.
- [18] M. N. Gueye *et al.*, “Structure and Dopant Engineering in PEDOT Thin Films: Practical Tools for a Dramatic Conductivity Enhancement,” *Chemistry of Materials*, vol. 28, no. 10, pp. 3462–3468, May 2016, doi: 10.1021/acs.chemmater.6b01035.
- [19] M. N. Gueye, A. Carella, R. Demadrille, and J.-P. Simonato, “All-Polymeric Flexible Transparent Heaters,” *ACS Appl. Mater. Interfaces*, vol. 9, no. 32, pp. 27250–27256, Aug. 2017, doi: 10.1021/acsami.7b08578.
- [20] A. Kumar and C. Zhou, “The Race To Replace Tin-Doped Indium Oxide: Which Material Will Win?,” *ACS Nano*, vol. 4, no. 1, pp. 11–14, 2010, doi: 10.1021/nn901903b.
- [21] T. M. Barnes *et al.*, “Comparing the Fundamental Physics and Device Performance of Transparent, Conductive Nanostructured Networks with Conventional Transparent Conducting Oxides,” *Advanced Energy Materials*, vol. 2, no. 3, pp. 353–360, Mar. 2012, doi: 10.1002/aenm.201100608.
- [22] S. Ye, A. R. Rathmell, Z. Chen, I. E. Stewart, and B. J. Wiley, “Metal Nanowire Networks: The Next Generation of Transparent Conductors,” *Adv. Mater.*, vol. 26, no. 39, pp. 6670–6687, Oct. 2014, doi: 10.1002/adma.201402710.
- [23] S. Pirsalami, S. M. Zebarjad, and H. Daneshmanesh, “An Overview of Metallic Nanowire Networks, Promising Building Blocks for Next Generation Transparent Conductors: Emergence, Fundamentals and Challenges,” *Journal of Elec Materi*, vol. 46, no. 8, pp. 4707–4715, Aug. 2017, doi: 10.1007/s11664-017-5467-z.
- [24] J. Gao, Z. Xian, G. Zhou, J.-M. Liu, and K. Kempa, “Nature-Inspired Metallic Networks for Transparent Electrodes,” *Advanced Functional Materials*, vol. 28, no. 24, p. 1705023, 2018, doi: 10.1002/adfm.201705023.
- [25] D. Bellet *et al.*, “Transparent Electrodes Based on Silver Nanowire Networks: From Physical Considerations towards Device Integration,” *Materials*, vol. 10, no. 6, p. 570, May 2017, doi: 10.3390/ma10060570.
- [26] H. Sohn, C. Park, J.-M. Oh, S. W. Kang, and M.-J. Kim, “Silver Nanowire Networks: Mechano-Electric Properties and Applications,” *Materials*, vol. 12, no. 16, p. 2526, Aug. 2019, doi: 10.3390/ma12162526.
- [27] J. Jung *et al.*, “Stretchable/flexible silver nanowire electrodes for energy device applications,” *Nanoscale*, vol. 11, no. 43, pp. 20356–20378, 2019, doi: 10.1039/C9NR04193A.

- [28] F. Xu *et al.*, “Preparation and cold welding of silver nanowire based transparent electrodes with optical transmittances >90% and sheet resistances <10 ohm/sq,” *Journal of Colloid and Interface Science*, vol. 512, pp. 208–218, Feb. 2018, doi: 10.1016/j.jcis.2017.10.051.
- [29] Y. Li, X. Yuan, H. Yang, Y. Chao, S. Guo, and C. Wang, “One-Step Synthesis of Silver Nanowires with Ultra-Long Length and Thin Diameter to Make Flexible Transparent Conductive Films,” *Materials*, vol. 12, no. 3, p. 401, Jan. 2019, doi: 10.3390/ma12030401.
- [30] B. Li, S. Ye, I. E. Stewart, S. Alvarez, and B. J. Wiley, “Synthesis and Purification of Silver Nanowires To Make Conducting Films with a Transmittance of 99%,” *Nano Lett.*, vol. 15, no. 10, pp. 6722–6726, Oct. 2015, doi: 10.1021/acs.nanolett.5b02582.
- [31] H. Yang, T. Chen, H. Wang, S. Bai, and X. Guo, “One-pot rapid synthesis of high aspect ratio silver nanowires for transparent conductive electrodes,” *Materials Research Bulletin*, vol. 102, pp. 79–85, Jun. 2018, doi: 10.1016/j.materresbull.2018.02.010.
- [32] S. Aghazadehchors *et al.*, “Versatility of bilayer metal oxide coatings on silver nanowire networks for enhanced stability with minimal transparency loss,” *Nanoscale*, 2019, doi: 10.1039/C9NR05658K.
- [33] S. Wang *et al.*, “Mechanically and thermally stable, transparent electrodes with silver nanowires encapsulated by atomic layer deposited aluminium oxide for organic optoelectronic devices,” *Organic Electronics*, vol. 78, p. 105593, Mar. 2020, doi: 10.1016/j.orgel.2019.105593.
- [34] L. Ge, Q. Li, M. Wang, J. Ouyang, X. Li, and M. M. Xing, “Nanosilver particles in medical applications: synthesis, performance, and toxicity,” *Int J Nanomedicine*, vol. 9, pp. 2399–2407, May 2014, doi: 10.2147/IJN.S55015.
- [35] S. Jeong *et al.*, “High Efficiency, Transparent, Reusable, and Active PM2.5 Filters by Hierarchical Ag Nanowire Percolation Network,” *Nano Letters*, vol. 17, no. 7, pp. 4339–4346, Jul. 2017, doi: 10.1021/acs.nanolett.7b01404.
- [36] M. R. Nateghi and M. Shateri-Khalilabad, “Silver nanowire-functionalized cotton fabric,” *Carbohydrate Polymers*, vol. 117, pp. 160–168, Mar. 2015, doi: 10.1016/j.carbpol.2014.09.057.
- [37] “<https://www.seia.org/solar-industry-research-data>.”
- [38] “<https://www.iea.org/reports/lighting>.”
- [39] S. Liang, Q. Zhou, X. Li, M. Zhong, and H. Wang, “Electrical and Optical Properties of a Transparent Conductive ITO/Ga<sub>2</sub>O<sub>3</sub>/Ag/Ga<sub>2</sub>O<sub>3</sub> Multilayer for Ultraviolet Light-Emitting Diodes,” *Nanomaterials (Basel)*, vol. 9, no. 3, Mar. 2019, doi: 10.3390/nano9030403.
- [40] S.-E. Park, S. Kim, D.-Y. Lee, E. Kim, and J. Hwang, “Fabrication of silver nanowire transparent electrodes using electrohydrodynamic spray deposition for flexible organic solar cells,” *J. Mater. Chem. A*, vol. 1, no. 45, pp. 14286–14293, Oct. 2013, doi: 10.1039/C3TA13204H.
- [41] A. R. Madaria, A. Kumar, and C. Zhou, “Large scale, highly conductive and patterned transparent films of silver nanowires on arbitrary substrates and their application in touch screens,” *Nanotechnology*, vol. 22, no. 24, p. 245201, Jun. 2011, doi: 10.1088/0957-4484/22/24/245201.

- [42] V. Scardaci, R. Coull, P. E. Lyons, D. Rickard, and J. N. Coleman, “Spray Deposition of Highly Transparent, Low-Resistance Networks of Silver Nanowires over Large Areas,” *Small*, vol. 7, no. 18, pp. 2621–2628, 2011, doi: 10.1002/smll.201100647.
- [43] D. Y. Choi, H. W. Kang, H. J. Sung, and S. S. Kim, “Annealing-free, flexible silver nanowire–polymer composite electrodes via a continuous two-step spray-coating method,” *Nanoscale*, vol. 5, no. 3, pp. 977–983, Jan. 2013, doi: 10.1039/C2NR32221H.
- [44] D. Langley, G. Giusti, C. Mayousse, C. Celle, D. Bellet, and J.-P. Simonato, “Flexible transparent conductive materials based on silver nanowire networks: a review,” *Nanotechnology*, vol. 24, no. 45, p. 452001, Nov. 2013, doi: 10.1088/0957-4484/24/45/452001.
- [45] X. Dong *et al.*, “Flexible nonfullerene organic solar cells based on embedded silver nanowires with an efficiency up to 11.6%,” *J. Mater. Chem. A*, vol. 7, no. 5, pp. 1989–1995, Jan. 2019, doi: 10.1039/C8TA11378E.
- [46] H. Zhou *et al.*, “A facile approach towards chemical modification of Ag nanowires by PEDOT as a transparent electrode for organic solar cells,” *J. Mater. Chem. C*, vol. 6, no. 2, pp. 312–319, Jan. 2018, doi: 10.1039/C7TC04673A.
- [47] W. Li *et al.*, “Releasing the Trapped Light for Efficient Silver Nanowires-Based White Flexible Organic Light-Emitting Diodes,” *Advanced Optical Materials*, vol. 7, no. 21, p. 1900985, 2019, doi: 10.1002/adom.201900985.
- [48] “<https://www.verdict.co.uk/wearables-shipments-2018/>.”
- [49] “<https://www.marketsandmarkets.com/Market-Reports/flexible-heater-market-51373429>.”
- [50] “<https://www.geomatec.com/products-and-solutions/heating/transparent-heaters/>.”
- [51] C. Kim, M. J. Lee, S.-J. Hong, Y.-S. Kim, and J.-Y. Lee, “A flexible transparent heater with ultrahigh thermal efficiency and fast thermal response speed based on a simple solution-processed indium tin oxide nanoparticles-silver nanowires composite structure on photo-polymeric film,” *Composites Science and Technology*, vol. 157, pp. 107–118, Mar. 2018, doi: 10.1016/j.compscitech.2018.01.029.
- [52] Q. Huang, K. N. Al-Milaji, and H. Zhao, “Inkjet Printing of Silver Nanowires for Stretchable Heaters,” *ACS Appl. Nano Mater.*, vol. 1, no. 9, pp. 4528–4536, Sep. 2018, doi: 10.1021/acsnm.8b00830.
- [53] D. T. Papanastasiou *et al.*, “Transparent Heaters: A Review,” *Advanced Functional Materials*, vol. 30, no. 21, p. 1910225, 2020, doi: 10.1002/adfm.201910225.
- [54] D. Langley, “Silver nanowire networks: Effects of percolation and thermal annealing on physical properties,” PhD thesis, University of Grenoble Alpes (France), University of Liège (Belgium), 2014.
- [55] D. P. Langley, M. Lagrange, N. D. Nguyen, and D. Bellet, “Percolation in networks of 1-dimensional objects: comparison between Monte Carlo simulations and experimental observations,” *Nanoscale Horizons*, vol. 3, no. 5, pp. 545–550, 2018, doi: 10.1039/C8NH00066B.
- [56] D. P. Langley *et al.*, “Metallic nanowire networks: effects of thermal annealing on electrical resistance,” *Nanoscale*, vol. 6, pp. 13535–13543, Sep. 2014, doi: 10.1039/C4NR04151H.

- [57] M. Lagrange, D. P. Langley, G. Giusti, C. Jiménez, Y. Bréchet, and D. Bellet, "Optimization of Silver Nanowire-Based Transparent Electrodes: Effects of Density, Size and Thermal Annealing," *Nanoscale*, vol. 7, no. 41, pp. 17410–17423, Oct. 2015, doi: 10.1039/C5NR04084A.
- [58] M. Lagrange, "Physical analysis of percolating silver nanowire networks used as transparent electrodes for flexible applications," PhD thesis, University of Grenoble Alpes (France), 2015.
- [59] M. Lagrange *et al.*, "Understanding the mechanisms leading to failure in metallic nanowire-based transparent heaters, and solution for stability enhancement," *Nanotechnology*, vol. 28, no. 5, p. 055709, 2017, doi: 10.1088/1361-6528/28/5/055709.
- [60] T. Sannicolo *et al.*, "Direct Imaging of the Onset of Electrical Conduction in Silver Nanowire Networks by Infrared Thermography: Evidence of Geometrical Quantized Percolation," *Nano Letters*, vol. 16, no. 11, pp. 7046–7053, Nov. 2016, doi: 10.1021/acs.nanolett.6b03270.
- [61] T. Sannicolo, "Transparent Electrodes based on Silver Nanowire Networks: Electrical Percolation, Physical Properties, and Applications," PhD thesis, University of Grenoble Alpes (France), 2017.
- [62] V. H. Nguyen *et al.*, "Low-cost fabrication of flexible transparent electrodes based on Al doped ZnO and silver nanowire nanocomposites: impact of the network density," *Nanoscale*, vol. 11, no. 25, pp. 12097–12107, 2019, doi: 10.1039/C9NR02664A.
- [63] V. H. Nguyen, "Development of transparent electrodes by vacuum-free and low cost deposition methods for photovoltaic applications," PhD thesis, University of Grenoble Alpes (France), 2018.
- [64] D. (Theodora) Papanastasiou, "Investigation of Silver Nanowire Networks: physical properties, stability and integration into devices," PhD thesis, University of Grenoble Alpes (France), 2020.
- [65] H. Majidi and J. B. Baxter, "Electrodeposition of CdSe coatings on ZnO nanowire arrays for extremely thin absorber solar cells," *Electrochimica Acta*, vol. 56, no. 6, pp. 2703–2711, Feb. 2011, doi: 10.1016/j.electacta.2010.12.044.
- [66] T. Lei *et al.*, "Bendable and foldable flexible organic solar cells based on Ag nanowire films with 10.30% efficiency," *J. Mater. Chem. A*, vol. 7, no. 8, pp. 3737–3744, Feb. 2019, doi: 10.1039/C8TA11293B.
- [67] A. G. Ricciardulli, S. Yang, G.-J. A. H. Wetzelaer, X. Feng, and P. W. M. Blom, "Hybrid Silver Nanowire and Graphene-Based Solution-Processed Transparent Electrode for Organic Optoelectronics," *Adv. Funct. Mater.*, vol. 28, no. 14, p. 1706010, Apr. 2018, doi: 10.1002/adfm.201706010.
- [68] A. R. bin M. Yusoff, S. J. Lee, F. K. Shneider, W. J. da Silva, and J. Jang, "High-Performance Semitransparent Tandem Solar Cell of 8.02% Conversion Efficiency with Solution-Processed Graphene Mesh and Laminated Ag Nanowire Top Electrodes," *Advanced Energy Materials*, vol. 4, no. 12, p. 1301989, 2014, doi: 10.1002/aenm.201301989.
- [69] A. Kim, Y. Won, K. Woo, S. Jeong, and J. Moon, "All-Solution-Processed Indium-Free Transparent Composite Electrodes based on Ag Nanowire and Metal Oxide for Thin-Film Solar Cells," *Adv. Funct. Mater.*, vol. 24, no. 17, pp. 2462–2471, May 2014, doi: 10.1002/adfm.201303518.
- [70] X. Zhang, J. Wu, J. Wang, Q. Yang, B. Zhang, and Z. Xie, "Low-Temperature All-Solution-Processed Transparent Silver Nanowire-Polymer/AZO Nanoparticles Composite Electrodes for Efficient ITO-Free



Polymer Solar Cells,” *ACS Applied Materials & Interfaces*, vol. 8, no. 50, pp. 34630–34637, Dec. 2016, doi: 10.1021/acsami.6b11978.

- [71] K. S. Lee, Y. Lee, J. Y. Lee, J.-H. Ahn, and J. H. Park, “Flexible and Platinum-Free Dye-Sensitized Solar Cells with Conducting-Polymer-Coated Graphene Counter Electrodes,” *ChemSusChem*, vol. 5, no. 2, pp. 379–382, 2012, doi: 10.1002/cssc.201100430.
- [72] A. Garcia-Leis, I. Rivera-Arreba, and S. Sanchez-Cortes, “Morphological tuning of plasmonic silver nanostars by controlling the nanoparticle growth mechanism: Application in the SERS detection of the amyloid marker Congo Red,” *Colloids and Surfaces A: Physicochemical and Engineering Aspects*, vol. 535, pp. 49–60, Dec. 2017, doi: 10.1016/j.colsurfa.2017.09.013.
- [73] Y. Sun and Y. Xia, “Large-Scale Synthesis of Uniform Silver Nanowires Through a Soft, Self-Seeding, Polyol Process,” *Advanced Materials*, vol. 14, no. 11, pp. 833–837, 2002, doi: 10.1002/1521-4095(20020605)14:11<833::AID-ADMA833>3.0.CO;2-K.
- [74] T. K. Sau and C. J. Murphy, “Room Temperature, High-Yield Synthesis of Multiple Shapes of Gold Nanoparticles in Aqueous Solution,” *Journal of the American Chemical Society*, vol. 126, no. 28, pp. 8648–8649, Jul. 2004, doi: 10.1021/ja047846d.
- [75] E. Hao, R. C. Bailey, G. C. Schatz, J. T. Hupp, and S. Li, “Synthesis and Optical Properties of ‘Branched’ Gold Nanocrystals,” *Nano Letters*, vol. 4, no. 2, pp. 327–330, Feb. 2004, doi: 10.1021/nl0351542.
- [76] P. Pallavicini *et al.*, “Triton X-100 for three-plasmon gold nanostars with two photothermally active NIR (near IR) and SWIR (short-wavelength IR) channels,” *Chem. Commun.*, vol. 49, no. 56, pp. 6265–6267, Jun. 2013, doi: 10.1039/C3CC42999G.
- [77] I. Seshadri, G. L. Esquenazi, T. Cardinal, T. Borca-Tasciuc, and G. Ramanath, “Microwave synthesis of branched silver nanowires and their use as fillers for high thermal conductivity polymer composites,” *Nanotechnology*, vol. 27, no. 17, p. 175601, Mar. 2016, doi: 10.1088/0957-4484/27/17/175601.
- [78] S. Mertens and C. Moore, “Continuum Percolation Thresholds in Two Dimensions,” *Physical Review E*, vol. 86, no. 6, Dec. 2012, doi: 10.1103/PhysRevE.86.061109.
- [79] J. P. Gonzalez-Vazquez, J. A. Anta, and J. Bisquert, “Determination of the electron diffusion length in dye-sensitized solar cells by random walk simulation: Compensation effects and voltage dependence,” *The Journal of Physical Chemistry C*, vol. 114, no. 18, pp. 8552–8558, 2010, doi: 10.1021/jp100874e.



## **Chapter 1**

**Transparent electrodes based on silver nanowire networks, synthesis of nanowires, properties of networks and applications in opto-electronic devices**



In this chapter, we will present a brief review of the importance of transparent conductive materials in modern electro-optical devices. Although transparent conductive oxides (TCO) based on rare metals like Indium doped Tin Oxide (ITO), show electro-optical properties which are acceptable for many applications, sheet resistances below  $10 \Omega\text{sq}^{-1}$  and optical transmittance above 90%, there are several limitations which promote the need to find substitutional materials to replace ITO. Transparent electrodes based on metallic nanowires (MNWs), mostly silver NWs, are among the most interesting candidates to replace ITO. Optimization of AgNW based TEs, from synthesis process of solutions containing NW to obtaining efficient junctions between NWs and forming conductive random networks along with electro-optical properties of networks is discussed in this chapter. Finally, we will present a brief review on some of the successful integration of AgNWs in functional devices, discussing advantages of this material over classic transparent metal oxides, as well as the limitations of using AgNWs.

### **1.1. Transparent Conductive Materials**

There has been extensive research in past decades devoted to transparent conductive materials (TCMs). Transparent electrodes (TEs) have a wide range of applications in many modern opto-electronic devices, such as organic light-emitting diodes (OLEDs), touch screens, solar cells, e-papers, transparent heaters (THs), and sensors.[1] Wide bandgap conductive metal oxides like Indium doped Tin Oxide (ITO), Fluorine doped Tin Oxide (FTO), or Aluminum doped Zinc Oxide (Al:ZnO) have been widely used as TCMs.[2] The most successfully commercialized transparent conductive material to date, ITO, shows interesting electrical and optical properties, sheet resistance below  $10 \Omega\text{sq}^{-1}$  and total transmittance above 90% for a wavelength of 550 nm. Despite these interesting properties, there has been extensive research in the last years to introduce alternative materials to replace ITO. The scarcity of indium, together with the vacuum-based expensive fabrication methods like sputtering and the lack of mechanical flexibility of ITO, are the main reasons behind this urge to replace ITO by new candidates.[3] Several potential emerging materials include random networks of MNWs, conductive polymers[4], [5] or carbon-based materials like Carbon Nano Tubes (CNTs) or graphene.[3], [6] In particular, percolative networks composed of high aspect ratio metallic MNWs are promising candidates among these emerging materials.[7]–[9] MNW networks exhibit excellent electro-optical properties comparable to ITO, along with high mechanical flexibility.[10] Many research groups have optimized MNW networks with optical transmittance above 90% and sheet resistance of less than  $10 \Omega\text{sq}^{-1}$ , confirming that MNW networks stand as an outstanding candidate among other TCMs in terms of the trade-off between transparency and electrical resistance.[9] In addition, the consumption of metal is much reduced in these MNW based electrodes as compared to the required indium amount in ITO based electrodes to obtain similar properties. As an example, Silver nanowire (AgNW) based networks with Ag areal mass density around 100 to 200

mg/m<sup>2</sup> show electrical sheet resistance below 5 Ωsq<sup>-1</sup> and total transmittance around 89% at 550 nm,[11] while for ITO films with thickness of 150 nm and similar electro-optical properties, In areal mass density is around 900 mg/m<sup>2</sup>. [12] Table 1-1 shows the geographical distribution of indium and silver resources around the world in last few years, and clearly confirms the advantage of silver over indium in its overall abundance and availability.

<b>Indium</b>			<b>Silver</b>			
<i>Countries</i>	<i>2015</i>	<i>2016</i>	<i>Countries</i>	<i>2016</i>	<i>2017</i>	<i>Reserves</i>
United states	-	-	United states	1150	1020	25000
Canada	70	65	Bolivia	1,350	1,200	22,000
Belgium	20	25	Australia	1,420	1,200	89,000
China	350	290	Chile	1,500	1,200	27,000
France	41	-	China	2,380	2,500	39,000
Japan	70	70	Kazakhstan	1,180	1,200	NA
Republic of Korea	195	195	Mexico	5,360	5,600	37,000
Peru	9	5	Peru	4,370	4,500	93,000
Russia	4	5	Poland	1,270	1,400	89,000
			Russia	1,570	1,600	55,000
			Other countries	4,100	3,600	57,000
<b>World total (rounded)</b>	<b>759</b>	<b>655</b>	<b>World total (rounded)</b>	<b>25,700</b>	<b>25,000</b>	<b>530,000</b>

Table 1-1: World Indium resources and mine production and reserves of silver, confirming the abundance of silver compared to indium. Numbers are in metric ton. Reported by U.S. Geological Survey (there were no reported numbers for reserves of Indium). [13]

## 1.2. AgNWs: synthesis and properties of single NWs

Random networks of various MNWs (mainly silver, copper or cupronickel) are among the most attractive candidates to replace conventional TCOs like ITO. Among the different MNW networks, the ones based on AgNWs

appear to be the most attractive candidate thanks to the simple synthesis of AgNWs and since they meet the required electro-optical properties for many applications, due to the fact that silver has the highest electrical conductivity at room temperature. Low-cost and scalable synthesis of silver NWs has been studied in the last two decades. In this section, we will present a brief review over production methods of AgNWs, followed by electrical properties of a single AgNW and junction between two NWs before and after sintering process.

### 1.2.1. Synthesis of AgNWs: polyol process

Solution-based techniques, mainly based on the polyol process are used for mass production of AgNWs. Polyol method, initially introduced by Xia et al. has been widely used to synthesize high aspect ratio AgNWs.[14] The process involves reduction of silver salts (silver nitrate) by ethylene glycol in the presence of Poly Vinyl Pyrrolidone (PVP).[14], [15] Schematic representation of polyol process is presented in Figure 1-1.a-b. The growth starts with multiply twin particles (MTPs) of Pt or Ag with diameters of few nanometers which have 5-fold symmetry, with surface bounded by {111} crystallographic face. PVP strongly interacts with {100} face of nanoparticles and leaves {111} faces free for adsorption of silver atoms, the growth occurs on these faces. As a result we obtain one-dimensional NWs, while there is an amorphous thin layer of PVP present around {100} faces as shown in the Transmission electron microscopy (TEM) image in Figure 1-1.c. The cross-sectional TEM image in Figure 1-1.d clearly shows the 5-fold symmetry of AgNWs.[16] This synthesis process leads to the formation of AgNWs with average diameters between 20 to 150 nm and lengths in the ranges of few tens of  $\mu\text{m}$ . Commercially synthesized AgNWs are available from many companies like Cambrios, Sigma Aldrich, BASF (former Seashell), blue nano and ACS materials. AgNWs used in this study are mainly purchased from ACS materials and Seashell companies. A Scanning electron microscopy (SEM) image of ACS MNWs with average diameter of 90 nm is presented in 1-1.e. Final products of AgNWs are in solvents like water or alcohols including ethanol, methanol or Isopropyl alcohol (IPA). Methods for deposition and post-deposition treatments which are performed on AgNWs to form high-quality TEs will be discussed in details in chapter 2.

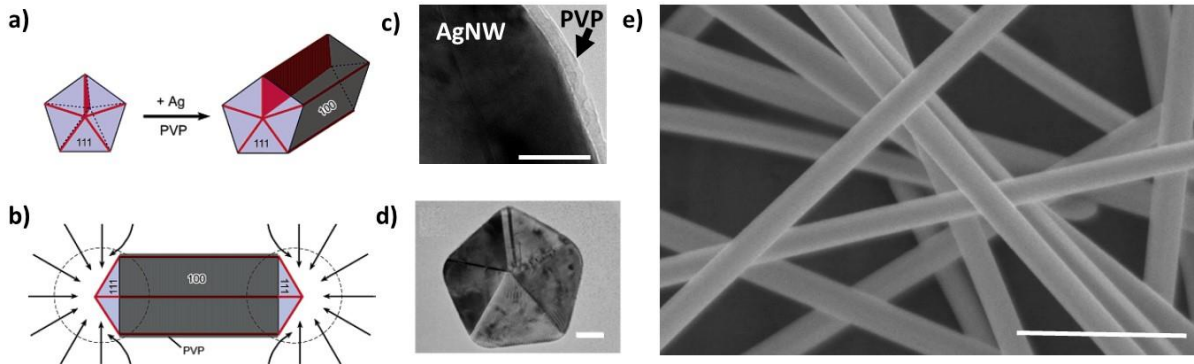


Figure 1-1. a-b) Schematic illustration of Polyol process based growth of AgNWs. a) Growth of high aspect ratio nanowire from five-fold symmetric twin plane in presence of PVP. PVP interacts strongly with {100} and leaves {111} giving rise to an anisotropic growth. b) Silver atoms can be adsorbed on both free ends of a nano-rod, then increasing the aspect ratio. [14] c) TEM image of ACS material AgNW with diameter of 90 nm, scale bar is 5 nm. d) The cross-section TEM image of the as-prepared nanowire, scale bar is 20 nm.[16] e) SEM image of ACS material AgNW, average diameter of NWs around 90 nm, scale bar is 500 nm. [17]

### 1.2.2. The electrical conductivity of an individual silver NW

Although bulk silver has the highest conductivity at room temperature, silver NWs might show different electrical resistance due to the surface scattering of electrons when the diameter of NWs is about the electrons mean free path of bulk Ag. The relationship between single nanowire resistance and its diameter was first formulated and experimentally confirmed by Bid et al.[18] They suggest that electrical resistance of single NWs follows as:

$$\rho_{NW}^{Ag} = \rho_{bulk}^{Ag} \left( 1 + \frac{\lambda}{2D_{NW}} \right) \quad (1-1)$$

Where  $\rho_{NW}^{Ag}$  and  $\rho_{bulk}^{Ag}$  are the resistivity of nanowire and bulk nanowire, respectively,  $D_{NW}$  is the diameter of nanowire and  $\lambda$  bulk silver free path (around 40 nm).[18] While AgNW with a diameter of 15 nm has the resistivity of 4.11  $\mu\Omega$  cm, bigger NWs, i.e NW with diameter of 200 nm exhibit a resistivity of 2.33  $\mu\Omega$  cm. However, even thinner NWs can meet the required electrical resistance in many applications.[11] The main issue regarding the thin NWs can be their lower stability while they undergo high electrical or thermal stresses as we will discuss in section 3.1.



### 1.2.3. Sintering junctions between adjacent AgNWs to form conductive networks

Although individual AgNWs have rather low resistivity values (few  $\mu\Omega\text{cm}$ ), as deposited AgNW networks often suffer from high electrical resistance. The reason behind this issue is a lack of efficient wire to wire contacts. Song et al. showed that as-deposited NW junctions can have resistances up to  $10^{10} \Omega$ . [19] High contact resistance in junction points arises from two main sources: i, as discussed in section 1.2.1, AgNWs are encapsulated with a thin (few nanometers) layer of insulating surfactant PVP during the synthesis process and this insulating layer, limits the conductivity in junction points. ii, the contact area between two NWs is very limited as shown in Figure 1.2.a1. This makes essential to perform an extra post-deposition treatment to form an intimate contact between the junctions. Thermal annealing,[11] mechanical pressure,[20] joule heating,[19], [21] plasmonic welding,[22], [23] coating NWs by metal oxide layers like Al:ZnO, Titanium dioxide ( $\text{TiO}_2$ ), CNTs[24] or graphene,[25] and applying pulse laser rapid heating[26] are among well-described processes to treat NW to NW junctions. A full junction optimization process, includes two main mechanisms which allow the formation of efficient junctions between NWs, first the PVP surfactant softening or deformation, second the surface diffusion of silver in the junction points to allow the atoms to diffuse around and on to other NWs to create higher junction area. Figure 1-2.a1-a2 show schematic illustration of two adjacent NWs before and after sintering the junction, respectively.

Some of the post-treatment techniques focus only on the deformation, softening or thinning of PVP surfactant. Glass transition temperature (the temperature which polymers become rubbery) of PVP surfactant strongly depends on the molecular weight, Buera et al. showed that for ( $M_w = 40\,000 \text{ g mol}^{-1}$ ), glass transition of PVP is close to 140-150 °C. [27] Therefore, energy applied on the NWs using thermal annealing, electrical annealing, or plasmonic welding can lead to softening of PVP shell. On the other hand, PVP is hygroscopic, which means it tends to absorb high humidity. Absorption of water leads to a decrease in the glass transition temperature down to (45-85 °C). Therefore, PVP layer can melt down and allow NWs to efficiently intercalate. [28] Weiß et al. showed that humidity assisted welding of AgNWs, can be as efficient as conventional annealing at high temperatures. They confirmed that exposing AgNW network to 85% room humidity at temperatures around 60°C for 50 minutes is enough to sinter AgNWs with diameter of 90 nm and reduce the network overall resistance by two orders of magnitude. [28] Figure 1-2.b1 shows a SEM image of two AgNWs with average diameter of 90nm, which have been annealed at 70% room humidity and 70°C for 180 mins, white arrows illustrate better contact of NW to the substrate as well as improved NW to NW junction.

Another interesting approach to deal with PVP insulating layer is presented by Lee et al. where they have used a solution-based technique to wash PVP coated AgNWs in a polar solvent (methanol) and repeat the washing/ filtering

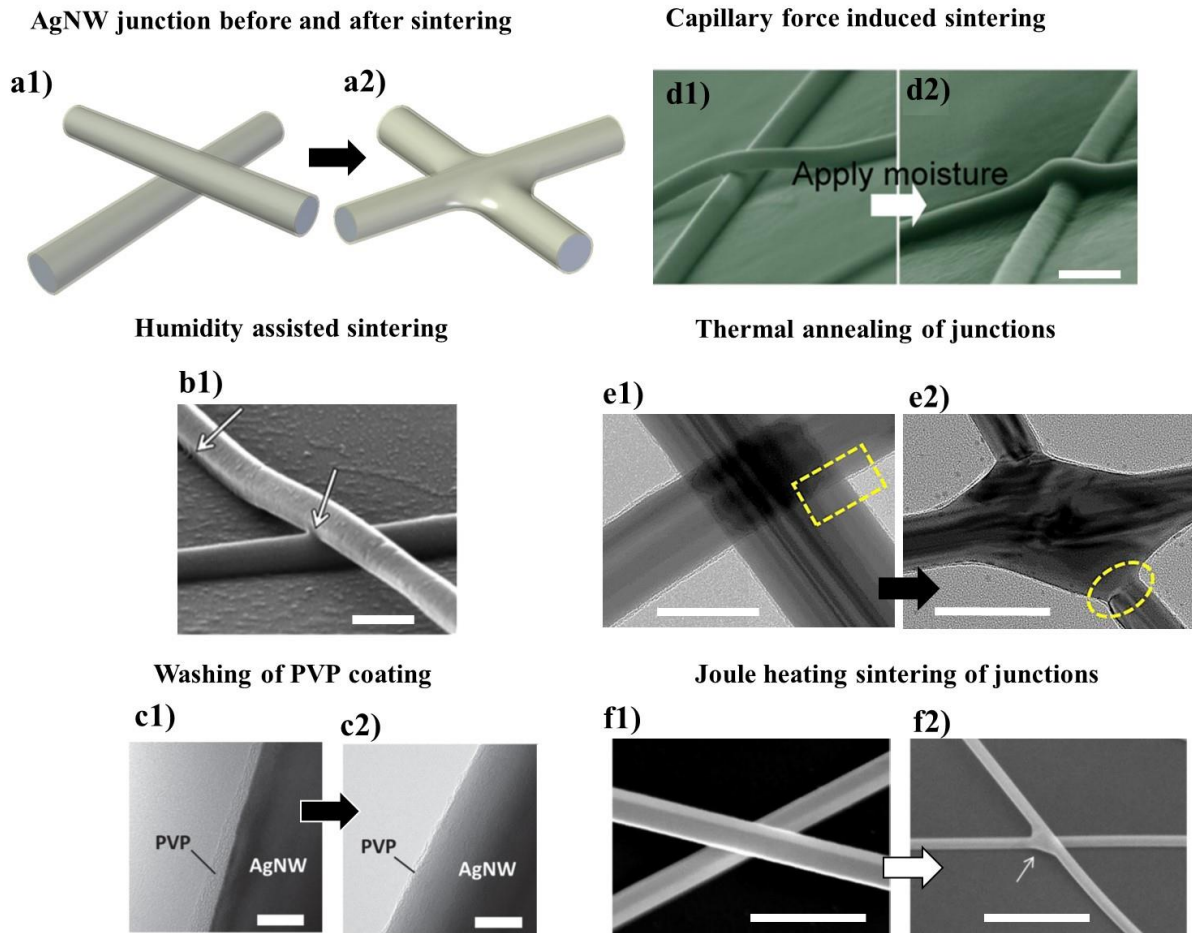


Figure 1-2. a1-2) Schematic view of two NWs before and after junction sintering. b1) SEM image of humidity assisted NW junction, scale bar is 200nm. [28] c1) SEM image of one time and c2) five times solvent washed AgNW, showing the lowering of PVP thickness by the number of washing cycles, scale bar is 10 nm. [29] d1-2) SEM images of a Ag NW to NW junction before and after moisture treatment, Scale bar is 200 nm. [30] e1) TEM image of junction between Seashell AgNWs after deposition, scale bar 50 nm, e2) TEM image of junction between Seashell AgNWs after annealing at 180°C for 60 minutes, morphological reorganization of the junction is clearly visible. Scale bar is 100 nm. [31] f1) SEM of a AgNW junction before (scale bar is 200 nm) and f2) after the electrowelding treatment, scale bar is 500 nm. [19]

steps for 5 consecutive steps which leads to a decrease in the thickness of PVP layer from 4 nm to 0.5 nm as shown in Figure 1-2.c1-2.[29] The decrease in the PVP thickness leads to a drop in the sheet resistance of a vacuum filtering deposited AgNW network from 71  $\Omega\text{sq}^{-1}$  to 18.9  $\Omega\text{sq}^{-1}$  (approximate transmittance 94%).

Another low-temperature technique to form sintered junctions between AgNWs is using the capillary force during drying of applied vapour on the nanowire network. Liu et al. showed that capillary force induced between adjacent NWs can be as efficient as mechanical pressing for welding AgNWs and reach up to 10 MPa to GPa levels.[30] As

a result, a more intimate junction is observed between adjacent NWs as shown in Figure 1-2.d1 and d2 which present two adjacent NWs before and after applying moisture. Controlled applying of moisture can enhance the electrical conductivity of the entire AgNW network, from the ranges of several  $\text{k}\Omega\text{sq}^{-1}$  to tens of  $\Omega\text{sq}^{-1}$ , while it does not have the limitations of thermal annealing or mechanical pressing in the used substrate. [30]

However, although the techniques discussed above improve the junction resistance between two adjacent AgNWs and have been proved to have a considerable effect on the electrical resistance of the AgNW network, a full optimization of the junctions and therefore electrical conductivity of the network requires reduction of the total surface energy of NWs and sintering of junctions which leads to surface/body diffusion of silver atoms and formation of fully sintered junctions. Therefore, thermal annealing is one of the most popular and well-studied techniques to optimized AgNW networks electro-optical properties.[11], [32]

A good example of characterization of NW-NW junction before and after thermal annealing has been presented by Sannicolo et al.[31] They have performed TEM observations on as-deposited and thermally annealed Seashell AgNWs. AgNWs were spray coated on copper-based TEM grids filled with an amorphous holed carbon matrix. Junction of as-deposited networks were compared to those annealed at  $180^{\circ}\text{C}$  for 60 mins. As shown in Figure 1-2.e1, non-annealed adjacent AgNWs are totally straight, covered with a thin PVP shell. While annealed networks clearly illustrate diffusion of Ag atoms which leads to the morphological reorganization of the junctions, see Figure 1-2.e2. However, these TEM images show that PVP layer is still present around the “optimized” junctions, although its chemical nature might be affected by annealing process. Since the annealing temperature is higher than glass transition of PVP, diffusion of PVP has also occurred at the junction points, allowing physical contact of adjacent AgNWs and full sintering of junctions.[31]

Because of its simplicity, thermal annealing at temperature ranges around  $140\text{--}250^{\circ}\text{C}$  remains the most favoured method for optimization of electrical resistance of AgNW networks. However, the utilization of thermal annealing is a long and high power consumption process which is restricted in the case of organic electronics and especially for flexible substrates. One fast and low-power consumption way to improve electrical resistance of AgNW network is current assisted localized joule heating. Song et al. confirmed that the use of localized reactions induced by an electrical current flow can significantly improve the contact properties of adjacent NW in MNW network as shown in Figure 1-2.f1-2. [19] Sintering of junction by electromigration due to joule heating will be discussed in details in section 3.1.2. The main advantage of electrical welding to thermal annealing process is the fact that the temperature of the adjacent device layers can be kept close to room temperature during the process, therefore unlike thermal

annealing this method is suitable for use in devices which contain thermally sensitive materials such as polymer solar cells.

### 1.3. Properties of networks consisted of AgNWs: the study of electro-optical properties and figure of merit versus network density

#### 1.3.1. Electrical resistance of AgNW networks

So far we have discussed the electrical properties of single NWs and junctions between adjacent NWs. Another critical parameter which affects the overall electrical resistance of a AgNW network is the density of network,  $n$ , which defines the number of NWs per unit area. As we will discuss in the framework of percolation theory, in section 4.3 and 4.4, for each geometry of NWs, there is a critical network density,  $n_c$ , where the possibility of occurring percolation equals to 50%. The occurrence of percolation is mandatory in order to have electrical conductivity in the network, therefore in the study of electrical resistance, we focus on networks which have densities up to few times  $n_c$ , to guarantee percolation. Monte Carlo simulations show a link between the average length of NWs,  $L_{nw}$ , and critical density,  $n_c$ , as :[33]

$$n_c \cdot L_{nw}^2 = 5.64 \quad (1-2)$$

Coleman et al.[34] have shown that for transparent electrodes composed of silver NWs or CNTs, graphene or silver platelets, in the cases of rather thin networks with optical transmittance above 90%, conductivity falls in percolation regime and can be modelled as :

$$\sigma \propto (n - n_c)^v \quad (1-3)$$

Where for 2D networks,  $v$  equals to  $\frac{4}{3}$ . [34] but this is more practical to deal with areal mass density ( $amd$ ), which is usually reported as mass of NWs per unit area (often expressed in  $mg/m^2$ ), rather than  $n_c$ , therefore Lagrange et al.[11] re-wrote Equation 1-3 as:

$$\sigma \propto (amd - amd_c)^v \quad (1-4)$$

$$amd_c = \text{average mass of NW} \times n_c = \left( \frac{d_{bulk}^{Ag} \cdot \pi D_{nw}^2 \cdot L_{nw}}{4} \times \frac{5.64}{L_{nw}^2} \right) \quad (1-5)$$

Where  $d_{bulk}^{Ag}$  is the mass density of bulk silver and  $L_{nw}$  and  $D_{nw}$  are the dimensions of NWs (Assuming cylindrical shape for NWs in spite of their pentagonal cross-section). Therefore, the dependency of sheet resistance upon  $amd$  can be modelled as:

$$R = R_0 + C \cdot \rho_{NWs}^{Ag} (amd - amd_c)^{-\gamma} \quad (1-6)$$

Where  $R_0$  is the contact resistance and  $C$  is a fitting parameter. Lagrange et al. have developed the model for network resistance as based on Equation 1-1, 1-5 and 1-6 as [11]

$$R(amd, D_{nw}, L_{nw}) = R_0 + C \cdot \rho_{bulk}^{Ag} \cdot \left( 1 + \frac{\Lambda}{2 \cdot D_{nw}} \right) \left( amd - \frac{5.64 \cdot d_{bulk}^{Ag} \cdot \pi D_{nw}^2}{4 \cdot L_{nw}} \right)^{-\gamma} \quad (1-7)$$

The only unknown parameters are  $R_0$ , (contact resistance) and  $C$  which can be obtained by fitting experimental data with formula. Experimental data are obtained from AgNW networks fabricated by spin coating of Seashell AgNWs (synthesized by Polyol process). AgNWs with  $D_{nw}$  of 117 nm and  $L_{nw}$  of 42.9  $\mu\text{m}$  are spin-coated on corning glass substrates, annealed at 200°C for 2 hours to reach their minimum sheet resistance.  $R_0$  and  $C$  have been reported 0.8  $\Omega$  and  $7 \times 10^{10} \text{ mg}^{4/3} \cdot \text{m}^{-11/3}$  respectively. [10] Figure 1-3.a shows good agreement between the experimental values of  $R_{sh}$  versus model described by Equation 1-7.

## 1.3.2. Optical properties of AgNW networks

### 1.3.2.1. Total Transmittance

Optimized AgNW networks, must have both high electrical conductivity and optical transparency. Figure 1-3.a confirmed that increasing the network density leads to higher electrical conductivity, however, there have been several studies which confirm that the optical transmittance of AgNW networks decreases linearly with the network areal mass density.[11], [35], [36] Shadowing effect is a simple explanation which can be used to justify the correlation between optical transmittance and network area covered with AgNWs. Lagrange et al. used a

slightly more sophisticated approach and showed that AgNW network total transmittance,  $T_{opt}^{net}$ , can be written

$$\text{as: } T_{opt}^{net} = 1 - \beta \cdot amd \quad (1-8-a)$$

where  $\beta$ , mainly depends on the dimensions of NWs and independent of  $amd$ .

$$\beta = \frac{4}{\pi \cdot d_{bulk}^{Ag} \cdot D_{nw}} \cdot (1 - (1 - R_{opt}^{AgNW}) \cdot T_{opt}^{AgNW}) \quad (1-8-b)$$

where  $R_{opt}^{AgNW}$  and  $T_{opt}^{AgNW}$  are the average optical reflectance and transmittance of a single AgNW respectively.

Although there is no experimental measurement for reflectance and transmittance values of single NWs, we can assume that  $R_{opt}^{AgNW}$  will be close to unit, like for bulk silver, therefore the dominant part of  $\beta$  values is the prefactor

$\frac{4}{\pi \cdot d_{bulk}^{Ag} \cdot D_{nw}}$ . Similar to  $R_{sh}$  values, there is as well, good agreement between the experimental values of total

transmittance versus model described by Equation 1-8 as shown in Figure 1-3.a.

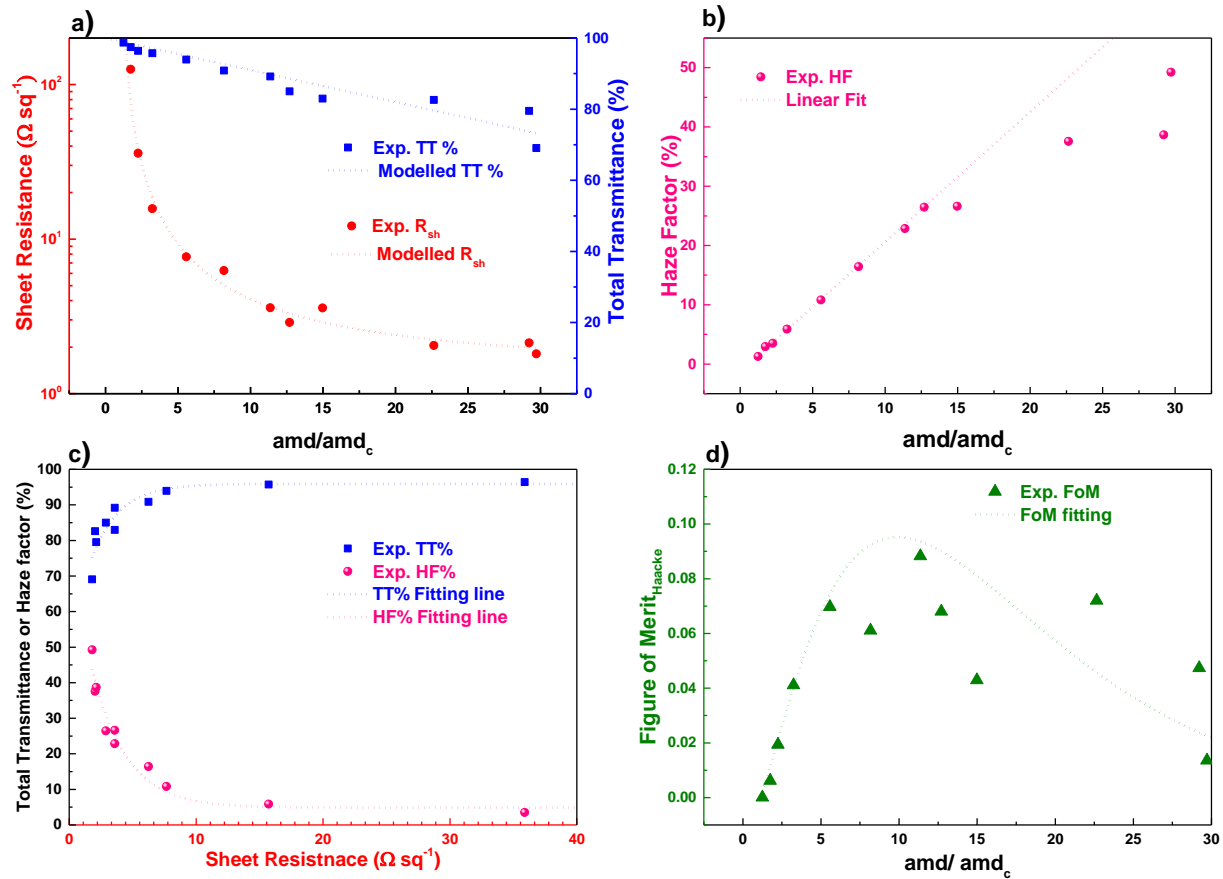


Figure 1-3. Electrical and optical properties of AgNWs (Average diameter 117 nm and average length 42.5  $\mu\text{m}$ ) purchased from Seashell and spin-coated on the glass substrate. a) Dependence of sheet resistance and optical transmittance versus reduced areal mass density ( $amd/amd_c$ ) of AgNW networks. Sheet resistance was measured after thermal annealing at 200°C for 120 mins. The dashed line corresponds to Equation (1-7). Total transmittance values are the average of two measurements at 550nm and dashed line corresponds to Equations (1-8-a and b).[11] b) Haze factor measurements of Seashell AgNW network versus reduced areal mass density, dashed line is guideline for the eye, confirming linear dependency of haze factor on areal mass density.[11] c) Optical transmittance and haze factor (both measured at 550 nm) dependence on sheet resistance.[10] d) Haacke's FoM values versus reduced amd, showing a trade-off between optical transmittance and electrical resistance to obtain best performance of the AgNW network.[11]

### 1.3.2.2. Diffuse transmittance and haze factor

The haze factor is a parameter that quantifies the amount of light scattered by the investigated material and is simply defined as the ratio between diffuse transmittance and total transmittance.

$$\text{haze factor} = \frac{\text{diffuse transmittance}}{\text{total transmittance}} \quad (1-9)$$

Depending on the target application, different properties regarding haziness are required. For example, low haze factor is essential to ensure the performance of touch panels and transparent heaters placed on windows in order to have unblurred viewing, while performance of solar cells might be enhanced by a high haze factor.[37], [38]

Finite difference time domain (FDTD) method to solve Maxwell equation, [39], [40] and Mie scattering theory have been used to estimate haze factor of AgNWs.[41] Results of both methods confirm that haze factor of AgNWs strongly depends on the diameter of NWs, and smaller NWs have smaller haze factor values. Lagrange et al. studied haze factor of Seashell AgNWs and clearly confirmed that haze factor is directly proportional to the areal mass density as shown in Figure 1-3.b.[11] Total transmittance and haze factor of AgNW networks is also plotted against  $R_{sh}$  values in Figure 1-3.c. This can be used as a guideline to find optimum network properties considering both electrical resistance and optical properties.

### 1.3.3. Figure of Merit

A standard way to evaluate the performance of transparent electrodes in terms of their electrical and optical properties is to define a figure of merit ( $FoM$ ) depending on the network density. Dense networks provide enough pathways for the electrical current, therefore they have low values of electrical resistance as shown in Figure 1-3.a, however due to shadowing effect the optical transmittance values will be rather low. On the contrary, sparse networks with high optical transmittance values, will not provide enough conductive paths and suffer from high resistance values. It is essential to find a trade-off between electrical resistance and optical transmittance. There are several ways to define  $FoM$ , in this study we used the definition by Haacke, which proposes the following  $FoM$  for finding a trade-off between electrical resistance and optical transmittance of TEs: [42]

$$FoM = \frac{T^{10}}{R_{sh}} \quad (1-10)$$

where  $T$  is the total transmittance measured at 550 nm, which is standard for instance when solar cells applications are considered, and  $R_{sh}$  is the sheet resistance values. As shown in figure 1-3.d, the  $FoM$  values, take a bell shape, and there is an optimum network density which provides best electro-optical properties. This density depends on several parameters, like the geometry of NW, deposition method and post-deposition treatments of networks, and has been reported around 100-200 mg/m<sup>2</sup> for AgNW networks.[11]



## **1.4. Applications of AgNWs in opto-electronic devices**

### **1.4.1. AgNW networks in solar cells**

Solar cells are one of the green alternatives to replace fossil fuels to meet today's increasing demand for energy. TCM is one of the key elements which is required in any type of solar cell devices, high transparency is required to allow the entrance of incident light and high electrical conductivity is essential to ensure sufficient harvesting of photo-generated charge carriers. ITO, due to its interesting electro-optical properties is one of the most widely used TCMs in different solar cell technologies. However, there are several limitations which induce large amount of research to find substitutional materials as the replacement of ITO. In general solar cells require relatively thick layers of transparent conductive materials (few hundreds of nm) compared with the relatively low thickness needed for display technologies (few tens of nm). The need for thick layers of TCMs along with the large area of solar cells results in high consumption of TCMs.[43], [44] This is critical due to drained resources of indium as we discussed in section 1.1. Moreover, the brittle nature of ITO, makes it incompatible with flexible solar cells, which have drawn intense attention due to very low-cost installation procedure.[45] Eventually third drawback, raises from high-cost, vacuum required and high-temperature deposition techniques of ITO which makes it a poor candidate for organic solar cells or any low-cost fabrication process. Solution-based organic solar cells have been the subject of high interest in both academy and industry due to their easy fabrication process which makes them economically competent although in general they have lower Power Conversion Efficiency (PCE) compared to crystalline silicon or thin film solar cells.[45] Substitutional materials have been studied as a replacement for ITO in flexible solar cells, including carbon nanotubes (CNT),[46] graphene,[47] metallic grids,[48] conductive polymers.[49] Metallic nanowire based network, especially AgNW based networks are among interesting candidates due to high electro-optical properties, high mechanical flexibility and low material consumption and solution-based scalable fabrication techniques. So far there have been several works reporting integration of AgNWs networks in solar cell devices including Organic Solar Cells (OSCs),[50]–[56] Dye Synthesized Solar Cells DSSCs,[57] thin film SCs like Cadmium Telluride (CdTe) or Cu(In,Ga)(S,Se)<sub>2</sub> (CIGSSe) SCs,[54] Polymer solar cells,[58] on glass or flexible substrates like Polyethylene terephthalate (PET). Main limiting factors in the implementation of AgNW networks in solar cell devices are, low work function of AgNWs and its adjacent film,[9], [59] which leads to lack of efficient ohmic contact between AgNWs and active layer, and the short-circuits due to highly non-uniform topography of as-deposited AgNW network.[56], [60] As deposited AgNWs, might not be aligned well along the substrate and cause shortening. This is more critical when using AgNWs as lower electrode which results in low shunt resistance, high dark current and poor final PCE values. [56] The latter can be improved by mechanical pressing of as deposited network. [61]

In spite of these limitations, successful integration of AgNWs into solar cells especially Organic PVs (OPV)s have been reported. For all of these configurations, an adjacent transparent conductive layer is utilized along with AgNWs. This additional layer can be ZnO,[44] AZO[54] or conducting polymers like poly (3,4-ethylenedioxythiophene) poly(styrenesulfonate) (PEDOT:PSS).[57] The reason behind this configuration is that percolating NW networks are composed of very high aspect ratio elements which have quite big voids between conducting paths. These wide openings lead to loss of photo-generated carriers due to recombination within n-type or buffer layer before being collected by the conducting network. Using this composite enhances the effective area for charge collection and leads to higher PCE values.[44]

Polymer solar cells are the main area for which most of the successful integration of AgNWs is reported. AgNW network due to its low-cost and solution-based fabrication process is compatible with other layers in polymer solar cells. Reinhard et al presented a fully solution-processed semi-transparent organic polymer solar cell which comprises AgNW as front electrode, the PCE of their solar cell is equivalent as the reference metal electrode-based opaque solar cells while the transmittance of front electrode is around 85% in the whole visible range. [52] Two different materials have been used between active layer (P3HT: PCBM) and AgNWs in order to facilitate charge extraction. They showed that conductive polymer (PEDOT:PSS) performs better than TCO ( $V_2O_5$ ) as buffer layer and results in higher PCE (2.3% instead of 0.57% ). [52] Yu et al. used the similar nanocomposite of AgNWs/ PEDOT:PSS over PCBM active layer on polymer substrates and showed that first, AgNWs/ PEDOT:PSS front electrode can provide similar PCE to ITO reference electrode (2.97% instead of 3%) and second, photovoltaic characteristics remain unchanged after one cycle of bending with radius of 5mm. [53] Similarly, Yang et al. reported PCE of 2.5% for AgNW/ PEDOT:PSS/PCBM/Ca/Al solar cell on PET substrate under large deformation with curvature radius of  $120^\circ$ . [59] Ajuria et al. demonstrated that ZnO nanoparticles can also be efficiently used next to AgNWs in PCBM organic solar cells to achieve PCE up to 3.2%. [62] Finally Kang et al. reported a highly flexible and efficient organic solar cell, which is completely fabricated by using brush painting. As shown in Figure 1-4.a AgNW network, adjacent PEDOT:PSS layer, PCBM based active layer, ZnO electron transporting and Al electrode layers are all deposited simply using paint brush with PCE of 2.055%. They confirmed superior flexibility of two-brush-painted AgNW to the reference ITO anode as a function of bending and showed its easy installation on different platforms as shown in Figure 1-4.b. Although the efficiency of AgNW based polymer solar cell is slightly lower than ITO based reference electrode, see Figure 1-4.c, its feasibility shows the potential of cost-efficient and flexible organic solar cell.

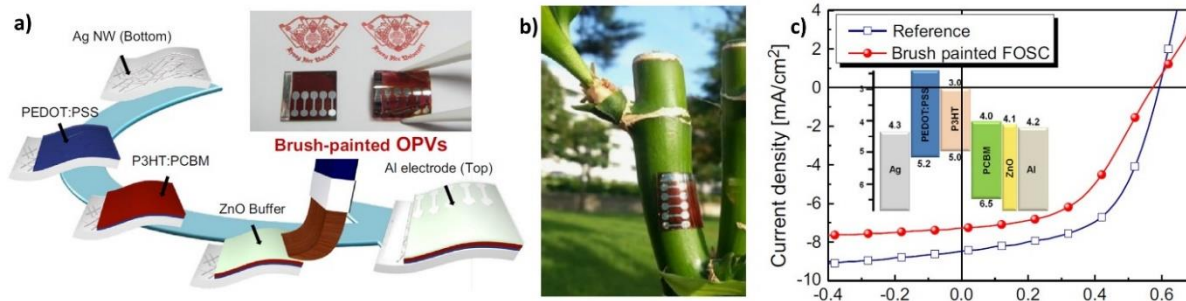


Figure 1-4. a) Schematic presentation of fully brush painting process of PCBM based solar cell using AgNW network as anode. b) Flexible brush painted organic solar cell. c)  $J-V$  curves of brush painted organic solar cell along with reference solar cell deposited on ITO/PET substrate. [45]

#### 1.4.2. AgNW networks in Light Emitting Diodes

Light emitting diodes (LEDs) are among the main applications of transparent electrodes based on MNWs. LED panels bear similarities to solar cells in their structure. Like solar cell devices, an active layer is sandwiched between two electrodes which at least one of them must be transparent to allow emission of light. Charge carriers are injected into the active layer and the electron-hole recombination leads to photon emission. Similar to previous applications mentioned above, ITO based electrodes are the most commonly used TEs in LED devices. However, the lack of flexibility of ITO and its vacuum required expensive fabrication techniques promotes the need to find substitutional materials to replace ITO. Organic LEDs (OLEDs) and Polymer-based LEDs are main types of lighting panels which require flexible and solution-based, low-cost transparent electrodes to be compatible with other elements of these devices. Although MNW based electrodes showed performances close to ITO based electrodes in LED devices by several groups,[63]–[69] an adjacent transparent conductive layer, PEDOT:PSS layer, is used next to MNW networks. The reason behind this structure are the following: i) avoiding current leakage due to high roughness of MNW networks, ii) adjusting work function of anode to enable higher injection of holes and iii) increasing the efficiency of charge carrier distribution. [64], [65], [67], [69] The latter is similar to the issue which MNW networks have in solar cell applications, due to the large voids between adjacent NWs electron-hole pairs, tend to recombine before arriving at the opposite electrodes. In Light emitting panels, the adjacent PEDOT:PSS layer can ease charge distribution to the semiconductor/ active layer. As shown in Figure 1-5.a by Li et al. use of PEDOT:PSS layer on AgNWs in a White Polymer LED, considerably improves current efficiency. [66]

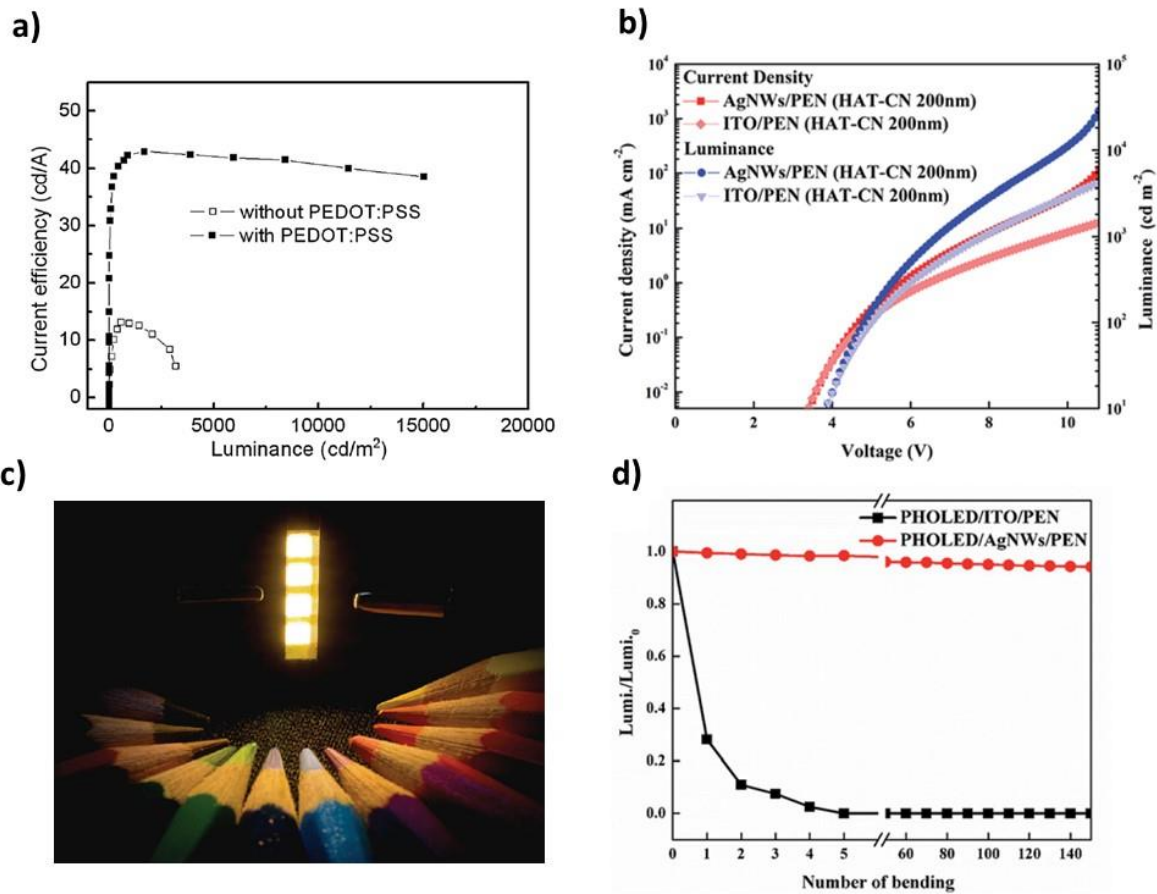


Figure 1-5. a) The comparison of current efficiency–luminance characteristics of the AgNW based OLED device with and without PEDOT:PSS layer. [66] b) Current density–voltage–luminance (J–V–L) characteristics of a flexible PHOLED with the AgNW/PEN and ITO/PEN transparent electrode. [70] c) Photographic image of operating AgNW based OLED with angular colour stability. [64] d) Comparison between mechanical flexibility test of the OLEDs based on AgNW/PEN and ITO/PEN transparent electrodes. [70]

Current efficiency, external quantum efficiency and luminous efficacy are among the main parameters which are used to evaluate the performance of lighting panels. Here, we have compared luminous efficacy (LE) of AgNW based and ITO based control devices with similar architecture. Zeng et al. [63] were among the first groups who showed that AgNW/PEDOT:PSS electrodes can provide higher power efficacy when compared to commercial ITO electrodes,  $2.43 \text{ lmW}^{-1}$  instead of  $1.62 \text{ lmW}^{-1}$ . One reason behind the higher efficiency for AgNWs based devices maybe light scattering. [63] Lee et al. showed that OLEDs employing n-type hole injection layers show higher power efficacy of  $35.8 \text{ lmW}^{-1}$  for AgNW based devices when compared to ITO based reference LEDs ( $28.1 \text{ lmW}^{-1}$ ). As

shown in Figure 1-5.b, current density- voltage- luminance (J-V-L) characterization of AgNW based OLEDs show similar performance as OLEDs fabricated on glass (using ITO electrodes). [70]

Along with high efficiency and low-cost fabrication process, modern LED devices require Lambertian emission. The latter means that the apparent brightness of the surface is the same than the observant regardless of its angle toward the lightning surface. Gaynor et al. were the first group who demonstrated a transparent electrode based on AgNWs can have angular colour stability as shown in Figure 1-5.c. [64]

Flexibility, both stretchability and bendability, is another critical property which MNW based TEs offer opposite to classic and brittle ITO based electrodes. [67], [68], [70] Lee et al. compared the mechanical flexibility of OLEDs of two different type of electrodes, AgNW/PEN and ITO/PEN.[70] As shown in Figure 1-5.d, device operation is tested after it was rolled around a bending radius of 7.5 mm and unrolled to the initial flat status. The luminous intensity is measured after each rolling cycle, as expected ITO based OLED sharply degrades its luminous intensity due to appearance of cracks in the ITO layer after initial bending cycles, while AgNWs based OLED remained almost unchanged after 150 cycles of wrapping, which is good proof of higher flexibility of MNW based LEDs compared to ITO based devices.

### **1.4.3. AgNW networks in transparent heaters**

History of Transparent heater (TH) films goes back to decades ago during World War II when these films were designed and used in order to defrost the windshield of aircrafts in high altitude and low-temperature conditions.[71] Although defogging and defrosting the windows of cockpits and automobiles still is one of the major demands which force the studies on THs, wide ranges of other applications, for example, outdoor security cameras, low-temperature operating display panels, sports goggles, helmets of motorcycles require fast and high-quality THs. Another interesting application is transparent microfluidic channels on glass or polymers which allows the study of biological samples in precisely controlled temperature, for example continuous polymer chain reaction (PCR),[72] or similar cell culturing microfluidic chips.[73] Although initial TH used conventional TCO films like ITO,[72]–[74] FTO [75], alternative materials like CNT,[76] graphene[77] have been successfully utilized as THs.

Simonato's group was the first one which demonstrated the concept of using AgNW network as flexible film heaters on the glass on PEN substrates.[78] Flexibility, high optical transmittance, excellent heating performance, fast response (steady-state temperature achieve in less than 200 s) and low silver consumptions (few tens of mg/m<sup>2</sup>) are

properties which make AgNWs interesting candidate for THs as well. [78] The power generated in TH films,  $P$ , follow Joule's first law:

$$P = \frac{V^2}{R} = R.I^2 \quad (1-11)$$

Where  $V$  is applied DC voltage and  $R$  is the total resistance, due to low resistances of AgNW networks high heat dissipation can be achieved for a low applied voltage ( below 12 volts). The temperature gets stabilized when heating power is equal to heat loss due to radiation, air convection and conduction through the substrate and support. Celle et al. showed that TH based on AgNWs can be stable during heating up and cooling down cycles for nearly 30 hours from room temperature up to 40° C.[78] Their idea was followed up by several groups.[79]–[83] Sorel et al.[81] were the first ones who provided a comprehensive description of power generated by joule heating on THs based on AgNWs as:

$$(1-12)$$

$$R.I^2 = (m_1C_1 + m_2C_2)\frac{dT(t)}{dt} + A(h_1 + h_2)\Delta T(t) + \sigma A(\epsilon_1 + \epsilon_2)(T(t)^4 - T_0^4) + \sigma_{cond}\Delta T(t)$$

In Equation 1-12, the term in the left represents power generated by joule heating. In the right side of the equation first term corresponds to heat generated in the substrate and the AgNW network,  $C$  the specific heat capacity and  $m$  the mass. The second term represents the heat loss by convection per time, where  $h$  is the convective heat transfer coefficient and  $A$  the area of the network. The third term corresponds to the part of heat loss by radiation, where  $\sigma$  is the Stefan-Boltzmann constant. Finally, the last term illustrates the outward conduction losses of the system. The latter can be through the conducting wires (used for electrical temperature measurement and electrical current apply) or the TH support. In all parameters index, 1 and 2 correspond to the AgNW network and substrate, respectively.  $\Delta T$  is the temperature difference between sample temperature  $T(t)$  and ambient temperature  $T_0$ . [81] Although there is no straightforward analytical solution for Equation 1-12, for small temperature raises, it can be solved as:

$$T(t) \approx T_0 + \frac{R.I^2}{\alpha A} \left[ 1 - \exp\left(-\frac{\alpha}{mC/A}t\right) \right] \quad (1-13)$$

Where  $\alpha = (h_1 + h_2) + 4(\epsilon_1 + \epsilon_2)\sigma T_0^3 + \alpha_{cond}$ . Therefore an increasing exponential decay function fit describes well the heat increment profile in the reported studies. The experimental values in the study of Sorel et.al fitted well

the fitting line from Equation 1-13 as illustrated in Figure 1-6.a for different applied currents.[81] Similar profiles for time-dependent temperature of AgNW based THs has been observed by other groups.[78]–[80], [83]

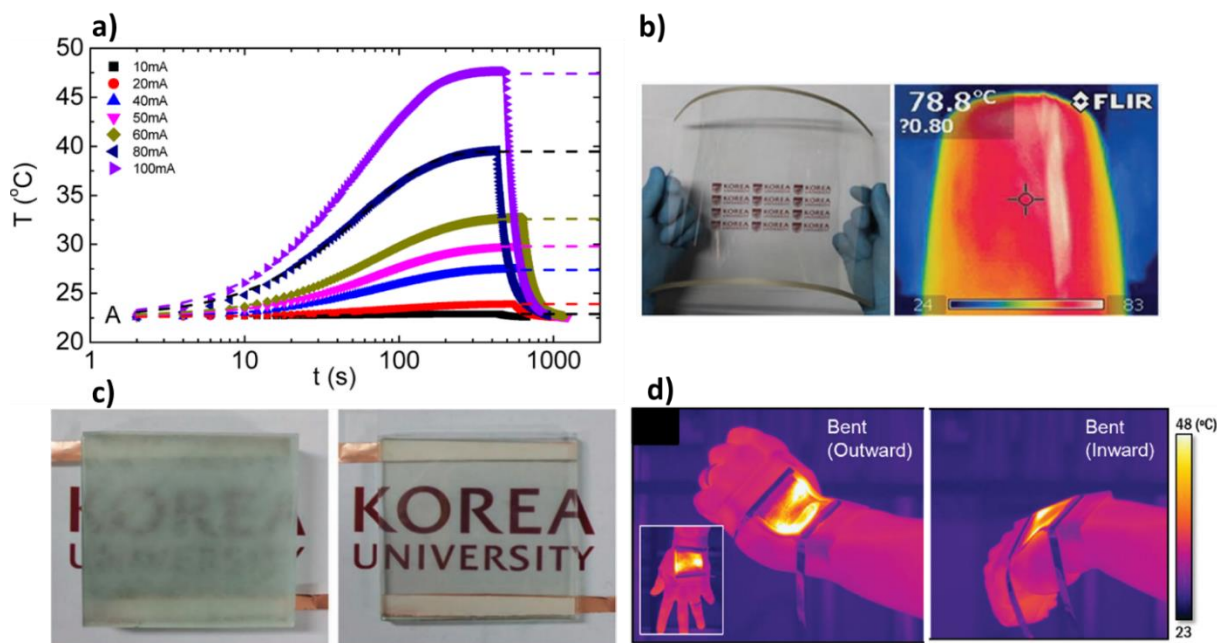


Figure 1-6.a) Time dependency of temperature rise for a AgNW network under different applied currents. The dashed lines represent fits to Equation 1-13.[81] b) A photograph and infrared image of the large-area AgNW-based TH (250 mm × 200 mm), confirming its mechanical flexibility. [79] c) Defrosting test results of a AgNW film heater: before and after frost removal due to applied 12 V.[79] d) infrared image of stretchable TH fixed to a human wrist at outward bending (left) and inward bending (right) conditions. Inset is an infrared image captured from a different angle.[83]

As we have discussed in the previous applications, the flexibility of AgNWs (both in bending and stretching) is one of the major advantages of these materials over conventional TCMs. Therefore, the possibility of using THs based on AgNW network on flexible substrates has been investigated widely in the literature. Kim et al designed and fabricated large area (250 mm × 200 mm) THs based on AgNWs on polyethylene terephthalate (PET) substrates and confirmed their mechanical flexibility as shown in Figure 1-6.b.[79] They showed the importance of homogenous NWs coating which leads to a uniform distribution of heat over the surface of TH, otherwise hot spots were detected on the heater surface and large gradient of temperature over the surface was observed. [79] They illustrated another potential application of AgNWs THs in Figure 1-6.c. AgNW network deposited on glass substrate has been kept in the fridge for 30 minutes in order to form a frost all over the AgNW network and glass.

The frost was removed after a 12 Volt DC voltage was applied on the AgNW network for only 60 seconds while making the logo below clearly visible.[79]

Hong et al. showed for the first time that stretchable THs can have the potential to be used in wearable electronics.[83] Wearable electronics have the application in personal thermal management[84] and health care.[85] They embedded randomly oriented AgNW network on Polydimethylsiloxane (PDMS) and showed their operation under 60% of strain in real-time deformation which mimics human motion. Figure 1-6.d illustrates temperature profiles at high temperature for two different conditions of inward and outward bending confirming the performance of TH in compressive and tensile strains.

## 1.5. Closing remarks

In this chapter, we discussed the great potential of AgNW based TEs to be integrated into many functional devices. High electro-optical properties, along with mechanical flexibility, vacuum-free, low-cost, and solution-based deposition technique and the low required amount of silver, are main reasons which make AgNW networks a competent candidate to replace ITO. However, there are some issues regarding TEs based on AgNWs which we are tackling within this project. Lack of stability, under thermal, electrical or environmental stress, is one of the main issues regarding successful integration of AgNW networks in functional devices. One efficient way to enhance stability is to coat AgNWs with transparent oxide layers like ZnO, Al<sub>2</sub>O<sub>3</sub>, or TiO<sub>2</sub>. However, conventional ways to deposit these metal oxide layers, like sputtering, CVD or ALD, are vacuum required and rather expensive, which is in contrast with one of the main advantages of AgNW networks. In this work, we examine the metal oxide layers, deposited by a novel vacuum-free and scalable technique called Spatial ALD (SALD) and compare different oxides in their stability improvement using different thickness values. Finally, last chapter of the study is dedicated to Monte Carlo simulations and studying the percolation behaviour of networks composed of different nano-objects. Thanks to recent advances in the synthesis of metallic nanoparticles which enables one to control the growth mechanism of these elements, more elaborated geometrical shapes like nano-stars or nano-cubes can be achieved. We search among different geometries to find nano-objects which have the lowest percolation threshold. Lowering the required total length of the material to reach percolation is critical since it enables us to fabricate lighter, cheaper and more transparent functional devices. We also studied the effect of the orientation of nano-objects on the



Chapter 1: Transparent electrodes based on silver nanowire networks, synthesis of nanowires, properties of networks and applications in opto-electronic devices \_\_\_\_\_

percolation of the networks they create and observed that, as the anisotropy of the network is increased, its percolation threshold increases as well.

## References:

- [1] D. Ginley, H. Hosono, and D. C. Paine, *Handbook of Transparent Conductors*. Springer Science & Business Media, 2010.
- [2] E. Fortunato, D. Ginley, H. Hosono, and D. C. Paine, “Transparent conducting oxides for photovoltaics,” *MRS Bulletin*, vol. 32, no. 03, pp. 242–247, 2007, doi: 10.1557/mrs2007.29.
- [3] D. S. Hecht, L. Hu, and G. Irvin, “Emerging transparent electrodes based on thin films of carbon nanotubes, graphene, and metallic nanostructures,” *Advanced Materials*, vol. 23, no. 13, pp. 1482–1513, 2011, doi: 10.1002/adma.201003188.
- [4] M. N. Gueye *et al.*, “Structure and Dopant Engineering in PEDOT Thin Films: Practical Tools for a Dramatic Conductivity Enhancement,” *Chemistry of Materials*, vol. 28, no. 10, pp. 3462–3468, May 2016, doi: 10.1021/acs.chemmater.6b01035.
- [5] M. N. Gueye, A. Carella, R. Demadrille, and J.-P. Simonato, “All-Polymeric Flexible Transparent Heaters,” *ACS Appl. Mater. Interfaces*, vol. 9, no. 32, pp. 27250–27256, Aug. 2017, doi: 10.1021/acsami.7b08578.
- [6] A. Kumar and C. Zhou, “The Race To Replace Tin-Doped Indium Oxide: Which Material Will Win?,” *ACS Nano*, vol. 4, no. 1, pp. 11–14, 2010, doi: 10.1021/nn901903b.
- [7] T. M. Barnes *et al.*, “Comparing the Fundamental Physics and Device Performance of Transparent, Conductive Nanostructured Networks with Conventional Transparent Conducting Oxides,” *Advanced Energy Materials*, vol. 2, no. 3, pp. 353–360, Mar. 2012, doi: 10.1002/aenm.201100608.
- [8] S. Ye, A. R. Rathmell, Z. Chen, I. E. Stewart, and B. J. Wiley, “Metal Nanowire Networks: The Next Generation of Transparent Conductors,” *Adv. Mater.*, vol. 26, no. 39, pp. 6670–6687, Oct. 2014, doi: 10.1002/adma.201402710.
- [9] T. Sannicolo, M. Lagrange, A. Cabos, C. Celle, J.-P. Simonato, and D. Bellet, “Metallic Nanowire-Based Transparent Electrodes for Next Generation Flexible Devices: a Review,” *Small*, vol. 12, no. 44, pp. 6052–6075, Nov. 2016, doi: 10.1002/smll.201602581.
- [10] D. Bellet *et al.*, “Transparent Electrodes Based on Silver Nanowire Networks: From Physical Considerations towards Device Integration,” *Materials*, vol. 10, no. 6, p. 570, May 2017, doi: 10.3390/ma10060570.
- [11] M. Lagrange, D. P. Langley, G. Giusti, C. Jiménez, Y. Bréchet, and D. Bellet, “Optimization of Silver Nanowire-Based Transparent Electrodes: Effects of Density, Size and Thermal Annealing,” *Nanoscale*, vol. 7, no. 41, pp. 17410–17423, Oct. 2015, doi: 10.1039/C5NR04084A.
- [12] S. K. Choi and J. I. Lee, “Effect of film density on electrical properties of indium tin oxide films deposited by dc magnetron reactive sputtering,” *Journal of Vacuum Science & Technology A: Vacuum, Surfaces, and Films*, vol. 19, no. 5, pp. 2043–2047, Sep. 2001, doi: 10.1116/1.1371326.

- [13] "<https://www.usgs.gov/centers/nmic/indium-statistics-and-information>." .
- [14] Y. Sun, B. Mayers, T. Herricks, and Y. Xia, "Polyol Synthesis of Uniform Silver Nanowires: A Plausible Growth Mechanism and the Supporting Evidence," *Nano Lett.*, vol. 3, no. 7, pp. 955–960, Jul. 2003, doi: 10.1021/nl034312m.
- [15] A. Tao *et al.*, "Langmuir–Blodgett Silver Nanowire Monolayers for Molecular Sensing Using Surface-Enhanced Raman Spectroscopy," *Nano Letters*, vol. 3, no. 9, pp. 1229–1233, Sep. 2003, doi: 10.1021/nl0344209.
- [16] J. Wang *et al.*, "The comprehensive effects of visible light irradiation on silver nanowire transparent electrode," *Nanotechnology*, vol. 29, no. 43, p. 435701, Aug. 2018, doi: 10.1088/1361-6528/aad619.
- [17] "<https://www.acsmaterial.com/silver-nanowire-500mg.html>."
- [18] A. Bid, A. Bora, and A. K. Raychaudhuri, "Temperature dependence of the resistance of metallic nanowires of diameter  $\geq 15$ nm: Applicability of Bloch–Grüneisen theorem," *Phys. Rev. B*, vol. 74, no. 3, pp. 035426–035426–8, Jul. 2006, doi: 10.1103/PhysRevB.74.035426.
- [19] T.-B. Song *et al.*, "Nanoscale Joule Heating and Electromigration Enhanced Ripening of Silver Nanowire Contacts," *ACS Nano*, vol. 8, no. 3, pp. 2804–2811, Mar. 2014, doi: 10.1021/nn4065567.
- [20] T. Tokuno *et al.*, "Fabrication of silver nanowire transparent electrodes at room temperature," *Nano Research*, vol. 4, no. 12, pp. 1215–1222, Oct. 2011, doi: 10.1007/s12274-011-0172-3.
- [21] H. Tohmyoh and S. Fukui, "Manipulation and Joule heat welding of Ag nanowires prepared by atomic migration," *Journal of Nanoparticle Research*, vol. 14, no. 9, Sep. 2012, doi: 10.1007/s11051-012-1116-x.
- [22] E. C. Garnett *et al.*, "Self-limited plasmonic welding of silver nanowire junctions," *Nature Materials*, vol. 11, no. 3, pp. 241–249, Feb. 2012, doi: 10.1038/nmat3238.
- [23] S. Han *et al.*, "Fast Plasmonic Laser Nanowelding for a Cu-Nanowire Percolation Network for Flexible Transparent Conductors and Stretchable Electronics," *Advanced Materials*, vol. 26, p. 10.1002/adma.201400474, Sep. 2014, doi: 10.1002/adma.201400474.
- [24] A. J. Stapleton *et al.*, "Planar silver nanowire, carbon nanotube and PEDOT:PSS nanocomposite transparent electrodes," *Sci Technol Adv Mater*, vol. 16, no. 2, Mar. 2015, doi: 10.1088/1468-6996/16/2/025002.
- [25] M.-S. Lee *et al.*, "High-Performance, Transparent, and Stretchable Electrodes Using Graphene–Metal Nanowire Hybrid Structures," *Nano Lett.*, vol. 13, no. 6, pp. 2814–2821, 2013, doi: 10.1021/nl401070p.
- [26] J. A. Spechler, K. A. Nagamatsu, J. C. Sturm, and C. B. Arnold, "Improved Efficiency of Hybrid Organic Photovoltaics by Pulsed Laser Sintering of Silver Nanowire Network Transparent Electrode," *ACS Appl. Mater. Interfaces*, vol. 7, no. 19, pp. 10556–10562, May 2015, doi: 10.1021/acsami.5b02203.

- [27] M. del P. Buera, G. Levi, and M. Karel, "Glass transition in poly(vinylpyrrolidone): effect of molecular weight and diluents," *Biotechnology Progress*, vol. 8, no. 2, pp. 144–148, Mar. 1992, doi: 10.1021/bp00014a008.
- [28] N. Weiß *et al.*, "Humidity assisted annealing technique for transparent conductive silver nanowire networks," *RSC Adv.*, vol. 5, no. 25, pp. 19659–19665, Feb. 2015, doi: 10.1039/C5RA01303H.
- [29] J. Lee, I. Lee, T.-S. Kim, and J.-Y. Lee, "Efficient Welding of Silver Nanowire Networks without Post-Processing," *Small*, vol. 9, no. 17, pp. 2887–2894, Sep. 2013, doi: 10.1002/smll.201203142.
- [30] Y. Liu *et al.*, "Capillary-Force-Induced Cold Welding in Silver-Nanowire-Based Flexible Transparent Electrodes," *Nano Letters*, vol. 17, no. 2, pp. 1090–1096, Feb. 2017, doi: 10.1021/acs.nanolett.6b04613.
- [31] T. Sannicolo, "Transparent Electrodes based on Silver Nanowire Networks: Electrical Percolation, Physical Properties, and Applications," PhD thesis, University of Grenoble Alpes (France), 2017.
- [32] T. Sannicolo *et al.*, "Direct Imaging of the Onset of Electrical Conduction in Silver Nanowire Networks by Infrared Thermography: Evidence of Geometrical Quantized Percolation," *Nano Letters*, vol. 16, no. 11, pp. 7046–7053, Nov. 2016, doi: 10.1021/acs.nanolett.6b03270.
- [33] M. E. J. Newman and R. M. Ziff, "Efficient Monte Carlo Algorithm and High-Precision Results for Percolation," *Phys. Rev. Lett.*, vol. 85, no. 19, pp. 4104–4107, Nov. 2000, doi: 10.1103/PhysRevLett.85.4104.
- [34] S. De *et al.*, "Silver Nanowire Networks as Flexible, Transparent, Conducting Films: Extremely High DC to Optical Conductivity Ratios," *ACS Nano*, vol. 3, no. 7, pp. 1767–1774, 2009, doi: 10.1021/nm900348c.
- [35] S. Zhu *et al.*, "Transferable self-welding silver nanowire network as high performance transparent flexible electrode," *Nanotechnology*, vol. 24, no. 33, p. 335202, Aug. 2013, doi: 10.1088/0957-4484/24/33/335202.
- [36] S. M. Bergin, Y.-H. Chen, A. R. Rathmell, P. Charbonneau, Z.-Y. Li, and B. J. Wiley, "The effect of nanowire length and diameter on the properties of transparent, conducting nanowire films," *Nanoscale*, vol. 4, no. 6, p. 1996, 2012, doi: 10.1039/c2nr30126a.
- [37] T. Chih-Hung *et al.*, "Influences of textures in fluorine-doped tin oxide on characteristics of dye-sensitized solar cells," *Organic Electronics*, vol. 12, no. 12, pp. 2003–2011, Dec. 2011, doi: 10.1016/j.orgel.2011.08.027.
- [38] Y. Chiba, A. Islam, Y. Watanabe, R. Komiya, N. Koide, and L. Han, "Dye-Sensitized Solar Cells with Conversion Efficiency of 11.1%," *Jpn. J. Appl. Phys.*, vol. 45, no. 7L, p. L638, Jul. 2006, doi: 10.1143/JJAP.45.L638.
- [39] C. Preston, Y. Xu, X. Han, J. N. Munday, and L. Hu, "Optical haze of transparent and conductive silver nanowire films," *Nano Research*, vol. 6, no. 7, pp. 461–468, May 2013, doi: 10.1007/s12274-013-0323-9.
- [40] M. Marus *et al.*, "Optical haze of randomly arranged silver nanowire transparent conductive films with wide range of nanowire diameters," *AIP Adv.*, vol. 8, no. 3, p. 035201, Mar. 2018, doi: 10.1063/1.5020033.

- [41] M. M. Menampambath *et al.*, “Reduced haze of transparent conductive films by smaller diameter silver nanowires,” *Nanotechnology*, vol. 27, no. 46, p. 465706, Nov. 2016, doi: 10.1088/0957-4484/27/46/465706.
- [42] G. Haacke, “New figure of merit for transparent conductors,” *Journal of Applied Physics*, vol. 47, no. 9, pp. 4086–4089, 1976, doi: 10.1063/1.323240.
- [43] J. Müller, B. Rech, J. Springer, and M. Vanecek, “TCO and light trapping in silicon thin film solar cells,” *Solar Energy*, vol. 77, no. 6, pp. 917–930, Dec. 2004, doi: 10.1016/j.solener.2004.03.015.
- [44] A. Kim, Y. Won, K. Woo, C.-H. Kim, and J. Moon, “Highly Transparent Low Resistance ZnO/Ag Nanowire/ZnO Composite Electrode for Thin Film Solar Cells,” *ACS Nano*, vol. 7, no. 2, pp. 1081–1091, Feb. 2013, doi: 10.1021/nm305491x.
- [45] S.-B. Kang, Y.-J. Noh, S.-I. Na, and H.-K. Kim, “Brush-painted flexible organic solar cells using highly transparent and flexible Ag nanowire network electrodes,” *Solar Energy Materials and Solar Cells*, vol. 122, pp. 152–157, Mar. 2014, doi: 10.1016/j.solmat.2013.11.036.
- [46] M. W. Rowell *et al.*, “Organic solar cells with carbon nanotube network electrodes,” *Appl. Phys. Lett.*, vol. 88, no. 23, p. 233506, Jun. 2006, doi: 10.1063/1.2209887.
- [47] X. Wang, L. Zhi, and K. Müllen, “Transparent, Conductive Graphene Electrodes for Dye-Sensitized Solar Cells,” *Nano Lett.*, vol. 8, no. 1, pp. 323–327, Jan. 2008, doi: 10.1021/nl072838r.
- [48] C. J. M. Emmott, A. Urbina, and J. Nelson, “Environmental and economic assessment of ITO-free electrodes for organic solar cells,” *Solar Energy Materials and Solar Cells*, vol. 97, pp. 14–21, Feb. 2012, doi: 10.1016/j.solmat.2011.09.024.
- [49] S.-I. Na, S.-S. Kim, J. Jo, and D.-Y. Kim, “Efficient and Flexible ITO-Free Organic Solar Cells Using Highly Conductive Polymer Anodes,” *Advanced Materials*, vol. 20, no. 21, pp. 4061–4067, 2008, doi: 10.1002/adma.200800338.
- [50] M. Song *et al.*, “Highly Efficient and Bendable Organic Solar Cells with Solution-Processed Silver Nanowire Electrodes,” *Adv. Funct. Mater.*, vol. 23, no. 34, pp. 4177–4184, Sep. 2013, doi: 10.1002/adfm.201202646.
- [51] J.-W. Lim, D.-Y. Cho, Jihoon-Kim, S.-I. Na, and H.-K. Kim, “Simple brush-painting of flexible and transparent Ag nanowire network electrodes as an alternative ITO anode for cost-efficient flexible organic solar cells,” *Solar Energy Materials and Solar Cells*, vol. 107, pp. 348–354, Dec. 2012, doi: 10.1016/j.solmat.2012.07.012.
- [52] M. Reinhard, R. Eckstein, A. Slobodskyy, U. Lemmer, and A. Colmann, “Solution-processed polymer–silver nanowire top electrodes for inverted semi-transparent solar cells,” *Organic Electronics*, vol. 14, no. 1, pp. 273–277, Jan. 2013, doi: 10.1016/j.orgel.2012.10.039.

- [53] Z. Yu, L. Li, Q. Zhang, W. Hu, and Q. Pei, "Silver Nanowire-Polymer Composite Electrodes for Efficient Polymer Solar Cells," *Advanced Materials*, vol. 23, no. 38, pp. 4453–4457, 2011, doi: 10.1002/adma.201101992.
- [54] A. Kim, Y. Won, K. Woo, S. Jeong, and J. Moon, "All-Solution-Processed Indium-Free Transparent Composite Electrodes based on Ag Nanowire and Metal Oxide for Thin-Film Solar Cells," *Adv. Funct. Mater.*, vol. 24, no. 17, pp. 2462–2471, May 2014, doi: 10.1002/adfm.201303518.
- [55] J. Krantz *et al.*, "Spray-Coated Silver Nanowires as Top Electrode Layer in Semitransparent P3HT:PCBM-Based Organic Solar Cell Devices," *Advanced Functional Materials*, vol. 23, no. 13, pp. 1711–1717, 2013, doi: 10.1002/adfm.201202523.
- [56] D.-S. Leem, A. Edwards, M. Faist, J. Nelson, D. D. C. Bradley, and J. C. de Mello, "Efficient Organic Solar Cells with Solution-Processed Silver Nanowire Electrodes," *Advanced Materials*, vol. 23, no. 38, pp. 4371–4375, 2011, doi: 10.1002/adma.201100871.
- [57] G. Y. Margulis *et al.*, "Spray Deposition of Silver Nanowire Electrodes for Semitransparent Solid-State Dye-Sensitized Solar Cells," *Adv. Energy Mater.*, vol. 3, no. 12, pp. 1657–1663, Dec. 2013, doi: 10.1002/aenm.201300660.
- [58] J.-S. Yu *et al.*, "Silver front electrode grids for ITO-free all printed polymer solar cells with embedded and raised topographies, prepared by thermal imprint, flexographic and inkjet roll-to-roll processes," *Nanoscale*, vol. 4, no. 19, pp. 6032–6040, Sep. 2012, doi: 10.1039/C2NR31508D.
- [59] L. Yang, T. Zhang, H. Zhou, S. C. Price, B. J. Wiley, and W. You, "Solution-Processed Flexible Polymer Solar Cells with Silver Nanowire Electrodes," *ACS Appl. Mater. Interfaces*, vol. 3, no. 10, pp. 4075–4084, 2011, doi: 10.1021/am2009585.
- [60] D. P. Langley *et al.*, "Silver nanowire networks: Physical properties and potential integration in solar cells," *Solar Energy Materials and Solar Cells*, vol. 125, pp. 318–324, Jun. 2014, doi: 10.1016/j.solmat.2013.09.015.
- [61] T. Tokuno, M. Nogi, J. Jiu, T. Sugahara, and K. Suganuma, "Transparent Electrodes Fabricated via the Self-Assembly of Silver Nanowires Using a Bubble Template," *Langmuir*, vol. 28, no. 25, pp. 9298–9302, 2012, doi: 10.1021/la300961m.
- [62] J. Ajuria, I. Ugarte, W. Cambarau, I. Etxebarria, R. Tena-Zaera, and R. Pacios, "Insights on the working principles of flexible and efficient ITO-free organic solar cells based on solution processed Ag nanowire electrodes," *Solar Energy Materials and Solar Cells*, vol. 102, pp. 148–152, Jul. 2012, doi: 10.1016/j.solmat.2012.03.009.
- [63] X.-Y. Zeng, Q.-K. Zhang, R.-M. Yu, and C.-Z. Lu, "A New Transparent Conductor: Silver Nanowire Film Buried at the Surface of a Transparent Polymer," *Advanced Materials*, vol. 22, no. 40, pp. 4484–4488, 2010, doi: 10.1002/adma.201001811.
- [64] W. Gaynor *et al.*, "Color in the Corners: ITO-Free White OLEDs with Angular Color Stability," *Advanced Materials*, vol. 25, no. 29, pp. 4006–4013, 2013, doi: 10.1002/adma.201300923.

- [65] L. Li, Z. Yu, W. Hu, C. Chang, Q. Chen, and Q. Pei, "Efficient Flexible Phosphorescent Polymer Light-Emitting Diodes Based on Silver Nanowire-Polymer Composite Electrode," *Advanced Materials*, vol. 23, no. 46, pp. 5563–5567, 2011, doi: 10.1002/adma.201103180.
- [66] L. Li *et al.*, "Efficient white polymer light-emitting diodes employing a silver nanowire–polymer composite electrode," *Phys. Chem. Chem. Phys.*, vol. 14, no. 41, pp. 14249–14254, Oct. 2012, doi: 10.1039/C2CP41562C.
- [67] H.-G. Im *et al.*, "Flexible Transparent Conducting Hybrid Film Using a Surface-Embedded Copper Nanowire Network: A Highly Oxidation-Resistant Copper Nanowire Electrode for Flexible Optoelectronics," *ACS Nano*, vol. 8, no. 10, pp. 10973–10979, Oct. 2014, doi: 10.1021/nm504883m.
- [68] Z. Yu *et al.*, "Highly Flexible Silver Nanowire Electrodes for Shape-Memory Polymer Light-Emitting Diodes," *Advanced Materials*, vol. 23, no. 5, pp. 664–668, 2011, doi: 10.1002/adma.201003398.
- [69] S. Coskun, E. Selen Ates, and H. Emrah Unalan, "Optimization of silver nanowire networks for polymer light emitting diode electrodes," *Nanotechnology*, vol. 24, no. 12, p. 125202, Mar. 2013, doi: 10.1088/0957-4484/24/12/125202.
- [70] H. Lee, D. Lee, Y. Ahn, E.-W. Lee, L. S. Park, and Y. Lee, "Highly efficient and low voltage silver nanowire-based OLEDs employing a n-type hole injection layer," *Nanoscale*, vol. 6, no. 15, pp. 8565–8570, Jul. 2014, doi: 10.1039/C4NR01768D.
- [71] Harold A. McMaster, "Conductive coating for glass and method of application," US2429420 A, 1947.
- [72] K. Sun, A. Yamaguchi, Y. Ishida, S. Matsuo, and H. Misawa, "A heater-integrated transparent microchannel chip for continuous-flow PCR," *Sensors and Actuators B: Chemical*, vol. 84, no. 2–3, pp. 283–289, May 2002, doi: 10.1016/S0925-4005(02)00016-3.
- [73] S. Petronis, M. Stangegaard, C. Bovöge Christensen, and M. Dufva, "Transparent polymeric cell culture chip with integrated temperature control and uniform media perfusion," *BioTechniques*, vol. 40, no. 3, pp. 368–376, Mar. 2006, doi: 10.2144/000112122.
- [74] K. Im, K. Cho, J. Kim, and S. Kim, "Transparent heaters based on solution-processed indium tin oxide nanoparticles," *Thin Solid Films*, vol. 518, no. 14, pp. 3960–3963, May 2010, doi: 10.1016/j.tsf.2009.10.164.
- [75] C. Hudaya, B. J. Jeon, and J. K. Lee, "High Thermal Performance of SnO<sub>2</sub>:F Thin Transparent Heaters with Scattered Metal Nanodots," *ACS Appl. Mater. Interfaces*, vol. 7, no. 1, pp. 57–61, Jan. 2015, doi: 10.1021/am507497u.
- [76] D. Jung, D. Kim, K. H. Lee, L. J. Overzet, and G. S. Lee, "Transparent film heaters using multi-walled carbon nanotube sheets," *Sensors and Actuators A: Physical*, vol. 199, pp. 176–180, Sep. 2013, doi: 10.1016/j.sna.2013.05.024.
- [77] J. Kang *et al.*, "High-Performance Graphene-Based Transparent Flexible Heaters," *Nano Lett.*, vol. 11, no. 12, pp. 5154–5158, Dec. 2011, doi: 10.1021/nl202311v.

- [78] C. Celle, C. Mayousse, E. Moreau, H. Basti, A. Carella, and J.-P. Simonato, "Highly flexible transparent film heaters based on random networks of silver nanowires," *Nano Research*, vol. 5, no. 6, pp. 427–433, 2012, doi: 10.1007/s12274-012-0225-2.
- [79] T. Kim, Y. W. Kim, H. S. Lee, H. Kim, W. S. Yang, and K. S. Suh, "Uniformly Interconnected Silver-Nanowire Networks for Transparent Film Heaters," *Advanced Functional Materials*, vol. 23, no. 10, pp. 1250–1255, 2013, doi: 10.1002/adfm.201202013.
- [80] M. Lagrange *et al.*, "Understanding the mechanisms leading to failure in metallic nanowire-based transparent heaters, and solution for stability enhancement," *Nanotechnology*, vol. 28, no. 5, p. 055709, 2017, doi: 10.1088/1361-6528/28/5/055709.
- [81] S. Sorel, D. Bellet, and J. N. Coleman, "Relationship between Material Properties and Transparent Heater Performance for Both Bulk-like and Percolative Nanostructured Networks," *ACS Nano*, vol. 8, no. 5, pp. 4805–4814, May 2014, doi: 10.1021/nm500692d.
- [82] S. M. Lee, J. H. Lee, S. Bak, K. Lee, Y. Li, and H. Lee, "Hybrid windshield-glass heater for commercial vehicles fabricated via enhanced electrostatic interactions among a substrate, silver nanowires, and an over-coating layer," *Nano Res.*, vol. 8, no. 6, pp. 1882–1892, Mar. 2015, doi: 10.1007/s12274-014-0696-4.
- [83] S. Hong *et al.*, "Highly Stretchable and Transparent Metal Nanowire Heater for Wearable Electronics Applications," *Adv. Mater.*, vol. 27, no. 32, pp. 4744–4751, Aug. 2015, doi: 10.1002/adma.201500917.
- [84] P.-C. Hsu *et al.*, "Personal Thermal Management by Metallic Nanowire-Coated Textile," *Nano Letters*, vol. 15, no. 1, pp. 365–371, Jan. 2015, doi: 10.1021/nl5036572.
- [85] R. C. Webb *et al.*, "Ultrathin conformal devices for precise and continuous thermal characterization of human skin," *Nat Mater*, vol. 12, no. 10, pp. 938–944, Oct. 2013, doi: 10.1038/nmat3755.



## Chapter 2

**Experimental methods related to deposition and characterization along with preliminary results of bare AgNW networks**



## 2.1. Introduction

Techniques of deposition of AgNW networks have been already optimized in LMGP during the Ph.D. thesis of Daniel Langley and Mélanie Lagrange, with spin coating as a major technique for depositing different types of AgNWs (with different diameter and length of NWs). Although this method is fast, cheap, and straightforward, it has some limitations. For instance, the preferential orientation of AgNWs is observed, its origin stems from centrifugal forces.[1] Moreover, it is not possible to upscale the spin coating deposition to large substrates (i.e. spin coating is roughly limited to  $5 \times 5$  cm<sup>2</sup> substrate otherwise the deposition is not homogeneous). These arguments prompt the search for substitutional deposition techniques. Spray coating using an air-brush was chosen during this thesis due to several advantages. It is a fast and repeatable technique which is easily scalable and can generate homogeneously and randomly deposited AgNW networks on various types of substrates, from rigid ones like glass to polymeric ones like PolyEthylene Naphthalate (PEN) and Neopulim. Deposition parameters have been optimized, and homogenous large area samples (i.e.  $> 100$  cm<sup>2</sup>) were acquired during this thesis. Furthermore, details about the characterization of morphological, optical, and electrical properties of AgNW networks, the result of bending tests on the electrical resistance, and post-deposition treatments, the main focus being on thermal annealing, on AgNW networks are discussed in this chapter. The latter covers the experimental conditions which were used to fabricate and analyze the samples in Chapter 3, where the main experimental results of this thesis will be presented.

## 2.2. Deposition of AgNW networks

The majority of AgNWs used in this study were purchased from Seashell Technology (meanwhile this technology had been acquired by BASF) and ACS materials companies. Seashell AgNWs (average diameter 117 nm, and average length 37.5  $\mu$ m), and ACS-Ag90 AgNWs (average diameter 90 nm, and average length 15  $\mu$ m) were both dispersed in isopropyl alcohol (IPA) with an initial concentration of 20 g L<sup>-1</sup>. These suspensions were used to prepare diluted ones, and the concentration is chosen based on the deposition technique and targeted network density by adding IPA. The presence of the PVP layer around AgNWs prevents agglomeration of NWs in the solution, yet a short sonication treatment, 30 seconds long, was performed on the NW solutions to ensure homogenized deposition without aggregates. Lagrange et al. [2] showed that long-time ultrasonication could lead to the scission

of NWs and shortening of average length. However, sonication for 30 to 60 seconds is too short to have any considerable effect on the length of NWs; therefore, it has been used to produce a homogenized solution of AgNWs. Substrates that were used in this study were purchased from Delta Technologies (Corning alkaline glasses) and MGCMINC (Neopulim). A three-step cleaning process was applied on glass substrates to remove any possible contamination before deposition: initially, the substrates were sonicated in acetone then ethanol bath for approximately 10 minutes each. Then the substrates were rinsed by deionized water and eventually a N<sub>2</sub> flow gun was used to completely dry them out. Such a cleaning process was not essential for Neopulim substrates since they had double side protection layers around them to avoid any contamination. Neopulim films were put in an O<sub>2</sub> plasma treatment chamber for 90 seconds to enhance wettability of surface and to ease distribution of AgNW containing solvents over the substrate. Therefore, homogenous coatings of AgNW networks could be obtained.

### **2.2.1. Spin coating of AgNWs**

Spin coating was the initial technique used to deposit uniform AgNW networks since this is an easy, well-mastered, room-temperature, solution-based technique.[3] A total amount of 1 mL of AgNW solution was placed at the center of the substrate which is rotating rapidly (1500 rpm). Solution pulses were manually controlled around one drop per second. Langley [3] observed that it is better to perform two steps of deposition (0.5 mL each step) while keeping a 30 seconds pause between steps to allow drying the surface. The procedure takes only a few minutes for a 25×25 mm<sup>2</sup> size sample. Figure 2-1.a shows the spin coating setup (SPIN150), which we use in LMGP. The inset shows the placement of the sample on the rotating substrate holder, where the substrate is fixed due to the suction effect by the pump installed underneath. Since the deposition procedure was optimized for a two-step process, the density of the final network can be controlled by changing the density of the AgNW solution. We have varied this value from 0.2 to 2 g L<sup>-1</sup>.

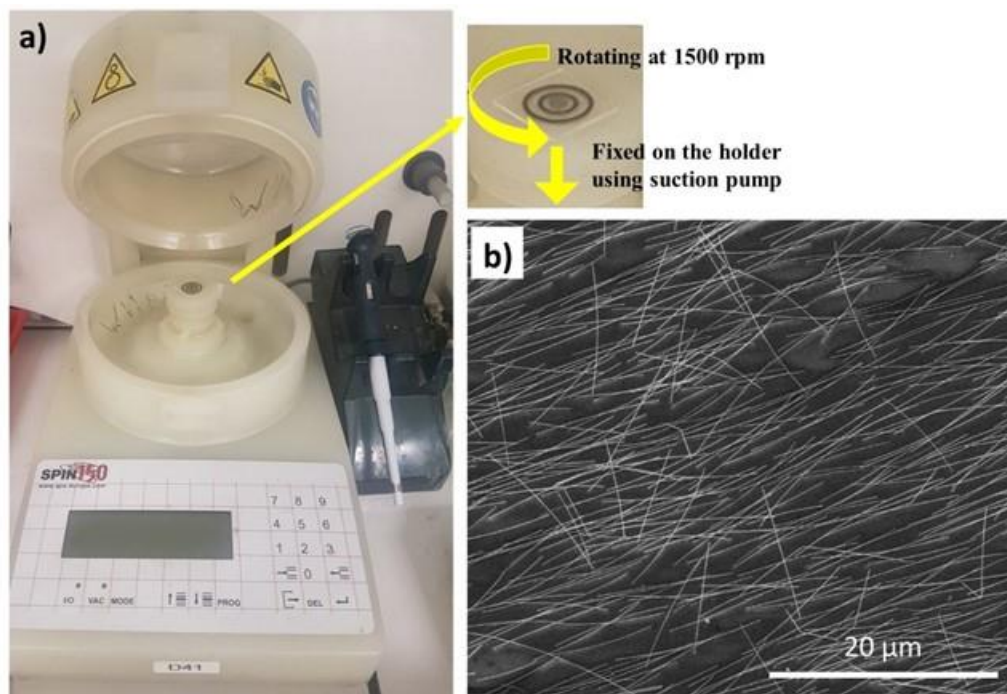


Figure 2-1.a) Picture of the spin coating setup (SPIN150). The inset shows the placement of the  $25 \times 25 \text{ mm}^2$  sample in the setup. b) SEM image of a ACS-Ag90 NW network deposited by spin coating. 1 mL of AgNW solution with  $1 \text{ g L}^{-1}$  concentration was deposited on a glass substrate, showing the preferential orientation of AgNWs due to centrifugal force.

Table 2-1 shows the electrical resistance, optical transmittance and Haacke's  $FoM$ , see 1.3.3 Chapter 1, values of ACS Ag-90 NWs while changing AgNW solution density. As density of AgNW networks is increased, sheet resistance and total transmittance values both decrease ( see section 1.3.1 and 1.3.2). However,  $FoM$  values have increased by increasing network density. Considering the bell shape curve of  $FoM$  versus relative network density ( network density over critical density at percolation threshold ) , see 1.3.3, we are still in the growing part of  $FoM$  curve. However, using AgNW solution with the density of  $2 \text{ g L}^{-1}$ , leads to AgNW networks with sheet resistance values below  $10 \text{ } \Omega \text{sq}^{-1}$  and total transmittance over 90% . These values seemed optimal for the next step of our study, improving AgNW network density using metal oxide coatings, see section 3.5 of Chapter 3.

<i>ACS-Ag 90, Solution density (g L<sup>-1</sup>)</i>	<i>Sheet resistance (Ω sq<sup>-1</sup>)</i>	<i>Total Transmittance at 550nm (%)</i>	<i>Haacke's Figure of Merit</i>
0.2	79±5.6	96.9	9
0.5	42.5±2.3	95.2	14
1	17.2±1.5	92.9	28
1.5	12.5±0.7	93.6	43
2	9.2±0.6	92.3	47

*Table 2-1. Sheet resistance, total transmittance (after subtracting substrate contribution) and Haacke's FoM values of ACS-Ag90 NWs, spin-coated on Corning glass substrate using the procedure described in 2.2.1. Sheet resistance values have been measured at four corners and the center of each sample and the average value along with standard deviation is reported. Increasing the solution density leads to larger network density and FoM values.*

Although spin coating is a straightforward process to fabricate AgNW networks with controlled network density and electro-optical properties, it is suffering from some drawbacks: spin coating requires the substrate to be flat and smooth. This can be problematic especially for polymer substrates like Neopulim where the substrate can easily buckle while rotating at high speeds. Another example concerns the deposition of AgNW networks on a substrate where silver contacts have been deposited at the edges. The thickness of evaporated silver contacts (see section 2.2.3) is around tens of nanometers (relatively comparable to the diameter of AgNWs). Therefore, for those substrates, the homogenous deposition of AgNW networks is not feasible using spin coating. Another major issue related to the spin coating process is the preferential orientation of AgNWs due to centrifugal forces. Figure 2-1.b clearly shows such an orientation in a ACS-Ag90 AgNW network. As will be discussed in Chapter 4, see 4.5.6, AgNW network with random angular orientation has the lowest percolation threshold. Therefore, any preferential orientation of NWs leads to a higher percolation threshold, causing lower conductivity at a fixed network density (see Chapter 1, section 1.4.1). This is the main motivation behind the replacement of this procedure, with a spray coating technique which will be described in the following section.

### 2.2.2. Air-brush spray coating of AgNWs

Spray coating has been used widely in the literature to produce scalable, high quality (low electrical resistance along with high optical transmittance) AgNW networks on various types of substrates.[3]–[6] In the present work, an airbrush (Harder & Steenbeck) was used to spray the AgNW networks. In principle, an air-brush performs by atomizing a liquid using compressed carrier gas. Carrier gas ( $N_2$  in this case) passes through an aspirator and creates a suction that allows the withdrawing of solvent from the connected reservoir. The solvent containing AgNW is atomized into very tiny droplets due to the high velocity of  $N_2$ . Formed droplets are blown vertically on the deposition substrate and conductive networks of AgNWs are fabricated, where electro-optical properties can be controlled by deposition parameters. [3] In this work the following parameters were used for the deposition: A nozzle of 0.15 mm diameter was chosen for the air-brush head and was fixed at the height of 10 cm above the substrate. 3 bars was the optimum pressure of carrier gas,  $N_2$ , and flow rate of liquid (solvent containing AgNW) was kept around  $0.2 \text{ mL min}^{-1}$ .

These parameters were optimized to form fine solvent droplets containing AgNWs to enable coatings with homogenous morphology. Carrier gas pressure applies shear stress on the AgNW solvent and increases liquid dispersion generating then smaller droplets; therefore enough pressure must be applied.[3] However, we observed that  $N_2$  pressure higher than 3 bars, can cause damages to AgNWs. The target substrates were placed on the top of a hot plate during the deposition, so the solvent in the sprayed droplets could evaporate as soon as it reaches the substrate leaving behind the silver nanowires without the formation of any coffee rings. When a drop falls on a substrate with high wettability, formed layer is not uniform: the layer is thinner on the edges compared to the center of the drop. Therefore, the evaporation rate is faster at the edges, and a capillary flow is formed from the interior toward the edges. At the end of the evaporation process, nearly all the deposited material is accumulated at the edges of the droplet. This process is called the formation of “coffee rings” and one efficient way to avoid it is to control the substrate temperature to cause immediate evaporation of droplets.[7] Therefore, the desired substrate temperature depends on the used solvent in AgNW solution, i.e. it was optimized at  $90^\circ\text{C}$  for IPA solution and  $110^\circ\text{C}$  for methanol solution. Schematic of the air-brush and the spray setup is shown in Figure 2-2.a and b, respectively. Air-brush is mounted on a platform that moves thanks to a dual-axis RCP2 linear electric actuator by IAI Corporation. The deposition area can be programmed by the user depending on the sample size. The air-brush is programmed to move in a “Zig-Zag” pattern as shown in Figure 2-2.b. It scans the substrate in x and y directions, respectively, and completes a full “cycle” of deposition. The network density, therefore the electro-optical properties of AgNW network can be controlled through the number of deposition cycles. Figure 2-2.c represents an

example of spray-coated AgNW with a sheet resistance of  $5.9 \Omega\text{sq}^{-1}$  and total transmittance of 84.3% at 550 nm, and Haack's figure of merit value of  $30 \times 10^{-3} \Omega^{-1}$ .

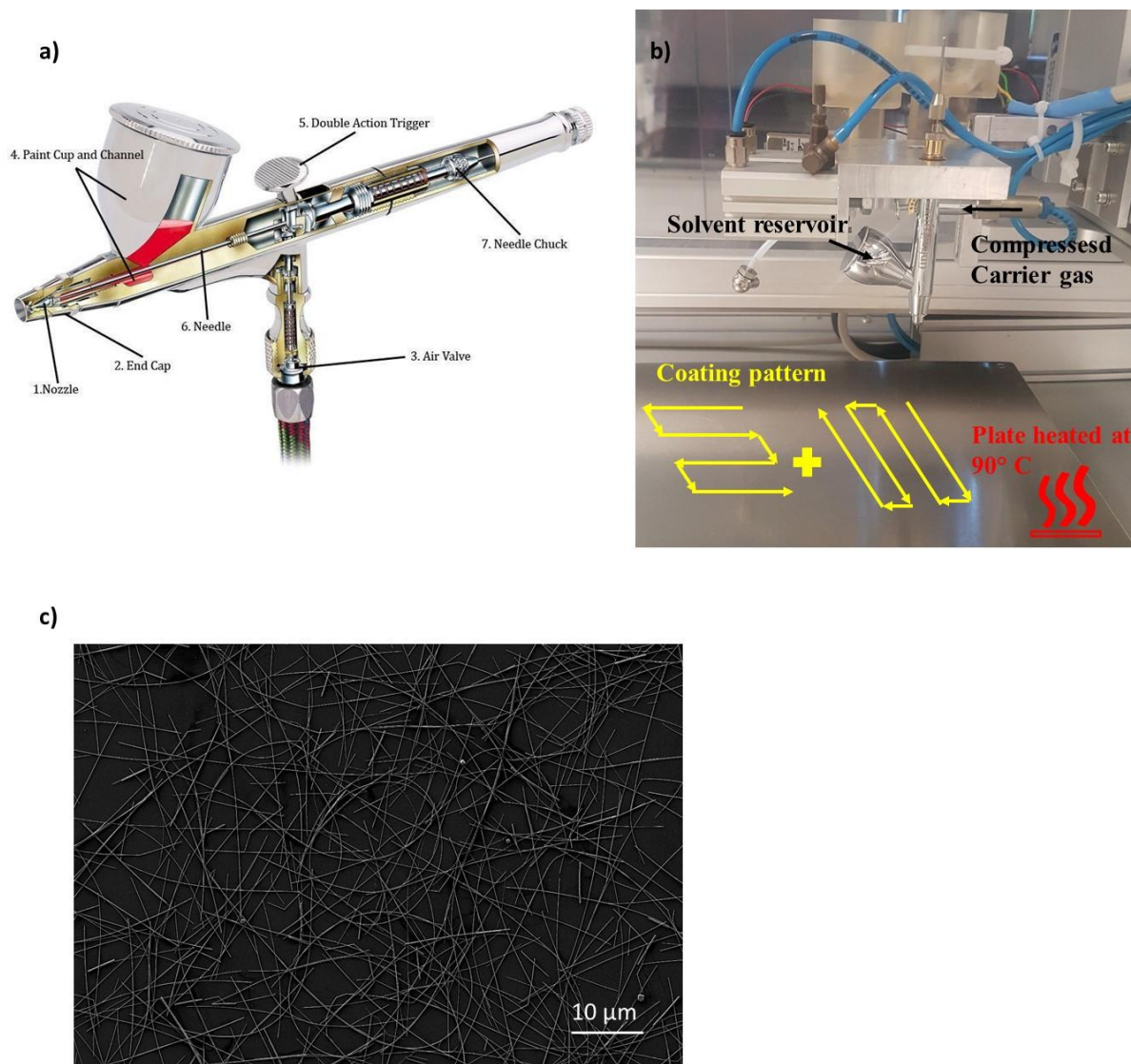


Figure 2-2. a) Schematic of an air-brush to deposit AgNWs. b) Deposition setup in LMGP, using a flow of  $N_2$  as carrier gas. Zig-Zag deposition pattern in x and y direction is shown. c) SEM image of a AgNW network deposited by spray coating of AC-Ag90 NW, solution density of  $0.1 \text{ g L}^{-1}$ .

The main objective of this thesis in the experimental part is to study the enhanced stability of metal oxide coated AgNW networks, as discussed in Chapter 3. Therefore, optimization of the electro-optical properties of spray-coated



AgNW networks was out of the scope of current work. However, AgNW networks with changing “number of cycles”, were spray-coated on the Corning substrate to optimize spray coating process for required electro-optical values during the internship of Tomy Chatin [8] and NiL Fontanals Lozano [9] in LMGP. Evolution of areal mass density (*amd*), with the “number of cycles” and evolution of sheet resistance and total transmittance values of AgNW networks with *amd* is discussed in details by Chatin and Fontanals.

### 2.2.3. Silver contacts deposited by evaporation

After deposition of optimized AgNW networks a thin layer of silver contact with a width of 2.5 mm, was evaporated at the opposite edges of the network to enable two-point electrical measurements. Silver contacts evaporation was performed using an Edwards Auto 306 thermal evaporator. Ag wires with a diameter of 0.05 mm and purity of 99.99% purchased from Goodfellow & co were used as filament for the evaporation process, which was performed by applying up to 3.8 Amp current on the filaments for 3 minutes. In the case of metal oxide coated AgNW networks, deposited to enhance thermal/ electrical stability, an additional contact layer was pasted on the electrode area. A DuPont conductive silver paste was applied after metal oxide deposition to ensure good electrical contact. The silver paste can get cured and dried at room temperature during (16-20 hours) or annealed for 1 hour or less at (60-100°C). Figure 2-3.a and b show the schematic of bare and metal oxide coated AgNW networks, respectively. Details of metal oxide layer deposition, ZnO and Al<sub>2</sub>O<sub>3</sub> films in this study, will be discussed in Chapter 3, 3.3.

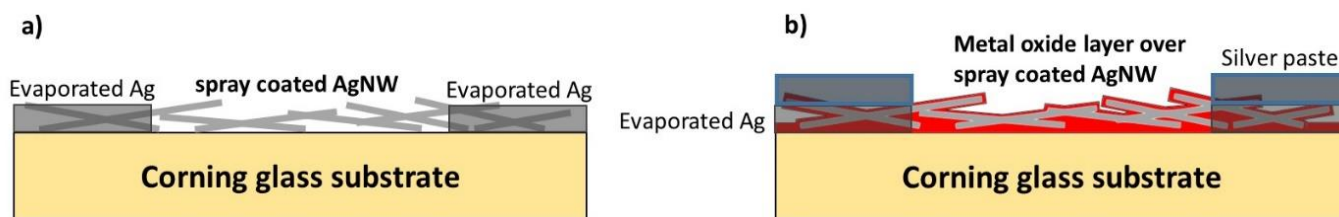


Figure 2-3. a) Scheme of the silver contact deposited over the bare AgNW network on the Corning substrate. b) Scheme of the metal oxide coated AgNW network with additional silver paste added over the contact area.

Evaporation of Ag contacts was performed on Silicon (as reference) and Corning glass substrate, as presented in Figure 2-4. Silicon substrate was chosen so the cross-sectional SEM measurements could be performed to measure the thickness of the Ag film. Atomic Force Microscope (AFM) measurements, using Burker Dimension AFM, were done in the tapping mode, on both Silicon and Corning substrates to measure Ag film thickness as well. Similar

evaporation conditions lead to different thickness of silver for Silicon (125 nm) and Corning glass (70 nm) substrates as shown in Figures 2-4.c and d, respectively. Such a difference in the growth rate might raise from different crystallographic morphology of studied substrates.[10] Different mobility of Ag atoms along the surface of the substrate during the process of nucleation and coalescence of nuclei is another reason which could lead to different growth rates. [11]

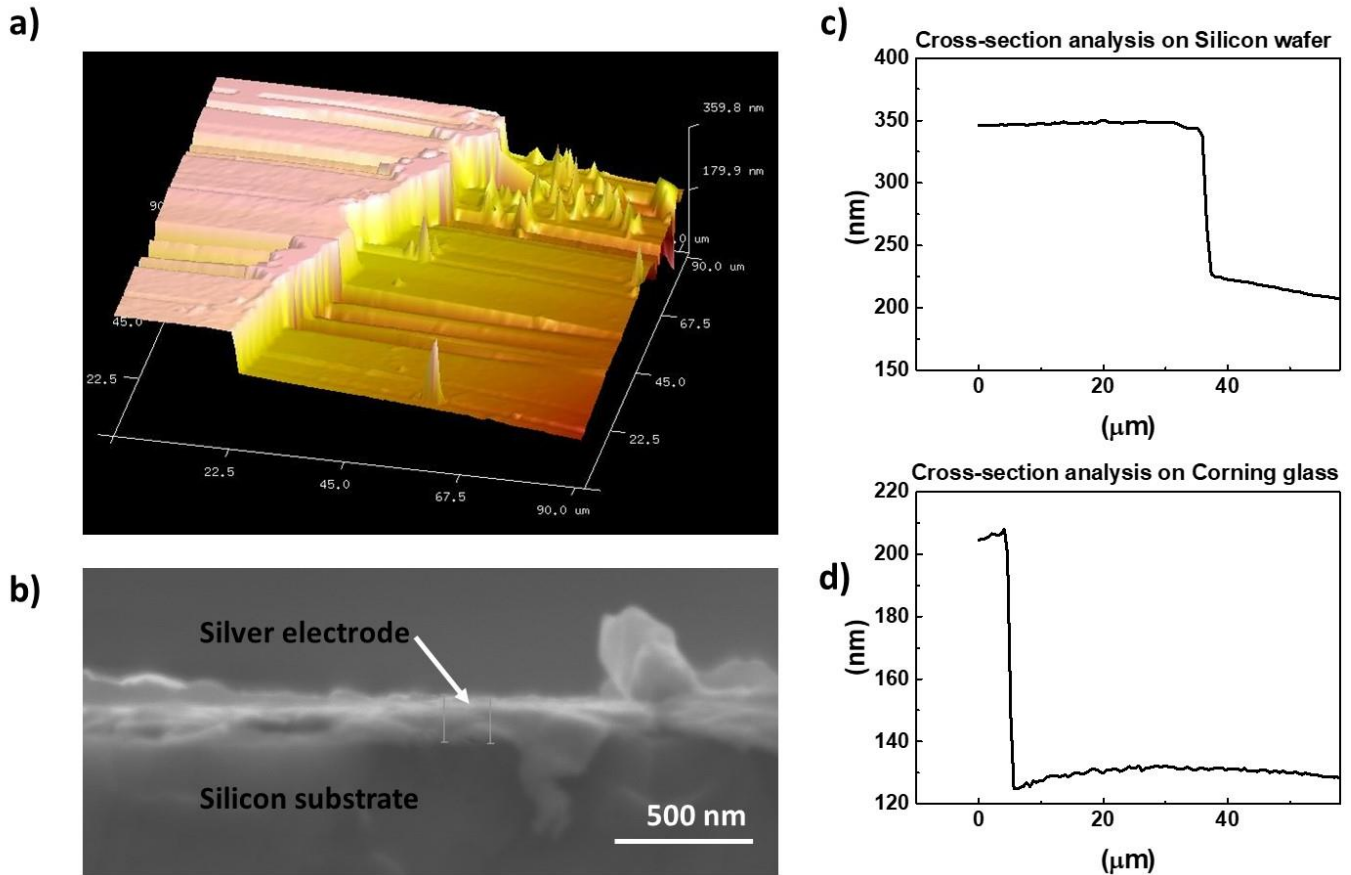


Figure 2-4. a) 3D AFM image of the Ag electrode evaporated on Silicon wafer using Tip ARROW-NC-20 from nanoworld. b) Cross-sectional SEM images of Ag electrodes deposited on silicon Substrate confirming similar thickness (to AFM measurement) around 130 nm. Cross-section AFM analysis on c) Silicon wafer, steps of 0.7 μm, and d) Corning glass, steps of 0.5 μm.

### **2.3.Characterization of AgNW based transparent electrodes: electrical, morphological and optical properties, the effect of bending on the electrical resistance**

#### **2.3.1. Four-point probe method for measuring the sheet resistance**

Sheet resistance is a commonly used feature that is pertinent to characterize electrically thin films in general, and also in the TCM field. Sheet resistance reports a local measurement of resistance, which is essential to assess both the electrical properties and homogeneity of deposited thin films. Sheet resistance is generally reported in  $\Omega \text{ sq}^{-1}$ , it is equivalent to  $\Omega$  but is used only for sheet resistances to avoid confusion with bulk resistances. For square-shaped samples, the values of sheet resistance and 2-probe resistances are theoretically identical; however there is no contribution of contact resistance in the reported sheet resistance values using four-point probe measurement systems. The Four-point probe setup used to measure the sheet resistance of the AgNW samples in LMGP, is a Lucab Labo 4 apparatus. Tungsten probe pins with a pin radius of 40  $\mu\text{m}$ , separated by 1 mm, are put in contact with the sample by mechanical pressure. Keithley 2400 sourcemeter, was used to apply the current and measure the voltage. Measurements were repeated on 5 locations on each sample, and the mean values were reported as measured sheet resistance for each sample.

#### **2.3.2. Scanning Electron Microscopy (SEM)**

Scanning Electron Microscopy (SEM) was used to study the morphology of AgNWs and ZnO or  $\text{Al}_2\text{O}_3$  coatings over the nanowire network. Images were obtained with a field-emission gun (FEG) SEM Environmental FEI QUANTA 250 using an accelerating voltage between 5-10 keV. This setup has a typical spatial resolution between 1.2 nm at 30 kV and 3 nm at 1 kV. The acceleration voltage was chosen based on the density of AgNW network (therefore electrical resistance) and metal oxide coating type. Although a higher acceleration voltage leads to a better spatial resolution, it might lead to an accumulation of charges on the specimen (e.g. for sparse networks on glass or  $\text{Al}_2\text{O}_3$  coated AgNWs) and noisy images. Both secondary electron (SE) imaging (inelastic electron interaction) and backscattered electrons (BSE) imaging (elastic electron interaction) modes were used in this work. SE images were mainly used for the topographical study of AgNWs, and BSE images were used in the case of ZnO or  $\text{Al}_2\text{O}_3$  coated samples to differentiate between AgNWs and oxide layers. Samples were placed at a working distance of 10 mm under the detectors.

### **2.3.3. Transmission Electron Microscopy (TEM)**

Transmission electron microscopy (TEM) was used to observe the AgNW and ZnO or Al<sub>2</sub>O<sub>3</sub> coatings thickness and crystallinity, plus the evolution of AgNWs and ZnO or Al<sub>2</sub>O<sub>3</sub> coatings after thermal degradation. TEM images were obtained using a JEOL 2010 LaB6 microscope operating at 200 kV with a 0.19 nm point-to-point resolution. Energy-dispersive X-ray spectroscopy (EDS) was used for the elemental analysis of ZnO or Al<sub>2</sub>O<sub>3</sub> coated AgNW networks. EDS measurements were performed by STEM with a JEOL 2100F FEG microscope operating at 200 kV with a 0.2 nm resolution in the scanning mode. The novel JEOL SDD Centurio detector with a large solid angle of up to 0.98 steradian was used for the EDS experiments.

Preparation of TEM samples was performed by direct dip coating of AgNW solutions on holey carbon-coated copper grid. Kapton scotch at the edges of the grid was used to fix them on the Corning substrate. Followed by the deposition of AgNWs, required thermal annealing was performed to sinter the junctions between NWs (i.e. annealing step of 230°C for 60 minutes on ACS-Ag90 NWs). Finally, coatings of ZnO and Al<sub>2</sub>O<sub>3</sub> were deposited by Atmospheric Pressure Spatial Atomic Layer Deposition (AP-SALD). Using this approach there was no need for specimen preparation of coated AgNWs on to the TEM grids; therefore we acquired high-quality images with no damage on the NWs and coatings. The TEM and EDS imaging were performed by Dr. Laetitia Rapenne in LMGP.

### **2.3.4. UV-Visible-IR spectrophotometer for optical measurements**

Optical transmittance and haze factor are among critical parameters to evaluate the performance of AgNW based networks. A lambda 950 UV/Visible/NIR Spectrophotometer from Perkin Elmer with an integrating sphere was used to measure the transmittance of the different samples. Transmission values were measured in the wavelength range from 250 to 2500 nm, steps between each measurement being 5 nm. Light is produced thanks to two different lamps: a deuterium lamp for UV range, and a halogen lamp for visible and IR spectrum. Similarly, a photomultiplier detector is used for the UV-Visible range and an InGaAs sensor for the IR range. Measurements were repeated on several parts of each sample, and average values were reported. Figure 2-5 shows the configuration diagram of the integrated sphere setup for the measurement of transmission and reflection components of the incident light beam.

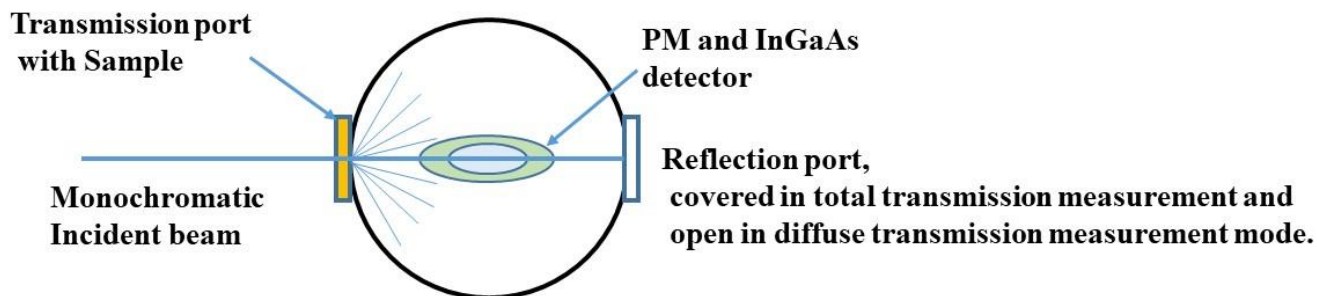


Figure 2-5. Schematic illustration of total or diffuse transmittance measurement using an integrating sphere, from <http://www.perkinelmer.com>.

### 2.3.5. Mechanical bending measurement setup

Flexibility tests were performed in bending mode on bare and ZnO or Al<sub>2</sub>O<sub>3</sub> coated AgNW networks deposited on neopulim substrates with a bending radius of 5 mm using a home-made setup in LMGP. To perform bending tests, samples were clamped on two jaws as presented in Figure 2-6.a. One of the jaws is fixed, and the other one is moved using a Transtechnik integrated servomotor. The length of the displacement, speed, and direction is controlled using Labview software by the user. A Keithley 2400 sourcemeter is connected to the metallic jaws to allow *in-situ* measurement of resistance after each bending cycle. The voltage applied by Keithley sourcemeter was fixed on 0.1 V to minimize potential effects of Joule heating on AgNW network during a high number of bending cycles/measurements. Figure 2-6.b shows the side view of a AgNW network on neopulim substrate while using a bending radius of 5 mm. An example of the evolution of bare ACS-Ag90 NW resistance during 300 cycles of bending is presented in Figure 2-6.c. A slight increase in the electrical resistance (2%) is observed after 300 cycles of bending. While AgNW networks have been reported to be mechanically flexible in many studies,[12]–[14] the slight increase can be explained by rather poor adhesion of AgNW to underneath substrate therefore detaching of NWs from substrate while bending. [15]

Further discussions over mechanical behavior of bare and metal oxide coated AgNWs are reported in detail in section 3.7 of Chapter 3.

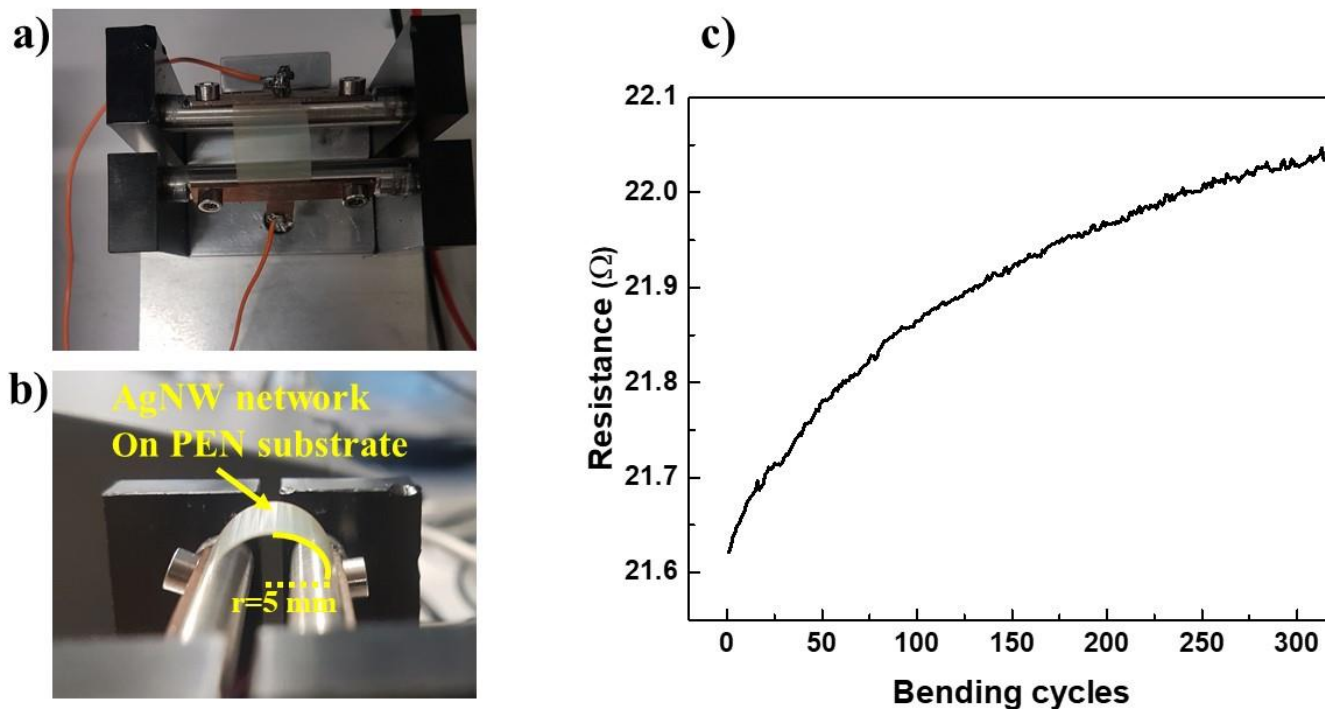


Figure 2-6. Mechanical bending setup in LMGP. a) Top view of AgNW network placement on movable contacts, the top jaw is fixed and bottom jaw is moved by a Transtechnik integrated servomotor. b) Side view of a bent sample, with a bending radius of 5 mm. c) In-situ electrical measurement of a AgNW network, with initial resistance of 21.6  $\Omega$ .

## 2.4. Post deposition treatments, main focus on thermal annealing

### 2.4.1. Ramped thermal annealing of AgNW networks

Another home-made setup in LMGP is the setup used to investigate the impact of thermal annealing on the electrical properties of AgNW networks. It enables the *in-situ* measurement of the network resistance during heating and cooling cycles, with a sourcemeter Keithley 2400. Samples were placed on the hot plate where the temperature was controlled using an MKS INSTRUMENTS controller. It is possible to program the controller so that either isothermal or ramp annealing, with various duration and temperature increasing rates, can be performed. As shown in Figure 2-7.a, the electrical contacts from the Keithley to the sample is made by using metallic probes. The *in-situ* resistance and temperature were recorded and displayed on a computer thanks to a Labview software. The measurement voltage was fixed at 1 V, and the resistance measurement was performed every second. This setup enables us to investigate the full evolution of bare AgNW network during thermal annealing as initially performed by Langley et al.[16], and more recently at LMGP on metal oxide coated AgNW network. An example of such evolution with a ramp of  $2\text{ }^{\circ}\text{C min}^{-1}$ , on spin-coated bare ACS-Ag90 NWs is presented in Figure 2-7.b. Several

mechanisms are behind the evolution of the electrical resistance of AgNWs: first desorption of residual organic solvents from deposition process, IPA in this case, and softening (and probably degradation) of PVP is observed between room temperature to 100-150 °C. Sintering of junctions is the reason behind the second decrement in the electrical resistance; the process of sintering is discussed in section 1.3.3 of Chapter 1. Surface and bulk diffusion of silver atoms allow the formation of sintered junctions. As a result of this process, as shown in Figure 2-7.b electrical resistance of ACS-Ag 90 NW network is decreased by around 65%, and there is a minimum value observed around 200-300 °C. SEM image of as-deposited and sintered junctions of AgNWs is presented in Figure 2-7.b.i and ii, respectively. Further temperature increase results in the degradation process of AgNWs due to Plateau-Rayleigh instability and leads to spheroidization, see Figure 2-7.b.iii. Degradation starts with disconnections along the NWs and junction points and leads to the final phase of spheroidization, shown in Figure 2-7.b.iv, changing the form of NWs into disconnected spheres of silver nanoparticles, as discussed in details in Chapter 3, 3.1.1. It is worth mentioning that the exact temperatures, where the stages mentioned above occur, depend strongly on the diameter of NWs [17]. Studying the evolution of electrical resistance of AgNW networks during thermal annealing cycles, enables assessment of thermal stability for bare and metal oxide coated AgNW networks.

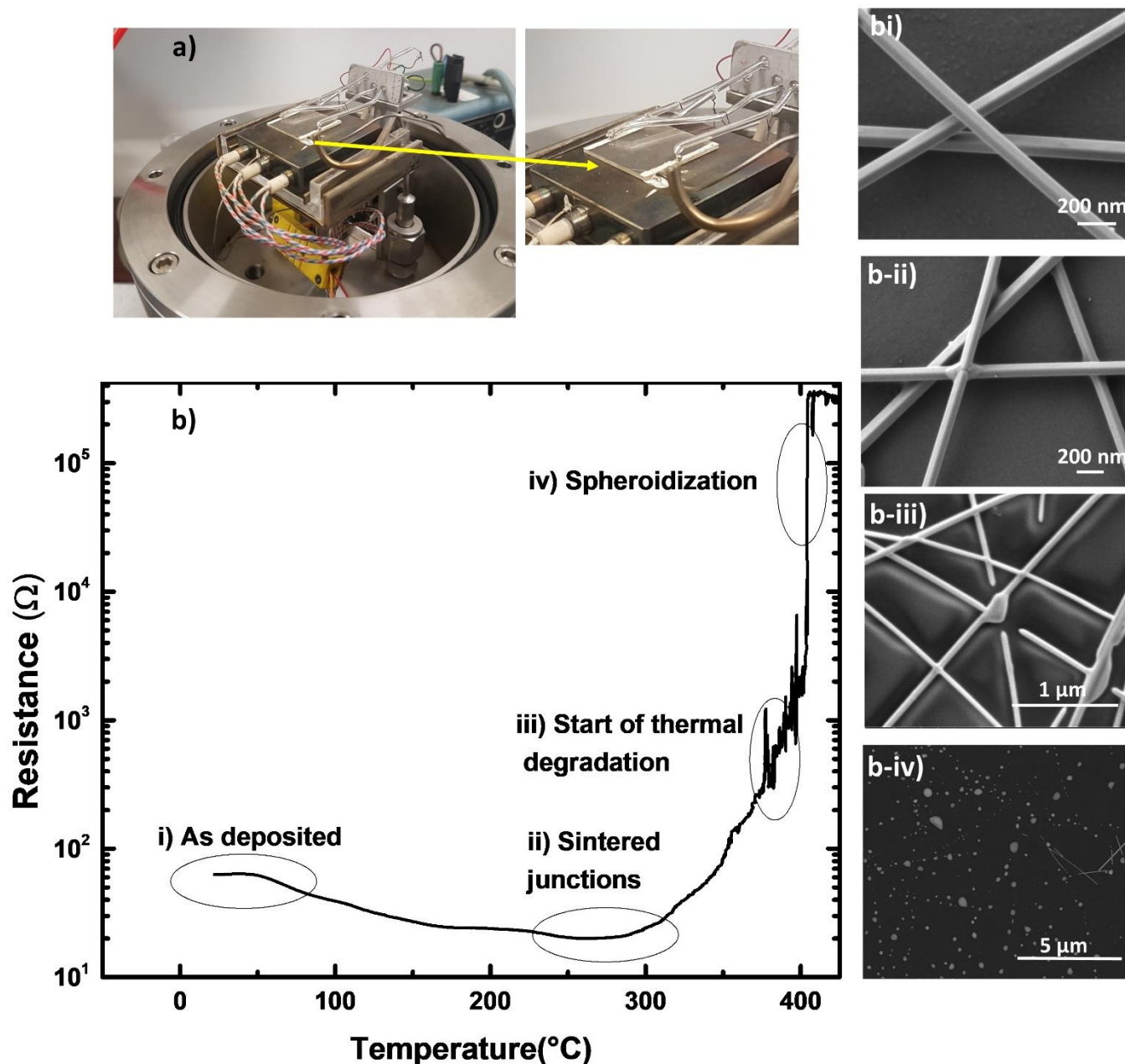


Figure 2-7. a) In-situ thermal annealing setup in LMGP, the inset shows the placement of the sample on the hot plate as well as electrical probes allowing measurements. b) Electrical resistance evolution of a AgNW network during a continuous thermal ramp of  $2^{\circ}\text{C min}^{-1}$  from room temperature to  $400^{\circ}\text{C}$  in the air (sample spin-coated from a  $1 \text{ g L}^{-1}$  ACS-Ag90 solution). Several SEM pictures are reported: b-i) as-deposited sample before thermal treatment; b-ii) Appearance of sintered junctions after annealing up to  $250^{\circ}\text{C}$  with a ramp of  $2^{\circ}\text{C min}^{-1}$ ; b-iii) start of degradation of junctions and AgNWs after annealing up to  $300^{\circ}\text{C}$  with a ramp of  $2^{\circ}\text{C min}^{-1}$ ; b-iv) complete spheroidization as a result of Plateau-Rayleigh instability, nanoparticles are observed at the original position of the wires.



## 2.4.2. Isothermal annealing

Ramped thermal annealing of AgNW networks, enables us to understand the thermal mechanism involved in the evolution of the AgNW network. An alternative way to optimize AgNW networks is to anneal them at a constant temperature on a hot plate, in a process called isothermal annealing. The similar thermally-induced mechanisms discussed in 2.4.1 can be observed during the isothermal annealing process as well. We have studied the effect of isothermal annealing on a series of similar ACS-Ag 90 NW networks, spin-coated on Corning glass using a solution of  $1 \text{ g L}^{-1}$ . Annealings were performed for 1-hour at different temperatures from the range of  $140^\circ\text{C}$  to  $270^\circ\text{C}$ . As shown in Figure 2-8.a and b, SEM images of AgNW networks annealed at  $140^\circ\text{C}$  are similar to as-deposited ones, showing no visible sign of the junction sintering. Increasing the temperature to  $200^\circ\text{C}$  causes the appearance of some sintered junctions. The network annealed at  $230^\circ\text{C}$  for 1 hour, shows the maximum number of sintered junctions before the appearance of any damage through the NW network, see Figure 2-8.c. Increasing temperature beyond this value leads to severe degradation of AgNW network as it has been shown in Figure 2-8.d and e. Therefore, we have chosen an annealing step of  $230^\circ\text{C}$  in air for 1 hour to be optimum to treat ACS-Ag90 NW networks and achieve the best electro-optical properties. Thus, samples used in Chapter 3 of this study, which are composed of ACS-Ag90 NW, all have been treated using this isothermal process.

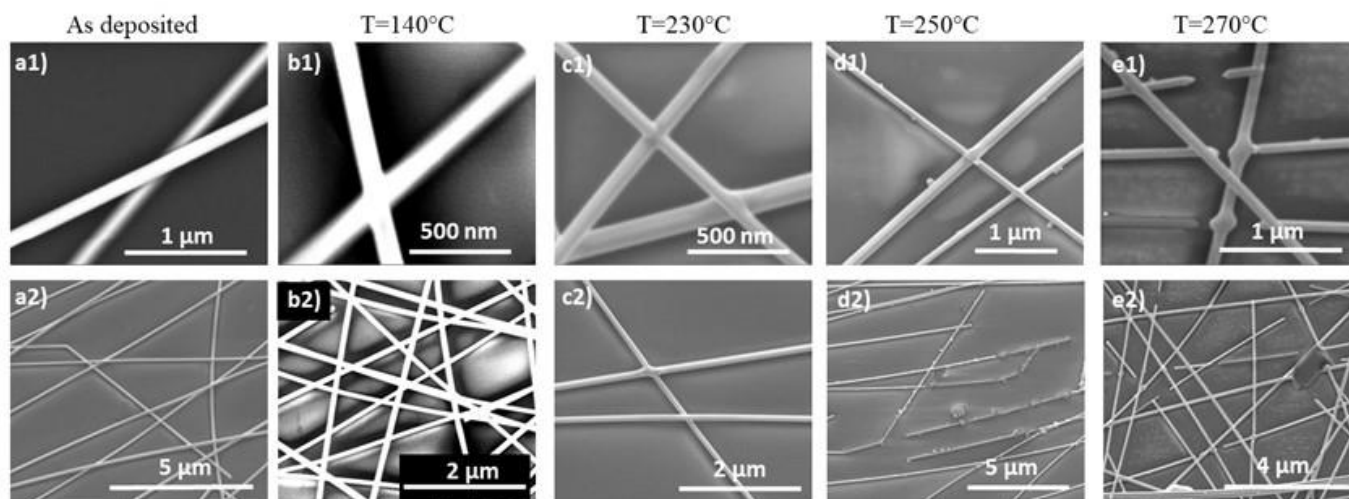


Figure 2-8. SEM images of spin-coated ACS Ag-90 networks: a) as-deposited network. b-e) annealed network at  $140^\circ\text{C}$ ,  $230^\circ\text{C}$ ,  $250^\circ\text{C}$ , and  $270^\circ\text{C}$  in air for 1 hour respectively. With high (top) and low (bottom) magnification.

## **2.5. Conclusions:**

In this chapter, we have briefly reviewed the major techniques which are used to deposit and characterize AgNW based TEs. Spin coating and air-brush spray coating are the two major deposition techniques which have been used to deposit AgNW based TEs in LMGP, they have been discussed. Although Spin coating is a more simple and straightforward technique to form NW networks, air-brush spray coating is generally preferred since it leads to more homogenous and randomly deposited AgNW networks and it is more easily scalable. Details about the formation of efficient silver contact pads at the edges of TEs using thermal evaporation are discussed following by the deposition of AgNWs.

Morphological studies of uncoated and later on metal oxide coated AgNW networks are generally performed using SEM and TEM and AFM imaging techniques. Details about the preparation of samples and parameters used to perform these imagings are discussed in this chapter. The setup to perform UV-visible spectroscopy as another major technique to evaluate optical properties (total transmission and haze factor) is also presented briefly.

Eventually, home-made setups to perform post-deposition treatments on AgNW networks that involve applying mechanical or thermal stress on AgNW networks are introduced. All together, tools to prepare and evaluate AgNW based TEs are reviewed in this chapter that enables us to take a step forward in chapter 3 and tackle one of the main objectives of this thesis, studying the stability of uncoated and metal oxide coated AgNW networks.

## References:

- [1] D. P. Langley, M. Lagrange, N. D. Nguyen, and D. Bellet, "Percolation in networks of 1-dimensional objects: comparison between Monte Carlo simulations and experimental observations," *Nanoscale Horiz.*, vol. 3, no. 5, pp. 545–550, 2018, doi: 10.1039/C8NH00066B.
- [2] M. Lagrange, "Physical analysis of percolating silver nanowire networks used as transparent electrodes for flexible applications," PhD thesis, University of Grenoble Alpes (France), 2015.
- [3] V. Scardaci, R. Coull, P. E. Lyons, D. Rickard, and J. N. Coleman, "Spray Deposition of Highly Transparent, Low-Resistance Networks of Silver Nanowires over Large Areas," *Small*, vol. 7, no. 18, pp. 2621–2628, 2011, doi: 10.1002/sml.201100647.
- [4] T. Akter and W. S. Kim, "Reversibly Stretchable Transparent Conductive Coatings of Spray-Deposited Silver Nanowires," *ACS Appl. Mater. Interfaces*, vol. 4, no. 4, pp. 1855–1859, Apr. 2012, doi: 10.1021/am300058j.
- [5] M. J. Large, J. Burn, A. A. King, S. P. Ogilvie, I. Jurewicz, and A. B. Dalton, "Predicting the optoelectronic properties of nanowire films based on control of length polydispersity," *Sci. Rep.*, vol. 6, p. 25365, May 2016, doi: 10.1038/srep25365.
- [6] J. Krantz *et al.*, "Spray-Coated Silver Nanowires as Top Electrode Layer in Semitransparent P3HT:PCBM-Based Organic Solar Cell Devices," *Adv. Funct. Mater.*, vol. 23, no. 13, pp. 1711–1717, 2013, doi: 10.1002/adfm.201202523.
- [7] S. Liu *et al.*, "Coffee-Ring-Free Ultrasonic Spray Coating Single-Emission Layers for White Organic Light-Emitting Devices and Their Energy-Transfer Mechanism," *ACS Appl. Energy Mater.*, vol. 1, no. 1, pp. 103–112, Jan. 2018, doi: 10.1021/acsaem.7b00011.
- [8] T. Chatin, "silver nanowire networks and nanocomposites for energy harvesting and resistive switching application," Master thesis University Grenoble Alpes France., 2019.
- [9] N.F Lozano, "Silver nanowire networks: Fabrication, characterization and failure mechanisms.," Master thesis University Grenoble Alpes France, 2018.
- [10] D. W. Pashley, M. J. Stowell, M. H. Jacobs, and T. J. Law, "The growth and structure of gold and silver deposits formed by evaporation inside an electron microscope," *Philos. Mag. J. Theor. Exp. Appl. Phys.*, vol. 10, no. 103, pp. 127–158, Jul. 1964, doi: 10.1080/14786436408224212.
- [11] R. Petrović, S. Štrbac, N. Bundaleski, and Z. Rakočević, "Surface roughness minimum: Ag thin layer deposited on a glass," *J. Serbian Chem. Soc.*, vol. 66, no. 7, pp. 483–490, 2001, doi: 10.2298/JSC0107483P.
- [12] B. Hwang *et al.*, "Highly Flexible and Transparent Ag Nanowire Electrode Encapsulated with Ultra-Thin Al<sub>2</sub>O<sub>3</sub>: Thermal, Ambient, and Mechanical Stabilities," *Sci. Rep.*, vol. 7, p. 41336, Jan. 2017, doi: 10.1038/srep41336.
- [13] V. H. Nguyen *et al.*, "Low-cost fabrication of flexible transparent electrodes based on Al doped ZnO and silver nanowire nanocomposites: impact of the network density," *Nanoscale*, p. 10.1039/C9NR02664A, 2019, doi: 10.1039/C9NR02664A.
- [14] R. E. Triambulo, J.-H. Kim, and J.-W. Park, "Highly flexible organic light-emitting diodes on patterned Ag nanowire network transparent electrodes," *Org. Electron.*, vol. 71, pp. 220–226, Aug. 2019, doi: 10.1016/j.orgel.2019.05.035.
- [15] S. Wang *et al.*, "Mechanically and thermally stable, transparent electrodes with silver nanowires encapsulated by atomic layer deposited aluminium oxide for organic optoelectronic devices," *Org. Electron.*, vol. 78, p. 105593, Mar. 2020, doi: 10.1016/j.orgel.2019.105593.
- [16] D. P. Langley *et al.*, "Metallic nanowire networks: effects of thermal annealing on electrical resistance," *Nanoscale*, vol. 6, pp. 13535–13543, Sep. 2014, doi: 10.1039/C4NR04151H.
- [17] M. Lagrange, D. P. Langley, G. Giusti, C. Jiménez, Y. Bréchet, and D. Bellet, "Optimization of Silver Nanowire-Based Transparent Electrodes: Effects of Density, Size and Thermal Annealing," *Nanoscale*, vol. 7, no. 41, pp. 17410–17423, Oct. 2015, doi: 10.1039/C5NR04084A.



## Chapter 3

### **Enhancing the stability of AgNW networks thanks to conformal metal oxide coatings deposited by AP-SALD**



### 3.1. Introduction

As discussed in Chapter 1, the lack of sufficient stability of AgNW-based networks limits the successful integration of these electrodes into functional and commercialisable devices. Here, we will present a brief review of examples of unstable AgNW networks where the origin of instability is either surface/bulk diffusion or oxidation/sulphidation of silver. Diffusion of silver is caused by thermal,[1] and/or electrical[2] stresses, the driving force being to reduce the total surface energy. Oxidation/ sulphidation [3], [4] of silver is also observed while AgNW networks are stored in the atmospheric conditions. Passivation of metallic nanowire networks by thin and transparent coatings of graphene, [5], [6] amorphous carbon film,[7] small organic molecules of 11-mercaptoundecanoic acid (MUA) [8] or polymer coatings of PolyDiMethylSiloxane (PDMS)[9] and PolyMethylMethAcrylate (PMMA) [10] are among well-known methods to improve stability of metallic nanowire networks.

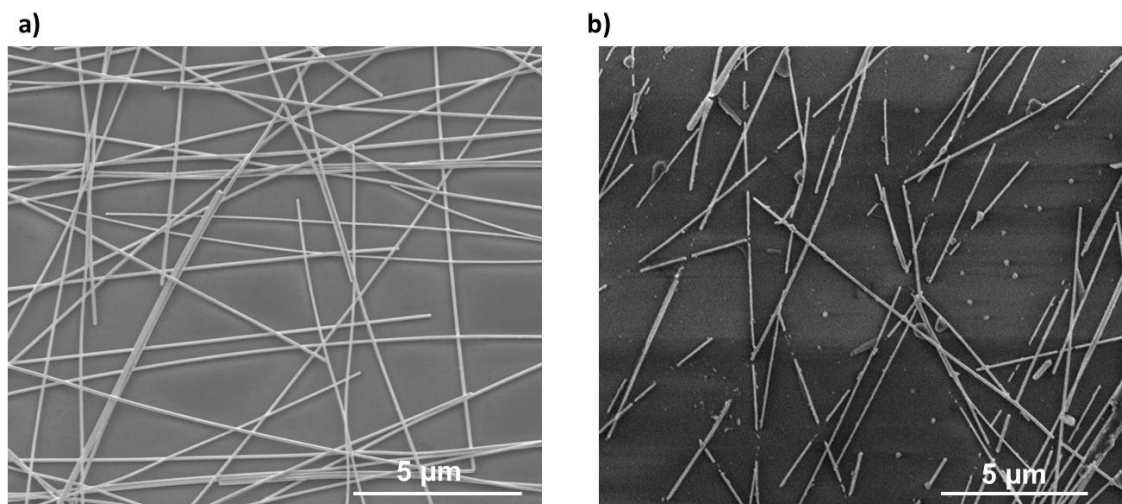
One of the efficient ways to improve the stability of AgNW-based electrodes is to coat them with thin (few tens of nanometers), conformal and homogenous layers of metal oxides.[11]–[13] Previously, during her PhD in LMGP, Mélanie Lagrange reported the enhanced thermal stability of AgNW electrodes with 5 nm of ALD deposited TiO<sub>2</sub> coatings.[14] In LMGP, we replaced conventional ALD with a more modern technique called AP-SALD to deposit coatings of ZnO, Al<sub>2</sub>O<sub>3</sub> and Al:ZnO on AgNWs. The AP-SALD set-up used was designed and developed by David Muñoz-Rojas and his team.[15] We have performed a comprehensive study on the thermal and electrical stability of bare and metal-oxide-coated AgNW networks and compared the performance of oxides in the stability enhancement as well as the optical properties of composite electrodes. Finally, a bilayer coating of ZnO/ Al<sub>2</sub>O<sub>3</sub> was proposed to benefit from the anti-reflection effect of Al<sub>2</sub>O<sub>3</sub> over the ZnO coating, as well as the superior thermal stability of the bilayer as compared to ZnO or Al<sub>2</sub>O<sub>3</sub> coatings solely. Parts of the results which will be presented in this chapter have been already published by our team in ACS-Applied Materials and Interfaces,[16] and Nanoscale. [17]

### 3.2. Lack of sufficient stability as a major drawback of AgNW networks

#### 3.2.1. Plateau-Rayleigh instability

Although silver has the highest thermal and electrical conductivity of all materials at room temperature, the electrical performance of as-deposited electrodes based on AgNWs can be limited due to high contact resistance between adjacent NWs. As discussed in Chapter 1, the residual organic layer of PVP as the result of polyol process for the synthesis of AgNWs, section 1.3.1, and the limited contact area between adjacent NWs after deposition,

section 1.3.1, are the main reasons beyond the high electrical resistance of as-deposited AgNW networks. There are reports of several methods to decrease the electrical resistance of AgNW networks, which are all based on sintered junctions between adjacent NWs. Applying heat,[18] mechanical pressure,[19] coatings by metal oxide layers like ZnO (Zinc Oxide),[20] or graphene[21] and applying pulse laser rapid heating[22] are among the well-described processes to treat NW to NW junctions. Although thermal annealing[1], [23] is beneficial for reducing junction resistance thanks to local sintering, it is also known that reaching too high a temperature leads to a morphological instability which is called “spheroidization” of the AgNWs. Spheroidization is the process of non-reversible evolution from silver NWs into disconnected particles/spheres of silver, causing the loss of the percolating nature of the network and eventually leading to infinite electrical resistance.[1] The origin of the spheroidization is called Plateau-Rayleigh instability and has already been observed in other metallic NWs, for example by Karim et al. on gold NWs.[24] While the melting point of bulk silver is above 960 °C, degradation induced by thermal annealing, spheroidization, can occur at a much lower temperature (i.e. < 300 °C) due to the high surface-to-volume ratio in NWs.[18] Increased atomic surface diffusion of Ag atoms at high temperatures leads them to adopt a spherical shape to decrease the total surface energy of NWs. This atomic surface diffusion is the main mechanism behind spheroidization. SEM observations in Figure 3-1.a exhibit ACS-Ag90 AgNW networks spin-coated on Corning glass substrates. As-deposited network shows no sign of damage or degradation of the NWs, however after a thermal ramp up to 400 °C (2 °C min<sup>-1</sup>) in air, degradation and spheroidization of NWs are visible in Figure 3-1.b.



*Figure 3-1. SEM images showing the a) as-deposited ACS-Ag90 AgNW network, and b) Spheroidization after a thermal ramp of 2 °C min<sup>-1</sup> up to 400 °C in air.*



### 3.2.2. Breakdown of silver NWs as a result of high electrical current and electromigration

In Chapter 2, 2.4, we have discussed some post-deposition techniques to improve the electrical performance of the as-deposited AgNW networks, the main focus being on the thermal annealing. Although this technique is efficient and well controllable, it is rather time-consuming and might cause damage to thermally sensitive substrates. One of the efficient, fast and low-power consumption ways to improve the electrical contact properties between metallic NWsNWs is a process called electrical welding, as we mentioned in Chapter 1, 1.2.3.[25]–[27] Electrical welding occurs due to two major effects, namely, current assisted Joule heating (especially at junctions as a result of high electrical resistance and high current density of junctions) and electromigration. [25] Electromigration or electron transport is a well-known phenomenon in thin metal films, which corresponds to the atomic motion of metals under the influence of electrical current. [28] Electromigration is enhanced at the nanoscale due to two main reasons: first, increased current density and second, reduced dimensions. Song et al., have reported that a two nanowire contact system with initial electrical resistance larger than  $10^{10} \Omega$ , can be treated to a junction of reduced resistance to  $185 \Omega$ , as a result of current density around  $1.5 \times 10^7 \text{ A cm}^{-2}$  (the diameter of NWsNWs is around 50 nm).[25] The high temperature at the junctions will induce surface and bulk diffusion of silver atoms allowing adjacent NWsNWs to weld together and create higher junction area. This treatment can stabilize the resistance of AgNWs junctions in just 30 seconds. A similar treatment can be applied at the level of the entire network, instead of a single nanowire junction, and decrease the electrical resistance of random AgNW networks. However, electromigration and localised Joule heating will not stop after the initial seconds of treatment and can affect the network morphology while high voltage is applied to the network for a longer time. Nur Kholid et al. have reported breakdown of AgNW networks with an average diameter of 150 nm and sheet resistance of  $40 \Omega \text{ sq}^{-1}$ , with current densities around  $25 \text{ A cm}^{-2}$  at the network level.[27] This can be detrimental in the applications where high current densities are applied to the AgNW networks for a longer time; one example of such applications is transparent heaters.[4] To demonstrate electrical instability in our study, AgNW network sprayed by using ACS-Ag90 solutions, with initial electrical resistance of  $30 \Omega \text{ sq}^{-1}$  underwent an increasing electrical voltage with a ramp of  $0.1 \text{ V min}^{-1}$  up to 9 V. As shown in Figure 3-2.a, increased voltage causes damages in NWsNWs, which initiate from the smaller ones.[25] Figure 3-2.b shows a typical junction just before the breakdown, where the bigger nanowire stays stable, and the smaller one degrades. However, the degradation of smaller NWs will not directly lead to the breakdown of the entire AgNW network. Sannicola et al. have comprehensively studied the failure mechanism of AgNW networks under high electrical voltage.[29] While increasing applied electrical voltage on an AgNW network, the first observed stage is “optimization” of the network as we discussed above. Following optimization, increasing voltage causes

degradation in some NWs and finally “breakdown” occurs. They have observed experimentally that breakdown of AgNWs networks under high voltage is a local phenomenon, unlike thermal degradation which affects the entire network. For the former, an initial defect appears on AgNW network due to the high applied voltage and rapidly creates and propagates a crack in the network (parallel to the bias electrodes). While the initial crack propagates, some part of AgNWs might remain untouched, therefore they can act as secondary conductive path for the current. As a result, multiple breakdowns occur before the complete failure of the network.[29]

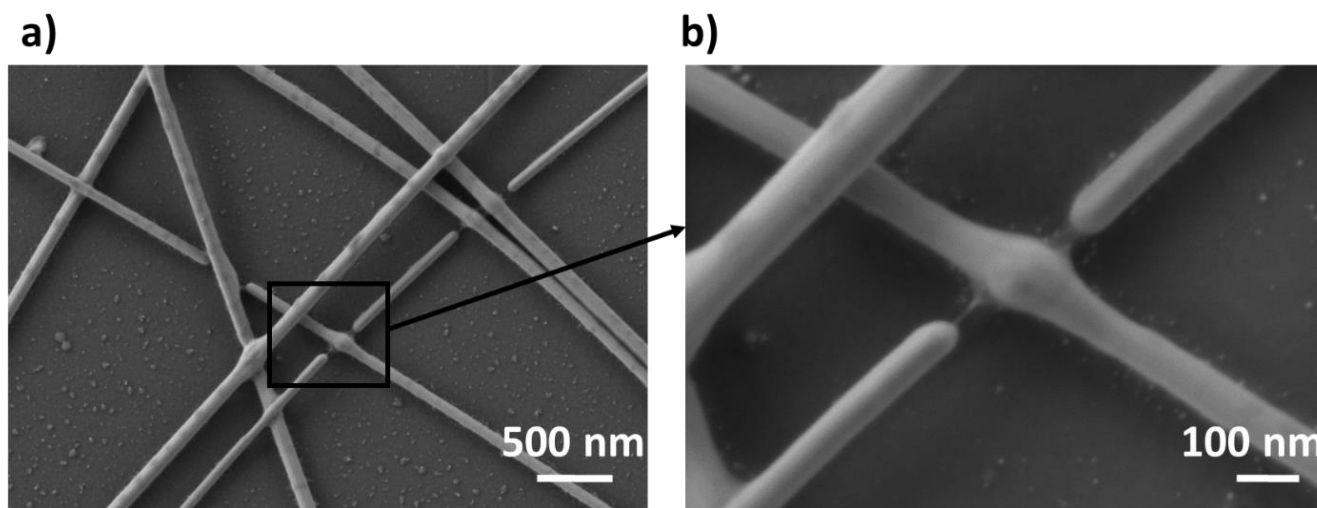


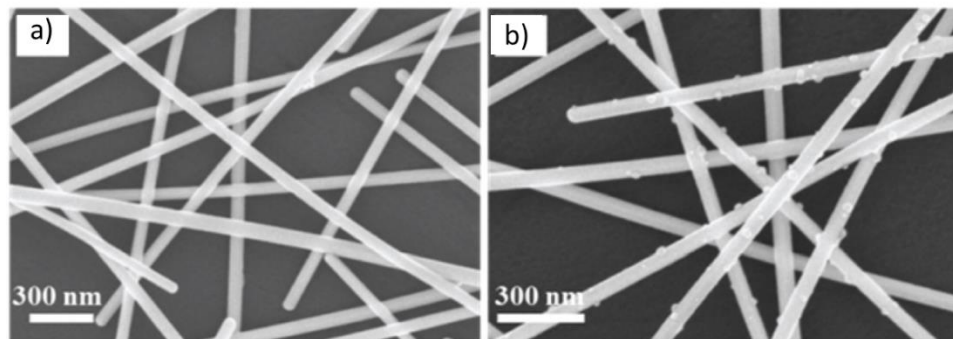
Figure 3-2. a) SEM image of ACS-Ag90 AgNW network with initial resistance of  $11 \Omega$ , after voltage ramp of  $0.1 \text{ V min}^{-1}$  is applied up to 9 V. b) Zoom showing a junction between AgNWs, where smaller nanowire breaks earlier.

### 3.2.3. Sulphidation or oxidation of silver NWs

Another mechanism behind the observed changes in the morphology or the electrical resistance of AgNW based TEs can be chemical instability during the storage of electrodes in ambient or high temperature/humidity conditions. Electrodes based on AgNW networks have shown to have different ageing kinetics which raises from the differences in the surface chemistry due to different synthesis, purification, deposition or post-deposition treatments. Moon et al. have studied chemical, thermal and corrosion stability of AgNWs networks while storing them at environmental, high temperature or hydrogen sulphide ( $\text{H}_2\text{S}$ ) gas conditions.[3] Silver, unlike many metals, does not form a natural oxide layer; however, sulphidation of bulk silver is a well-known phenomenon.[30], [31] Since AgNWs are more sensitive to hydrogen sulphide ( $\text{H}_2\text{S}$ ) than sulfur dioxide ( $\text{SO}_2$ ), sulphidation tests are conducted in  $\text{H}_2\text{S}$ . According to Moon et al., exposure to air for 60 days eases the process of oxidation and increases the resistance of AgNWs

more than 200%. Conversely, in the presence of H<sub>2</sub>S the degradation was much faster and after 20 minutes a 896% increment in the electrical resistance of AgNW networks was observed.[3]

However, other groups have reported different stability behaviour of AgNWs in environmental conditions, which probably arises from the difference in the surface chemistry of tested AgNWs. [4] Mayousse et al. have observed perfect stability of AgNW networks deposited by both spin coating and spray coating techniques, stored in the laboratory atmosphere and protected from light.[4] There was no evidence of the change in the electrical properties of networks after two years and a half. Conversely, they have observed elevation in the AgNW network electrical resistance while samples were stored in high temperature and humidity chambers: relative humidity of (90%) and two different temperatures (38°C and 60°C). They observed that acceleration of the ageing process in humidity depends on the temperature. Although the networks stored at 38 °C did not show any increase in electrical resistance, samples stored at 60 °C for 10 days showed an 80% increase in the resistance. AgNW network exposed to a 50 ppm flow rate of H<sub>2</sub>S in dry air for 8 hours did not show any evidence of change in electrical resistance. Nevertheless, SEM images as shown in Figure 3-3 confirm the appearance of tiny particles along the NWs, which NWs are confirmed to contain Ag<sub>2</sub>S according to XPS analysis based on TEM images.



*Figure 3- 3. SEM images of AgNW network: a) before and b) after exposure to a 50 ppm flow of H<sub>2</sub>S for 8 hours. Reproduced from reference. [4]*

One efficient way to hinder the instabilities discussed above is to protect AgNW networks with thin layers (tens of nanometers) of metallic oxides like ZnO, [16], [32], [33] Al: ZnO [34], [35], Titanium dioxide (TiO<sub>2</sub>)[36] or Aluminium oxide (Al<sub>2</sub>O<sub>3</sub>).[33], [37] Conformal coatings of thin metal oxide layers have been shown to have a drastic enhancement of the stability of AgNW networks. So far sol-gel,[36], [38] sputtering,[32], [35] spin

coating[39], [40] and ALD[41] have been used to deposit metal oxide coatings over AgNW networks. However, some characteristics of the used deposition methods such as either the requirement of vacuum, low-deposition rate or low-scalability, are in contrast with one of the main advantages of AgNW based TEs, which is its compatibility with low-cost and high-throughput scalable fabrication techniques. In previous reports, we have shown that AP-SALD is a very appealing technique to engineer AgNW electrodes.[16]

### **3.3. AP-SALD as a novel technique to coat AgNWs and its advantages over spin coating, ALD or sputtering**

AP-SALD is a promising recent approach to replace ALD that can operate at atmospheric pressure, is easily scalable and up to two orders of magnitude faster than conventional ALD. [42]–[44] This is so thanks to the spatial separation of precursors in AP-SALD, which eliminates the need for purging steps between successive precursor injections in conventional ALD.[42], [45], [46] Figure 3-4.a and b illustrate the schematic of successive precursor injection and spatial separation in ALD and SALD respectively. The AP-SALD set-ups that are being developed at LMGP use the “close-proximity” approach, in which the different precursors are supplied via a manifold injection head along parallel channels kept away by adjacent inert gas-flow channels, as shown in Figure 3-4.c (precursors shown in this image are examples for the deposition of  $\text{Al}_2\text{O}_3$ ). The close proximity between head and substrate prevents the mixing of the different flows in the gap between the injection head and the substrate. Precursor concentration in the different flows must also be tuned to prevent diffusion of precursor molecules between the different channels. In such optimized conditions, ALD takes place, and reactions are limited to the surface and are self-terminating. Relative motion between the substrate and head provides the ALD cycles yielding film growth. As a result, the system is completely atmospheric and operates in the open air, without the use of a deposition chamber. AP-SALD has already been used to deposit high-quality oxide films as passive and active components for new generation solar cells and other devices.[42], [44]

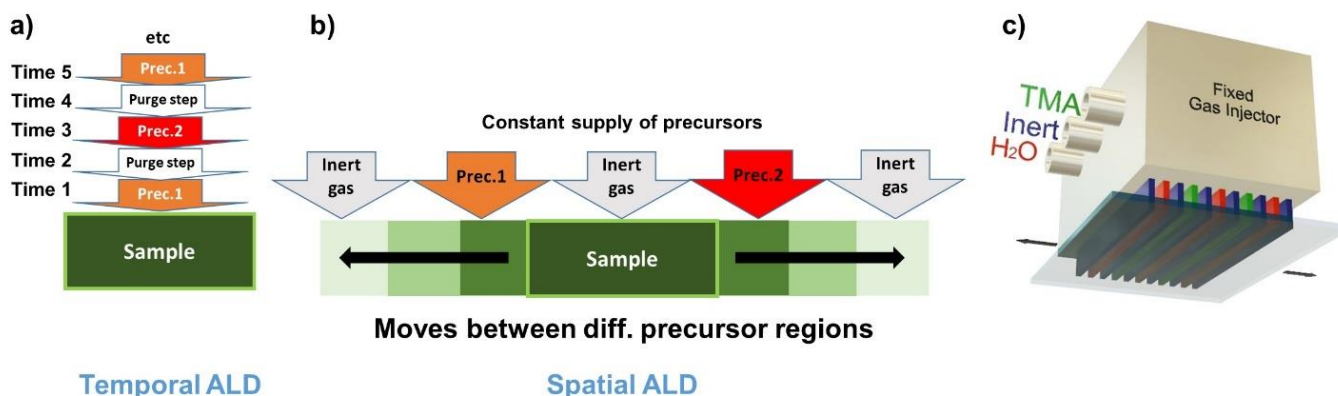


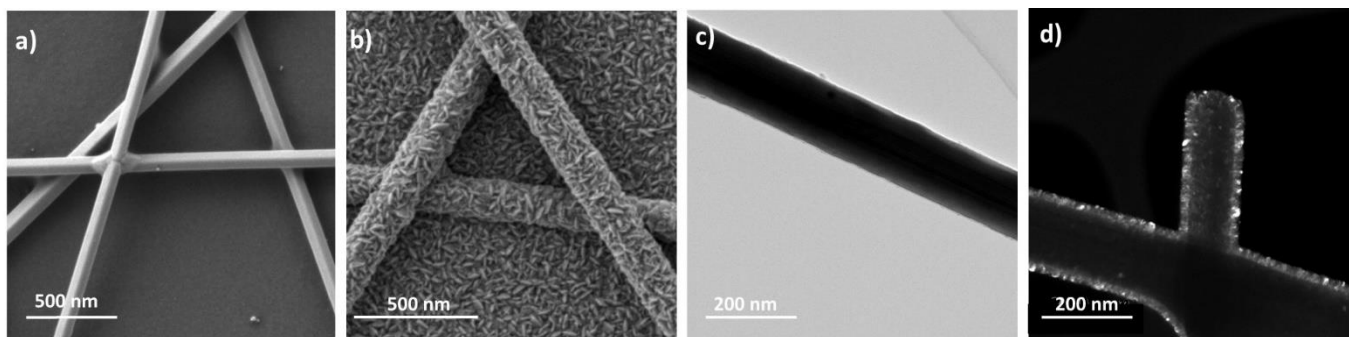
Figure 3-4. a-b) Comparison between the temporal (and more traditional) ALD (a) and of SALD principles (b): the separation between the two reactive precursors is performed either in time or space, respectively. c) An AP-SALD gas injector with three gas inlets of trimethylaluminum (TMA), inert gas ( $N_2$ ), and  $H_2O$ , which are then continuously injected to a moving substrate, the gas exhaust channels are not shown in this Figure. Reproduced from reference [15]

### 3.4. ZnO coating of the AgNW network with AP-SALD

AP-SALD was used to deposit ZnO thin layers to improve the thermal and electrical stability of AgNW networks. The deposition parameters were optimised and then ZnO AP-SALD growth was carried out at 200 °C, using diethylzinc ( $(C_2H_5)_2Zn$ ; DEZ) and water vapour as precursors for zinc and oxygen, respectively. The samples were placed at a distance of 200  $\mu m$  under the injection head oscillating at 10  $cm\ s^{-1}$ . In our deposition head, there are two channels for the metal precursor. Thus, each sample oscillation (forth and back) corresponds to four ALD cycles.[47] The system allows depositing over an area of  $5 \times 5\ cm^2$ . The SALD deposition of ZnO and  $Al_2O_3$  coatings for this Thesis was performed by Dr. Viet H. Nguyen, from the SALD team.

An SEM image of the bare AgNW networks of ACS-Ag90 annealed at 230 °C for 60 minutes is shown in Figure 3-5.a, where effective sintering of the wires at the junctions is visible. A similar coated network, after the same annealing treatment, with a 40 nm thick ZnO coating deposited with AP-SALD is shown in Figure 3-5.b. The distinct polycrystalline morphology of the ZnO coating can be observed both in the NWs and the glass surface. As shown in Figure 3-5.a, the surface of the bare NWs appears smooth while that of ZnO-coated AgNWs show the typical granular morphology of ZnO coatings deposited by AP-SALD.[48]

Figures 3-5.c and d show TEM images of a bare and 30 nm ZnO coated AgNW with a diameter around 90 nm, which enables to highlight the polycrystalline nature of ZnO coating. Such coating appears very conformal: this point is crucial since this is a prerequisite for efficient protection against any instability. As in ALD, in AP-SALD the ZnO layer thickness is proportional to the number of AP-SALD cycles, i.e. sample oscillations under the head. The growth rate,  $r$ , was thus estimated from the thickness measured for the thicker ZnO layer deposited on AgNWs divided by the number of AP-SALD oscillations. The thickness of 80 cycles of AP-SALD ZnO coating was estimated to be 40 nm. The growth rate was thus  $\sim 0.50$  nm/oscillation (as stated above, in our AP-SALD system a sample oscillation is equivalent to 4 conventional ALD cycles),[48] yielding a growth per cycle (GPC) of about  $1.25 \text{ \AA/ALD cycle}$ .



*Figure 3- 5. SEM image of the bare and ZnO coated AgNW networks, all networks were annealed at  $230^\circ\text{C}$  in air for 60 minutes (prior to oxide deposition). a) SEM image of the bare AgNWs. b) SEM image of a ZnO coated AgNW with an average coating thickness of 40 nm. c) A TEM image of a AgNW with a diameter of 90 nm. d) Dark Field TEM image of a ZnO coated AgNW, showing the polycrystalline nature of the 30 nm AP-SALD ZnO layer.*

### 3.4.1. Effect of ZnO coating on the adhesion of AgNWs on the glass substrate

Before focusing on the impact of ZnO coating on the electrical and thermal stability of AgNW networks, we first considered the impact on both the network adhesion and optical transparency. It is known that low adhesion of AgNW networks to the substrate can be one of the drawbacks of these materials when used as TEs, since even a gentle rub can remove NWs from the substrate.[49] The influence of the AP-SALD ZnO coating on the adherence of AgNW network on the glass substrate was thus investigated by Afzal Khan and Viet H.Nguyen. To do so a scotch tape test was applied to both the bare and the coated networks to qualitatively compare their adhesion strength

to the substrates. AgNW suspensions in isopropanol were purchased from Seashell technology. The average length of AgNWs was 32  $\mu\text{m}$ , whereas their average diameter was 130 nm. AgNW solution was deposited on Corning glass using spin coating process as described in Chapter 2, 2.2.1. Post-deposition thermal annealing at 250  $^{\circ}\text{C}$  for 30 minutes step was performed to decrease the electrical resistance of the junctions between adjacent AgNWs. Figure 3-6 shows SEM images of the bare (top) and the 20 nm ZnO coated (bottom) AgNW networks. The right images correspond to the areas on which the scotch tape test was applied, while the left parts correspond to regions outside the tested zone.[16]

It can be seen from Figure 3- 6 that for bare AgNW networks most of the NWs are removed, showing the very low adhesion of the bare AgNWs to the substrate. Conversely, for coated networks numerous NWs remained on the substrate, thereby showing definite improvement in AgNWs adhesion to the substrate.

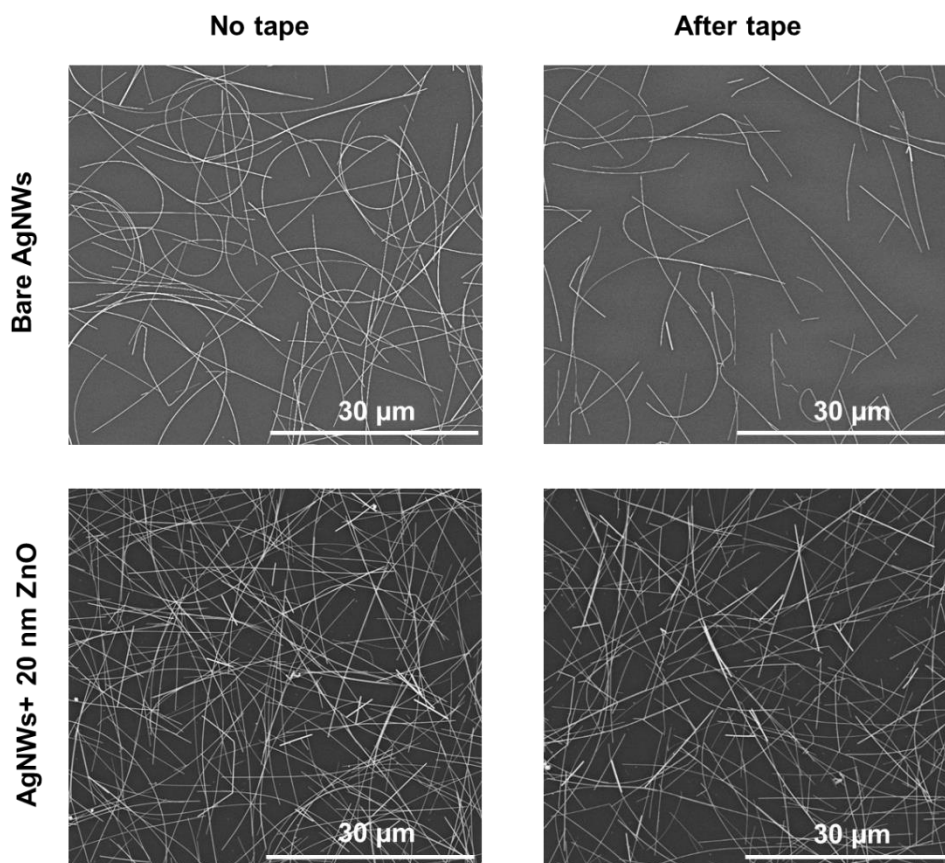


Figure 3- 6. SEM images of bare (top) and ZnO coated (20 nm) (bottom) AgNW networks. The right (left) half is the region where the tape was (not) applied. This shows the effect of the scotch tape test.

### 3.4.2. Effect of ZnO coating thickness on the optical transmittance and haze factor of AgNW networks

The effect of the ZnO coatings on the transparency of AgNW networks was evaluated. AgNW networks were deposited using airbrush spray of ACS-Ag90 and annealed at 230 °C in air for 60 minutes. Bare AgNW networks had an initial sheet resistance of 5  $\Omega$  sq<sup>-1</sup> and the total and diffuse transmittance at 550 nm was 85.6% and 7.26% respectively. Figure 3-7.a reports the influence of the ZnO coating thickness (from 10 to 50 nm) on the total transparency (measured for a wavelength range of 250 to 2500 nm) of coated AgNW networks. In a first approximation, a linear decrease of the optical transparency from 85 % for bare AgNWs to 76 % for 50 nm ZnO coated AgNWs, both in the visible wavelength range (380-700 nm), can be observed. An example of a 200 nm coating of Al:ZnO coating on AgNW network was also studied. As has been reported in the literature, Al:ZnO films are less transparent in the infrared region compared to the visible range. [50], [51] This is due to the increase in reflectance caused by the plasma resonance of electron gas (free carriers) in the conduction band. In the electrical field of a light wave, the conduction band electrons form collective plasma oscillation or plasmons. From an optical point of view, TCO films generally behave like metals and reflect or absorb light at the longer wavelength. [52]

For an optimized integration of coated AgNW networks, a compromise should be considered, depending on the application targeted. Indeed, as seen below in sections 3.4.3, 3.4.4 and 3.4.6, increasing the ZnO coating thickness leads to a higher environmental, electrical and thermal stability of the AgNW networks. However, such a boost in the stability comes along with the degradation of the optical performance of the coated AgNW networks. The decrease of optical transparency is nevertheless still acceptable for some applications, such as transparent heaters, where applying voltage leads to a non-reversibility in the electrical resistance [16], [53], [54] and ZnO coating has been proven to enhance reversibility and stability at the same voltage conditions. [16]



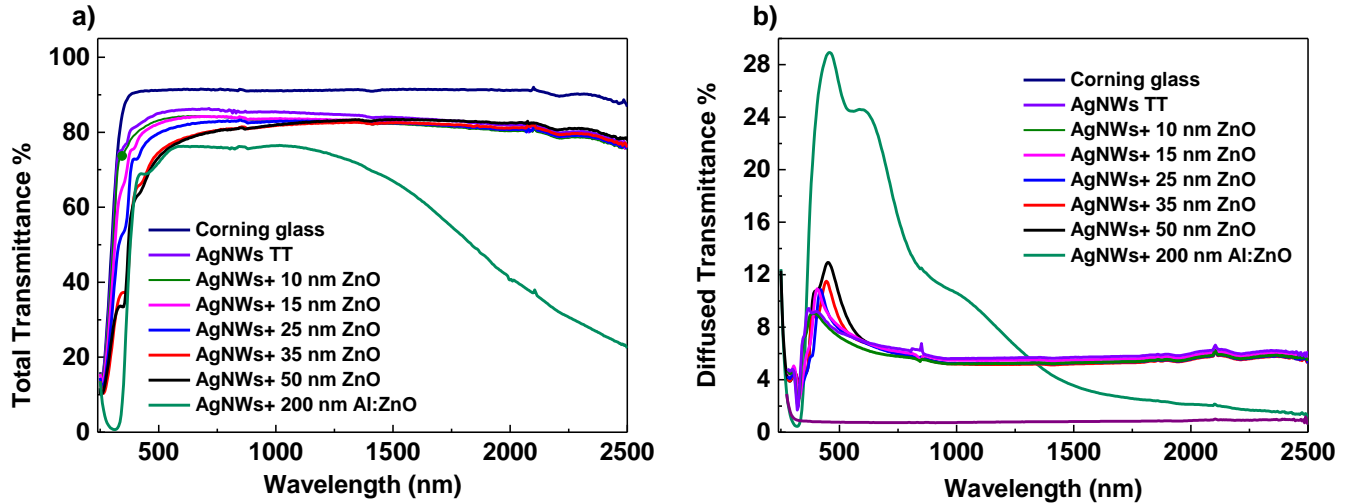


Figure 3- 7. a) Optical total transmittance and (b) diffuse transmittance (substrate contribution non-subtracted) of a bare substrate of Corning glass (in blue), bare AgNW network deposited by spray coating and five AgNW networks coated by increasing thickness of ZnO coatings. AgNW network coated by 200 nm of Al:ZnO which is not transparent in the NIR region unlike bare or ZnO coated AgNW networks is also reported in this Figure.

Figure 3-7.b, represents the diffuse transmittance of bare, ZnO and Al:ZnO coated AgNWs, which is essential to calculate the haze factor of these films. Higher diffuse transmittance of thicker ZnO coatings as observed in Figure 3- 7.b, can be explained due to the presence of larger grain size and higher roughness of thicker ZnO films. Nguyen et al. have reported the change of roughness in AP-SALD coated Al:ZnO films, as thickness increased from 205 to 525 nm.[55] They have shown that thicker films have a bigger grain size which can eventually lead to higher diffusion of light.[55] The haze factor is a parameter that quantifies the amount of light scattered by the investigated material and is simply defined as the ratio between diffuse transmittance and total transmittance, as discussed in Chapter 1, section 1.4.2.2. Figure 3-8.a and b show the dependency of the haze factor on ZnO film thickness, the thicker the ZnO film, the higher the haze factor. This observation can be explained by considering two effects: first, the decrease in total transmittance and second, the increase in diffuse transmittance of ZnO coated AgNW networks as the thickness of coating increases.

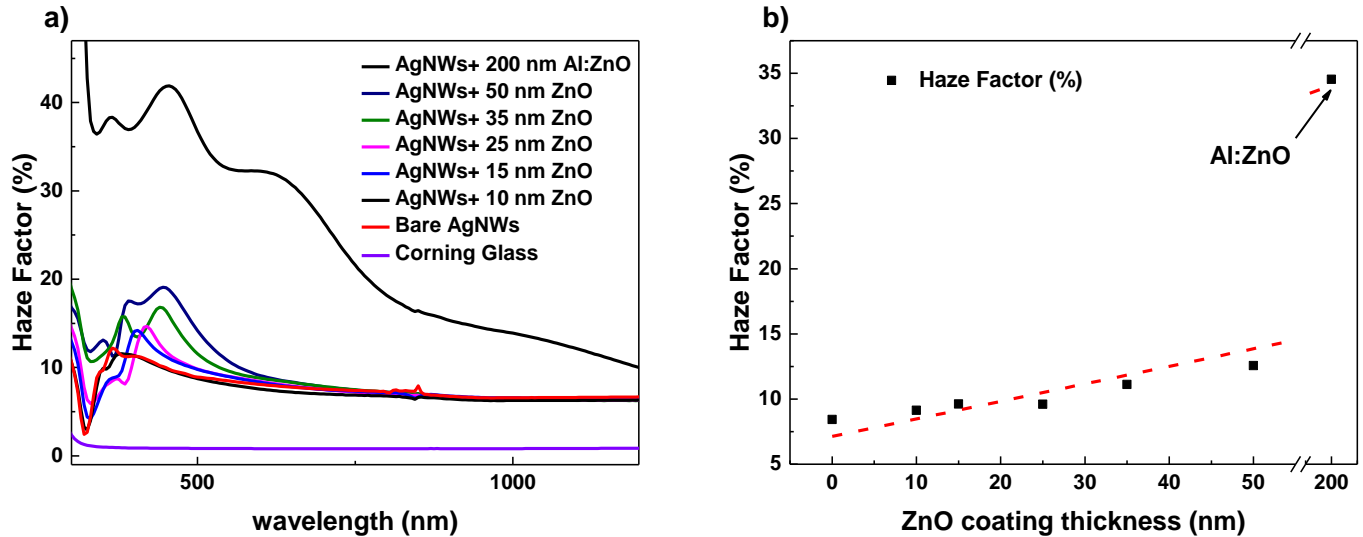


Figure 3- 8. a) Optical haze factor (%) of Corning glass, bare and ZnO coated AgNW networks with increasing ZnO thickness from 10 to 50 nm. A 200 nm Al:ZnO coated AgNW network is also presented. b) Haze factor (%) of bare, and ZnO coated AgNW networks in the visible range (380-700 nm) versus ZnO thickness. A 200 nm Al:ZnO coated AgNW network is also presented. The dashed line is a guide for the eye.

### 3.4.3. Effect of ZnO coatings on the ageing process of AgNW networks

As discussed in 3.2.3, TEs based on AgNWs might suffer from a lack of environmental stability depending on the type of used AgNWs and storage conditions.[3], [4] Here, we have studied the ageing process of bare and ZnO coated AgNW network to evaluate the effect of ZnO coating on the stability of AgNW based electrodes during a few years after deposition. ACS-Ag90 silver NWs were spin-coated on Corning glass substrates and annealed at 230 °C in air for 60 minutes. 6 samples were kept uncoated with initial average resistance of  $12.1 \pm 2.4 \Omega$  and total transmittance in the visible range (380 to 700 nm) of 85%. Coatings of 20 nm and 40 nm of ZnO were AP-SALD deposited on 8 samples of AgNW networks. Total transmittance of coated networks in the visible range (380-700 nm) for 20 nm and 40 nm ZnO coated AgNW networks was 80% and 74%, respectively. The average resistance of coated AgNW networks was  $8.1 \pm 1.5 \Omega$ . The decrease of resistance in the coated networks can be explained by increased conductive pathways between adjacent NWs due to metal oxide (ZnO in this case) coating.[36] Samples were kept in atmospheric laboratory conditions protected from direct sunlight while regular electrical resistance and SEM measurements were performed on both bare and ZnO coated samples. Up to 1 year after deposition, no apparent effect of ageing is observed either in terms of electrical resistance nor any morphological change in the AgNWs under SEM imaging as shown in Figure 3-9.a and 3-9.b, respectively. However, after 2 years

of storage, bare AgNWs have the highest increase in the electrical resistance, around 35%, while ZnO coating has preserved AgNW network from evolution in the resistance. While 20 nm coated ZnO AgNW networks show 25% increase in the electrical resistance, networks with 40 nm show only 5% increase in the electrical resistance. Although there are slight changes in the networks electrical properties, there is no trace of particles on AgNWs in SEM observations. This point needs further investigation using TEM and XPS analysis on them to investigate the Potential presence of Ag<sub>2</sub>S in the NWs.

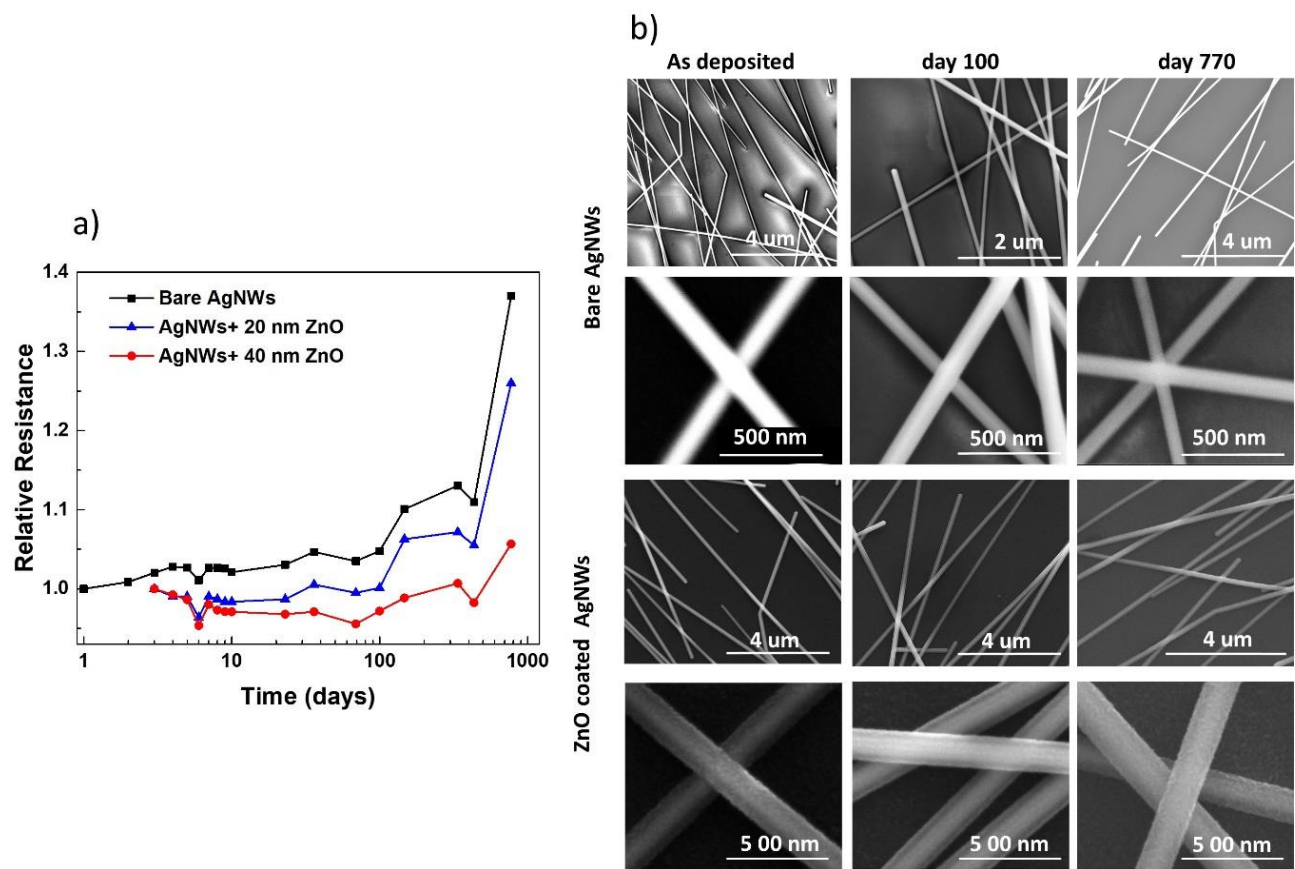


Figure 3-9. a) Plot of the evolution of relative resistance of bare AgNW network (colored in black), AgNW networks with 20 nm of AP-SALD ZnO coating (colored in blue) and 40 nm of AP-SALD ZnO coating colored in red). Samples were stored in the laboratory environment protected from direct sunlight for more than two years. b) SEM images of bare and 40 nm of ZnO coated AgNWs on the Corning substrate, right after, 100 days and 2 years of deposition low (top) and high (bottom) magnifications.

#### 3.4.4. Effect of ZnO coatings on the electrical stability of AgNW networks

As we have discussed earlier in section 3.2.1 and 3.2.2, the lack of stability of AgNWs against thermal and electrical stresses can lead to fast degradation of these NWs and affects the performance and reliability of the associated device in long term usage. The performance of bare and ZnO coated AgNW networks, against electrical stress was mainly studied by Khan et al. to see how ZnO can impact the electrical stability of AgNW networks. [16] Seashell AgNWs with average diameter of 130 nm were deposited on Corning glass using spin coating and annealed at 250 °C for 30 minutes.

The evolution of the electrical resistance of bare and ZnO coated (associated with different coating thicknesses) AgNW networks, during a voltage ramp of 0.1 V min<sup>-1</sup> is presented in Figure 3-10.a.[16] Generally, there are two phases observed for both bare and ZnO coated AgNW networks: first, a linear increase of the electrical resistance versus applied voltage (reversible) and second, electrical failure of the AgNW networks, as discussed in section 3.2.2 (irreversible). A slight linear increase in the electrical resistance of bare or ZnO coated AgNWs networks at low voltage values occurs due to the Joule heating effect. As electrical current flows through the network, electron-phonon interactions occur and lead to an increase in the temperature of the network, therefore its resistance as well. This is typical behaviour in metals.[56] A linear approximation is used to model the dependency of electrical resistivity on temperature as:

$$\rho(T_0 + \Delta T) = \rho_0(1 + \beta_R \times \Delta T) \quad (3-1)$$

where  $\rho_0$  is the electrical resistivity at the temperature  $T_0$  while  $\beta_R$  is the temperature coefficient of resistivity. For bare AgNW networks  $\beta_R$  is around  $(2.4 \pm 0.1) \times 10^{-3} \text{ K}^{-1}$ , while it is  $(2.6 \pm 0.1) \times 10^{-3} \text{ K}^{-1}$  and  $(2.3 \pm 0.1) \times 10^{-3} \text{ K}^{-1}$  for ZnO and Al<sub>2</sub>O<sub>3</sub>-coated AgNW networks, respectively.[17] Such values are very close to that reported for AgNW networks by Lagrange et al.[18] ( $(2.4 \pm 0.1) \times 10^{-3} \text{ K}^{-1}$ ). When compared with  $\beta_R$  for bulk silver,  $3.8 \times 10^{-3} \text{ K}^{-1}$ , [57] the  $\beta_R$  value for AgNW networks appears to be much smaller, probably due to surface effects within AgNWs, the presence of junctions between different AgNWs and possible defects such as grain boundaries or twins for instance.

The linear increase in the electrical resistance due to low applied voltages is reversible, while at high applied voltage values a sudden and irreversible increase of the electrical resistance of the network is observed due to the electromigration of Ag atoms. Figure 3-10.a shows that the failure voltage of AgNW networks strongly depends on the ZnO coating thickness, the higher the coating thickness, the higher the failure voltage. [16] While bare AgNW

network breakdowns due to the electrical failure at around 9 V, the network with 30 nm coating of ZnO can resist up to 18 V, which corresponds to a 100% increase of the associated failure voltage. Figure 3-10.b shows the correlation between the failure voltage and ZnO coating thickness for AgNW networks; this correlation will be discussed further in the following section.

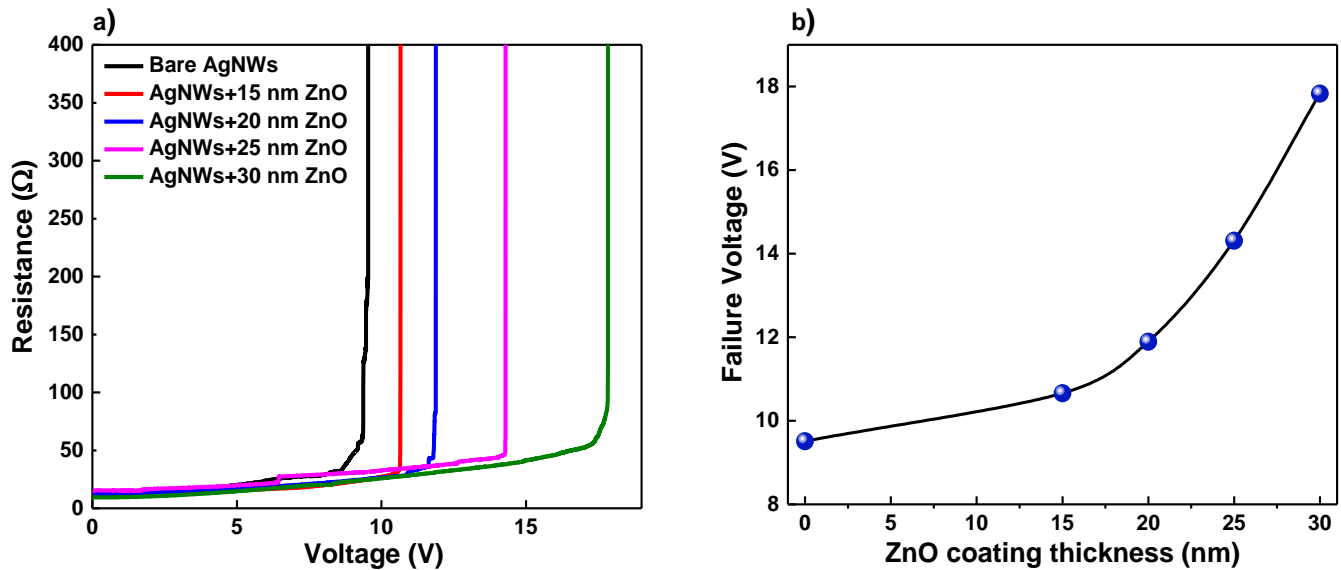


Figure 3-10. a) Evolution of electrical resistance of bare and ZnO-coated AgNW networks during a voltage ramp of  $0.1 \text{ V min}^{-1}$ . While the bare AgNW network breaks at 9 V, increasing ZnO coating thickness increases failure voltage: a 30 nm ZnO coated-AgNW network has increased failure voltage to 18 V. b) Dependency of failure voltage on ZnO coating thickness. There is a non-linear correlation between failure voltage and ZnO layer thickness. (the line is a guide for the eye). Reproduced from reference [16]

### 3.4.5. Formulation of the effect of the ZnO coating on the stability of AgNW networks

Reduction of surface energy is the main driving force behind instability, observed both in electrical and thermal degradation of AgNW networks. In the case of electrical degradation, junctions between adjacent AgNWs are more fragile points compared to straight parts of NWs. As we have discussed in Chapter 1, section 1.3.3, junctions have higher electrical resistance, which leads to higher local heating at these points causing a higher rate of surface diffusion. This is the reason why morphological evolution under electrical voltage appears initially in the junctions of the network. Figure 3-11.a presents an as-deposited junction between two NWs, where there is a lack of an efficient connection (limited contact area between adjacent NWs). Afterwards, increasing applied voltage on the

AgNW network promotes the formation of efficient junctions due to electrical sintering, as shown in Figure 3- 11. b. [16]The next stage, shown in Figure 3- 11.c, corresponds to junction breakage probably occurred first at the hottest spots of the network. Atomic surface diffusion is the main mechanism which makes all of the mentioned morphological modifications possible. However, such atomic diffusion can be hindered by a metal oxide coating layer. This is, in fact, a well-known effect, which is the reason why the sintering of metallic powders is normally operated in an oxygen-free atmosphere [58], [59] otherwise the formation of surface oxide layer would have prevented the successful process of sintering. Another example is the natural thin (of few nanometers) oxide layers over Silicon ( $\text{SiO}_2$ ), which lowers the thermal diffusion rate of metallic boron or arsenic into Silicon. [60], [61]

Figure 3-11.d shows a schematic representation of the coated AgNWs studied in this work (similar to AgNW networks presented in Figure 3-5. b and d). Figure 3-11.e shows an actual example of morphological instability, where a SEM image of an AgNW network subjected to electrical or thermal stress close to the failure limit (before a complete spheroidization occurs) is presented. For bare AgNW networks, surface diffusion affects more drastically low diameter NWs due to their enhanced surface to volume ratio; therefore thin NWs are initially involved in the degradation process.[18] For the coated AgNW networks, ZnO coatings here, surface diffusion process is delayed because silver atoms have the barrier of metal oxide layer ahead of them before the full diffusion and degradation of junctions can occur.

The model to formulate the effect of the ZnO coating on the electrical stability of AgNW networks was mainly developed by Prof. Bellet. One way to evaluate the effect of ZnO coating thickness ( $L_{ZnO}$ ) on the AgNW network electrical stability, as presented in Figure 3-10.b, is to consider the failure time of the network,  $t^{fail}$ . If we keep a constant voltage ramp of  $\dot{V}$ , failure voltage ( $V^{fail}$ ) will be associated with failure time as :  $V^{fail} = \dot{V} \cdot t^{fail}$ .

As we have observed in Figure 3-10.b, ZnO coating thickness has a direct effect on increasing the failure voltage, therefore the dependency of  $t^{fail}$  on ZnO coating thickness ( $L_{ZnO}$ ) can be written as follows:

$$t_{coated\ AgNW}^{fail}(L_{ZnO}) = t_{bare\ AgNW}^{fail} + \Delta t^{fail}(L_{ZnO}) \quad (3-2)$$

where  $t_{bare\ AgNW}^{fail}$  and  $t_{coated\ AgNW}^{fail}$  are the failure time (for which the AgNW network electrical resistance is diverging) for bare AgNW and ZnO coated AgNW networks, respectively.  $\Delta t^{fail}(L_{ZnO})$  is associated with the time delay, due to the presence of a thin oxide layer. This layer delays the diffusion of silver atoms, therefore the

occurrence of morphological instability in the case of metal oxide coated AgNWs. According to the basic diffusion law in a first approximation, the mentioned time delay,  $\Delta t^{fail}(L_{ZnO})$ , is directly correlated to the oxide layer thickness ( $L_{ZnO}$ ) as:

$$L_{ZnO} = \sqrt{2 \cdot D \cdot \Delta t^{fail}(L_{ZnO})} \quad (3-3)$$

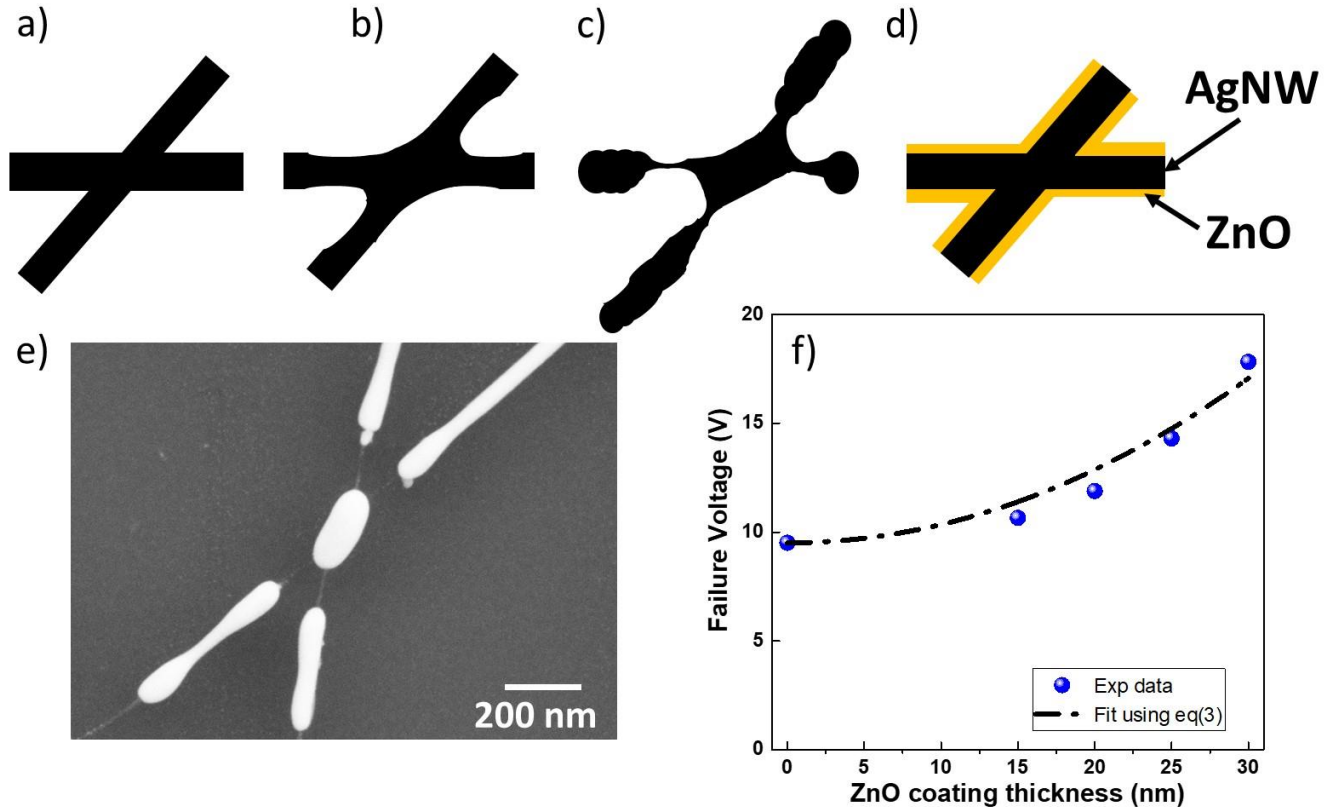


Figure 3-11. Schematic view of two adjacent AgNWs a) as-deposited and b) after the formation of efficient junction due to local sintering. c) Start of the degradation process of a junction. If the thermal or electrical load continues, degraded junctions can appear globally on the network and cause a complete breakdown. d) schematic view of an AgNW junction coated by AP-SALD deposited thin and conformal ZnO coating (of thickness  $L_{ZnO}$ ). e) SEM image of a AgNW junction which has been load by thermal or electrical stress, just before degradation f) the dependency of the experimental values of failure voltage against ZnO coating thickness, measured during a voltage ramp, showing good agreement with the calculated values using Equation (3-4). Images are reproduced from reference[16]

where  $D$  is the diffusion coefficient of Ag atoms through the oxide barrier. Therefore we can rewrite Equation 3-1 to provide a direct dependency between the voltage failure and ZnO coating thickness  $L_{ZnO}$  as:

$$V_{coated\ AgNW}^{fail}(L_{ZnO}) = V_{bare\ AgNW}^{fail} + \frac{\dot{V} \cdot L_{ZnO}^2}{2 \cdot D} \quad (3-4)$$

where  $\dot{V}$  is the voltage rate associated with the voltage ramp (equal to  $0.1 \text{ V min}^{-1}$ ). Experimental data shown in Figure 3-10.b, are presented again in Figure 3-11.f along with fitting form Equation 3-4. Although the model we described here was quite simple, it shows a very good agreement with the experimental data. [16] The diffusion coefficient of silver atoms through ZnO oxide,  $D$ , is the only unknown parameter in Equation 3-4. The fit presented in Figure 3-11.f yields a  $D$  value of  $7.4 \cdot 10^{-16} \text{ cm}^2 \text{ s}^{-1}$ . It is not straightforward to compare this  $D$  value, with already reported ones in the literature due to two main reasons: first, the diffusion coefficient drastically depends on the experimental conditions of oxide growths which affect the structural properties like the presence of defects, grain boundaries or voids. Second, the diffusion coefficient depends on the experiment temperature since diffusion itself is a thermally activated process. The low solubility limit of Ag ion in ZnO at equilibrium leads to very low diffusion coefficient  $D$  values. The reason behind the low solubility is the larger size of Ag ionic radius compared with Zn, as well as different valence states of Ag and Zn.[62] Sakaguchi et al. reported the diffusion coefficient of Ag in polycrystalline ZnO to be around  $7.8 \cdot 10^{-13} \text{ cm}^2 \text{ s}^{-1}$  at  $900 \text{ }^\circ\text{C}$ .[63] McBrayer et al.[64] studied the diffusion coefficient of metals in  $\text{SiO}_2$  oxide layers and reported that Ag diffusion coefficient  $D$  is equal to  $10^{-15} \text{ cm}^2 \text{ s}^{-1}$  at a temperature of  $221 \text{ }^\circ\text{C}$ , which is typically the temperature associated to the AgNW network failure. The order of magnitude of these  $D$  values from literature is thus in agreement with the value obtained from our model (3-4) (see Figure 3-11.f).

#### 3.4.6. Effect of the ZnO coating on the thermal stability of AgNW networks

The stability of AgNW networks against thermal stress is a critical point in the integration of TE based on AgNW networks in different applications, in particular when used as transparent heaters.[16], [54], [65] The degradation of the network due to an elevation of the temperature can cause irreversible changes in the network morphology and lead to an increase in the network resistance as discussed in section 3.2.1. Here we have compared the evolution of the electrical resistance of bare and ZnO coated AgNWs networks during thermal ramps from room temperature to over  $450 \text{ }^\circ\text{C}$  with a ramp of  $2 \text{ }^\circ\text{C min}^{-1}$ . Samples of spray deposited ACS-Ag90 bare, and ZnO coated AgNWs had the initial electrical resistance of  $6.04 \pm 0.8 \ \Omega$  regardless of the ZnO layer thickness. As presented in Figure 3-12.a, an increase of temperature from the room temperature to around  $250 \text{ }^\circ\text{C}$ , implies an increase in the electrical resistance for both bare and coated AgNW networks. The increase in the electrical resistivity due to phonon-electron interaction is discussed in section 3.4.4. After the linear increase of resistance, bare AgNW networks undergo the



well-known Plateau-Rayleigh instability around 280 °C, with the consequent sudden increase in the electrical resistance of the network.[1], [18] Unlike bare networks, ZnO coated AgNW networks stay conductive after a full thermal ramp up to 450 °C in this case. The dependency of thermal stability enhancement on the ZnO coating thickness is similar to electrical stability study, in which we demonstrated that thicker coatings are more efficient than thinner ones. Another approach to evaluate the thermal stability of bare ZnO and coated AgNW networks is to study the evolution of electrical resistance during an isothermal treatment. Here two samples of spray deposited ACS-Ag90 bare, and ZnO coated AgNWs with initial electrical resistance of  $8.5 \pm 0.7 \Omega$  were heated up from room temperature to 320 °C with a ramp of  $30 \text{ }^\circ\text{C min}^{-1}$  and kept at 320 °C for 1 hour. As shown in Figure 3-12.b bare network starts degradation after the initial 10 minutes and reaches Plateau-Rayleigh instability after 25 minutes. While a coating of 30 nm of ZnO protects the network from degradation and resistance stays stable around 10.5  $\Omega$  during 1 hour of the annealing.

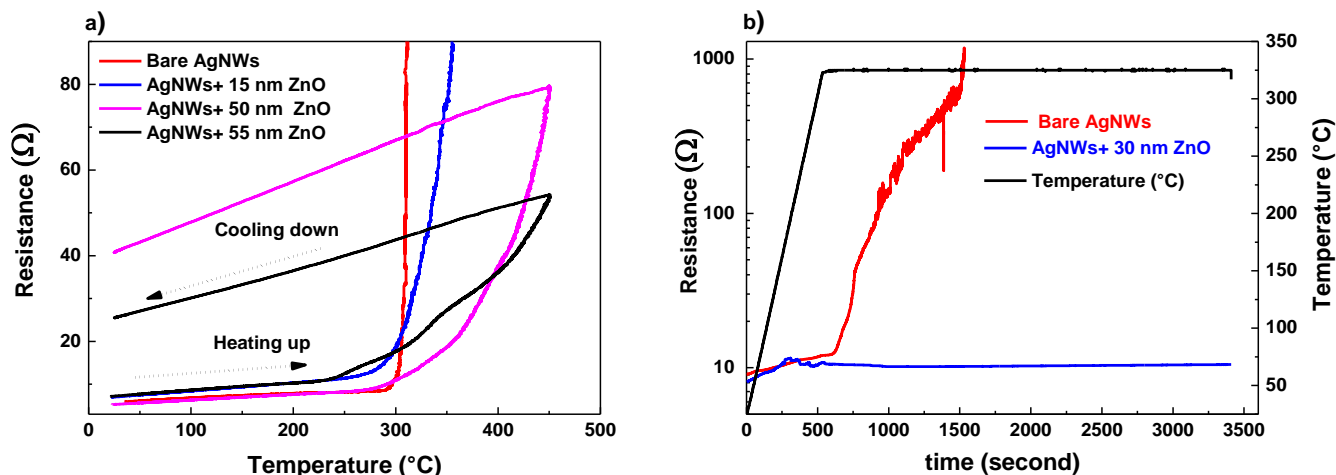


Figure 3- 12. a) In situ measured resistance of bare and ZnO coated ACS-Ag90 NWs from room temperature to 450 °C with a thermal ramp of  $2 \text{ }^\circ\text{C min}^{-1}$  in air, while ZnO thickness plays a crucial role in the stability enhancement. b) Evolution of bare and ZnO coated ACS-Ag90 NWs during an isothermal ramp at 320 °C in air for 1 h. As bare network degrades as soon as the temperature rises to 320 °C, 30 nm coating of AP-SALD deposited ZnO protects the AgNW network from any instability of the electrical resistance.

Figure 3-13 illustrates a diffusion process where an AgNW network coated with 45 nm of ZnO is annealed at 400 °C for 30 minutes. This figure confirms the predicted behaviour of Ag atoms diffusion through the ZnO layer in

section 3.4.5. Bright Field STEM and STEM EDS images, confirm that ZnO coating stays stable (Figure 3-13.c) while Ag diffuses through the ZnO barrier (Figure 3-13.b and d).

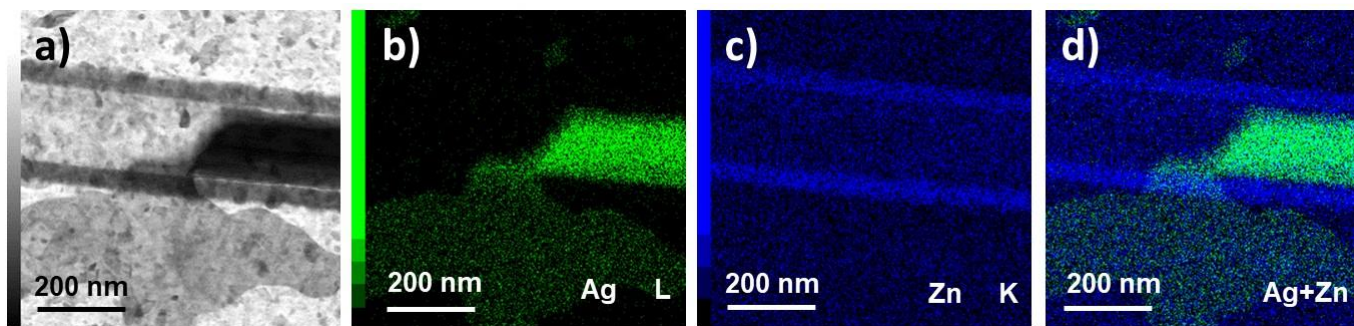


Figure 3- 13.a) Bright field STEM and (b-c-d) STEM EDS images showing the thermal degradation of 45 nm ZnO coated AgNW networks after thermal annealing at 400 °C in air for 30 minutes. Ag atoms (colored in green), diffuse through the ZnO coating (colored in blue) which stays stable at 400 °C.

### 3.5. Al<sub>2</sub>O<sub>3</sub> Coating of the AgNW network with AP-SALD

The next metal oxide coating that was studied in the stability enhancement of AgNW networks is Al<sub>2</sub>O<sub>3</sub>. The reason behind this choice is the wider bandgap of Al<sub>2</sub>O<sub>3</sub> compared to ZnO (8 eV versus 3.3 eV), respectively [15], [66], [67] so Al<sub>2</sub>O<sub>3</sub> coating is supposed to induce smaller optical losses as compared to ZnO coating.

Al<sub>2</sub>O<sub>3</sub> coatings were deposited using the AP-SALD system that was previously discussed. The deposition parameters were optimized to reach the growth condition of conventional ALD, and then Al<sub>2</sub>O<sub>3</sub> growth was carried out at 150 °C. Trimethylaluminum (TMA, Al<sub>2</sub>(CH<sub>3</sub>)<sub>3</sub>) and water vapour were used as precursors for aluminum and oxygen, respectively. The samples were placed at a distance of 200 μm under the injection head oscillating at 10 cm s<sup>-1</sup>. The thickness of coatings is proportional to the number of AP-SALD cycles performed, with a Growth Per Cycle (GPC) rate around 1.5 Å/ALD cycle.

A coated AgNW network with a 50 nm thick Al<sub>2</sub>O<sub>3</sub> coating deposited with AP-SALD is shown in the SEM image in Figure 3-14.a where a homogenous and conformal oxide coating over the AgNW network and glass substrate can be observed. This is so even for very thin coatings, as the 10 nm Al<sub>2</sub>O<sub>3</sub> coating shown in the TEM image in Figure 3-14.b. Such quality of the oxide film is crucial since any crack or uniformity in the coating can be

detrimental to the network stability.[16] Since the deposition of  $\text{Al}_2\text{O}_3$  is performed at  $150\text{ }^\circ\text{C}$ , which is low compared to the crystallisation temperature of  $\text{Al}_2\text{O}_3$  (around  $800\text{ }^\circ\text{C}$ ), we observe amorphous coatings in our study. Hwang et al. observed that ultra-thin (approximately  $5\text{ nm}$ ) amorphous coatings of  $\text{Al}_2\text{O}_3$  can act as a very efficient barrier against diffusion of Ag atoms.[37] Wang et al.[68] have also reported superior thermal stability of AgNW networks coated with  $2\text{ nm}$  of ALD deposited  $\text{Al}_2\text{O}_3$  coatings, compared to bare ones. Similarly, we observed that  $12\text{ nm}$  of  $\text{Al}_2\text{O}_3$  is more efficient against Ag diffusion compared to  $50\text{ nm}$  of ZnO coatings.[17] This is probably due to the absence of any grain boundaries in  $\text{Al}_2\text{O}_3$  coatings which act as a shortcut for Ag atoms diffusion. EDS STEM confirmed the presence of a significant layer of  $\text{Al}_2\text{O}_3$  as expected in the coating area, Figure 3- 14.(e-g), while silver is observed only in the inner interface, Figure 3- 14.(d).

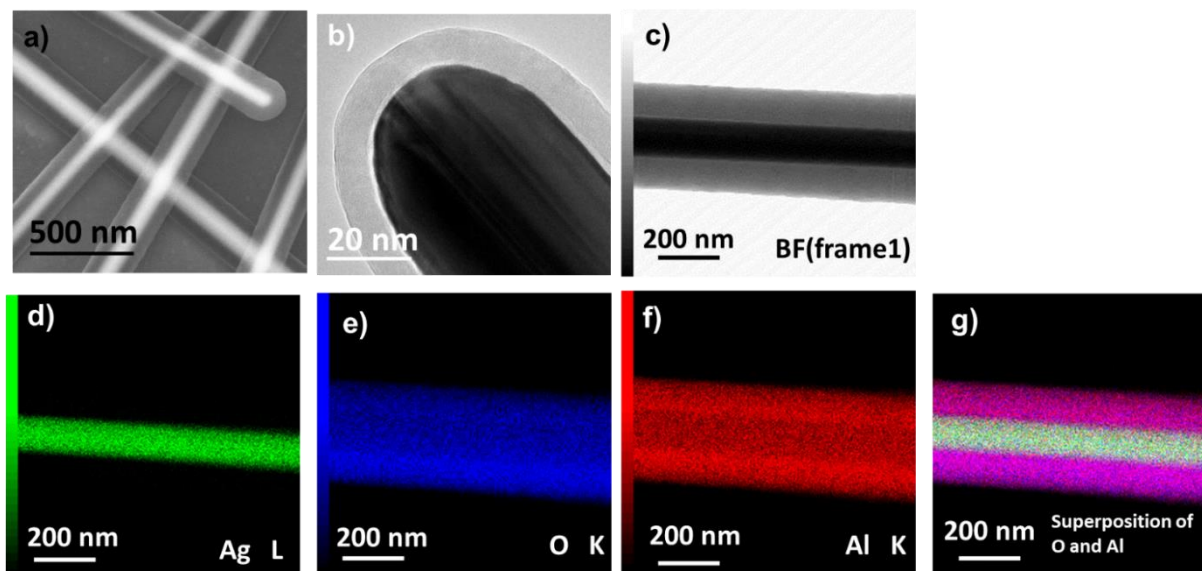


Figure 3-14.a) SEM image of an  $\text{Al}_2\text{O}_3$  coated AgNW with an average coating thickness of around  $50\text{ nm}$ . b) TEM image of an  $\text{Al}_2\text{O}_3$  coated AgNW, showing the amorphous nature of the AP-SALD  $\text{Al}_2\text{O}_3$  coating. c) Bright-field TEM and (d-e-f-g) EDS STEM images showing the Ag atoms (colored in green), covered by the Al coating (colored in red), O (colored in blue), superposition of Al and O (colored in violet).

### 3.5.1. Effect of $\text{Al}_2\text{O}_3$ coating on the optical transmittance of AgNW networks

As for the case of ZnO coatings, the expected improvement in thermal or electrical stability of  $\text{Al}_2\text{O}_3$  coated networks also comes at the expense of the total transmittance. Figure 3-15.a reports the influence of  $\text{Al}_2\text{O}_3$  coating

thickness on the total transmittance (in the wavelength range from 250 to 2500 nm) of coated AgNW networks while the oxide thickness varied from 20 to 90 nm. Although there is a linear decrease in total transmittance versus oxide thickness similar to the case of ZnO coated AgNWs, in the case of  $\text{Al}_2\text{O}_3$  the loss in transparency is less significant than for ZnO coating. This is shown in Figure 3-15.b which represents the total transmittance of ZnO and  $\text{Al}_2\text{O}_3$  coated AgNW networks as a function of oxide thickness. A 50 nm thick ZnO coating reduces the average total transmittance in the visible range (380-700 nm) from 85% for bare AgNWs to 73%, while for the same thickness of  $\text{Al}_2\text{O}_3$  the total transmittance varies from 85% to 80%.

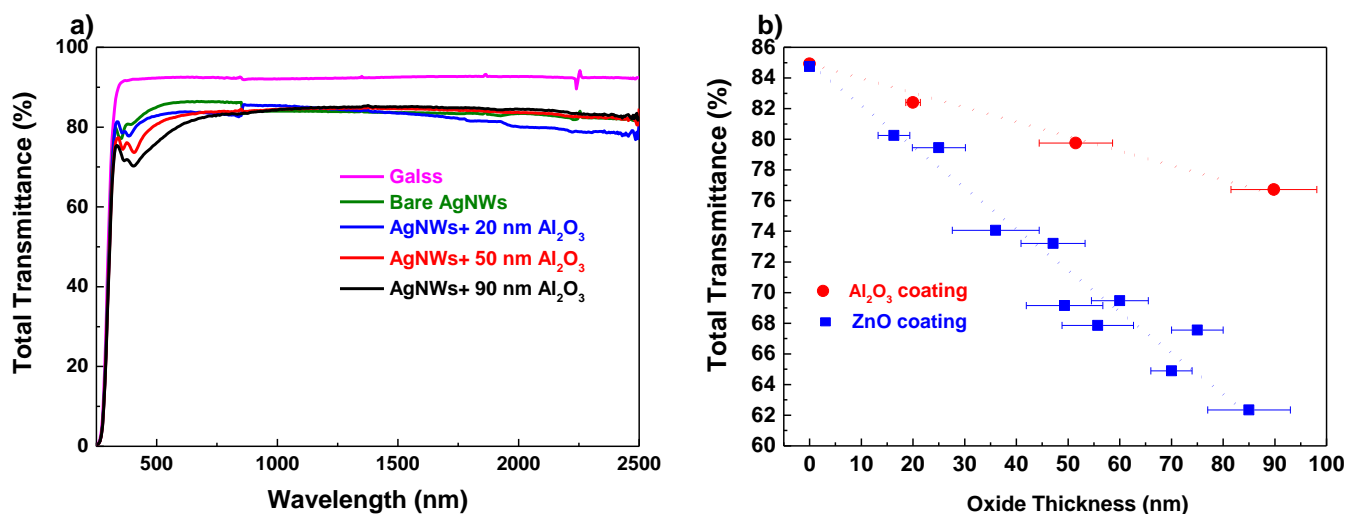


Figure 3- 15. a) Optical total transmittance of a bare substrate of Corning glass, bare AgNW network deposited by spin coating and three AgNW networks coated by increasing thickness of  $\text{Al}_2\text{O}_3$  coating. b) Average total transmittance of ZnO and  $\text{Al}_2\text{O}_3$  coated AgNW networks in the visible wavelength range (380-700 nm) versus oxide thickness, this shows that  $\text{Al}_2\text{O}_3$  coating induces smaller optical losses as compared to ZnO coating. Dashed lines are guide for the eye.

Although the wide bandgap of  $\text{Al}_2\text{O}_3$  has the advantage of lowering optical loss when compared with ZnO, it can be a bit too restrictive for some of the applications where excellent electrical conductivity along the substrate plane is required such as for collection or injection of electrical charges. Such a requirement concerns, for instance, the front electrode of thin film solar cells, where composite electrodes made with ZnO coatings on AgNW networks proved to increase the efficiency of solar-cell, as compared to the bare AgNWs, thanks to an improved charge collection efficiency.[32]

There are several criteria which should be considered while choosing a proper metal oxide coating to cover AgNW networks: first, the loss in the total transmittance after coating AgNW networks with the oxide layer should be as minimised as possible. Secondly, the deposited metal oxide layer should not increase the electrical resistance or decline mechanical flexibility of the AgNW network. Finally, the coating should enhance the thermal (therefore electrical) stability of coated AgNW networks in a reproducible manner. However, it is not feasible to reach all these features at the same time, for example, higher oxide coating thickness leads to higher thermal stability, see section 3.4.5, while at the same time it decreases mechanical flexibility, see section 3.7. Therefore a trade-off between these criteria should be considered, while such a trade-off depends on the targeted application and required electro-optical properties of AgNW networks.

### 3.5.2. Effect of Al<sub>2</sub>O<sub>3</sub> coating on the thermal stability of AgNW networks

The evolution of electrical resistance of bare and Al<sub>2</sub>O<sub>3</sub> coated AgNW networks has been compared and presented in Figure 3-16. ACS-Ag90 silver NWs were spin-coated on Corning glass. There was no post-deposition treatment on bare AgNW networks, therefore the initial electrical resistance of bare network was rather high (around 62 Ω). However, before deposition of Al<sub>2</sub>O<sub>3</sub> coatings, an annealing step at 230 °C in air for 60 minutes was performed on AgNW networks and decreased the average initial electrical resistance down to around 15 Ω. Both bare and Al<sub>2</sub>O<sub>3</sub> coated AgNW networks were exposed to thermal ramps in the air from room temperature to over 380 °C with a rate of 2 °C min<sup>-1</sup> and *in situ* electrical measurements were performed. Unlike bare or ZnO coated AgNWs (see Figure 3-12); there is no irreversible change in the electrical resistance of Al<sub>2</sub>O<sub>3</sub> coated AgNW networks after a similar annealing cycle. This confirms that Al<sub>2</sub>O<sub>3</sub> provides a very efficient barrier against diffusion of Ag atoms at high temperatures, see section 3-5. For the networks coated with 18 nm and 50 nm of Al<sub>2</sub>O<sub>3</sub>, we observe a linear dependency of the electrical resistance with temperature while heating electrodes to 380 °C and cooling down to the room temperature as expected by Equation 3-1. The temperature coefficient of resistivity,  $\beta_R$ , for Al<sub>2</sub>O<sub>3</sub> coated AgNW networks is around  $(2.3 \pm 0.1) \times 10^{-3}$ , which is close to previously reported values of  $\beta_R$  of bare AgNW networks by Lagrange et al. [18]  $((2.4 \pm 0.1) \times 10^{-3})$ .

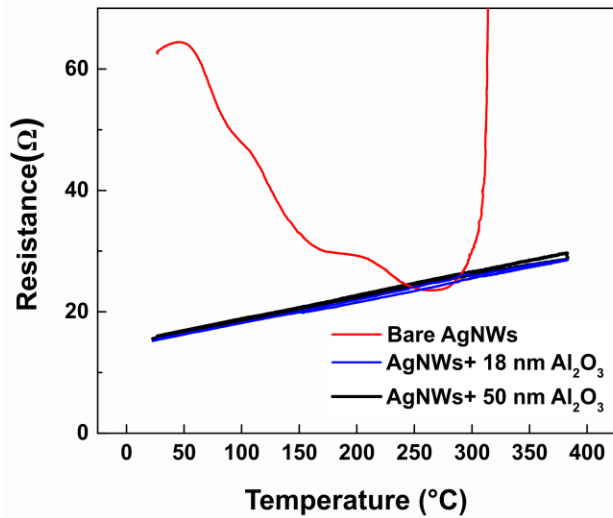


Figure 3- 16. *In situ* measured resistance of AgNW networks during a thermal ramp showing that after 18 nm and 50 nm  $\text{Al}_2\text{O}_3$  layer coating a clear thermal stability enhancement is observed since the network can undergo a thermal ramp of  $2\text{ }^\circ\text{C min}^{-1}$  up to  $315\text{ }^\circ\text{C}$  for bare AgNWs and more than  $380\text{ }^\circ\text{C}$  for coated AgNWs. Temperature coefficient of resistivity,  $\beta_R$ , for  $\text{Al}_2\text{O}_3$  coated AgNW networks is measured to be around  $(2.3 \pm 0.1) \times 10^{-3}$ .

### 3.5.3. Delamination of $\text{Al}_2\text{O}_3$ coated AgNW networks at elevated temperatures

$\text{Al}_2\text{O}_3$  coatings have been proven to have a significant effect on the improvement of the thermal stability of AgNW networks while having a milder impact on the total transmittance values compared to ZnO coatings. However, there are some properties which might limit the successful integration of AgNWs/  $\text{Al}_2\text{O}_3$  nanocomposite layer into functional devices. One issue observed is delamination at elevated temperatures, above  $400\text{ }^\circ\text{C}$ . This is indeed what has been presented in Figure 3-17, where there is breaking and/or delamination of the AgNWs/  $\text{Al}_2\text{O}_3$  nanocomposite layer.

One essential feature which must be considered to explain such an observation is the matching of thermal expansion coefficient of the metal oxide coatings and the substrate below. Such matching is vital to guarantee the performance of composite films at elevated temperature, assuming that AgNW will be able to sustain tensile or compressive stresses due to their superior flexibility. [49] ALD coated ZnO films (with the wurtzite structure), have a thermal expansion coefficient around  $15.7 \times 10^{-6}\text{ K}^{-1}$  [69], this value is higher than reported thermal expansion coefficient for glass substrates,  $9 \times 10^{-6}\text{ K}^{-1}$ . Therefore, ZnO coated AgNW network can easily follow the thermal expansion of the glass substrate. While for  $\text{Al}_2\text{O}_3$  films deposited by ALD, the expansion coefficient is reported to be only around  $4.2 \times 10^{-6}\text{ K}^{-1}$ . [70] Therefore,  $\text{Al}_2\text{O}_3$  coatings might not be as functional as ZnO coatings at following the thermal

expansion of glass at elevated temperatures. As a result, the stress in the interface of  $\text{Al}_2\text{O}_3$  coating and glass can initiate buckling and form microcracks in the  $\text{Al}_2\text{O}_3$  coating. The initial microcracks can elongate through the coating and cause ultimate delamination of the AgNW/  $\text{Al}_2\text{O}_3$  nanocomposite.

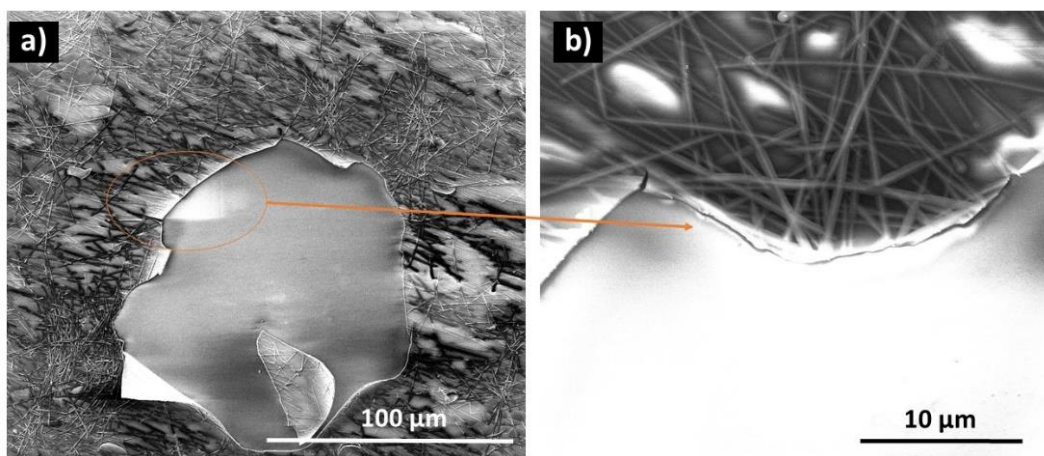


Figure 3- 17. Delamination of an  $\text{Al}_2\text{O}_3$  (80 nm) coated AgNW network deposited on a Corning glass after annealing up to 400 °C with a rate of 2 °Cmin<sup>-1</sup>. Reproduced from reference [17]

### 3.6. Bilayer metal oxide coatings on AgNW networks

#### 3.6.1. Anti-reflective bilayer coatings based on ZnO/ $\text{Al}_2\text{O}_3$ films on AgNW networks

As discussed in Section 3.5.1, ZnO coatings decrease the total transmittance of the composite electrodes with respect to the bare networks. One source of the loss in the ZnO layer is due to the reflection of light which stems from the difference in the refractive index of the medium (ZnO and glass substrate here) where the light propagates. Anti-reflective coatings are one of the basic elements in optical systems and can improve the multi-layers transmittance by reducing the reflection.  $\text{Al}_2\text{O}_3$  layers have been shown to be an efficient anti-reflective coating on ZnO layers in thin film devices.[71]–[73] The optimum thickness to reach a state of anti-reflection in multi-layer thin films can be found using the Fresnel equation which offers the basic mathematical model of reflection and refraction.[74] In this work, we have initialized the study of the anti-reflective effect of  $\text{Al}_2\text{O}_3$  coatings, by using an online simulator presented by PVlighthouse.com [75], OPAL2. This powerful calculator has been designed to calculate the transmission of light through the front surface of solar cells and to enable the optimization of anti-reflective

coatings. Figure 3-18 presents the transmission, absorption, and reflection (%) of incident light for coatings of 70 nm and 85 nm of ZnO on the glass before (a and c), and after (b and d) deposition of 70 nm and 85 nm of Al<sub>2</sub>O<sub>3</sub> coatings, respectively. OPAL2 suggests that, the addition of 70 nm of Al<sub>2</sub>O<sub>3</sub> coating, on 70 nm of ZnO on glass changes transmission and reflection values from 79.2% and 20%, to 94.5% and 5.2%, respectively. Similarly, the addition of 85 nm of Al<sub>2</sub>O<sub>3</sub> coating, on 85 nm of ZnO on glass changes transmission and reflection values from 82.9% and 16.6% to 93.9% and 5.5%, respectively. (Both cases in the visible wavelength range from 380 to 700 nm). The following materials have been chosen from the library of OPAL2 for these calculations: Low-Pressure Chemical Vapor Deposition (LPCVD) deposited ZnO and ALD deposited Al<sub>2</sub>O<sub>3</sub> coatings.

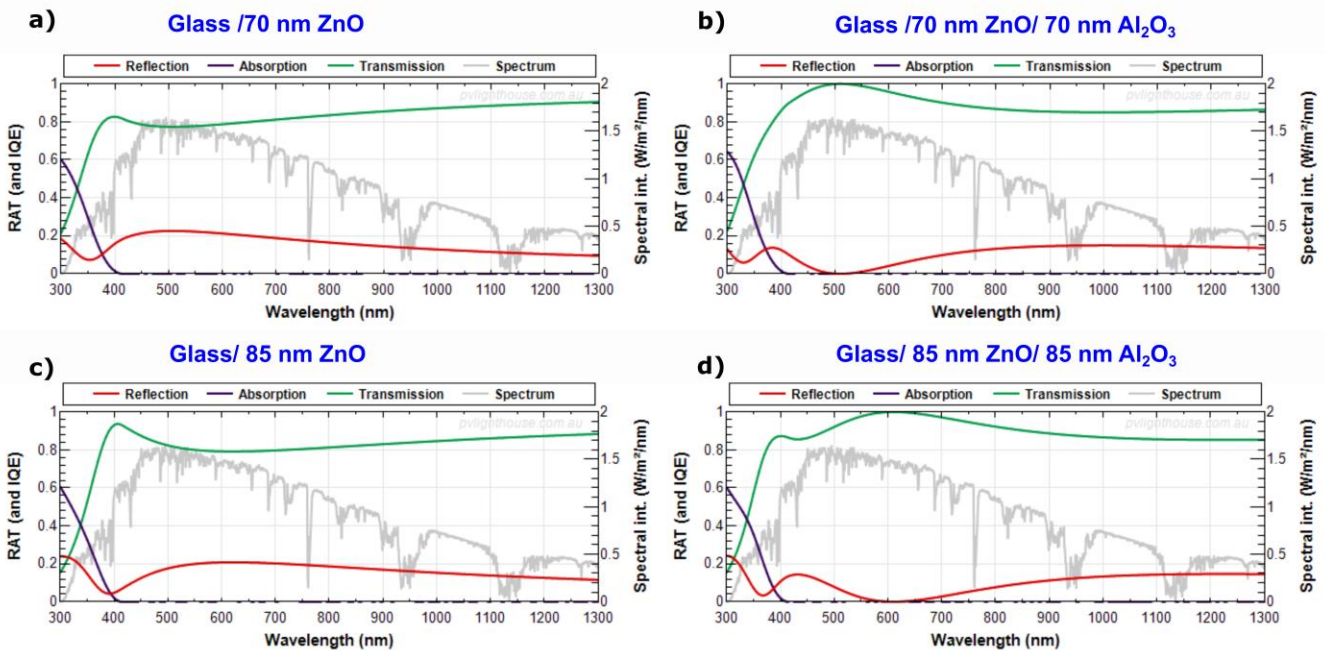


Figure 13-18. a-b) Transmission, absorption and reflection values of 70 nm ZnO coating before (a) and after (b) deposition of 70 nm Al<sub>2</sub>O<sub>3</sub>. c-d) Transmission, absorption and reflection values of 85 nm ZnO coating before (c) and after (d) deposition of 85 nm Al<sub>2</sub>O<sub>3</sub>. Images are reproduced from reference [75] using planar morphology for the glass substrate and LPCVD and ALD for ZnO and Al<sub>2</sub>O<sub>3</sub> coatings respectively.

Since preliminary calculations suggest that there is a considerable anti-reflective effect for the mentioned configurations of ZnO/ Al<sub>2</sub>O<sub>3</sub> on a glass substrate, we have experimentally investigated similar bilayer coatings on AgNWs. Figure 3-19.a and b illustrate TEM and cross-sectional SEM images of coatings of ZnO/ Al<sub>2</sub>O<sub>3</sub> on AgNWs with an estimated thickness of 70 nm for each oxide layer. Details about the preparation of TEM samples are



presented in Chapter 2, 2.3.3. To get high-resolution Cross-section SEM images, a cleanly cut section of the AgNWs/ ZnO/ Al<sub>2</sub>O<sub>3</sub> on Corning glass was prepared using diamond scribe pen. Afterwards, the samples were vertically mounted on the substrate holder. To avoid the problem of charge accumulation in glass, an electrical bridge from the composite to the sample holder stub was made using conductive carbon tape. Following these instructions, clear cross-section images were acquired where AgNWs, polycrystalline ZnO, and amorphous Al<sub>2</sub>O<sub>3</sub> coatings were visible, allowing us to measure the thickness of each coating layer.

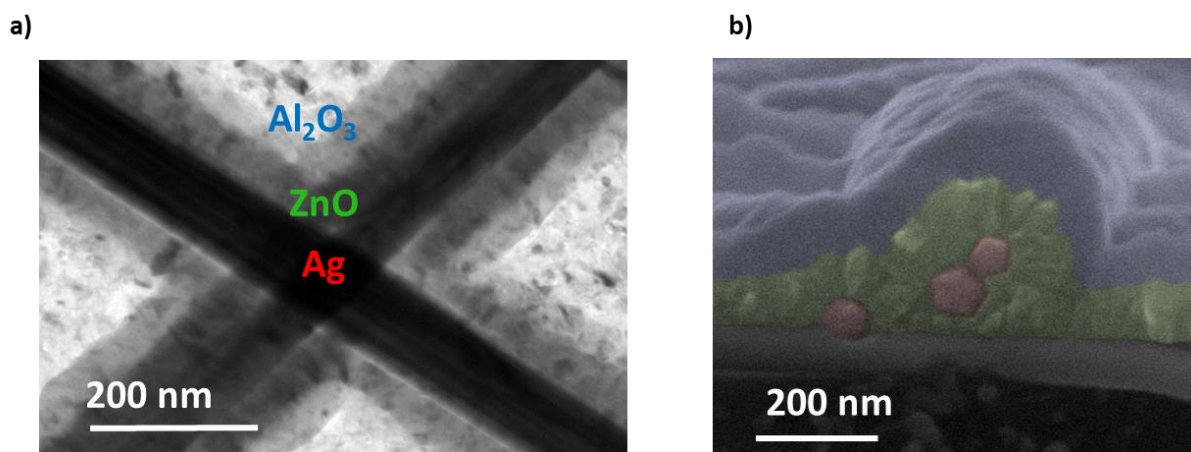


Figure 3-19. a) TEM and b) cross-sectional SEM image of bilayer coatings of 70 nm Al<sub>2</sub>O<sub>3</sub> / 70 nm ZnO on AgNWs. The SEM image has been colored for the sake of clarity. Reproduced from reference[17].

Figure 3-20.a and b represent the total transmittance (in the range 250-2500 nm) for a 70 nm ZnO/ 70 nm Al<sub>2</sub>O<sub>3</sub> bilayer on Corning glass and a AgNW network (previously deposited on Corning glass), respectively. Before depositing the bilayers on AgNW networks, optical measurement tests were made on Corning glass substrates to confirm the occurrence of the anti-reflection effect. In the visible range (380-700 nm), the average value of total transmittance obtained for networks coated with 70 nm of ZnO was 64.9%. Conversely, the total transmittance increased to 73.5% after an additional 70 nm thick layer of Al<sub>2</sub>O<sub>3</sub> was deposited. Similarly, Figure 3-20.c and d represent the total transmittance for a 85 nm ZnO/ 85 nm Al<sub>2</sub>O<sub>3</sub> bilayer on Corning glass and a AgNW network (previously deposited on Corning glass), respectively. The total transmittance value has increased from 62.3% for 85 nm ZnO coated AgNW networks to 69.5% for 85 nm ZnO/ 85 nm Al<sub>2</sub>O<sub>3</sub> bilayer coated AgNWs network.

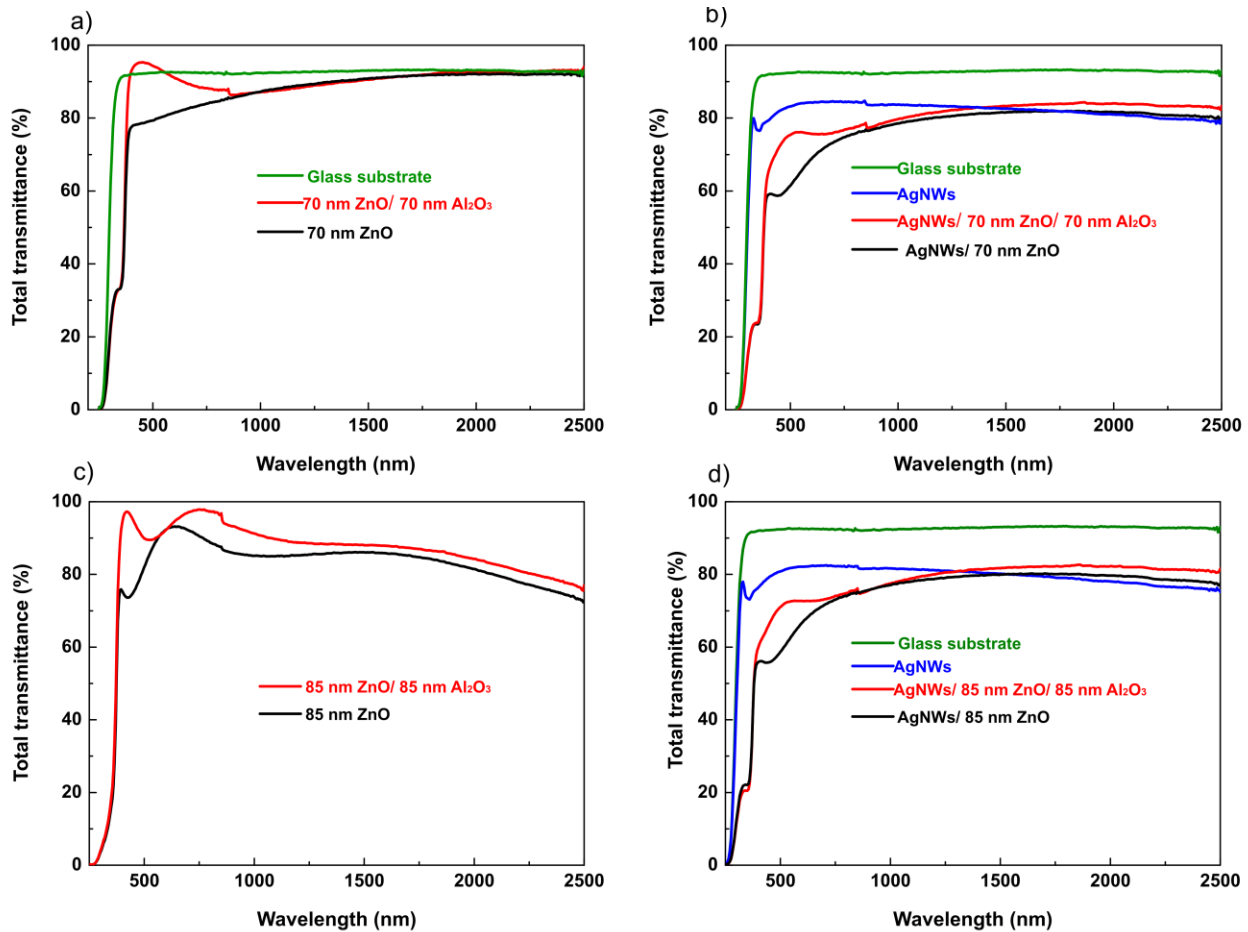


Figure 3-20. a) Total transmittance of the film of 70 nm ZnO deposited on the bare glass before and after deposition of 70 nm anti-reflective layer of Al<sub>2</sub>O<sub>3</sub>. b) Total transmittance of 70 nm ZnO deposited on AgNW network before and after the deposition of a 70 nm anti-reflective layer of Al<sub>2</sub>O<sub>3</sub>. c) Total transmittance of the film of 85 nm ZnO deposited on the bare glass before and after deposition of 85 nm anti-reflective layer of Al<sub>2</sub>O<sub>3</sub>. d) Total transmittance of 85 nm ZnO deposited on AgNW network before and after the deposition of an 85 nm anti-reflective layer of Al<sub>2</sub>O<sub>3</sub>.

The presented computational and experimental examples, confirm the concept of anti-reflection effect for ZnO/ Al<sub>2</sub>O<sub>3</sub> bilayer coatings on AgNW networks. However, there is a lack of a systematic study to find the optimized thickness of each metal oxide layer in order to minimize reflection of light from ZnO coated AgNW networks. Such a systematic study was performed mainly by Viet H. Nguyen and is summarized in the following discussion. [17]

One major assumption which has been made in these calculations is that absorption of light is negligible. [74] The absorption coefficient value of 70 nm ALD coated ZnO film has been reported to be below  $1.5 \times 10^5 \text{ cm}^{-1}$  (in 2.5-

4.5 eV energy range) by Palet al. [76] Similarly, She et al. have reported the absorption coefficient value of 50 nm ALD coated Al<sub>2</sub>O<sub>3</sub> film to be below 0.4×10<sup>5</sup> cm<sup>-1</sup> (in 1.2-12 eV energy range). [77] Therefore, neglecting absorption loss in these layers is an acceptable assumption that can lead to the simplicity of calculations.

A schematic representation of the ZnO/ Al<sub>2</sub>O<sub>3</sub> bilayer coating on a glass substrate is represented in Figure.3-21. The objective of these calculations is to minimize reflection of normal incidence light in the visible wavelength range, 380–700 nm. This is the same wavelength range which has been used to report the experimental total transmittance values for ZnO and Al<sub>2</sub>O<sub>3</sub> coatings, see Figure 3-15.b. The refractive indexes of air, Al<sub>2</sub>O<sub>3</sub>, ZnO and glass substrate are named as n<sub>0</sub>, n<sub>1</sub>, n<sub>2</sub> and n<sub>3</sub> respectively, and the thicknesses of Al<sub>2</sub>O<sub>3</sub> and ZnO layers, are named as t<sub>1</sub> and t<sub>2</sub> respectively. Equations 3-5, 3-6 and 3-7 represent light reflection form air/ Al<sub>2</sub>O<sub>3</sub> (noted as r<sub>1</sub>), Al<sub>2</sub>O<sub>3</sub>/ ZnO (noted as r<sub>2</sub>), and ZnO/ glass interfaces (noted as r<sub>3</sub>) respectively, according to Fresnel equation for thin films.

$$r_1 = \frac{n_0 - n_1}{n_0 + n_1} \quad (3-5)$$

$$r_2 = \frac{n_1 - n_2}{n_1 + n_2} \quad (3-6)$$

$$r_3 = \frac{n_2 - n_3}{n_2 + n_3} \quad (3-7)$$

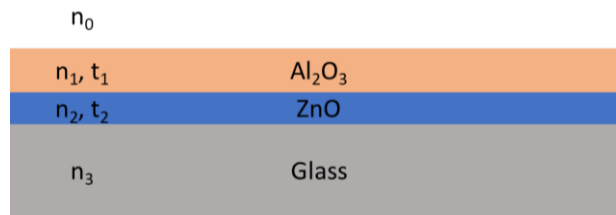


Figure 3-21. Schematic representation of a ZnO/ Al<sub>2</sub>O<sub>3</sub> bilayer coating on glass, refractive indices of air, Al<sub>2</sub>O<sub>3</sub>, ZnO and glass substrate is represented by n<sub>0</sub>, n<sub>1</sub>, n<sub>2</sub> and n<sub>3</sub> respectively. The thickness of Al<sub>2</sub>O<sub>3</sub> and ZnO layers is represented by t<sub>1</sub> and t<sub>2</sub> respectively. The image is reproduced from [17]

The phase change in Al<sub>2</sub>O<sub>3</sub> and ZnO layers can be expressed as:

$$\theta_1 = \frac{2\pi n_1 t_1}{\lambda} \quad (3-8)$$

$$\theta_2 = \frac{2\pi n_2 t_2}{\lambda} \quad (3-9)$$

where  $\lambda$  is the wavelength of incident light. The formula for the reflection of light  $R$ , from a bilayer coating on glass, for normal incidence of light, can be written as follows: [17], [78], [79]

$$R = \frac{R_A}{R_B} \quad (3-10)$$

where,  $R_A = r_1^2 + r_2^2 + r_3^2 + r_1^2 r_2^2 r_3^2 + 2r_1 r_2 (1 + r_3^2) \cos 2\theta_1 + 2r_2 r_3 (1 + r_1^2) \cos 2\theta_2 + 2r_1 r_2^2 r_3 \cos(2\theta_1 - 2\theta_2)$

and  $R_B = 1 + r_1^2 r_3^2 + r_1^2 r_2^2 + r_2^2 r_3^2 + 2r_1 r_2 (1 + r_3^2) \cos 2\theta_1 + 2r_2 r_3 (1 + r_1^2) \cos 2\theta_2 + 2r_1 r_2^2 r_3 \cos(2\theta_1 - 2\theta_2)$ .

In the mentioned equations, refractive indices values for thin film ZnO and Al<sub>2</sub>O<sub>3</sub> coatings are not constant, but dependent on the wavelength. Such dependency has been reported in the literature and in our work, we have used the empirical equations based on the experimental data presented by Kumar et al.[77] for Al<sub>2</sub>O<sub>3</sub> and Bond [80] for ZnO:

$$n_1^2 = 1.3325 + \frac{1.4068 \lambda^2}{\lambda^2 - 0.1199} \quad (3-11)$$

$$n_2^2 = 2.8149 + \frac{0.8797 \lambda^2}{\lambda^2 - 0.3042^2} - 0.0071 \lambda^2 \quad (3-12)$$

Therefore, for any given  $\lambda$  values, the refractive indices (using Equation 3-11 and 3-12), and the reflection values of bilayer coatings for each thickness of Al<sub>2</sub>O<sub>3</sub> and ZnO (using Equation 3-10) can be calculated. The reflection values in the Vis-NIR range of ZnO/ Al<sub>2</sub>O<sub>3</sub> bilayer coating on glass substrate versus wavelength for changing thickness combinations of oxide layers are presented in Figure 3-22.a. Average reflection values in the visible range (380-700 nm) as a function of oxide thickness (using similar thickness for ZnO and Al<sub>2</sub>O<sub>3</sub> coating) is presented in Figure 3-22.b. A minimum of the average reflection values is observed around 70 nm of each oxide thickness.

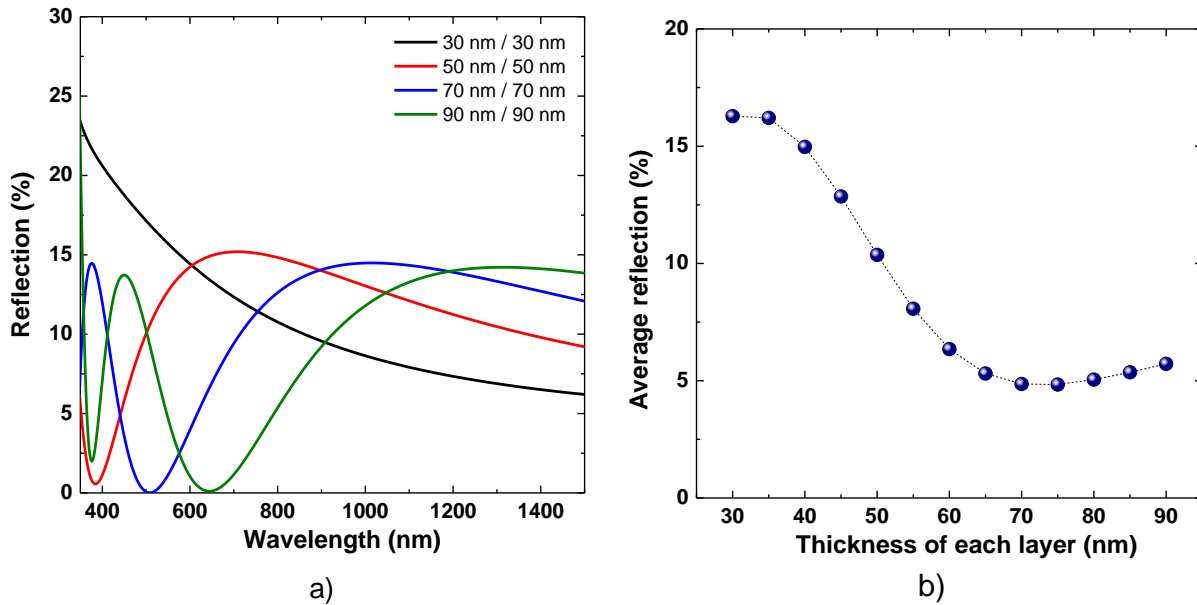


Figure 3-22. a) Optical reflection in the Vis-NIR range of a ZnO/ Al<sub>2</sub>O<sub>3</sub> bilayer coating on glass as a function of wavelength for different combinations of layer thicknesses; b) Average reflection of ZnO/ Al<sub>2</sub>O<sub>3</sub> bilayer coating on glass calculated in the visible range (380- 700 nm) as a function of coating thickness (in this example, both Al<sub>2</sub>O<sub>3</sub> and ZnO layers have a similar thickness). Reproduced from reference [17]

Another way of presenting mentioned calculations is tuning the thickness of Al<sub>2</sub>O<sub>3</sub> layer (from 20 to 95 nm) while the thickness of the first deposited oxide layer is fixed (70 nm and 85 nm of ZnO in this case). The objective is to find the thickness combination which leads to minimum reflection values as presented in Figure 3-23. According to this modelling, the minimum value of the reflection of the bilayer coating is obtained for 70 nm ZnO/ 65 Al<sub>2</sub>O<sub>3</sub> and 85 nm ZnO/ 60 nm Al<sub>2</sub>O<sub>3</sub> bilayer coatings.

In conclusion, the discussed model is very elementary and ignores several factors such as the light absorption in the films, the dependence of the film roughness on their thicknesses,[81] and the presence of the AgNW network between the bilayer coating and the glass substrate. Nevertheless, it provides a rapid estimation of the optimum values for the coating layers. A well-adapted application for optimizing the thickness of ZnO and Al<sub>2</sub>O<sub>3</sub> layers is integration of the nanocomposite as front transparent electrode in solar cells, which requires minimized reflection losses.

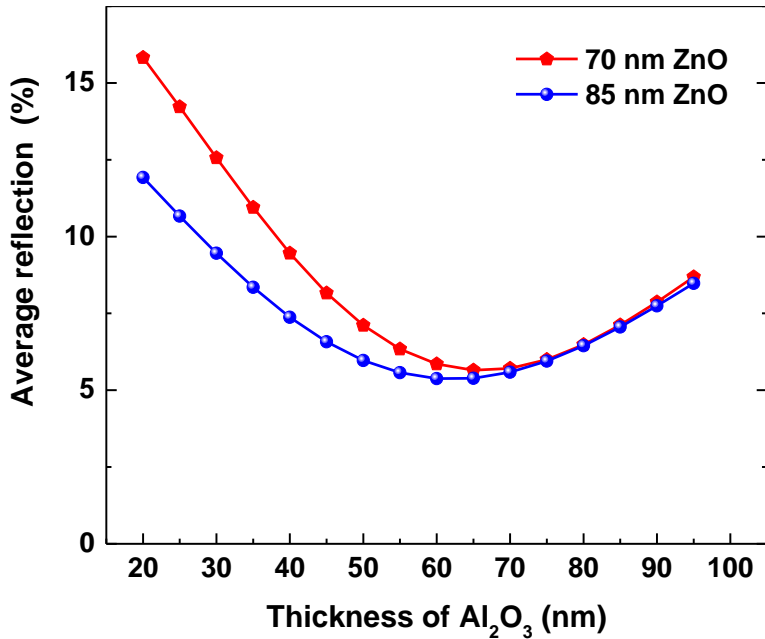


Figure 3-23. Variation of the calculated average reflection (%) in the visible range (380- 700 nm) as a function of Al<sub>2</sub>O<sub>3</sub> thickness when fixing ZnO thickness at 70 nm and 85 nm. For 70 nm of ZnO, a minimum of average reflection is observed for 65 nm of Al<sub>2</sub>O<sub>3</sub>, while for 85 nm of ZnO the minimum average reflection is obtained for 60 nm of Al<sub>2</sub>O<sub>3</sub>.

### 3.6.2. Thermal stability of bilayer metal oxide coated AgNW networks

After confirming the expected improvements in the optical transmittance of composites made with bilayer coatings of ZnO/ Al<sub>2</sub>O<sub>3</sub>, as compared to composites made with ZnO only, we evaluated the thermal stability of the former. Thus, the variation of the electrical resistance of AgNW networks coated with ZnO and ZnO/ Al<sub>2</sub>O<sub>3</sub> was compared when performing thermal annealing up to 450 °C with a ramp of 2 °C min<sup>-1</sup> in air. In both cases, the initial electrical resistance was 30 Ω. Figure 3-24.a shows the change in electrical resistance of ZnO coated AgNWs after three consecutive thermal annealing ramps. During the first thermal annealing ramp, there is a decrease of the electrical resistance around 200 °C as a result of sintering in the junctions between AgNWs. Increasing the temperature above 400 °C results in an irreversible change in the electrical resistance due to the diffusion of Ag atoms through ZnO coating. This causes the resistance to reach 200 Ω after three thermal cycles (up to 450 °C). Figure 3-24.b and c show the change in electrical resistance of ZnO/ Al<sub>2</sub>O<sub>3</sub> coated AgNW networks. As can be observed in Figure 3-24.b, the electrical resistance of the bilayer follows a linear relationship with the temperature, reaching 44.4 Ω at

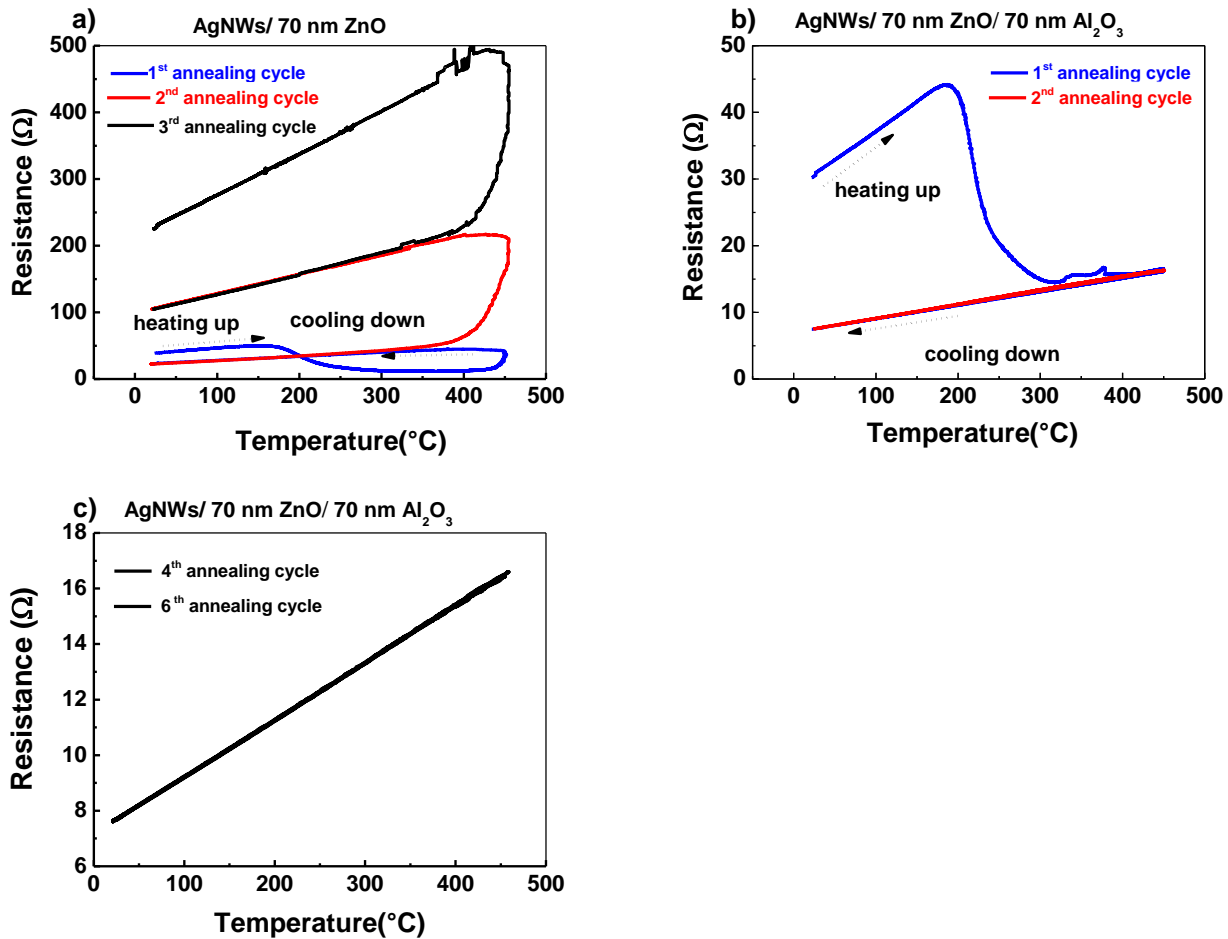


Figure 3-24. a) In situ measured resistance of a AgNW network coated with 70 nm of ZnO, from room temperature to 450 °C with a thermal ramp of 2 °C min<sup>-1</sup>. The first three cycles are shown. b) In situ measured resistance of a AgNW network coated with 70 nm ZnO/ 70 nm Al<sub>2</sub>O<sub>3</sub> bilayer during a thermal ramp up to 450 °C with a heating ramp of 2 °C min<sup>-1</sup>. The first two cycles are shown for the sake of clarity. Reproduced from reference [17] c) The 4<sup>th</sup> and 6<sup>th</sup> cycles are shown.

190 °C. A further increase in temperature drives the optimization of the junctions between AgNWs, which causes a decrease of the electrical resistance to 14.5 Ω at 320 °C. The sintering process seems to stop at this temperature, and a further increase of the temperature again results in a linear increase of the electrical resistance. Upon cooling, a clear linear relationship between electrical resistance and temperature is observed. After this initial cycle, the subsequent heating-cooling cycles, only showed the same linear dependency between resistance and temperature,

with a thermal coefficient of  $2.7 \times 10^{-3} \text{ K}^{-1}$  and no irreversible change in the electrical resistance, in contrast to ZnO coated AgNW networks, after each thermal cycle (Figure 3-24.c).

### 3.7. The flexibility of bare, ZnO and ZnO/ Al<sub>2</sub>O<sub>3</sub> coated AgNW networks

One of the main advantages of AgNW-based TEs, over conventional ITO films, is their superior mechanical stability under bending or stretching tests. This feature makes AgNW networks an outstanding candidate in flexible electronic devices.[49] When external bending stress is applied on the AgNW network, it gets distributed through the entire network. Therefore, there is no significant effect on every single nanowire. As a result, the electrical resistance of an AgNW network can remain stable during mechanical bending experiments.[37], [82], [83] The question that is discussed in this section is whether metal oxide coated AgNW networks preserve their superior mechanical flexibility while compared to conventional ITO films or not? ITO-coated PET films were commercially purchased from Sigma Aldrich. The reported thickness of ITO film was 300 nm and sheet resistance was measured to be around  $60 \text{ } \Omega \text{ sq}^{-1}$ . AgNWs networks and following metal oxide coatings were deposited on flexible Neopulim substrates, to perform *in situ* measurements of mechanical flexibility. Details regarding mechanical bending measurement setup are presented in 2.3.5, Chapter 2. Figure 3-25.a represents the evolution of electrical resistance of bare, ZnO and encapsulated AgNWs networks during 10,000 cycles of mechanical bending (with a bending radius of 5 mm). It can be observed that both bare and coated (ZnO or ) AgNW networks exhibit mechanical stability much better compared to ITO film. (Relative change of electrical resistance for ZnO/ Al<sub>2</sub>O<sub>3</sub> coated AgNWs after 10,000 cycles of bending is 40 times less compared to ITO).

The electrical resistance of bare AgNW networks shows only 11.4% increase after 10,000 cycles of bending. This increase is much lower when compared to the change of electrical resistance for ITO electrode (increase to 2 k $\Omega$  from initial resistance of 130  $\Omega$ , after only 100 cycles of bending). Mechanical flexibility of 40 nm ZnO coated AgNW network was even superior when compared to a bare AgNW network, only 4.7% increase in the relative resistance after 10,000 bending cycles. This improvement can be explained by poor adhesion of AgNWs to the beneath substrate as we discussed in section 3.4.1. The additional ZnO coating, can improve adhesion of AgNWs to the Neopulim substrate and limit the separation of NWs from the substrate during the bending cycles. Similar effect of enhanced adhesion of AgNW networks to the beneath substrate (therefore enhanced mechanical flexibility)



due to the metal oxide coating has been reported by other groups. Wang et al.[68] have observed that while electrical

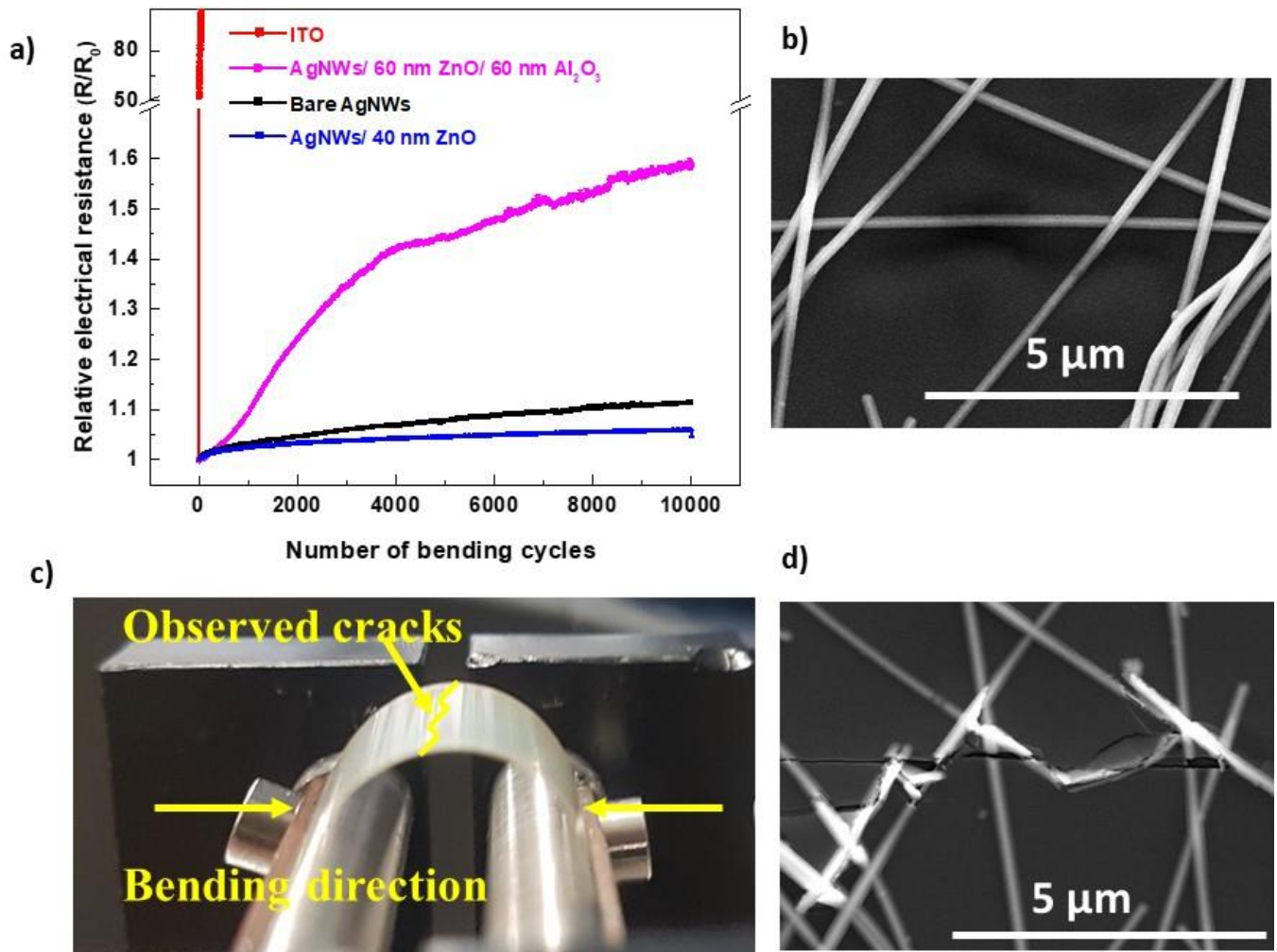


Figure 3-25. a) Relative electrical resistance change of ITO on PEN, and bare, 40 nm ZnO, 60 nm ZnO/ 60 nm  $Al_2O_3$  coated AgNW networks on Neopulim during 10,000 cycles of bending with bending radius of 5 mm. b) SEM observations showing the absence of cracks in the 40 nm ZnO coated AgNW network after 10,000 cycles of bending. A macroscopic illustration of observed cracks (c) and SEM image of cracks observed in a 60 nm ZnO/ 60 nm  $Al_2O_3$  coated AgNW network after 10,000 cycles of bending. Reproduced from reference [17]

resistance of bare AgNW networks on PET substrate increases about 10 times after 1000 cycles of bending, AgNW network coated with only 2 nm of  $Al_2O_3$  showed only a slight increase in the resistance after similar cycles (with a bending radius of 5 mm).

Furthermore, there is no trace of cracks in ZnO coated AgNW nanocomposite after 10,000 cycles of bending as shown in Figure 3-25.b. This is indeed what one might expect considering the studies in the literature which report high flexibility of thin metal oxide films deposited on polymeric substrates. Bending experiments on sputtered Al:ZnO,[84] sputtered ITO[85] or ALD deposited Al<sub>2</sub>O<sub>3</sub> [86] films on polymeric substrates, exhibit rather high critical tensile and compressive strain (strain that a film can endure before the appearance of fractures). They also observed a strong dependence of critical strain on the oxide thickness: the lower the thickness, the higher the critical strain values.

Eventually, 60 nm ZnO/ 60 nm Al<sub>2</sub>O<sub>3</sub> coating on AgNWs showed considerable cracks after 10,000 cycles of bending in the direction perpendicular to the bending, see Figure 3-25.c. Such cracks are visible in the SEM images of ZnO / Al<sub>2</sub>O<sub>3</sub> coated AgNW networks as shown in Figure 3-25.d. As expected, these cracks affect the electrical resistance of ZnO/ Al<sub>2</sub>O<sub>3</sub> coated AgNW networks and induce an increase of 45% in the relative electrical resistance, which is much higher compared to solely ZnO coated AgNW networks. There are several reasons which could explain the observed difference between mechanical flexibility of ZnO and ZnO / Al<sub>2</sub>O<sub>3</sub> coated AgNW networks: first, the overall metal oxide thickness in the ZnO/Al<sub>2</sub>O<sub>3</sub> coating is higher, as mentioned above higher metal oxide film thickness leads to the lower critical strain values. Therefore, similar deformation could induce more significant cracks in ZnO/Al<sub>2</sub>O<sub>3</sub> coating. Second, the critical strain values of ZnO and Al<sub>2</sub>O<sub>3</sub> coatings might not be identical. This is indeed, what Chawla et al. observed while studying the mechanical flexibility of ZnO, Al<sub>2</sub>O<sub>3</sub> and ZnO/ Al<sub>2</sub>O<sub>3</sub> nanolaminates deposited by ALD on PET substrates.[87] They have observed that the failure strain of Al<sub>2</sub>O<sub>3</sub> and bilayer (ZnO/Al<sub>2</sub>O<sub>3</sub>) films are lower when compared to ZnO films.

We have observed so far that there is a strong dependence between the thermal and electrical stability of metal oxide coated AgNWs with metal oxide thickness, higher the thickness, higher the stability. However, gained improvement in the stability comes along with lower optical transmittance and mechanical stability. Depending on the targeted application, a trade-off should be considered between stability in one hand and optical and mechanical performance on the other hand. It is worth reminding here, that adjusting AgNW network density is also a critical parameter which should be optimized for each application.

Although the main focus of this chapter, was on the stability of metal oxide coated AgNW networks, derived conclusions could be applicable on other metallic nanostructures, such as Ag nanoparticle networks. An interesting study in this regard is reported by Joh et al. where multifunctional temperature–strain sensors that are capable of

detecting simultaneously temperature and strain up to a temperature of 400 °C[88]. Such a sensor could have applications in the fields of bioelectronics and robotics.

Although Figure 3-25.a confirms relatively high stability in the electrical resistance of ZnO coated AgNW networks after 10,000 cycles of bending, the efficiency of this coating (after bending) against diffusion of Ag atoms at high temperature is still a place of question. Thermal annealing of bare and ZnO-coated AgNW network after bending cycles has been performed and the evolution of their electrical resistance is reported in figure 3-26. While the resistance of bare AgNW network increased from 18 Ω to 21 Ω, after annealing up to 285 °C and cooling back to room temperature, ZnO-coated AgNW network shows no change in electrical resistance (17.4 Ω before and after annealing). Superior thermal stability of ZnO-coated AgNW network is another proof that thin ZnO coating remains an efficient coating even after 10,000 cycles of bending with a bending radius of 5 mm.

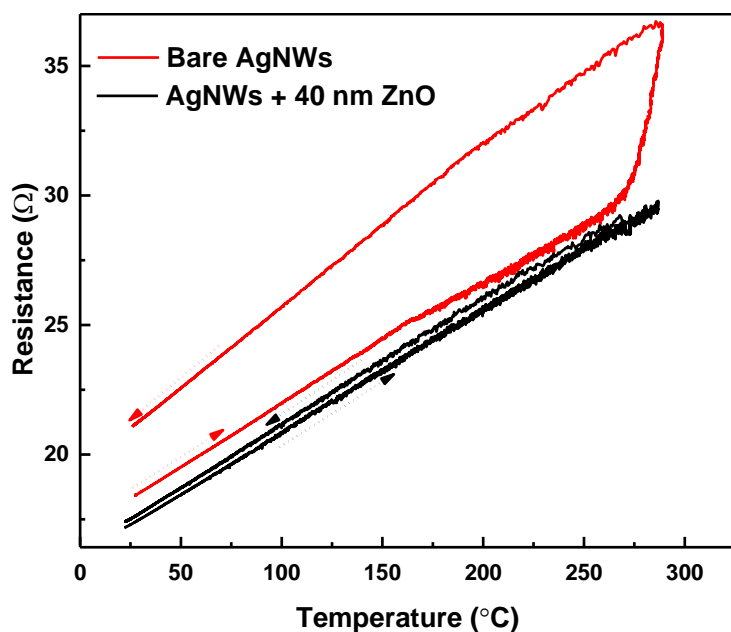


Figure 3- 26. Assessment of thermal behaviour of ZnO coated AgNW networks after mechanical bending, in situ measured resistance up to 285 °C with a thermal ramp of 2 °C min<sup>-1</sup> of bare AgNW network and 40 nm ZnO coated AgNW network; these thermal ramps were both performed after 10,000 cycles of bending (with a radius of curvature of 5 mm). The direction of the arrows show the heating up (from left to right) and cooling down (from right to left) cycles. Reproduced from reference [17]

### 3.8. Summary and Conclusions

The effects of thin ZnO, Al<sub>2</sub>O<sub>3</sub> coatings and ZnO/Al<sub>2</sub>O<sub>3</sub> bilayer coatings on the optical and electrical properties as well as thermal stability of TEs based on AgNW networks were thoroughly studied. A direct dependency between the oxide coating thickness and the improvement in the thermal stability of the composite electrodes were observed. In the case of ZnO coatings, the optical transmittance decreases as the ZnO thickness is increased, thus limiting the applicability of such composite electrodes. Al<sub>2</sub>O<sub>3</sub> coatings have a milder effect on the transmittance of composite electrodes, due to the wider bandgap of Al<sub>2</sub>O<sub>3</sub> with respect to ZnO (8 eV versus 3.3 eV, respectively).[15], [66], [67] However, due to thermal expansion coefficient mismatch between Al<sub>2</sub>O<sub>3</sub> coating and the glass substrate, delamination issues were observed for this composite.

A bilayer coating of ZnO/Al<sub>2</sub>O<sub>3</sub> over AgNWs has been thus proposed and tested. The extra Al<sub>2</sub>O<sub>3</sub> coating on top of the initial ZnO layer acts as an efficient anti-reflective coating: while AgNWs/ 70 nm ZnO composites show an average transmittance in the visible range (380-700 nm) of 64.9%, bilayer coatings of AgNWs/ 70 nm ZnO/ 70 nm Al<sub>2</sub>O<sub>3</sub> show an average transmittance of 73.5%. This improvement in the total transmittance is also associated with the superior thermal stability of bilayer coatings compared to ZnO single-layer coating. Mechanical bending test showed that composite electrodes of ZnO, Al<sub>2</sub>O<sub>3</sub> and AgNWs are all far more stable during bending tests when compared to ITO based electrodes. The best results were obtained for AgNWs/ZnO composite electrodes while the brittleness of Al<sub>2</sub>O<sub>3</sub> coatings somehow limits the bending stability of bilayer composites; therefore a compromise in terms of Al<sub>2</sub>O<sub>3</sub> thickness between enhanced stability and flexibility, which depends upon the application, has to be considered. The results presented in this work indicate a path to low-cost, highly stable and transparent composite electrodes based on AgNWs and oxide coatings. Depending on the specific applications, a trade-off can be searched for, and the present chapter can help in determining an optimal design for efficient integration into industrial devices.

## References

- [1] D. P. Langley *et al.*, “Metallic nanowire networks: effects of thermal annealing on electrical resistance,” *Nanoscale*, vol. 6, pp. 13535–13543, Sep. 2014, doi: 10.1039/C4NR04151H.
- [2] H. H. Khaligh and I. A. Goldthorpe, “Failure of silver nanowire transparent electrodes under current flow,” *Nanoscale Res. Lett.*, vol. 8, no. 1, p. 235, May 2013, doi: 10.1186/1556-276X-8-235.
- [3] I. K. Moon, J. I. Kim, H. Lee, K. Hur, W. C. Kim, and H. Lee, “2D Graphene Oxide Nanosheets as an Adhesive Over-Coating Layer for Flexible Transparent Conductive Electrodes,” *Sci. Rep.*, vol. 3, pp. 1–7, Jan. 2013, doi: 10.1038/srep01112.
- [4] C. Mayousse, C. Celle, A. Fraczkiewicz, and J. Simonato, “Stability of silver nanowire based electrodes under environmental and electrical stresses,” *Nanoscale*, pp. 2107–2115, 2015, doi: 10.1039/c4nr06783e.
- [5] Y. C. G. Kwan, Q. L. Le, and C. H. A. Huan, “Time to failure modeling of silver nanowire transparent conducting electrodes and effects of a reduced graphene oxide over layer,” *Sol. Energy Mater. Sol. Cells*, vol. 144, pp. 102–108, Jan. 2016, doi: 10.1016/j.solmat.2015.08.005.
- [6] S. R. Das *et al.*, “Single-Layer Graphene as a Barrier Layer for Intense UV Laser-Induced Damages for Silver Nanowire Network,” *ACS Nano*, vol. 9, no. 11, pp. 11121–11133, Nov. 2015, doi: 10.1021/acsnano.5b04628.
- [7] H.-J. Seok, J.-K. Kim, and H.-K. Kim, “Effective passivation of Ag nanowire network by transparent tetrahedral amorphous carbon film for flexible and transparent thin film heaters,” *Sci. Rep.*, vol. 8, no. 1, pp. 1–12, Sep. 2018, doi: 10.1038/s41598-018-31927-z.
- [8] A. Madeira, M. Plissonneau, L. Servant, I. A. Goldthorpe, and M. Tréguer-Delapierre, “Increasing Silver Nanowire Network Stability through Small Molecule Passivation,” *Nanomater. Basel Switz.*, vol. 9, no. 6, p. 899, Jun. 2019, doi: 10.3390/nano9060899.
- [9] Z. Yang *et al.*, “Wearable electronics for heating and sensing based on a multifunctional PET/silver nanowire/PDMS yarn,” *Nanoscale*, vol. 12, no. 31, pp. 16562–16569, Aug. 2020, doi: 10.1039/D0NR04023A.
- [10] J. Mock *et al.*, “Aqueous Synthesis, Degradation, and Encapsulation of Copper Nanowires for Transparent Electrodes,” *Nanomaterials*, vol. 8, no. 10, p. 767, Sep. 2018, doi: 10.3390/nano8100767.
- [11] H. Yu *et al.*, “Use of solution-processed zinc oxide to prevent the breakdown in silver nanowire networks,” *Nanotechnology*, vol. 31, no. 18, p. 18LT01, Feb. 2020, doi: 10.1088/1361-6528/ab6fe4.
- [12] Y. Huang *et al.*, “TiO<sub>2</sub> Coated Core–Shell Ag Nanowire Networks for Robust and Washable Flexible Transparent Electrodes,” *ACS Appl. Nano Mater.*, vol. 2, no. 4, pp. 2456–2466, Apr. 2019, doi: 10.1021/acsanm.9b00337.

- [13] V. H. Nguyen *et al.*, “Low-cost fabrication of flexible transparent electrodes based on Al doped ZnO and silver nanowire nanocomposites: impact of the network density,” *Nanoscale*, vol. 11, no. 25, pp. 12097–12107, Jun. 2019, doi: 10.1039/C9NR02664A.
- [14] M. Lagrange, “Physical analysis of percolating silver nanowire networks used as transparent electrodes for flexible applications,” PhD thesis, University of Grenoble Alpes (France), 2015.
- [15] D. Muñoz-Rojas, V. H. Nguyen, C. Masse de la Huerta, S. Aghazadehchors, C. Jiménez, and D. Bellet, “Spatial Atomic Layer Deposition (SALD), an emerging tool for energy materials. Application to new-generation photovoltaic devices and transparent conductive materials,” *Comptes Rendus Phys.*, vol. 18, no. 7, pp. 391–400, Sep. 2017, doi: 10.1016/j.crhy.2017.09.004.
- [16] A. Khan *et al.*, “Stability Enhancement of Silver Nanowire Networks with Conformal ZnO Coatings Deposited by Atmospheric Pressure Spatial Atomic Layer Deposition,” *ACS Appl. Mater. Interfaces*, vol. 10, no. 22, pp. 19208–19217, Jun. 2018, doi: 10.1021/acsami.8b03079.
- [17] S. Aghazadehchors *et al.*, “Versatility of bilayer metal oxide coatings on silver nanowire networks for enhanced stability with minimal transparency loss,” *Nanoscale*, vol. 11, no. 42, pp. 19969–19979, Nov. 2019, doi: 10.1039/C9NR05658K.
- [18] M. Lagrange, D. P. Langley, G. Giusti, C. Jiménez, Y. Bréchet, and D. Bellet, “Optimization of silver nanowire-based transparent electrodes: effects of density, size and thermal annealing,” *Nanoscale*, vol. 7, no. 41, pp. 17410–23, Oct. 2015, doi: 10.1039/c5nr04084a.
- [19] T. Tokuno *et al.*, “Fabrication of silver nanowire transparent electrodes at room temperature,” *Nano Res.*, vol. 4, no. 12, pp. 1215–1222, Oct. 2011, doi: 10.1007/s12274-011-0172-3.
- [20] D. Kumar, V. Stoichkov, E. Brousseau, G. C. Smith, and J. Kettle, “High performing AgNW transparent conducting electrodes with a sheet resistance of  $2.5 \Omega \text{ Sq}^{-1}$  based upon a roll-to-roll compatible post-processing technique,” *Nanoscale*, vol. 11, no. 12, pp. 5760–5769, Mar. 2019, doi: 10.1039/C8NR07974A.
- [21] M.-S. Lee *et al.*, “High-Performance, Transparent, and Stretchable Electrodes Using Graphene–Metal Nanowire Hybrid Structures,” *Nano Lett.*, vol. 13, no. 6, pp. 2814–2821, 2013, doi: 10.1021/nl401070p.
- [22] J. A. Spechler, K. A. Nagamatsu, J. C. Sturm, and C. B. Arnold, “Improved Efficiency of Hybrid Organic Photovoltaics by Pulsed Laser Sintering of Silver Nanowire Network Transparent Electrode,” *ACS Appl. Mater. Interfaces*, vol. 7, no. 19, pp. 10556–10562, May 2015, doi: 10.1021/acsami.5b02203.
- [23] T. Sannicolo *et al.*, “Direct Imaging of the Onset of Electrical Conduction in Silver Nanowire Networks by Infrared Thermography: Evidence of Geometrical Quantized Percolation,” *Nano Lett.*, vol. 16, no. 11, pp. 7046–7053, Nov. 2016, doi: 10.1021/acs.nanolett.6b03270.
- [24] S. Karim *et al.*, “Morphological evolution of Au nanowires controlled by Rayleigh instability,” *Nanotechnology*, vol. 17, no. 24, pp. 5954–5959, Dec. 2006, doi: 10.1088/0957-4484/17/24/009.
- [25] T.-B. Song *et al.*, “Nanoscale Joule Heating and Electromigration Enhanced Ripening of Silver Nanowire Contacts,” *ACS Nano*, vol. 8, no. 3, pp. 2804–2811, Mar. 2014, doi: 10.1021/nm4065567.

- [26] A. T. Bellew, H. G. Manning, C. Gomes da Rocha, M. S. Ferreira, and J. J. Boland, "Resistance of Single Ag Nanowire Junctions and Their Role in the Conductivity of Nanowire Networks," *ACS Nano*, vol. 9, no. 11, pp. 11422–11429, Nov. 2015, doi: 10.1021/acsnano.5b05469.
- [27] F. N. Kholid, H. Huang, Y. Zhang, and H. J. Fan, "Multiple electrical breakdowns and electrical annealing using high current approximating breakdown current of silver nanowire network," *Nanotechnology*, vol. 27, no. 2, p. 025703, 2016, doi: 10.1088/0957-4484/27/2/025703.
- [28] P. S. Ho and T. Kwok, "Electromigration in metals," *Rep. Prog. Phys.*, vol. 52, no. 3, p. 301, Mar. 1989, doi: 10.1088/0034-4885/52/3/002.
- [29] T. Sannicolo *et al.*, "Electrical Mapping of Silver Nanowire Networks: A Versatile Tool for Imaging Network Homogeneity and Degradation Dynamics during Failure," *ACS Nano*, vol. 12, no. 5, pp. 4648–4659, May 2018, doi: 10.1021/acsnano.8b01242.
- [30] D. W. Rice, P. Peterson, E. B. Rigby, P. B. P. Phipps, R. J. Cappell, and R. Tremoureux, "atmospheric corrosion of copper and silver," *Electrochem. Soc.*, vol. 128, no. 2, 1981, doi: 10.1002/chin.198124032.
- [31] T. E. Graedel, "Corrosion Mechanisms for Silver Exposed to the Atmosphere," *J. Electrochem. Soc.*, vol. 139, no. 7, pp. 1963–1970, Jul. 1992, doi: 10.1149/1.2221162.
- [32] A. Kim, Y. Won, K. Woo, C.-H. Kim, and J. Moon, "Highly Transparent Low Resistance ZnO/Ag Nanowire/ZnO Composite Electrode for Thin Film Solar Cells," *ACS Nano*, vol. 7, no. 2, pp. 1081–1091, Feb. 2013, doi: 10.1021/nn305491x.
- [33] A.-T. Pham, X.-Q. Nguyen, D.-H. Tran, V. Ngoc Phan, T.-T. Duong, and D.-C. Nguyen, "Enhancement of the electrical properties of silver nanowire transparent conductive electrodes by atomic layer deposition coating with zinc oxide," *Nanotechnology*, vol. 27, no. 33, p. 335202, Aug. 2016, doi: 10.1088/0957-4484/27/33/335202.
- [34] X. Yan, J. Ma, H. Xu, C. Wang, and Y. Liu, "Fabrication of silver nanowires and metal oxide composite transparent electrodes and their application in UV light-emitting diodes," *J. Phys. Appl. Phys.*, vol. 49, no. 32, p. 325103, Aug. 2016, doi: 10.1088/0022-3727/49/32/325103.
- [35] Q. Huang *et al.*, "Highly Thermostable, Flexible, Transparent, and Conductive Films on Polyimide Substrate with an AZO/AgNW/AZO Structure," *ACS Appl. Mater. Interfaces*, vol. 7, no. 7, pp. 4299–4305, Feb. 2015, doi: 10.1021/am508704u.
- [36] T.-B. Song *et al.*, "Highly Robust Silver Nanowire Network for Transparent Electrode," *ACS Appl. Mater. Interfaces*, vol. 7, no. 44, pp. 24601–24607, Nov. 2015, doi: 10.1021/acсами.5b06540.
- [37] B. Hwang *et al.*, "Highly Flexible and Transparent Ag Nanowire Electrode Encapsulated with Ultra-Thin Al<sub>2</sub>O<sub>3</sub>: Thermal, Ambient, and Mechanical Stabilities," *Sci. Rep.*, vol. 7, no. 1, p. 41336, Jan. 2017, doi: 10.1038/srep41336.
- [38] W. Shin, W. Cho, and S. J. Baik, "Silver nanowires network encapsulated by low temperature sol–gel ZnO for transparent flexible electrodes with ambient stability," *Mater. Res. Express*, vol. 5, no. 1, p. 015050, Jan. 2018, doi: 10.1088/2053-1591/aaa67a.

- [39] R. Liu *et al.*, “Solution-processed composite electrodes composed of silver nanowires and aluminum-doped zinc oxide nanoparticles for thin-film solar cells applications,” *Sol. Energy Mater. Sol. Cells*, vol. 174, pp. 584–592, Jan. 2018, doi: 10.1016/j.solmat.2017.09.042.
- [40] W. Lan *et al.*, “Novel transparent high-performance AgNWs/ZnO electrodes prepared on unconventional substrates with 3D structured surfaces,” *Appl. Surf. Sci.*, vol. 433, pp. 821–828, Mar. 2018, doi: 10.1016/j.apsusc.2017.10.054.
- [41] M. Göbelt *et al.*, “Encapsulation of silver nanowire networks by atomic layer deposition for indium-free transparent electrodes,” *Nano Energy*, vol. 16, pp. 196–206, Sep. 2015, doi: 10.1016/j.nanoen.2015.06.027.
- [42] D. Muñoz-Rojas and J. MacManus-Driscoll, “Spatial atmospheric atomic layer deposition: a new laboratory and industrial tool for low-cost photovoltaics,” *Mater. Horiz.*, vol. 1, no. 3, pp. 314–320, Apr. 2014, doi: 10.1039/C3MH00136A.
- [43] D. Muñoz-Rojas, T. Maindron, A. Esteve, F. Pierrat, J. C. S. Kools, and J.-M. Decams, “Speeding up the unique assets of atomic layer deposition,” *Mater. Today Chem.*, vol. 12, pp. 96–120, Jun. 2019, doi: 10.1016/j.mtchem.2018.11.013.
- [44] D. Muñoz-Rojas, V. Huong Nguyen, C. Masse de la Huerta, C. Jiménez, and D. Bellet, “Spatial Atomic Layer Deposition,” in *Chemical Vapor Deposition for Nanotechnology*, P. Mandracci, Ed. IntechOpen, 2019.
- [45] A. Illiberi, F. Roozeboom, and P. Poodt, “Spatial atomic layer deposition of zinc oxide thin films,” *ACS Appl. Mater. Interfaces*, vol. 4, no. 1, pp. 268–72, Jan. 2012, doi: 10.1021/am2013097.
- [46] P. Poodt *et al.*, “Spatial atomic layer deposition: A route towards further industrialization of atomic layer deposition,” *J. Vac. Sci. Technol. Vac. Surf. Films*, vol. 30, no. 1, p. 010802, 2012, doi: 10.1116/1.3670745.
- [47] D. Muñoz-Rojas *et al.*, “High-speed atmospheric atomic layer deposition of ultra thin amorphous TiO<sub>2</sub> blocking layers at 100 °C for inverted bulk heterojunction solar cells: AALD for inverted bulk heterojunction solar cells,” *Prog. Photovolt. Res. Appl.*, vol. 21, pp. 393–400, 2013, doi: 10.1002/pip.2380.
- [48] V. H. Nguyen *et al.*, “Deposition of ZnO based thin films by atmospheric pressure spatial atomic layer deposition for application in solar cells,” *J. Renew. Sustain. Energy*, vol. 9, no. 2, p. 021203, Mar. 2017, doi: 10.1063/1.4979822.
- [49] T. Sannicolo, M. Lagrange, A. Cabos, C. Celle, J.-P. Simonato, and D. Bellet, “Metallic Nanowire-Based Transparent Electrodes for Next Generation Flexible Devices: a Review,” *Small*, vol. 12, no. 44, pp. 6052–6075, Nov. 2016, doi: 10.1002/sml.201602581.
- [50] T. Dhakal *et al.*, “Transmittance from visible to mid infra-red in AZO films grown by atomic layer deposition system,” *Sol. Energy*, vol. 86, no. 5, pp. 1306–1312, May 2012, doi: 10.1016/j.solener.2012.01.022.
- [51] É. P. da Silva, M. Chaves, S. F. Durrant, P. N. Lisboa-Filho, and J. R. R. Bortoleto, “Morphological and electrical evolution of ZnO: Al thin films deposited by RF magnetron sputtering onto glass substrates,” *Mater. Res.*, vol. 17, no. 6, pp. 1384–1390, Dec. 2014, doi: 10.1590/1516-1439.281214.



- [52] K. Ellmer, “Past achievements and future challenges in the development of optically transparent electrodes,” *Nat. Photonics*, vol. 6, no. 12, pp. 809–817, 2012, doi: 10.1038/nphoton.2012.282.
- [53] S. M. Lee, J. H. Lee, S. Bak, K. Lee, Y. Li, and H. Lee, “Hybrid windshield-glass heater for commercial vehicles fabricated via enhanced electrostatic interactions among a substrate, silver nanowires, and an over-coating layer,” *Nano Res.*, vol. 8, no. 6, pp. 1882–1892, Mar. 2015, doi: 10.1007/s12274-014-0696-4.
- [54] M. Lagrange *et al.*, “Understanding the mechanisms leading to failure in metallic nanowire-based transparent heaters, and solution for stability enhancement,” *Nanotechnology*, vol. 28, no. 5, p. 055709, 2017, doi: 10.1088/1361-6528/28/5/055709.
- [55] V. H. Nguyen, U. Gottlieb, A. Valla, D. Muñoz, D. Bellet, and D. Muñoz-Rojas, “Electron tunneling through grain boundaries in transparent conductive oxides and implications for electrical conductivity: the case of ZnO:Al thin films,” *Mater. Horiz.*, vol. 5, no. 4, pp. 715–726, 2018, doi: 10.1039/C8MH00402A.
- [56] A. Bid, A. Bora, and A. K. Raychaudhuri, “Temperature dependence of the resistance of metallic nanowires of diameter  $\geq 15$  nm: Applicability of Bloch-Grüneisen theorem,” *Phys. Rev. B*, vol. 74, no. 3, Jul. 2006, doi: 10.1103/PhysRevB.74.035426.
- [57] D.R. Lide, *CRC Handbook of chemistry and physics 2004-2005: A ready-reference book of chemical and physical data*. CRC press, 2004.
- [58] A. Vagnon *et al.*, “3D statistical analysis of a copper powder sintering observed in situ by synchrotron microtomography,” *Acta Mater.*, vol. 56, no. 5, pp. 1084–1093, Mar. 2008, doi: 10.1016/j.actamat.2007.11.008.
- [59] A. Vagnon, O. Lame, D. Bouvard, M. D. Michiel, D. Bellet, and G. Kapelski, “Deformation of steel powder compacts during sintering: Correlation between macroscopic measurement and in situ microtomography analysis,” *Acta Mater.*, vol. 54, no. 2, pp. 513–522, Jan. 2006, doi: 10.1016/j.actamat.2005.09.030.
- [60] N. D. Nguyen *et al.*, “Use of p- and n-type vapor phase doping and sub-melt laser anneal for extension junctions in sub-32 nm CMOS technology,” *Thin Solid Films*, vol. 518, pp. S48–S52, Jan. 2010, doi: 10.1016/j.tsf.2009.10.053.
- [61] S. Takeuchi *et al.*, “Vapor Phase Doping with N-type Dopant into Silicon by Atmospheric Pressure Chemical Vapor Deposition,” *ECS Trans.*, vol. 16, no. 10, pp. 495–502, Oct. 2008, doi: 10.1149/1.2986806.
- [62] S.-T. Kuo, W.-H. Tuan, J. Shieh, and S.-F. Wang, “Effect of Ag on the microstructure and electrical properties of ZnO,” *J. Eur. Ceram. Soc.*, vol. 27, no. 16, pp. 4521–4527, Jan. 2007, doi: 10.1016/j.jeurceramsoc.2007.02.215.
- [63] I. Sakaguchi *et al.*, “Ion implantation and diffusion behavior of silver in zinc oxide,” *J. Ceram. Soc. Jpn.*, vol. 118, no. 1375, pp. 217–219, 2010, doi: 10.2109/jcersj2.118.217.
- [64] J. D. McBrayer, R. M. Swanson, and T. W. Sigmon, “Diffusion of Metals in Silicon Dioxide,” *J. Electrochem. Soc.*, vol. 133, no. 6, pp. 1242–1246, Jun. 1986, doi: 10.1149/1.2108827.

- [65] D. T. Papanastasiou *et al.*, “Transparent Heaters: A Review,” *Adv. Funct. Mater.*, vol. 30, no. 21, p. 1910225, 2020, doi: 10.1002/adfm.201910225.
- [66] N. V. Nguyen *et al.*, “Band offsets of atomic-layer-deposited Al<sub>2</sub>O<sub>3</sub> on GaAs and the effects of surface treatment,” *Appl. Phys. Lett.*, vol. 93, no. 8, p. 082105, Aug. 2008, doi: 10.1063/1.2976676.
- [67] E. O. Filatova and A. S. Konashuk, “Interpretation of the Changing the Band Gap of Al<sub>2</sub>O<sub>3</sub> Depending on Its Crystalline Form: Connection with Different Local Symmetries,” *J. Phys. Chem. C*, vol. 119, no. 35, pp. 20755–20761, Sep. 2015, doi: 10.1021/acs.jpcc.5b06843.
- [68] S. Wang *et al.*, “Mechanically and thermally stable, transparent electrodes with silver nanowires encapsulated by atomic layer deposited aluminium oxide for organic optoelectronic devices,” *Org. Electron.*, vol. 78, p. 105593, Mar. 2020, doi: 10.1016/j.orgel.2019.105593.
- [69] M. Singh and M. Singh, “Thermal Expansion in Zinc Oxide Nanomaterials,” *Nanosci. Nanotechnol. Res.*, vol. 1, no. 2, pp. 27–29, Jan. 2013, doi: 10.12691/nnr-1-2-4.
- [70] D. C. Miller *et al.*, “Thermo-mechanical properties of alumina films created using the atomic layer deposition technique,” *Sens. Actuators Phys.*, vol. 164, no. 1–2, pp. 58–67, Nov. 2010, doi: 10.1016/j.sna.2010.09.018.
- [71] K. Marszałek, P. Winkowski, and M. Marszałek, “Antireflective bilayer coatings based on Al<sub>2</sub>O<sub>3</sub> film for UV region,” *Mater. Sci.-Pol.*, vol. 33, no. 1, pp. 6–10, Mar. 2015, doi: 10.1515/msp-2015-0011.
- [72] W.-C. Wang *et al.*, “Efficiency Enhancement and Anti-Corrosion Protection on Silicon Solar Cells by Atomic-Layer-Deposited Al<sub>2</sub>O<sub>3</sub> Conformal Shell Layer on Antireflective ZnO Nanorod Array,” *ECS J. Solid State Sci. Technol.*, vol. 3, no. 11, pp. Q221–Q226, Jan. 2014, doi: 10.1149/2.0101411jss.
- [73] K. Pfeiffer, U. Schulz, A. Tünnermann, and A. Szeghalmi, “Ta<sub>2</sub>O<sub>5</sub>/Al<sub>2</sub>O<sub>3</sub>/SiO<sub>2</sub> - antireflective coating for non-planar optical surfaces by atomic layer deposition,” San Francisco, California, United States, Feb. 2017, p. 1011513, doi: 10.1117/12.2250272.
- [74] H. K. Raut, V. A. Ganesh, A. S. Nair, and S. Ramakrishna, “Anti-reflective coatings: A critical, in-depth review,” *Energy Environ. Sci.*, vol. 4, no. 10, pp. 3779–3804, Sep. 2011, doi: 10.1039/C1EE01297E.
- [75] “<https://www2.pvlighthouse.com.au/calculators/opal%20/opa%20.aspx>” .
- [76] D. Pal *et al.*, “Tunable optical properties in atomic layer deposition grown ZnO thin films,” *J. Vac. Sci. Technol. A*, vol. 35, no. 1, p. 01B108, Nov. 2016, doi: 10.1116/1.4967296.
- [77] S. Shi, S. Qian, X. Hou, J. Mu, J. He, and X. Chou, “Structural and Optical Properties of Amorphous Al<sub>2</sub>O<sub>3</sub> Thin Film Deposited by Atomic Layer Deposition,” *Adv. Condens. Matter Phys.*, vol. 2018, pp. 1–10, 2018, doi: 10.1155/2018/7598978.
- [78] A. Vašiček, “The Reflection of Light from Glass with Double and Multiple Films,” *J. Opt. Soc. Am.*, vol. 37, no. 8, p. 623, Aug. 1947, doi: 10.1364/JOSA.37.000623.
- [79] “<https://www.pveducation.org/pvcdrom/design-of-silicon-cells/double-layer-anti-reflection-coatings>.”

- [80] W. L. Bond, "Measurement of the Refractive Indices of Several Crystals," *J. Appl. Phys.*, vol. 36, no. 5, pp. 1674–1677, May 1965, doi: 10.1063/1.1703106.
- [81] V. H. Nguyen, "Development of transparent electrodes by vacuum-free and low cost deposition methods for photovoltaic applications," PhD thesis, University of Grenoble Alpes (France), 2018.
- [82] P. Lee *et al.*, "Highly Stretchable and Highly Conductive Metal Electrode by Very Long Metal Nanowire Percolation Network," *Adv. Mater.*, vol. 24, no. 25, pp. 3326–3332, 2012, doi: 10.1002/adma.201200359.
- [83] M. S. Miller, J. C. O’Kane, A. Niec, R. S. Carmichael, and T. B. Carmichael, "Silver nanowire/optical adhesive coatings as transparent electrodes for flexible electronics," *ACS Appl. Mater. Interfaces*, vol. 5, no. 20, pp. 10165–10172, Oct. 2013, doi: 10.1021/am402847y.
- [84] B. C. Mohanty, H. R. Choi, Y. M. Choi, and Y. S. Cho, "Thickness-dependent fracture behaviour of flexible ZnO : Al thin films," *J. Phys. Appl. Phys.*, vol. 44, no. 2, p. 025401, Jan. 2011, doi: 10.1088/0022-3727/44/2/025401.
- [85] Y. Leterrier *et al.*, "Mechanical integrity of transparent conductive oxide films for flexible polymer-based displays," *Thin Solid Films*, vol. 460, no. 1–2, pp. 156–166, Jul. 2004, doi: 10.1016/j.tsf.2004.01.052.
- [86] A. Bulusu *et al.*, "29.3: Invited Paper : The Mechanical Reliability of Flexible ALD Barrier Films," *SID Symp. Dig. Tech. Pap.*, vol. 44, no. 1, pp. 361–364, Jun. 2013, doi: 10.1002/j.2168-0159.2013.tb06221.x.
- [87] V. Chawla *et al.*, "Fracture Mechanics and Oxygen Gas Barrier Properties of Al<sub>2</sub>O<sub>3</sub>/ZnO Nanolaminates on PET Deposited by Atomic Layer Deposition," *Nanomaterials*, vol. 9, no. 1, p. 88, Jan. 2019, doi: 10.3390/nano9010088.
- [88] H. Joh *et al.*, "Surface Design of Nanocrystals for High-Performance Multifunctional Sensors in Wearable and Attachable Electronics," *Chem. Mater.*, vol. 31, no. 2, pp. 436–444, Jan. 2019, doi: 10.1021/acs.chemmater.8b03914.



## Chapter 4

**Monte Carlo simulations to find critical network density ( $n_c$ ) and its effect on the properties of the networks**



So far the methods for the synthesis of AgNWs, the ways to deposit them on various substrates, and the techniques to optimize and prolong the lifetime of TEs based on AgNWs have been discussed. A critical condition for the functionality of these electrodes in any application is the occurrence of percolation in the nanowire network. The percolation threshold is the required density of AgNWs to obtain electrical conductivity through the network from one side to the other one. Therefore, major studies have been performed on the percolation behavior of MNW networks using either semi-analytical methods or computer-assisted statistical studies like Monte Carlo simulations. For instance, Daniel Langley (a previous Ph.D. student at the AgNWs group of LMGP, and SPIN at University of Liège) reported a comprehensive study on the percolation behavior of random sticks (with zero width) to model AgNW network percolation and the effect of percolation parameters on the physical properties of the resulting TEs. [1], [2]

Here we have extended such studies by introducing the possibility of using different nano-objects, in addition to nanowires, to form percolating networks, and we have compared their percolation threshold to NW-based networks. The aim was the search for the elemental morphology which could exhibit a lower percolation threshold than when using nanowires. Both symmetric m-fold periodic stick arrangements and regular polygons of m-edges have been evaluated. Our search for new nano-objects with different shapes has shown that shapes other than nanowires can lower the critical amount of material to reach network percolation by 50%. The lower percolation threshold leads to less material consumption and therefore to higher optical transparency. [3]

The second part of the numerical work is linked with the potential integration of AgNW based electrodes in solar cell devices. AgNW networks are an interesting candidate as TE for solar cells due to high optical transparency in the solar spectrum, which enables maximum absorption of solar energy, and low electrical resistance. However, the wide openings between adjacent NWs might restrict the efficient collection of photo-generated charge carriers. Here, this potential issue has been investigated and the probability maps of collecting charge carriers have been obtained. Our results showed that the average collection probability depends on the network density, length of NWs and the average lifetime of charge carriers in the active layer of each solar cell. This enables to perform a considerate choice of the appropriate length of NWs and the network density in each solar cell device, to obtain the best performance of these electrodes.

#### **4.1. Determination of the critical density $n_c$ by Monte Carlo simulations and study of its effect on the properties of networks**

Percolation theory, in general, and continuum percolation of 1D or 2D nano-objects, in particular, have been a very widely studied physical problems in the last few decades. The definition of percolation and related terms which are essential to understand this chapter can be easily found in the literature.[4]–[6] However, we will have a brief review of these terms to make a notion for the reader to follow our discussion. In a general definition, percolation refers to the formation of connecting clusters and creating pathways in a random graph. An example of percolation in physics is the process of formation of pathways for the transport of fluids through porous materials. [2] If there is a pathway from one side of the system to the other side, the system is considered percolating. The cluster, intersecting groups of nano-objects, which forms such a pathway is called the spanning cluster. The formation of a spanning cluster and the occurrence of percolation in a system leads to a phase transition in one (or more) properties of a system. The main purpose of percolation theory is to calculate the density of pathways, which leads to phase transition.

In general, there are two main types of model for the formation of paths in a percolating system: lattice (regular) and continuum (irregular) percolation. Lattice percolation models a system where paths are constrained to follow a fixed order of sets. All element of a given sets are identical in form. Lattice percolation is classified as site or bond percolation. Site percolation refers to systems where paths are formed of connected sites. Two sites are considered connected if they share a common side. Bond percolation refers to a slightly different definition which considers only the edges of sites. Closed bonds between the neighbour edges form percolating paths. Although these regular models are extensively studied in mathematics and statistical physics, they are not suitable to model random natural systems. For natural systems, continuum percolation is more widely used. It refers to systems where sites are not limited to the lattice arrangement and can be randomly positioned in a continuous system. Two adjacent sites are considered connected if there is contact or overlap between them. In this work, we have used continuum percolation theory since it provides a more realistic basis to study percolation behavior of TEs based on random nano-objects. The studied random nano-objects can be of any shape and are not restricted to any lattice arrangement. A more detailed discussion of these terms along with graphical illustrations are presented by Langley. [2]

Metallic or semiconductor nanowires,[7]–[10] metallic platelets,[11] single-walled/ double-walled carbon nanotubes (CNTs)[12]–[15] or graphene[16] are examples of conductive particles which can form transparent electrodes. Such planar electrodes have a wide range of applications in the fields of



optoelectronics, display technologies, thin-film solar cells, biological or physical sensors and transparent heaters.

In all of the above-mentioned applications, the associated critical network density ( $n_c$ ) plays a pivotal role. Areal density  $n$  is defined as the number of objects per unit area while  $n_c$  is the density for which there is a 50% probability for reaching percolation in the system. This means that if one generates numerous random networks (typically above  $10^3$  [17], [18]) with the network density of  $n_c$ , approximately 50% of formed networks will be percolating. Searching for a low  $n_c$  value is of prime interest since the functional devices are designed with a network density ( $n$ ) several times larger than  $n_c$ . Therefore lowering  $n_c$  leads to reliable devices with lower density, allowing to use less amount of material and thus decreasing for instance cost and optical transmittance losses due to the shadowing effects. [3], [19]

Monte Carlo simulations have been often used as a powerful tool to study the percolation behavior of random conductive nano-objects. The effects of parameters like nano-object size,[8], [20] density,[21] topology (curliness[22] or deformation of nano-objects), angular orientation distribution[23], [24] or electrical resistance of junctions between nano-objects have been studied on the electrical properties of random networks.[8] Bauhofer et al. reported a very comprehensive survey on the electrical conductivity of carbon nanotube-polymer composites.[25] They reported that for a given CNT concentration, lowering critical network density results in increasing the maximum reachable conductivity of random networks. They showed a good agreement between experimental data and theoretical prediction for the dependency of network conductivity versus network density  $n$ . For randomly-deposited networks, the conductivity follows the percolation scaling law as:

$$\sigma \propto (n - n_c)^v \quad (4-1)$$

where  $v$  is  $\frac{4}{3}$  for 2D random networks. [25] Coleman et al. have shown that for rather sparse networks of silver nanowires, CNTs, graphene or silver platelets having optical transmittance above 90%, the conductivity falls in the percolation regime and can be modelled with Equation 4-1 as well.[11], [26]

## 4.2. Nano-objects beyond sticks, experimental examples

So far Monte Carlo studies in continuum percolation have been mainly focused on sticks, which model high aspect ratio nano-objects such as nanowires or CNTs. However, thanks to the recent advances in material chemistry, new varieties of elemental nanoparticles such as gold nano-stars, Figure 4-1.a, nano-cubes/rods,[27], [28] silver nano-stars, Figure 4-1.b, [29], [30] or silver dendrites, Figure 4-1.c,[31] can now be synthesised. Branched AgNWs using microwave-assisted PVP process, have been reported by Madeira.[32] and Seshadri et al.[33] as presented in Figure 4-1.e-f and 4-1.g, respectively. These nano-objects cannot be treated as 1D sticks. The goal of the study is a systematic comparison between networks composed of nano-objects of different shape or symmetry. A search is performed to find the nano-object shape that can minimize either  $n_c$  or the total length of material at the percolation threshold. The studied nano-objects can be either m-fold periodic stick arrangement or 2D regular polygons. Circles are also studied as an ultimate polygon with an infinite number of edges. While the present contribution focuses on the study of the physical properties, it reciprocally aims as well at giving hints to chemists for the design and synthesis of novel nano-objects.

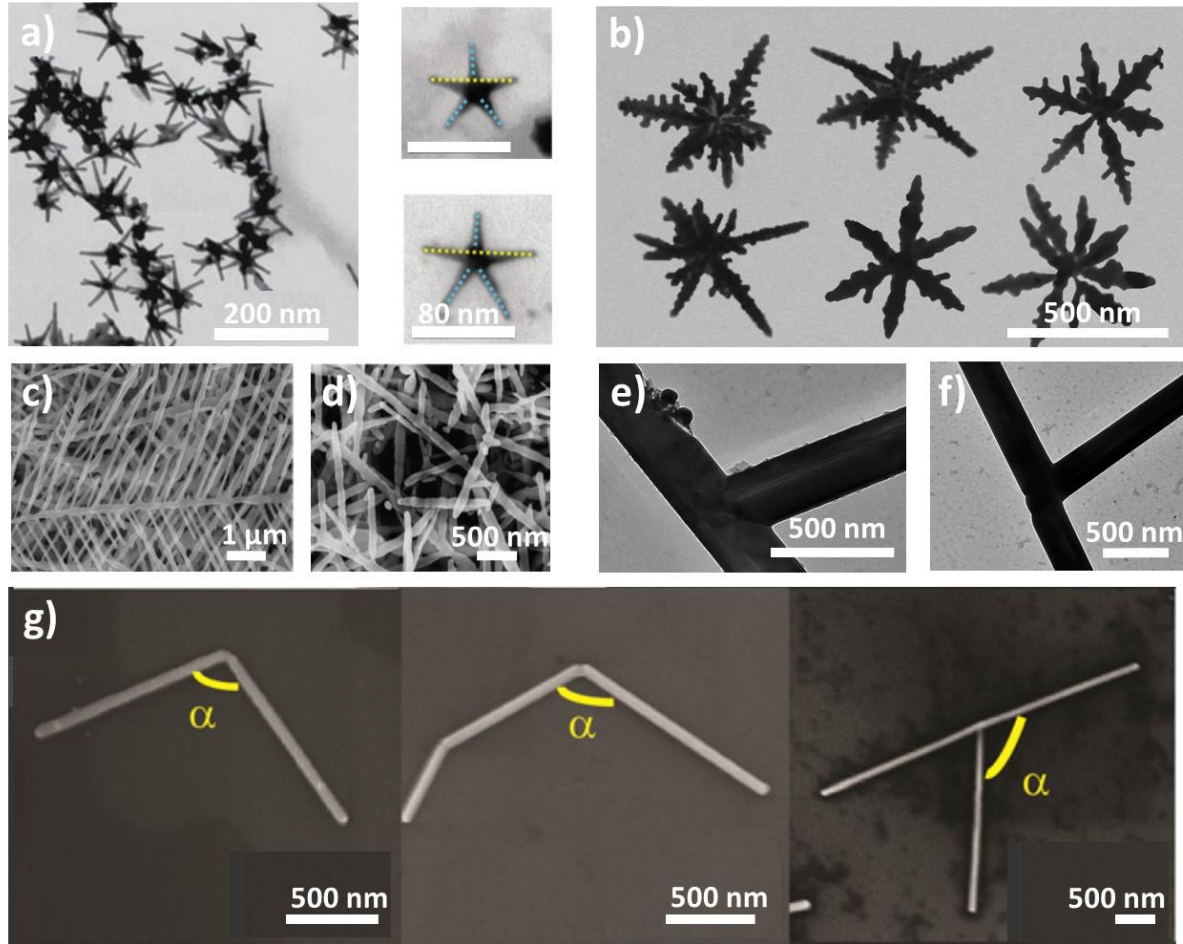


Figure 4-1 a) TEM images of five branch gold nano-stars obtained from seed-growth synthesis. Nano-stars generated from  $\text{AuCl}_4^-$  and Triton X-100. Reproduced from reference [34] b) TEM images of silver nano-stars grown by a two-step reduction of  $\text{Ag}^+$ . Reproduced from reference [29] c-d) Ag nano dendrites via an electrochemical Ostwald ripening (OR) driven branch fragmentation mechanism. Reproduced from reference [31] e-f) TEM images of microwave-assisted branched AgNWs. Reproduced from reference [32] g) SEM micrographs of branched nanowires showing various examples of branches at nanowire tips with  $110^\circ < \alpha < 160^\circ$ . Reproduced from reference [33]

### 4.3. Tree-based algorithm to find the percolation threshold

The site/bond percolation problem has been discussed widely using two general techniques, namely, the series expansion of the mean cluster size[35] and Monte Carlo analysis[17], [18] assisted by high performance computing. The latter approach is required to perform a high number of simulations in the range of  $10^4$  up to  $10^8$ , depending on the required accuracy for estimation of the percolation threshold. The series method is a powerful technique to find the percolation point and has been used in lattice and

continuum percolation [19], [36]–[38] and shows strong agreement with results obtained with the Monte Carlo methods. However, it has been mainly used for a few cases of arranged orders of site or bonds or circles/ellipses [39] and cannot be generalized for other geometric shapes. We have thus chosen Monte Carlo analysis in this work since, unlike series method, once a reliable algorithm has been defined to extract the percolation threshold, the geometry of the nano-objects can be investigated. Therefore, a thorough comparison between percolation threshold of different geometric shapes can then be performed. The study of percolation onset for 1D sticks in LMGP was first tackled by Daniel Langley. A tree-based algorithm was developed, in Matlab R2016a, which showed agreement with experimental results for AgNW based networks.[1], [2] The initial algorithm developed by Langley was upgraded in the framework of the current study, to explore different nano-objects entities.

To study the percolation threshold, first, several parameters should be specified, such as the shape and size of the studied systems and boundary conditions. While there are several methods for defining these criteria, we have used a modified form of the *RI* rule employed by Ziff [40] and initially introduced by Reynolds et al.[41] *RI* specifies a squared shaped system, where the right and left sides are in the open boundary and the top and bottom sides are in the close boundary condition, not connected and connected to the spanning cluster respectively.

We performed simulations mainly based on the tree-based method of Newman and Ziff super-fast algorithm for lattice percolation.[42], [43] We generate a network by adding randomly located nano-objects and checking connectivity after each addition until a percolating network is formed. Pseudorandom functions have been used to define both the location of the centre of nano-objects inside the system and a uniform distribution for their angular orientation to form isotropic networks. Each new nano-object is attributed to a new cluster number initially, then intersections with existing clusters are checked. If there is an intersection, the cluster number is updated to the number of the bigger cluster. Percolation occurs when both the top and bottom electrodes belong to the same cluster. The critical number of nano-objects in the system  $N_c$  is then stored as the outcome of one simulation. The critical network density  $n_c$  is then obtained by dividing  $N_c$  by the system area. This Monte Carlo algorithm was already compared either with other data extracted from literature and also compared with experimental data, both comparisons showing a fair agreement.[1]

Figure 4-2 represents examples of continuum percolation for random networks consisting of sticks, 3-fold periodic stick arrangement and hexagons. For all cases, top and bottom electrodes plus spanning clusters are colored in blue, while the rest of the network is colored in black.

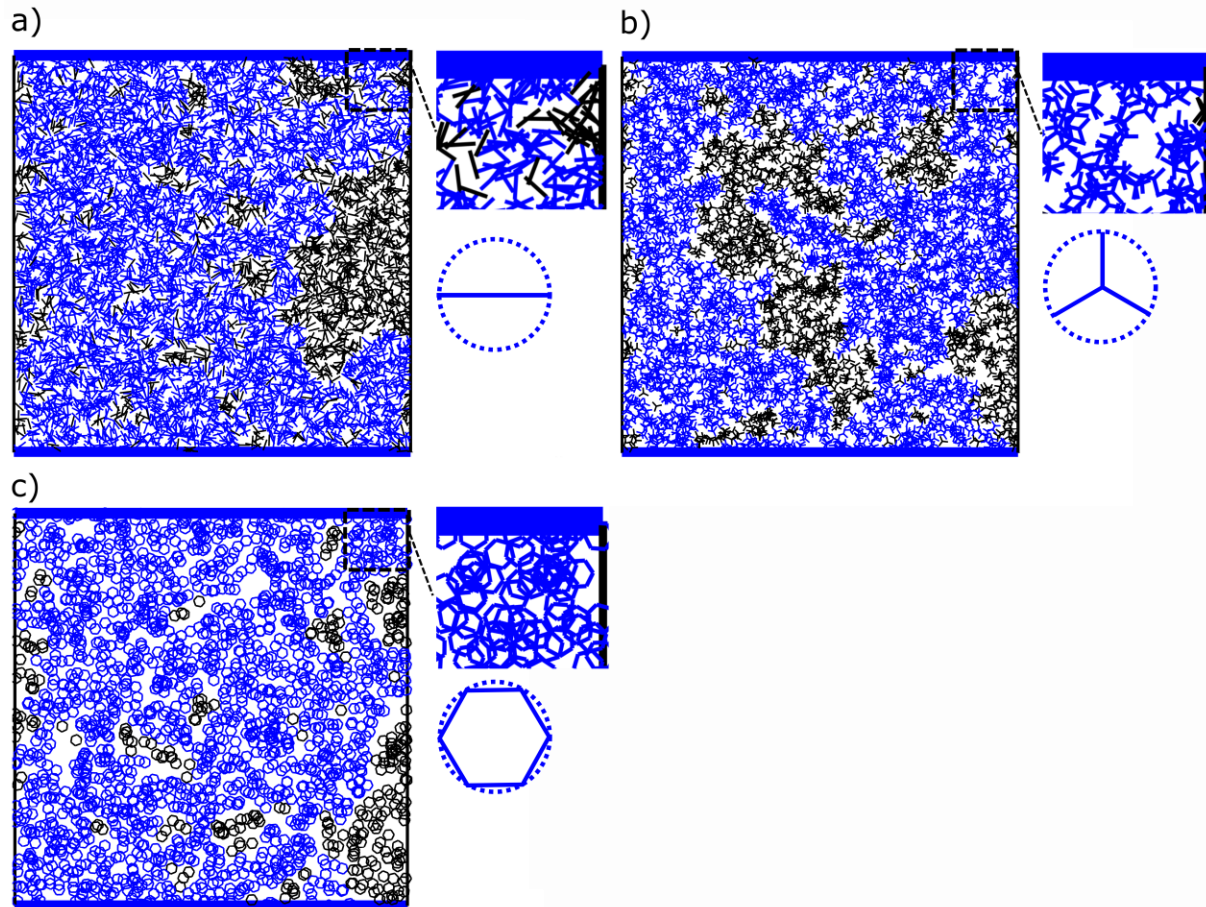


Figure 4-2 Continuum percolation simulations for different symmetric stick arrangements: a) stick alone, b) 3-fold periodic stick arrangement, c) hexagons. (inset of each figure, shows a close up of indicated areas) The studied nano-objects can fit inside a circle of unit radius, length of sticks is 2, while the system size is 70. The graphs correspond to the onset of percolation for which the spanning cluster is colored in blue and percolation occurs between the top and down sides.

In order to obtain statistical values of  $N_c$ , the generation of random networks was repeated for a high number of simulations and eventually the average value of  $N_c$  was calculated. For the studies of percolation threshold of 1D or 2D objects in the literature, the number of simulations was limited to around  $10^4$ . [44], [45] Li and Zhang used the fast algorithm of Newman and Ziff [42] and increased the number of simulations to  $10^8$ . [46] Of course, in all algorithms a higher number of simulations and system size (see section 4.4, finite-size scaling in continuum percolation) leads to more accurate estimations of  $n_c$ . However, the main motivation behind our study is to perform a comparison between the percolation threshold of different symmetric nano-objects, rather than finding the most accurate estimation of  $n_c$  itself. Figure 4-3 represents the mean values of  $N_c$  as function of the number of simulations associated to the percolation of random nano-squares: the first 100 simulations lead to large average  $N_c$  variations. After 100 simulations,  $N_c$  shows 1.15% variation from the final value (after  $10^5$  simulations). The

variation decreases to 0.37% and 0.07% after  $10^3$  and  $10^4$  simulations, respectively. The latter number was assumed to be sufficient for obtaining acceptable statistics for our study.

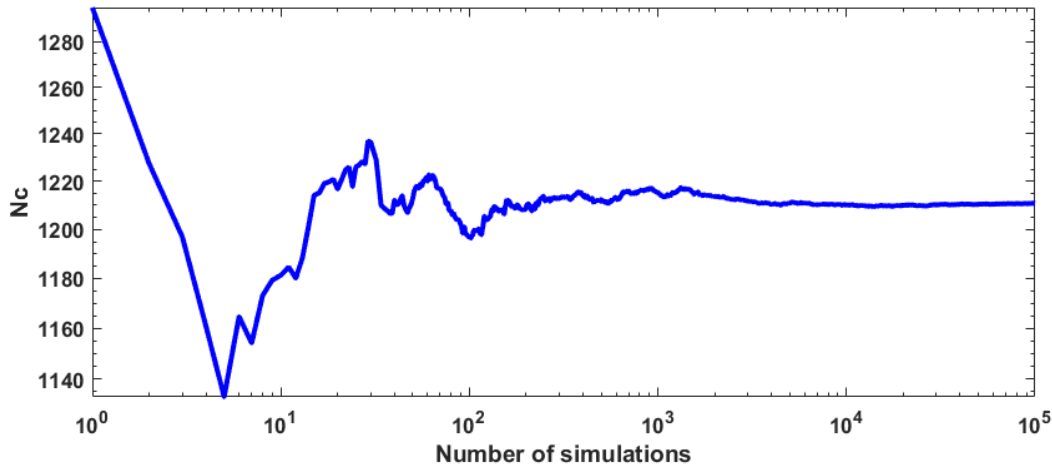


Figure 4-3. The convergence of  $N_c$  with increasing number of simulations for squares. The length of each edge of the square is unit and system size is 35.

#### 4.4. Introduction of the constant $\eta$ and effect of the nano-object size

One way to read the percolation threshold is to consider the probability,  $p(N)$ , that a system composed of  $N$  nano-objects reaches percolation. Figure 4-4.a represents  $p(N)$  for nano-squares. One can also define the cumulative probability distribution function  $cp(N)$ . In the case of finite-size systems  $p(N)$  typically takes the form of a Gaussian curve and results in a smoothed step function for  $cp(N)$ , as shown by Figure 4-4.a. The percolation threshold is the point where the probability of finding a percolating pathway is 50%, this is the way to extract the  $n_c$  value.

When studying the percolation threshold by Monte Carlo a critical factor is the studied system size. Lattice percolation can be studied for infinite system size, considering symmetries at the boundaries. However, this is not the case for continuum percolation systems.[46] Infinite system sizes cannot be studied due to computational limitations, however, studies have shown that continuum percolation can

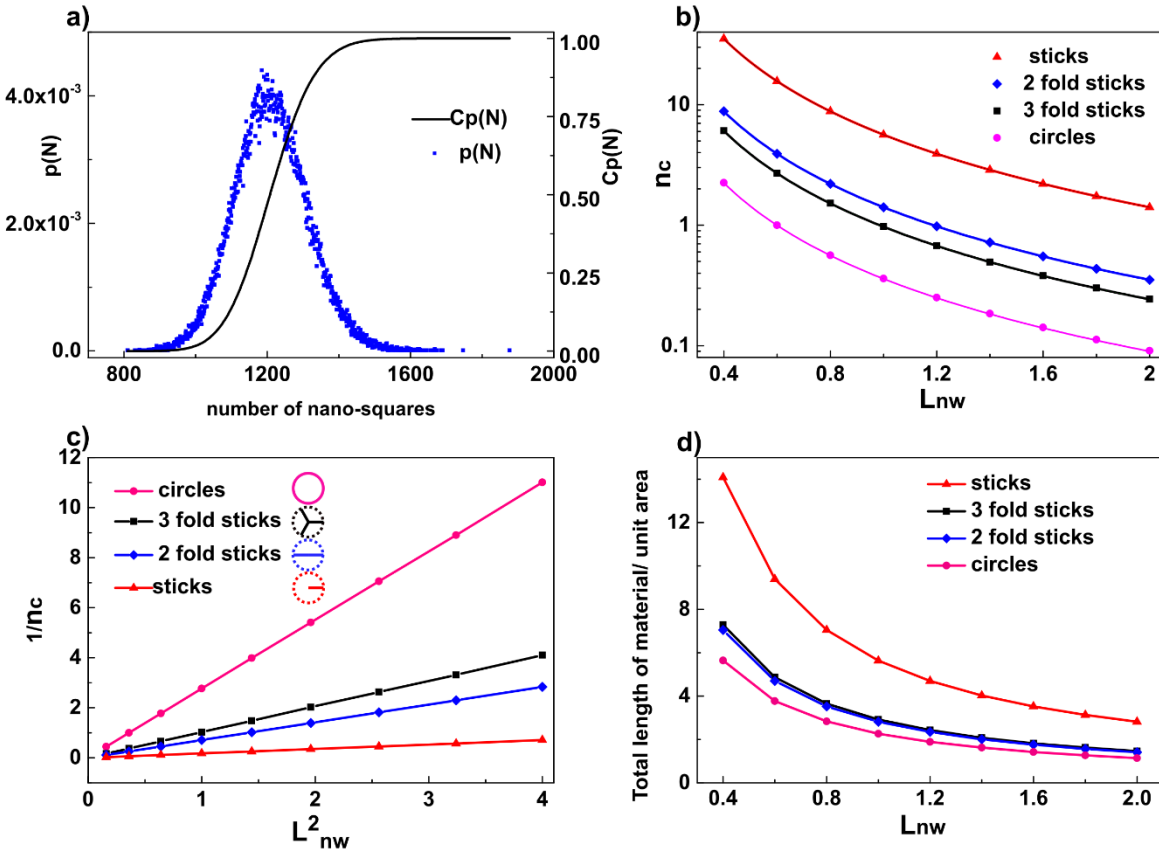


Figure 4-4. Monte Carlo simulations of percolation occurrence of nano-objects networks: a) Output of  $p(N)$  and  $cp(N)$  for square percolation for which the system/nano-object size ratio is 35; b)  $n_c$  values (symbols) for sticks, 2-fold and 3-fold arrangement of sticks and circles as a function of  $L_{nw}$ ; the lines are associated to Equation (4-3) for which  $\eta=5.64$  for sticks,  $\eta= 1.41$  for 2-fold,  $\eta=0.97$  for 3-fold periodic stick arrangements and  $\eta=1.13$  for circles; c) Linear correlation between  $1/n_c$  and  $L_{nw}^2$  for different nano-objects. d) The total length of material per unit area at the percolation threshold as a function of object size for different objects. The system size was fixed at 70 for b, c and d.

also fall into the same universal finite-size scaling as lattice percolation. A finite-size scaling function that is widely accepted for lattice and continuum percolation can be written as : [41], [46], [47]

$$n_{ceff} - n_c \propto L_s^{-n-\frac{1}{v}} \quad (4-2)$$

which relates the effective critical density,  $n_{ceff}$ , (for a specific finite-size system) to the critical density,  $n_c$  (for an infinite system), where  $L_s$  is the size of the square system and  $v=\frac{4}{3}$  is a universal critical exponent for 2D percolation.[48]. While  $n=0$  in general lattice percolation, Li and Zhang showed that stick percolation follows a more severe finite-size effect and scales as  $L_s^{-1-\frac{1}{v}}$  ( $n=1$  in Equation 4-2).

Mertens et al. did a similar study for percolation of 2D objects like squares and observed that for 2D objects, finite-size effect is even more severe and fits  $L_s^{-2-\frac{1}{\nu}}$  ( $\nu=2$  in Equation 4-2). [49]

These studies proved that increasing  $L_s$  leads to higher precision estimation of critical density values. However in the algorithms based on Newman and Ziff tree method, simulation time linearly increases with  $L_s^2$ . Therefore, a trade-off between simulation time and accuracy of estimated critical density should be considered. The minimum system/ stick size ratio for zero-width stick percolation is around 32 to show universal finite-size scaling behavior.[46] In most of the following results of this work, we have therefore considered systems at least 32 times the nano-objects sizes, otherwise, it has been mentioned.

The main criteria for studying percolation onset has been discussed, however, a parameter is still required to assess the influence of nano-objects shape and size on the percolation onset. In the case of stick percolation, Pike and Seagar [45] were the first ones to show that the relationship between  $n_c$  and the stick length,  $L_{nw}$ , is:

$$n_c \times L_{nw}^2 = \eta \quad (4-3)$$

where  $\eta$  is a constant product.[45] Figure 4-4.b illustrates the correlation between  $n_c$  and  $L_{nw}^2$  for 1-, 2- and 3-fold periodic stick arrangements and circles. As it is observed in this figure, the larger the  $L_{nw}$ , the lower  $n_c$ . A more quantitative way to show the dependence of  $n_c$  and  $L_{nw}$  is to plot the inverse of  $n_c$  versus  $L_{nw}^2$ : Figure 4-4.c exhibits indeed a linear dependence, the slope being  $1/\eta$ . The dimensionless product,  $\eta$ , is called the filling factor and has been the subject of extensive work in literature to find its value with high accuracy, at least for stick percolation.[45], [46], [49]–[51] One can use this concept not only for sticks but also for m-fold periodic stick arrangement shapes. However, a slightly different way can be used for closed shapes. For instance, for polygonal shapes their area,  $A_{polygon}$ , can be used instead of

$L_{nw}^2$  for sticks, and therefore:

$$n_c \times A_{polygon} = \eta \quad (4-4)$$

for polygons and circle. Comparing the  $\eta$  values deduced in those from literature can be used to validate the percolation algorithm used in this work. For instance, from the slope values observed in Figure 4-4.c, one gets  $\eta=5.64$ , 0.97 and 1.13 for sticks, squares and circles percolation, respectively. These values match well with reported numbers of  $\eta$  for sticks, squares and circles.[46], [49], [52] Mertens et al. have found precise values of  $\eta$  for these shapes at 5.6372 for sticks, 0.9822 for squares and 1.1281 for circles.[49] Small discrepancies between our reported values with their reported values rise from the



limited number of simulations and limited system size reported in this work, however, it can lead to useful physical insights.

For a fair comparison among different studied nano-object shapes,  $n_c$  or  $\eta$  are not the only parameters that should be considered. Indeed if one searches for the lowest percolation threshold in terms of matter quantity, the nano-object geometry should as well be considered. As we have discussed previously in Chapter 1, critical arealmass density ( $amd_c$ ) is a critical parameter since first, it shows the required matter quantity to reach desired electrical conductivity (see 1.3.1), and second, it has a linear correlation with the total transmittance of percolating networks (see 1.3.2.1). Therefore, the main motivation here is to search for nano-object shapes which have the lowest  $amd_c$  values. However,  $amd_c$  is more an experimental value, which depends on the cross-sectional area of nano-objects, as well as the density of material. Therefore, we have chosen to eliminate the effect of cross-sectional area and density of material from Equation 1-5 and deal with the total length of material per unit area ( $\frac{L_{total}}{unit\ area}$ ) instead:

$$amd_c = average\ mass_{n-o} \times n_c = L_{n-o} \times A_{n-o} \times \rho_{n-o} \times \frac{N_c}{unit\ area} \quad (4-5)$$

$$\frac{L_{n-o} \times N_c}{unit\ area} \times A_{n-o} \times \rho_{n-o} = \frac{L_{total}}{unit\ area} \times A_{n-o} \times \rho_{n-o}$$

where  $average\ mass_{n-o}$ ,  $L_{n-o}$ ,  $A_{n-o}$ ,  $\rho_{n-o}$  are average mass, length, cross-sectional area and density of nano-objects respectively. In the following sections, we will use  $\frac{L_{total}}{unit\ area}$  associated with the percolation threshold for comparing different shapes of nano-objects. The calculation of this value for m-fold periodic stick arrangement and regular polygons of m-edges is described below. For m-fold periodic stick arrangement ( $m$  number of branches with length of  $L_{nw}$ ), this leads to :

$$\frac{L_{total}}{unit\ area} = \frac{N_c \times L_{n.o}}{unit\ area} = \frac{N_c \times m \times L_{nw}}{unit\ area} = n_c \times m \times L_{nw} \quad (4-6-a)$$

If we combine Equation 4-3 and 4-6-a, we obtain:

$$\frac{L_{total}}{unit\ area} = m \times \frac{\eta}{L_{nw}} \quad (4-6-b)$$

Similarly, for regular polygons of m-edges where the polygon can fit inside a circle with the radius of  $L_{nw}$ , it follows :

$$\frac{L_{total}}{unit\ area} = \frac{N_c \times L_{polygon}}{unit\ area} = n_c \times L_{polygon} \quad (4-7-a)$$

If we combine Equation 4-4 and 4-7-a, we obtain:

$$\frac{L_{total}}{unit\ area} = \eta \times \frac{L_{polygon}}{A_{polygon}} \quad (4-7-b)$$

$$\frac{L_{polygon}}{A_{polygon}} = \frac{K}{L_{nw}} \quad (4-7-c)$$

where  $K$  changes for each polygonal shape and its values can be found in Table 4-1. Therefore, combining Equation 4-7-b and 4-7-c leads to:

$$\frac{L_{total}}{unit\ area} = \eta \times \frac{K}{L_{nw}} \quad (4-8)$$

Therefore,  $\frac{L_{total}}{unit\ area}$  is proportional to the inverse of  $L_{nw}$  in all the studied cases. Figure 4-4.d represents the dependence of  $\frac{L_{total}}{unit\ area}$  versus  $L_{nw}$ , where  $L_{nw}$  varies from 0.4 to 2 while system size is kept constant equal to 70. For all of the cases,  $L_{total}$  is inversely proportional to  $L_{nw}$ , therefore as a first approach reducing the total length of material can be obtained through an increase of object size. In the next sections, we will perform a comprehensive investigation of the different geometrical arrangement of nano-objects. This will enable us to also observe how the nano-objects symmetry affects the total length of material per unit area associated with the percolation onset.

#### 4.5. Effects of the symmetry of nano-objects on the percolation onset

The critical network density at percolation,  $n_c$ , the associated filling factor,  $\eta$ , and  $\frac{L_{total}}{unit\ area}$  values were calculated first in the case of networks formed by identical and symmetric nano-objects. Then, in a second step, statistical distributions were considered in angle, length and orientation of nano-objects. The effects of such distributions, which lead to imperfections in the morphology, have been studied on the percolation behavior of nano-objects.




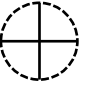



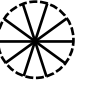





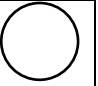
objects	stick	m-fold periodic stick arrangement						
	$m=1$	$m=2$	$m=3$	$m=4$	$m=5$	$m=6$	$m=7$	$m=10$
								
$\eta$	5.64	1.41	0.97	0.83	0.77	0.72	0.68	0.58
$\frac{L_{total}}{L_{sticks}^{total}}$	1	0.50	0.52	0.59	0.68	0.77	0.84	1.03
	<b>Polygonal nano-objects/circle</b>							
	$m=3$	$m=4$	$m=5$	$m=6$	$m=7$	circle		
								
$K$	3.99	2.83	2.47	2.31	2.22	2		
$\eta$	0.82	0.99	1.04	1.07	1.09	1.13		
$\frac{L_{total}}{L_{sticks}^{total}}$	0.58	0.47	0.46	0.44	0.43	0.42		

Table 4-1. For different geometries of studied nano-objects, the values of  $\eta$  and the total length are reported. For the sake of comparison,  $L_{total}$  has been divided by the total length associated to stick percolation threshold (considered then as the reference). For m-fold periodic stick arrangements, the length of each stick is  $L_{nw}$ , while for polygonal shapes, the length of each edge is set to fit the polygons inside a circle with the same radius of  $L_{nw}$ . The ratio between system size and  $L_{nw}$  is kept at 35.

#### 4.5.1. Effect of order of symmetry on percolation threshold, m-fold periodic stick arrangements and polygons/ circles

In Table 4-1 are reported values of  $\eta$  and total length associated with percolation onset of m-fold periodic stick arrangement or polygonal shapes. For the sake of comparison,  $L_{total}$ , has been normalized by the total length of a percolating system composed of sticks,  $L_{total}^{sticks}$ , and henceforth referred to as:  $\frac{L_{total}}{L_{sticks}^{total}}$ . It

is worth noting that while for  $m$ -fold periodic stick arrangement the length of each stick is  $L_{nw}$ , for polygonal shapes, the length of each edge is set to fit the polygons inside a circle with the same radius of  $L_{nw}$ . A first observed trend concerns the reduction of  $L_{total}$  for  $m$ -fold periodic stick arrangements, as opposed to single sticks. This observation can be explained by considering two competing effects resulting while “branches addition” in  $m$ -fold periodic arrangements. Initially, as more branches are added to  $m$ -fold periodic arrangements the probability of finding intersections between two adjacent objects increases. The increment in probability is due to the increment in the excluded area around each nano-object. The excluded area in the literature is defined as the area around an object, where it is prohibited to put the center of an adjacent object if overlapping of objects is not allowed. Higher excluded area, leads to a higher probability of finding intersections at a given network density, therefore lower  $\eta$  and  $L_{total}$  values. [53]

Secondly, as more branches are added to a  $m$ -fold periodic arrangement overall length of each nano-object increases. This leads to an increment in the total length of material per unit area at the percolation threshold. For high  $m$  values this effect surpasses the effect of increased excluded area values. In conclusion, increase in the excluded area is the dominant effect for small  $m$  values, explaining why nano-objects from 2-fold to 7-fold symmetries have  $\frac{L_{total}}{L_{sticks_{total}}}$  values lower than the unit. However, for the case of 10-fold symmetric shapes, the  $\frac{L_{total}}{L_{sticks_{total}}}$  is slightly larger than unity: the benefit of increasing intersection chance has been ruled out by the increase of the total length of each nano-object.

The second observed trend concerns data of the polygonal shapes. As  $m$  increases from 3 (triangles) to 7 (heptagons), the total length of material at the percolation threshold decreases even though all the shapes are defined to fit inside a circle with radius unity. A physical way to explain such observation is to consider the spatial compactness of the different polygons, through their moment of inertia. The latter, also known as the second moment of mass distribution, is a physical quantity that describes the mass distribution of an object regarding its centre of mass and is defined by:

$$I = \int_Q r^2 \cdot dm \quad (4-9)$$

Where  $r$  is the distance of a point from the object’s centre of mass and the integral is considered overall infinitesimal elements of mass  $dm$  in the two-dimensional space within the boundaries of the object  $Q$ . Since in our study we are dealing with zero-width nano-objects for which there is no mass, we, therefore, replace  $Q$  with  $P$  (the outer perimeter of the nano-objects) and define moment of inertia as:

$$I = \int_p r^2 \cdot dm \quad (4-10)$$

As the number of edges in polygons increases, the moment of inertia increases which means that objects are less compact spatially. This leads to lowering the percolation thresholds by enhancing the probability of finding intersections between adjacent objects. The relevance between the moment of inertia and percolation threshold will be further discussed in sections 4.5.2.1 and 4.5.5 where we will show that increasing the moment of inertia leads to the decrease of  $L_{total}$ .

#### **4.5.2. Morphological imperfections of network components and heterogeneous network compositions: effects on the percolation threshold**

Although all nano-objects studied so far were symmetric, it is unlikely to observe a perfect symmetry of nano-objects in real-world synthesized nanostructures.[54], [55] Asymmetrical features can consist of variations in the angles between different branches of stick arrangements, variations in the length of branches or be derived from mixing different types of nano-objects. The latter can result from suspensions containing for instance mixtures of sticks and nano-objects of another shape. The effects of these parameters on percolation properties for different geometries are reported below to assess their impact on total length per unit area at percolation onset.

##### ***4.5.2.1. Angular distribution in 2-and 3-fold periodic stick arrangement***

As reported in Table 4-1 and Figure 4-4.d, 2- and 3-fold periodic stick arrangements exhibit approximately 50% and 48% less  $L_{total}$  when compared with sticks. In this section, we investigate the effect of changes in the angles between adjacent sticks in 2- and 3-fold periodic stick arrangements on its percolation behavior.

The aim is to answer these two questions: i/ how deviations in the angles between adjacent sticks in a m-fold arrangement will affect the percolation behavior and ii/ which geometry yields the lowest  $L_{total}$ ?

Figure 4-5.a shows the variation of  $n_c$  for 2- and 3-fold periodic stick arrangements versus the angle between adjacent sticks. One stick was used as reference and  $\alpha$  is the angle between the extension of the reference stick with other sticks of m-fold periodic stick arrangements and it is changed between 0 and 180°. For 2-fold periodic stick arrangements (black curve in Figure 4-5.a), the larger  $\alpha$  the larger  $n_c$ . For

both extreme  $\alpha$  values we find back the overall length of 2-fold periodic stick arrangements:  $2L_{nw}$  for  $\alpha=0^\circ$  and  $L_{nw}$  for  $\alpha=180^\circ$ . In between these two values, there is a monotonous but non-linear dependence.

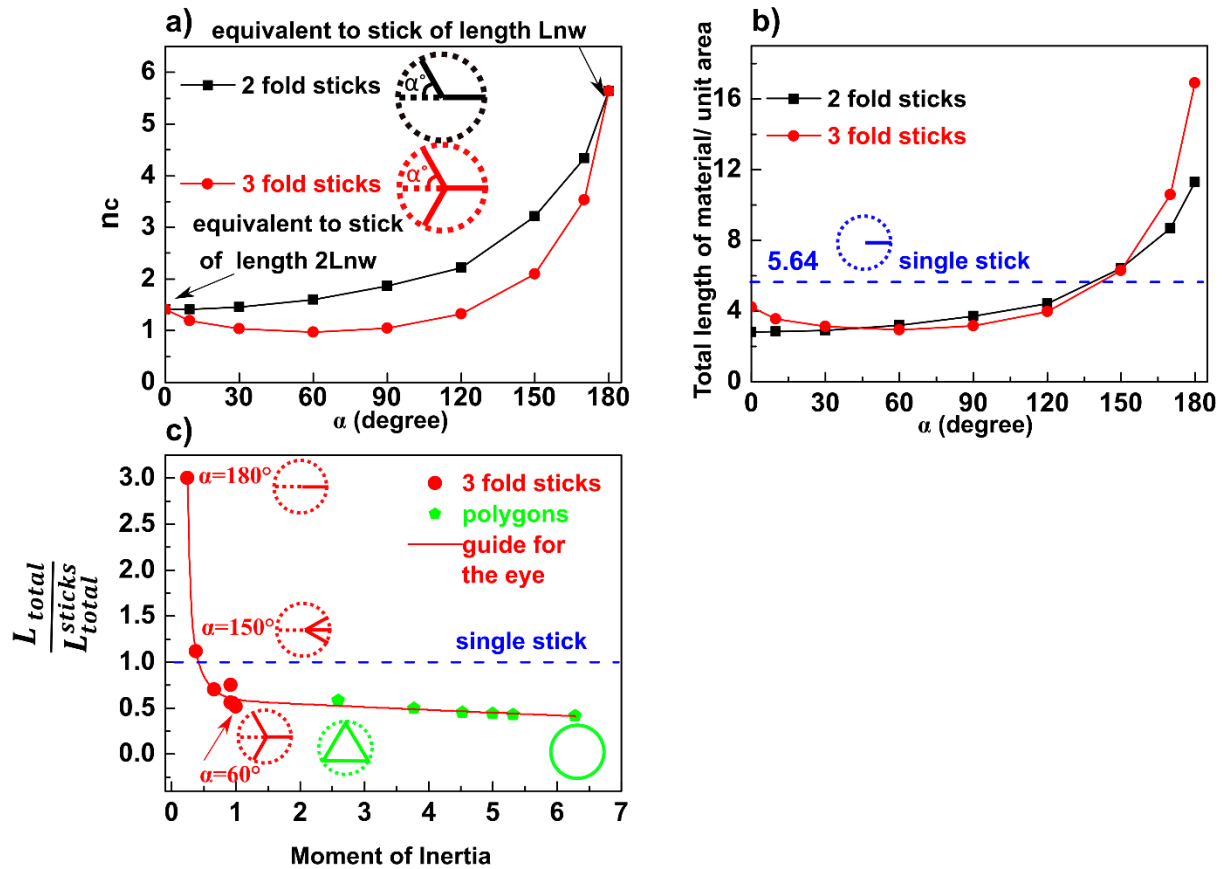


Figure 4-5. a) Effect of symmetry on the percolation threshold of 2- and 3-fold stick arrangements:  $n_c$  dependence versus  $\alpha$  values. b) The total length of material per unit area for 2- and 3-fold periodic stick arrangement versus  $\alpha$ . c) Correlation between total length relative to single-stick arrangement and moment of inertia for polygonal shapes and 3-fold periodic stick arrangement associated with various  $\alpha$  values. In all simulations system size is 35, length of sticks in 2- and 3-fold sets of sticks is 1 and polygonal shapes fit in a circle with the same radius of 1. In subfigure a, 2- and 3-fold stick arrangements are drawn larger to illustrate clearly the angle  $\alpha$ . Lines are guide for the eye.

For 3-fold stick arrangement (red curve in Figure 4-5.a),  $n_c$  versus  $\alpha$  is not monotonous anymore, since one can observe a minimum  $n_c$  value at  $\alpha=60^\circ$  which corresponds to the symmetric arrangement of 3 sticks. However, within the range of  $\alpha$  values between  $30^\circ$  and  $90^\circ$ , the relative variation of  $n_c$  is small (<10% compared to its minimum value at  $60^\circ$ ). Therefore a practical consequence of this result is that to minimize experimentally  $n_c$  values for 3-fold periodic stick arrangements, the  $\alpha$  values should not be a stringent parameter. The dependency of the total length of material per unit area ( $\frac{L_{total}}{unit\ area}$ ) versus  $\alpha$  values

are reported in Figure 4-5.b for 2- and 3-fold stick arrangements, while the dashed line corresponds to random sticks. This figure shows that even non-symmetric 2- or 3-fold periodic stick arrangements exhibit smaller  $L_{total}$  values compared to single sticks, the lowest value is 2.82 for 2-fold and 2.92 for 3-fold periodic stick arrangements. The low  $L_{total}$  values only correspond to  $\alpha$  values lower than about  $120^\circ$  since otherwise sticks are arranged in a too compact way. One possible way to quantitatively assess the compactness of stick arrangements is the use of the moment of inertia, as defined above by Equation 4-10. Previously in section 4.5.1, the moment of inertia has been used to compare spatial compactness of polygonal shapes. It was observed that a higher number of edges in polygons, leads to a higher moment of inertia, which respectively leads to lower  $L_{total}$  values. Figure 4-5.c exhibits a similar dependence of the relative total length (normalized by the single-stick arrangement) on the moment of inertia, the larger the moment of inertia the lower the total required material length to reach percolation. This can be easily interpreted physically by the fact that moment of inertia has higher values for non-compact structures associated to large spatial extension and those stick arrangements would span the interspace between opposite electrodes with a lower amount of sticks. In parallel to this intuitive statement, Figure 4-5.c shows that for very different shapes  $L_{total}$  versus moment of inertia indeed exhibit rather similar tendency.

#### ***4.5.2.2. Mixtures of sticks and circles, mixtures of sticks and 3-fold periodic stick arrangements***

Although experimental evidence of synthesized complex nanostructures like nano-stars and nano-cubes have been reported,[28], [29], [56], [57] in practice one might expect to consider a mixture of single sticks and  $m$ -fold periodic stick arrangement or polygons, instead of suspensions of solely one single arrangement. In literature, the percolation behavior of networks composed of multiple components has also been studied. [17]Ni et al. reported the percolation behavior of a thin film composed of 1D sticks and 2D disks and showed an almost linear relationship between densities of nano-objects,  $n_c$ , while changing the composition in mixed systems. This can be the case of mixture nanocomposites of Carbon Nano Tubes (CNTs) and Graphene NanoPlatelets (GNPs).[58] Here we study two type of networks composed of the first mixture of sticks and circles and the second mixture of sticks and 3-fold periodic stick arrangements. When dealing with networks composed of multiple nano-objects, the main question is how the percolation threshold of the mixture changes compared to a network which is occupied by solely sticks. Circles or 3-fold periodic stick arrangements are added to stick based networks and changes of  $\frac{L_{total}}{unit\ area}$  while changing composition are observed. Figure 4-6.a shows that adding a few

percentages of circles to a stick network significantly decreases the percolation threshold (both  $n_c$  and  $L_{total}$  values).

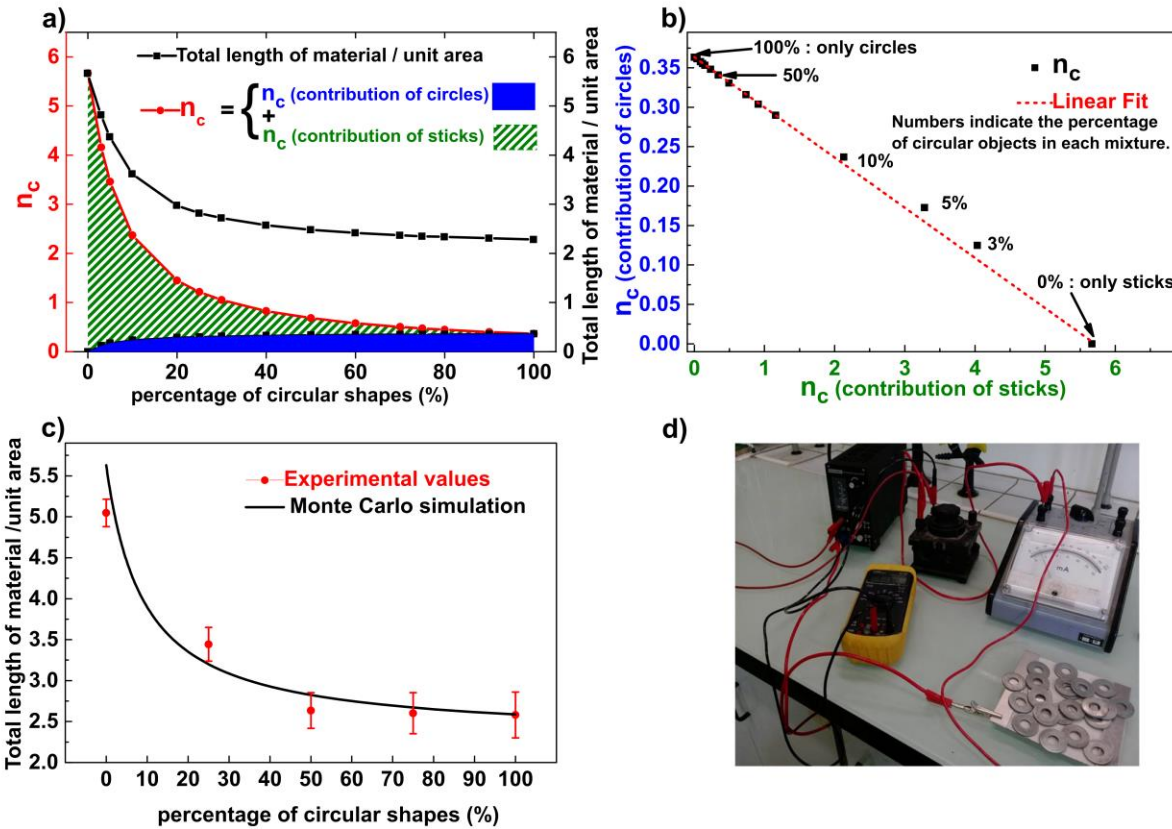


Figure 4-6. a) Values of  $n_c$  and the total length of the material per unit area at the percolation threshold for different mixtures of sticks and circles. B) Linear correlation between  $n_c$  values in systems composed of mixtures of circles and sticks. The branch lengths and circle radius are kept at 1 and the size of the system is 35. c) Comparison between numerical and experimental results for mixtures of sticks and circular shapes, where all lengths have been rescaled to  $L_{nw}=1$ ,  $R_{circle}=0.87$  and system size=12.9 to be coherent with the rest of presented results here. D) Experimental setup to do macro-scale percolation test for a combination of sticks and circles.

However the change is rather abrupt at the beginning, as adding 20% of circles reduces the total length of material at percolation threshold around 48% and as the impact becomes less and less significant as we add more circular shapes. The parts of  $n_c$  corresponding to sticks and circles at each composition is shown with dashed green lines and blue color respectively. If we plot these two components of  $n_c$  while changing the percentage of circular shapes, as shown in figure 4-6.b, a linear dependency between two nano-objects density is observed. Such a linear dependency can be explained by excluded area and has been already observed for networks composed of mixtures of sticks and circles.[17], [59]



A direct comparison of the Monte Carlo simulation reported here and experimental observations (by using macroscopic metallic objects) has been tackled for the sake of simulations assessment. The experimental studies was performed by a group of first year Phelma students for a class project entitled “percolation”, under supervision of Daniel Bellet. To do so, percolation thresholds have been measured experimentally for mixtures of sticks and circles deposited on a 120×120 mm<sup>2</sup> paperboard sheet onto which two opposite electrodes composed of 20 mm wide aluminium strips were positioned. Copper strands of 15.5 mm length were used as sticks and steel washers with outer diameter of 27 mm were used for circles. Washers were soaked in 13 mol/L HCl acid to remove the superficial native oxide layer to allow efficient electrical contacts. Sticks and washers were manually thrown randomly on top of the paperboard. A large magnet was used just below the sheet to exert a gentle downward force on the steel objects for improving the electrical contact between the percolating objects and both electrodes. The setup is presented in Figure 4-6.d. Five different mixtures of sticks and circles were investigated, with stick percentage values of 100, 75, 50, 25 and 0%. Percolation test of each mixture was performed 3 times and then averaged. Figure 4-6.c represents both the Monte Carlo predicted as well as experimental values of critical total length for mixtures. Despite the small statistics associated with experimental work and the fact that the ratio between the size of the system and the object was smaller than 35, a good agreement is observed between experimental and Monte Carlo values.

Finally, networks composed of mixtures of sticks and 3-fold periodic stick arrangements have been studied as shown in Figure 4-7.a. Results similarly suggest that adding a low percentage of 3-fold periodic stick arrangements to an initially sticks based network significantly decreases the percolation threshold, having a positive impact on both  $n_c$  and  $L_{total}$  values. As shown in Figure 4-7.b, adding 20% of 3-fold periodic stick arrangements to a network composed of sticks reduces the total length at the percolation threshold by 25%. Similarly to the analysis of networks composed of mixtures of sticks and circles, the parts of  $n_c$  corresponding to each entity of composition were separated and shown with dashed green lines for sticks and blue lines for 3-fold periodic stick arrangements. Again if we plot the two components of  $n_c$  while changing the percentage of 3-fold periodic stick arrangements, a linear dependency between nano-object density is observed, as shown in figure 4-7.c. One can then conclude that this is interesting, from a percolation occurrence point of view, to add 3-fold periodic stick arrangements in a stick network. On the other side if there are some sticks in a network composed of 3-fold periodic stick arrangements there is no much influence on the percolation threshold since  $L_{total}$  per unit area has a rather flat dependence with the low number of stick objects.

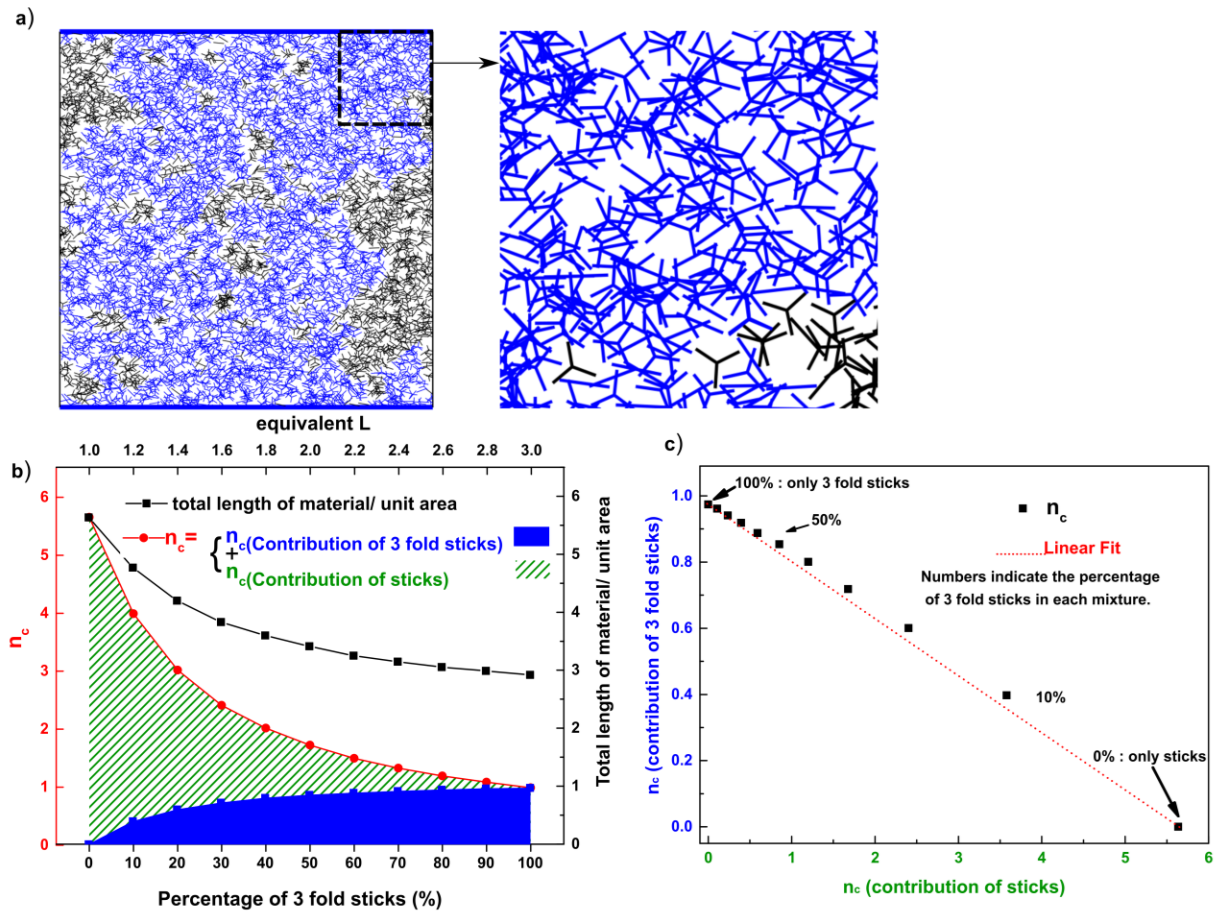


Figure 4-7. a) Continuum percolation simulations for a system composed of 50% of sticks and 50% of 3 fold periodic stick arrangements. The inset shows a close up of the indicated area. b) values of  $n_c$  and total length of the material per unit area at percolation threshold for different mixtures of sticks and 3-fold periodic stick arrangements. c) Correlation between  $n_c$  values in systems composed of mixtures of sticks and 3-fold periodic stick arrangements. For all of the cases, the stick length is kept at 1 and the system size is 35.

#### 4.5.3. Percolation threshold for random networks of finite-size regular grids

So far we have explored continuum percolation using Monte Carlo analysis for m-fold arrangements of sticks and polygonal shapes. Another approach to add local symmetry to percolating networks could be connecting sticks together to form finite-size grids. Experimentally this could be achieved through either growing nanowires using Y-shaped or cross-shaped nucleation seeds or adding Y-shaped or cross-shaped crosslinkers to a suspension of nanowires, to stick them together with links forming  $60^\circ$  or  $90^\circ$  angles. In Figure 4-8.a-c, we represent a schematic of the use of such bonding particles to form grids, a mechanism that bears similarities with the process of polymerization. Forming finite-size grids helps to

reduce percolation threshold considering two effects, first by enlarging nano-objects size, which has already been proven to decrease percolation threshold (see section 4.4) and second, by adding local

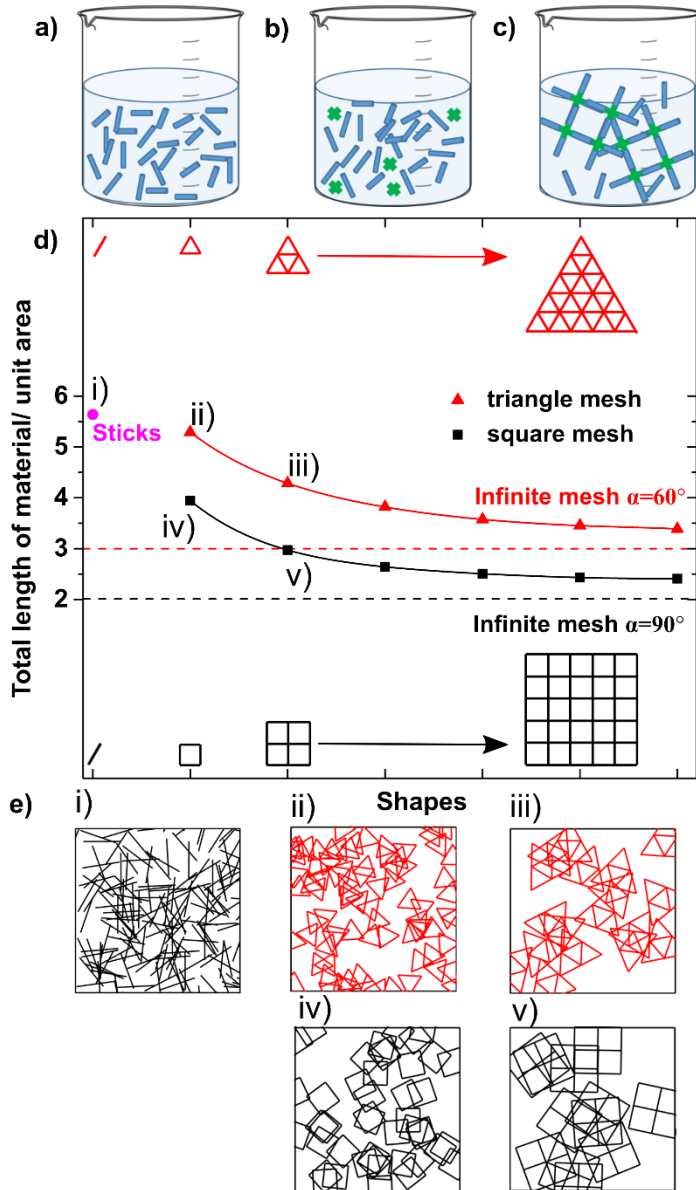


Figure 4-8. a) The initial solution of stick-shaped nanowires. b) Addition of cross-shaped crosslinkers to nanowire solution c) formation of finite-size regular grids composed of nanowires and crosslinkers. d) Total length of material per unit area for sticks and finite-size regular grids where the angle between sticks of grids is  $60^\circ$  and  $90^\circ$ . Lines are guide for the eye and the dashed lines show total length of material per unit area for networks composed of infinite meshes where the angles between adjacent sticks are  $60^\circ$  and  $90^\circ$ . e) insets of percolating networks composed of i) sticks, ii-iii)  $60^\circ$  grids composed of  $1 \times 1$  and  $2 \times 2$  set of sticks. iv-v)  $90^\circ$  grids composed of  $1 \times 1$  and  $2 \times 2$  sets of sticks. The ratio between system size and  $5 \times 5$  set of sticks (the biggest studied nano-objects) is 35.

symmetry to structures. As one can conclude from Table 4-1, adding orders of symmetries to nano-objects up to an extent leads to a decrease in total length at the percolation threshold. Figure 4-8.d represents the decrease in the total length of material per unit area while increasing the grid size for two types of finite-size grids where the angles between sticks are  $60^\circ$  or  $90^\circ$ . Triangle grids at each step are growing by adding a row to the bottom of the previous grid and square grids are growing by adding a new stick at each side of the mesh as shown in Figure 4-8.d. Each grid is named by the number of sticks at the edges, e.g.  $2 \times 2$  or  $3 \times 3$  sets of sticks. For rather big grids composed of  $3 \times 3$  sets of sticks or more, total length at percolation threshold converges to the cases corresponding to infinite meshes where the angles between adjacent sticks are  $60^\circ$  and  $90^\circ$ . The total number of nano-objects per unit area, for the latter networks, is  $3 (L_s/L_{nw})^2$  and  $2 (L_s/L_{nw})^2$ , respectively, where  $L_s$  is the system size. These values are a few times smaller than percolation threshold of random stick based networks, therefore networks composed of trigonal /tetragonal meshes are superior to random nanowire networks in terms of  $L_{total}$ . However, the driving force behind using random nanowire networks for TEs is the ease of fabrication and scalability of solution-based techniques. Here we show that finite size grids can approach infinite grids in terms of  $L_{total}$  to reach percolation threshold, and still benefit from the ease of fabrication for solution-based TEs.

#### 4.5.4. Percolation threshold for random networks of non-regular finite-size grids

Real-world nanowires always present a length distribution. The effect of the distribution in the length of nano-objects on the percolation onset has been studied using Monte Carlo simulations for metallic NWs and CNTs. For networks composed of metallic nanowires or carbon nanotubes, increasing length to diameter ratio or increasing length distribution [1], [60]–[62] or adding even a small fraction of high aspect ratio nanowires/tubes[8] reduces the electrical resistance at any object density. In the same vein, one can also investigate the effects of length distribution on the percolation occurrence of finite-size grids by considering a normal distribution, using Gaussian function, over the lengths of sticks. The latter can be associated with the following probability of having a length  $x$ :

$$P(x) = \frac{1}{\sqrt{2\pi\sigma^2}} e^{-\frac{(x-L_{nw})^2}{2\sigma^2}} \quad (4-11)$$

Where  $L_{nw}$  is average stick length, and  $\sigma$  is the standard deviation. For the length distribution of nanowires,  $\sigma = \frac{D_L L_{nw}}{4}$ , where  $D_L$  is the normalized length distribution width (length distribution

parameter).  $D_L=0$  and  $D_L=4$  correspond, respectively, to the cases where all the sticks have the same length of  $L_{nw}$  and where sticks have a standard deviation of length's distribution of  $L_{nw}$ .

Another aspect of mimicking real-world imperfection concerns deviation from regular angles at junctions between sticks. Variations in such angle ( $\theta$ ) would give rise to more asymmetric structures. We have investigated the effects of such asymmetries on the percolation threshold of networks made by finite-size  $2 \times 2$  grids. A normal distribution for  $\theta$  is also considered where the average value equals to zero and the standard deviation is named  $\alpha$ . In this work, we studied various disorder levels, namely  $\alpha=0$ ,  $10^\circ$  and  $20^\circ$ , while changing the length distribution with  $D_L$  values from 0 to 4. Figure 4-9.a shows an example of a percolating network composed of disordered finite-size  $2 \times 2$  grids, where  $D_L$  is 1 and  $\alpha = 5^\circ$ . Figure 4-9.b shows the total length of material per unit area values obtained for finite-size  $2 \times 2$  grids with different values of  $D_L$  and  $\alpha$ . We observed that increasing  $D_L$  induces a decrease of the percolation threshold. A similar correlation has been reported for sticks in literature. Balberg et al. [53], for instance, used the excluded area theory and confirmed that the excluded area has a general but not an exact correlation with the percolation threshold. They have calculated excluded area for fixed length and normal distribution of lengths for zero-width sticks and have compared both cases using Monte Carlo simulations. They suggest that normal distribution in length increases the average excluded area, therefore decreases the percolation threshold.

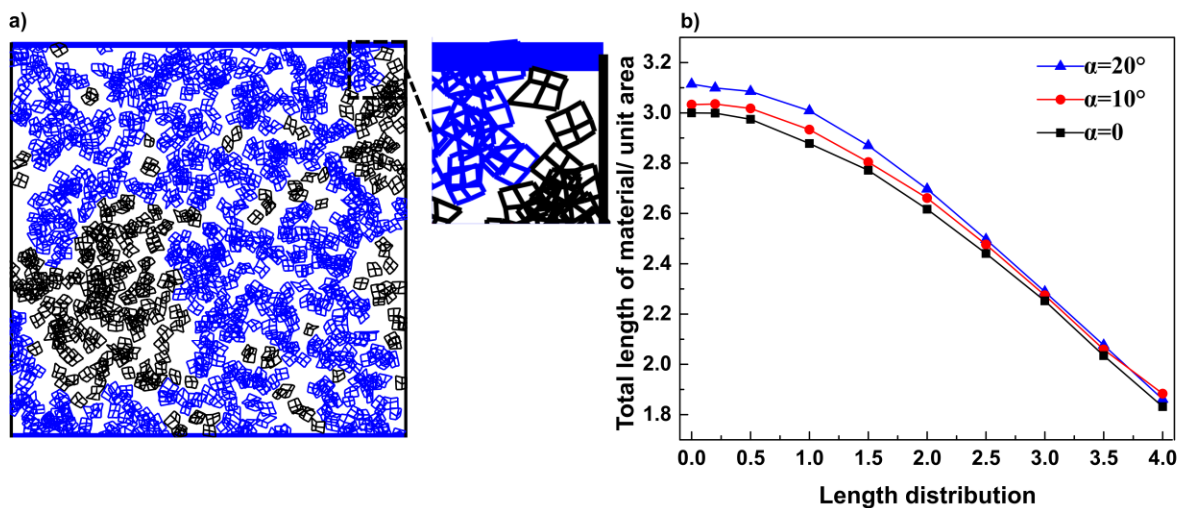


Figure 4-9 a) Study of the continuum percolation of a network composed of disordered finite size  $2 \times 2$  grids,  $D_L$  is 1 and  $\alpha = 5^\circ$ . The inset shows a close up of the indicated area. b) The total length of material per unit area at percolation threshold for irregular finite size  $2 \times 2$  grid structures while  $D_L$  is changing from 0 to 4, for  $\alpha=0$ ,  $10$  and  $20^\circ$ . Lines are guides for the eye.

They have confirmed the same behavior for circles and spheres and therefore concluded that a more general trend can be deduced. While the length distribution has clear effects, the angle distribution

appears to have a small influence on the total length of material per unit area as shown by Figure 4-9.b. One practical consequence is that preventing disorder is not a challenge for obtaining real finite size grid networks which could exhibit low percolation threshold compared to random sticks. However, a more systematic way to study the effect of angular perturbations is to find an analytical method to calculate the moment of inertia for  $2 \times 2$  meshes while changing both  $D_L$  and  $\theta$ . Such a study has not been performed in the framework of this thesis but can provide a more generalized understanding of the dependency of the moment of inertia and percolation threshold in random networks of nano-objects. As a result, the Moment of inertia can be used as a criterion to evaluate objects in their percolation onset. So, one could predict which shapes are more likely to be beneficial in terms of the reduced percolation threshold.

#### **4.5.5. Effect of compactness of elemental objects on the percolation threshold**

The length of nano-objects plays a crucial role in the total length of material per unit area ( $L_{total}$ ) at the percolation threshold, as clearly shown in Figure 4-4 and 4-8. Moreover, some object shapes exhibit different  $L_{total}$  values when compared with each other. As depicted in Figure 4-5.c, for either polygons or 3-fold periodic stick arrangements the moment of inertia appears to be correlated with  $L_{total}$ . To test further this idea, the moment of inertia of all possible forms of elemental grids composed of the same number of sticks has been compared. Grids formed of 16 sticks keeping two limitations have been studied: first, the connected sticks should always form complete squares, and second, each formed square should share at least one stick with an adjacent square. The reason behind these limitations and choosing 16 sticks is to keep the number of studied objects reasonably limited, considering the computation time. For arrangements of 16 sticks with these limitations, 11 morphologies with a wide range of compactness are feasible. Table 4-2 presents the morphology of the different studied grids, along with the total length of material at the percolation threshold. Figure 4-10.a demonstrates that there is a strong and rather smooth correlation between  $L_{total}$  at percolation threshold and the moment of inertia: the larger the moment of inertia the lower  $L_{total}$ . In other words, the compactness of the elemental objects has a drastic influence on the percolation threshold: when an elemental shape is elongated the percolation threshold is reached with a much lower density of objects. However, only limited number of shapes have been studied in this section.

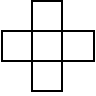
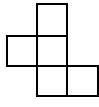
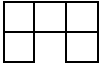
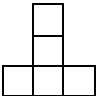
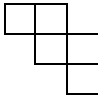
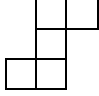
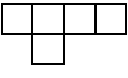
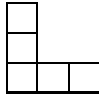
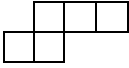
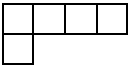
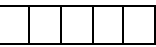
<b>Shapes</b>						
<b>Moment of Inertia</b>	21.33	23.77	24.27	25.08	26.14	27.33
$\frac{L_{total}}{unit\ area}$	2.72	2.56	2.57	2.44	2.49	2.40
<b>Shapes</b>						
<b>Moment of Inertia</b>	27.93	28.83	29.05	32.80	41.33	
$\frac{L_{total}}{unit\ area}$	2.35	2.29	2.33	2.20	2.16	

Table 4-2. Total length of material per unit area at percolation threshold and moment of inertia for grids composed of 16 sticks, changing from the most compact object to the most elongated one.

A more systematic approach to confirm the correlation between moment of inertia and percolation threshold, is to analyse a continuous series of shapes. Ellipses with changing semi-major to semi-minor axes ratio is an example of shapes with continuous moment of inertia. It's expected that  $L_{total}$  at percolation threshold value will be highest for the circular shapes and decrease while elongating ellipses (increasing semi-major to semi-minor axes ratio). Ellipses have not been studied in this chapter, but studying them can be an interesting step in understanding the association between percolation threshold and moment of inertia.

The last case that has been studied in this part is the comparison of the total length at the percolation threshold for single sticks and for different finite size grids where both the overall size of objects and their compactness is changing. Respective shapes can be found in table 4-3. Figure 4-10.b shows also the decrease in the total length of material at the percolation threshold for increasing object sizes.


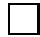

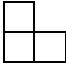
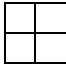
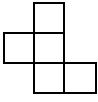
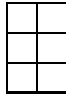
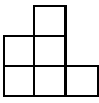
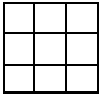
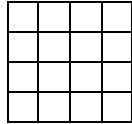
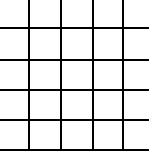
<b>Shapes</b>						
<b>Number of sticks in the object</b>	1	4	7	10	12	16
$\frac{L_{total}}{unit\ area}$	5.64	3.94	3.15	2.93	2.97	2.54
<b>Shapes</b>						
<b>Number of sticks in the object</b>	17	18	24	40	60	
$\frac{L_{total}}{unit\ area}$	2.73	2.55	2.65	2.51	2.42	

Table 4-3. Total length of material per unit area at percolation threshold for finite-size meshes ordered from smaller to larger size.

So far we have observed that there is a correlation between the moment of inertia values and the total length of material per unit area for some of the studied nano-objects, see Figure 4-5.c and 4-10.a: for m-fold periods sticks arrangements/ polygons and grids composed of 16 sticks, respectively. However, there is a lack of systematic study of the moment of inertia for all the studied nano-objects so far (disordered finite size 2x2 grids or different size growing grids) to propose a quantitative relation between the moment of inertia and the total length of material per unit area at the percolation threshold. However, such a study is not within the scope of this work but can indeed be an interesting subject for future studies.



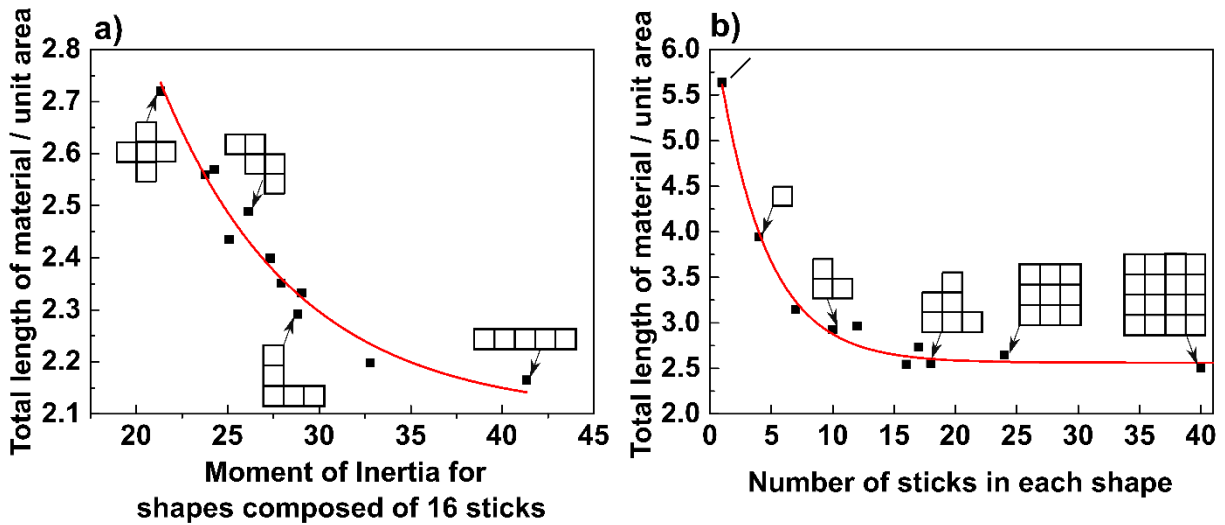


Figure 4-10.a) Correlation between the total length of material per unit area at the percolation threshold and the moment of inertia for different stick arrangements that are formed with the same number of sticks: 16. b) Total length of material per unit area at percolation threshold for grids with different grid size and spatial compactness. Lines are guide for the eyes.

#### 4.5.6. Percolation threshold for non-randomly oriented nanowires

So far in the present work, only isotropic networks (associated with a random orientational distribution) have been studied. Very often deposition techniques of nano-objects result in rather randomly distributed sets; this is the case for spray coating, inkjet printing, slot die,[63] Meyer rod,[64] techniques. However, it can be possible to align nano-objects in preferential directions. For instance, a magnetic-controlled deposition of copper-tin[65] nanowires or nickel-bismuth [66]nanowires has been reported. Another example of aligned NW networks is presented by Hu et al.[67] where agitation assisted alignment of AgNWs has led to formation of TEs with low sheet resistance ( $2.8 \Omega\text{sq}^{-1}$ ) and high transparency (85% at 550 nm).

The question which was addressed here was whether changes in the orientation of NWs from a random distribution to aligned NWs along two perpendicular directions can lead to a decrease of  $L_{total}$ . The impact of a slight deviation,  $\beta$ , from a perfectly vertical/ horizontal alignment (i.e. sticks angles are normally distributed within  $[-\beta, \beta]$  or  $[90^\circ - \beta, 90^\circ + \beta]$ ) has been considered as shown in Figure 4-11.a.

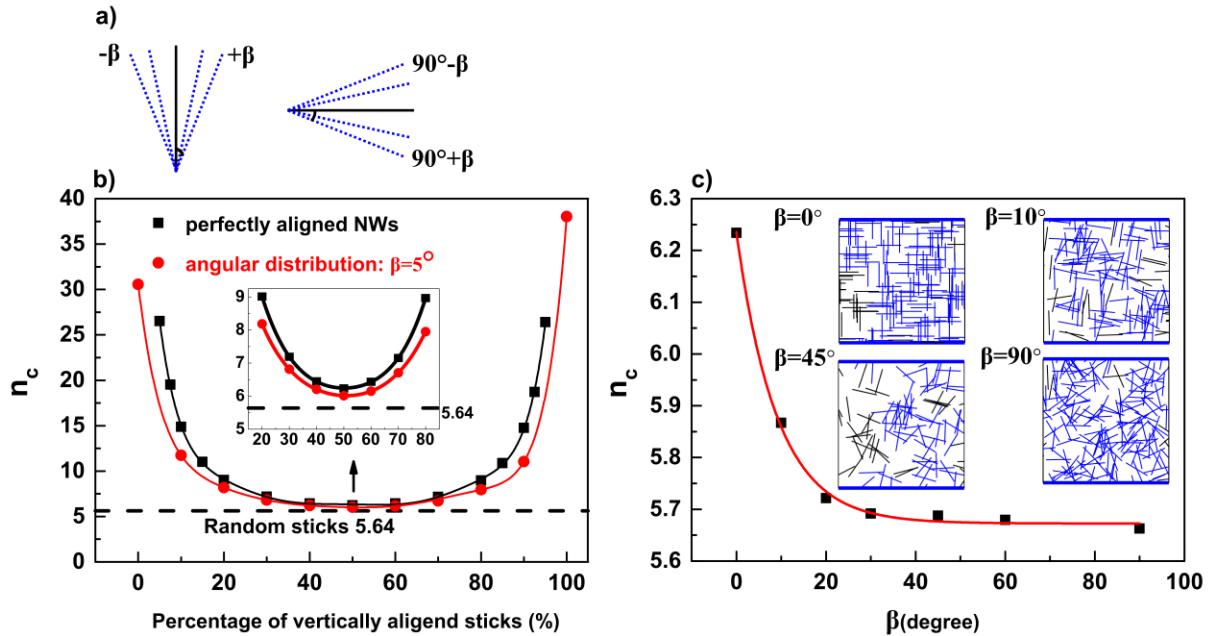


Figure 4-11.a) Examples of vertical and horizontal sticks where angles are normally distributed within  $[-\beta, \beta]$  or  $[90^\circ - \beta, 90^\circ + \beta]$ . b) The percolation threshold of networks composed of vertically or horizontally aligned sticks versus the percentage of vertically aligned sticks.  $n_c$  values for both perfectly aligned sticks and sticks with  $5^\circ$  deviation from vertical/horizontal directions are presented. c) The effect of angular deviation on the percolation threshold of networks composed of 50% vertical - 50% horizontal aligned sticks, as shown in the examples  $\beta=0^\circ$  corresponds to perfectly vertical/horizontal aligned sticks and  $\beta=90^\circ$  corresponds to randomly oriented networks.

Figure 4-11.b reports the critical network density,  $n_c$ , for aligned sticks while changing the percentage of vertically aligned sticks (in the direction of percolation) from nearly 0 to 100%. Let's note that since we are dealing with zero-width sticks in our simulations, for systems composed of all-perfectly aligned sticks no percolation can be attained. Data reported in Figure 4-11.b show that for aligned networks along two perpendicular directions  $n_c$  is always larger compared to random network (shown by the dashed line). This is in agreement with the study of Balberg et al.[44] who showed that the percolation threshold increases with the macroscopic anisotropy in the system. Figure 4-11.b shows that introducing a deviation of  $5^\circ$  slightly reduces the percolation threshold values, however, the obtained values are still higher when compared to a randomly oriented network. Another point which should be considered about Figure 4-11.b is that the percolation threshold, for both cases of perfectly aligned sticks and sticks with  $5^\circ$  deviation in the angles, is minimum when there are 50% of vertical and 50% of horizontal sticks. This point has been investigated further by studying a 50% vertical -50% horizontal sticks arrangement while changing the angle  $\beta$ , from 0 to  $90^\circ$  in Figure 4-11.c. Data shows that increasing  $\beta$  (i.e. approaching to more isotropic systems) decreases the percolation threshold. A similar trend has been reported before in literature about the alignment of random sticks. Langley et al. [1] have shown that replacing a uniform

distribution of angles between 0 and  $\pi$  by a delta-like function, for which all the sticks are parallel to each other with a small deviation in the angles, increases the percolation threshold. We also observed that  $n_c$  is slightly higher for networks with totally vertical sticks, both  $\beta=0$  and  $5^\circ$ , rather than totally horizontal ones. However, this point is not in agreement with some previous reports in the literature. Simoneau et al.[23] have studied the effect of the disordered alignment of CNTs on the percolation behavior and electrical properties of these networks. They have observed that, for the different statistical distribution of angles, uniform, Gaussian or Lorentzian, alignment of nano-rods in the direction of percolation reduces critical density compared to random networks. One possible reason behind this mismatch is the fact that, although studied shapes and orientational distributions are quite similar, they are dealing with nano-rod shapes with certain diameter, while we are dealing with zero-width sticks in our simulations. Therefore, our study for non-randomly oriented nanowires provides reliable values for solely high aspect ratio nano-objects.

#### **4.5.7. Conclusion over the effect of symmetries on the percolation onset of random nanoscale networks**

Monte Carlo simulations have been used to investigate the percolation behavior of networks composed of random nano-objects with different orders of symmetry. Our algorithm, which is based on Newman and Ziff super-fast method enabled us to study a wide range of elemental shapes. Since the results for the cases of zero-width sticks, squares and circles match well with the reported values in literature, the same algorithm can be applied to find percolation threshold of more elaborated geometries. In the current study, the focus has been on the total length of material at the percolation threshold, considering that using less material density at the percolation threshold leads to more transparent and more economic devices. The obtained results confirm that arranging sticks either in the form of m-fold symmetric shapes, polygonal shapes, or finite-size grids can decrease the total length of material at the percolation threshold down to 50%. Studies on angular and length perturbation of symmetric shapes showed that it is not critical to have fully symmetric shapes to reduce percolation threshold. It was shown that possible deviations from ideal shapes as a result of the synthesis process is acceptable to keep the benefits from the decrease in the required material to reach percolation. The Moment of inertia was utilized to consider the spatial distribution of different objects and provided an effective tool to compare the compactness of objects. As intuitively expected, objects with a higher moment of inertia have a better chance of having an intersection with adjacent objects, therefore a lower percolation threshold is required. There was a general (although not yet rationalized) correlation between the increasing moment of inertia and decreasing percolation threshold. Another question which has been investigated here was the effect of

the alignment of sticks in two perpendicular directions on the percolation threshold of the corresponding networks. Our results suggest that randomly oriented sticks have a minimum percolation threshold compared to aligned networks of sticks along two perpendicular directions.

#### 4.6. Collection efficiency of MNW based TEs for solar cell applications

So far in this work, Monte Carlo simulations have been used to investigate the percolation onset of networks composed of random nano-objects with different orders of symmetry. In the following sections, the main focus will be on one of the most widely synthesized and studied shapes, metallic nanowires. An insight will be taken on one of the major applications of TEs, solar cell devices, and the possibility of using MNW based TEs in these devices will be inquired from the modeling point of view.

Conventionally wide band gap metal oxides like ITO, FTO, ZnO or AZO are widely used as TEs for solar cells.[68]–[72] However, the outstanding electro-optical properties of MNWs along with high mechanical flexibility, solution-based synthesis process and deposition techniques, promote a performance study of these TEs in solar cells. Additionally, MNWs are more transparent in wavelengths above 1500 nm,[73] making them also interesting for Infra-Red (IR) applications.[74], [75] So far there have been several works reporting integration of AgNWs networks in solar cells including Organic Solar Cells (OSCs),[76]–[79] Dye Synthesized Solar Cells (DSSCs),[80]–[82] thin film solar cells like Cadmium Telluride (CdTe) or Cu(In,Ga)(S,Se)<sub>2</sub> (CIGSSe) SCs,[83]–[86] and Polymer solar cells,[87] on glass or flexible substrates like PET. In all of these configurations, a network of MNWs along with an adjacent transparent conductive layer is utilized. This additional layer can be ZnO,[88], [89] Al:ZnO[83], [90], [90] or conducting polymers like PEDOT:PSS.[80], [91] The reason behind this configuration is that percolating NW networks are formed of very high aspect ratio elements, there are then large voids between the conducting paths. These wide openings lead to the loss of photo-generated carriers due to the recombination within the n-type or buffer layer before arriving in the conducting network. Using a composite of MNWs and transparent conductive layer enhances the effective area for charge collection then the performance of solar cells.[88], [90]

So far there have been efforts in the literature to investigate the performance of AgNW based electrodes in solar cells using Monte Carlo analysis. Kumar, [92] modelled the efficiency of solar cell devices which use CNT, AgNW or template-based TEs. Optical absorption and charge collection are two main processes which dictate the solar cell efficiency. They confirmed that to gain maximum efficiency, the density of NWs, their aspect ratio, the thickness of the active layer and *Diffusion length* of charge carriers in the active layer are the critical parameters which should be optimized.

On the same topic, the efficiency of MNW based solar cells, Langley has investigated two different approaches of simulations during his thesis.[2] The first one was based on a mathematical model for the probability of finding electrons from its point of generation derived from the work of Gonzalez-Vazquez and Bisquert. [93] The second approach was based on directly using random walk Monte Carlo simulations, to find collection efficiency maps of AgNW networks. The latter approach provided more reliable maps for collection efficiency probabilities than using mathematical approximations. However, the random walk Monte Carlo method required  $10^8$  times more time to execute.

Although the model developed by Langley did not reach a level to generate conclusive results, it was used as a basis in the current study. As a first consideration, the density of NW network, length of NWs and the *Diffusion length* of electrons in the medium seemed to be critical parameters determining the efficiency of charge carrier collection.[92] Dense networks would provide high enough electrical pathways, along with smaller openings between NWs which facilitate the collection of charge carriers. However, the optical transmittance of dense networks would be smaller because of the shadowing effect of NWs, [3] decreasing consequently the overall cell efficiency. Concerning the length of MNW, an explicit example is using very long NWs to fabricate a conductive network, the electrical resistance of such a network would be low and optical transparency would be rather high, leading to high values in Figure of Merit (*FoM*).[3] However, the collection efficiency of the photo-generated carriers of such a sparse network would be very low due to large voids between NWs.

In this work, the probability of collecting carriers has been studied as function of the network density and of the NW length for random networks of NWs. Following this, the electrical resistance and optical transmittance values for networks were calculated, based on the models that were previously developed. [3] The combination of these parameters led to a new concept for *FoM* of MNWs network which will be presented in section 4.7.4. Following this strategy could provide a guideline for a careful choice of relevant parameters of MNWs based transparent electrodes, for each solar cell configuration.

In addition to limitations caused in collection efficiency by MNWs, electron diffusion length in n-type or buffer layer adjacent to the NWs network is a crucial parameter controlling the collection probability. The electron diffusion length is commonly determined from independent measurements of the electron diffusion coefficient  $D_n$  and the electron lifetime  $\tau_n$ : [94]

$$Diffusion\ length = \sqrt{D_n \tau_n} \quad (4-12)$$

*Diffusion length* values depend on the absorbing material used in each solar cell and can vary from a few micrometres in silicon-based devices[95] to tens of nanometers in Organic solar cells.[96], [97] Table 4-4 represents a report of different solar cell technology and Power Conversion Efficiency (PCE) and *Diffusion length* for each type.

<b>Solar cell Type</b>	Organic solar cells	Perovskite	polycrystalline silicon solar cells	DSSCs	Thin film (CuZnSnSe)	CIGS	CdS/CdTe
<b><i>Diffusion length</i></b>	below 20 nm	100 nm-1 $\mu$ m	up to 400 $\mu$ m	up to few $\mu$ m	up to 2 $\mu$ m	1 to 3 $\mu$ m	0.1 to 1 $\mu$ m
<b>Power Conversion Efficiency (%)</b>	10.6%	Up to 12%	13-15%	Up to 11%	11.6%	13.2 to 15.3%	Up to 15.8%
<b>Reference</b>	[96], [97]	[98]	[95]	[99]	[100]	[101]	[102], [103]

*Table 4-4. Examples of different technologies of solar cells with the respective Diffusion length of photo-generated carriers and PCE of final devices.*

#### 4.6.1. Obtaining collection efficiency maps for MNW based solar cells

Numerical modelling of collection efficiency starts with the generation of random NW networks. As already described in section 4.3, 2D square-shaped systems consisting of nanowires randomly distributed over the delimited area were simulated and the percolation was addressed from one side of the square to the opposite side via the conducting nanowires. In the study of collection efficiency, NW networks with density values between one time up to 20 times the critical densities,  $n_c$ , were computed.

Subsequently, the collection efficiency of charge carriers as a function of the 2D space coordinates was obtained as follows. The probability  $P$  of finding an electron at a given distance from its point of generation is evaluated by:

$$P(d) = e^{\frac{-|d|}{Diffusion\ length}} \quad (4-13)$$

where  $d$  is the travelled distance and *Diffusion length* is the electron diffusion length in the medium.[93] The probability values are normalized with respect to the most adjacent points to NWs. From there, a grid was applied on the NW network with a spatial resolution equal to *Diffusion length* /2. For every grid point, the shortest distance to each nanowire belonging to the closest spanning cluster was eventually determined. The probability of collecting an electron generated at that point is equal to the sum of the probabilities of that electron to be collected by every single nanowire of the spanning cluster capped by unity. By repeating this process for every grid point, ultimately a matrix of probability values was obtained, which provides the collection efficiency map. The average value over all points of the grid is reported as the global collection efficiency for each NW network configuration.

One of the simplifications which have been made in this series of simulations was to limit the size of the system studied. Unlike the percolation threshold study, here the ratio between system size and stick length was only 10, to keep computational time reasonable since the number of grids and simulation time will increase in proportion to the square of system size. In section 4.7.2 we will show how these simplifications provide still reliable values for collection efficiency.

#### 4.6.2. Collection efficiency maps for changing network density and *Diffusion length*

Figure 4-12 represents collection efficiency maps for different NW networks. Wires indicated by red are the ones connected to the spanning cluster, while not connected wires are marked in black. Red dots indicate the points for which the chance of collecting a charge carrier is equal to one, while blue regions correspond to areas where the carriers will be recombined. The first row is the map of a random network having the critical network density  $n_c$ , while the second and third rows indicate networks having densities equal to  $2n_c$  and  $4n_c$ , respectively.

As mentioned in section 4.7, the length of NWs and *Diffusion length* of carriers are two important factors that need to be taken into account while studying collection probability. Here the results have been reported for normalized values of *Length ratio* = *NW length* / *Diffusion length* so the data can be used for any length of NWs. *Diffusion lengths* between 500 nm and 2  $\mu\text{m}$  have been investigated here. Therefore the *Length\_Ratio* has been tuned between 75, 37.5, 18.75, while the length of NWs was 37.5  $\mu\text{m}$ . Figure

4-12 allows us to identify two main directions to increase the collection efficiency: first, increasing the network density from sparse networks to more dense ones; second, decreasing the *Length ratio* values. However, there is still a need for a more quantitative guideline to assess the exact characteristics of MNW networks for guaranteeing efficient charge collection. Such a guideline is the subject of the next section where Figure 4-13.a represents the collection efficiency values for networks of densities from  $n_c$  up to  $12 n_c$  while the *Length ratio* has been changed between 7.5, 9.375, 12.5, 18.75, 37.5, 75, and 150.

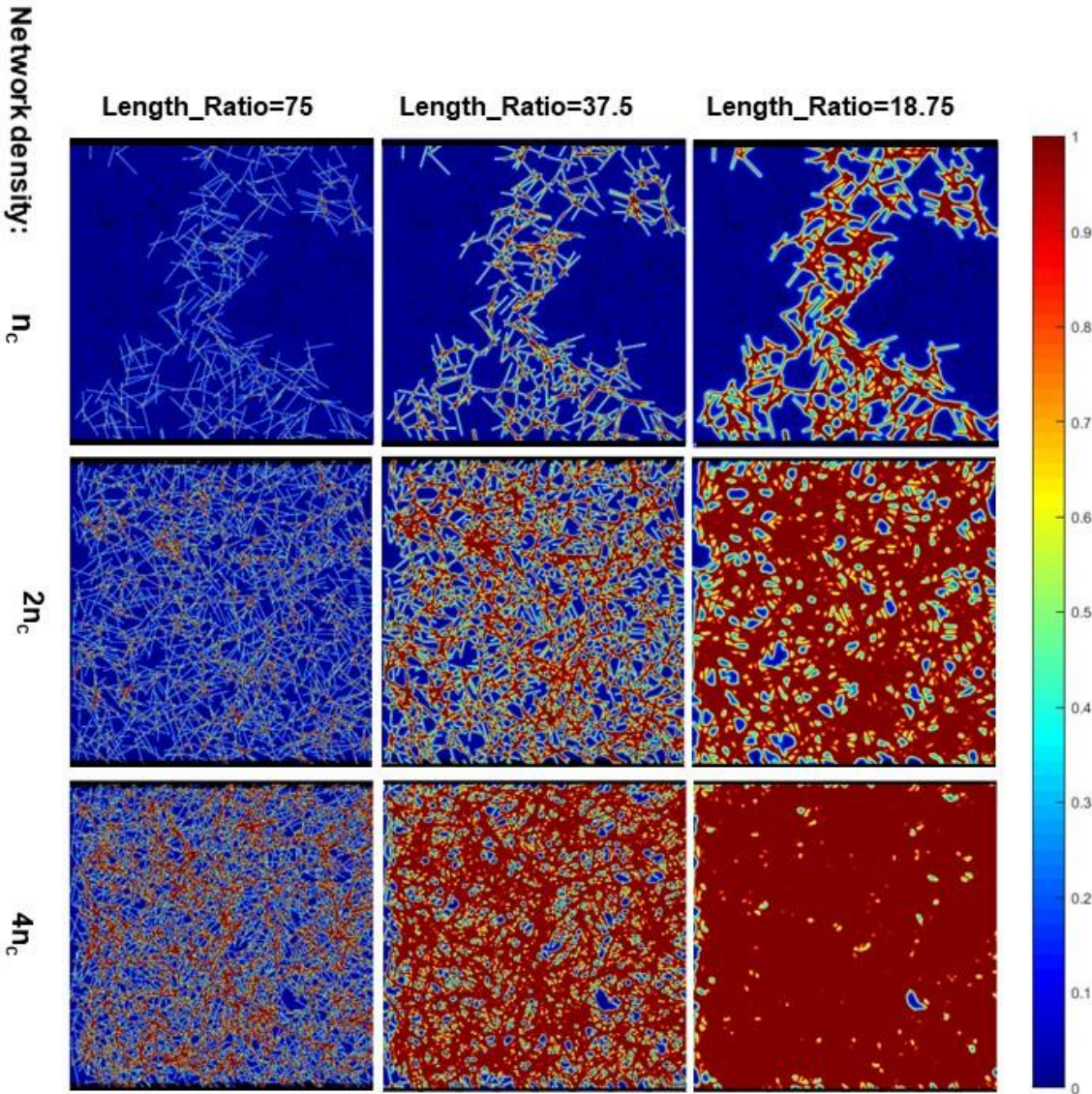


Figure 4-12. Collection efficiency map for networks of different densities and Length ratios. Network density changes from  $n_c$  to  $2n_c$  and  $4n_c$  up to down and NW length / Diffusion length is tuned between 75, 37.5 and 18.75 from left to right.



Similarly to the percolation threshold study, the number of simulations performed on each network density and *Length ratio* plays a vital role in the accuracy of the obtained results. Since for dense networks ( $n > n_c$ ), the number of sticks is already fixed (considering  $\eta=5.6374$ ) and a statistical average is made over entire grids in the networks, the deviation from one random network to another is not significant. This explains why 10 repetitions for each network parameters results in less than 0.5% standard deviation in the collection efficiency values, as shown in 4-13.a. Similar to Figure 4-12, increasing the network density results in an increase in collection efficiency ( $\eta$  in %). The lines indicate the fitting curve of an exponential function described as:

$$\eta\% = 100 \left( 1 - A \times e^{-\frac{n}{t_l n_c}} \right) \quad (4-14)$$

where  $t_l$  is the fitting factor. For very dense networks  $A \times e^{-\frac{n}{t_l n_c}}$  approaches to zero, therefore the efficiency reaches 100%. But the increase rate  $t_l$ , changes with the *Length ratio*. For the lowest *Length ratio* (7.5, corresponding to the highest *Diffusion length*)  $t_l$  is 0.27 which means the efficiency would reach its maximum quite rapidly. While for the highest *Length ratio* (150, corresponding to lowest *Diffusion length*)  $t_l$  is 10.65. This means the increase rate of  $\eta\%$  is limited. For example  $\eta\%$  reaches only 27.65% at  $4n_c$  which represents quite dense networks. One could define a threshold value for  $\eta\%$  in the electrode to evaluate if MNWs based electrode is proper for the solar cell or not. Figure 4-13.a will guide if any length and density of NWs are suitable for integration in the device according to such threshold value. For example, let's consider the case of ultra-long MNWs (which could have lengths up to 100  $\mu\text{m}$ , [104], [105]. *Diffusion length* in silicon solar cells could be up to 100  $\mu\text{m}$ , [95] therefore *Length ratio* would be around unit. This value is even smaller than 7.5, which is the lowest studied *Length ratio* in Figure 4-13.a. Therefore, one could expect that a network density of  $2n_c$  would already provide high enough efficiency for the collection of charge carriers. Another example could be Organic solar cells where the *Diffusion length* is limited to a few tens of nanometers. [96], [97] The *Length ratio* would be around 20,000 for the same length of NWs (100  $\mu\text{m}$ ). Such a *Length ratio* is way higher than the highest studied value in this part (150). Considering Figure 4-13.a, one could expect that ultra-long MNWs would provide very little carrier collection and would not constitute a suitable candidate for integration in Organic solar cells.

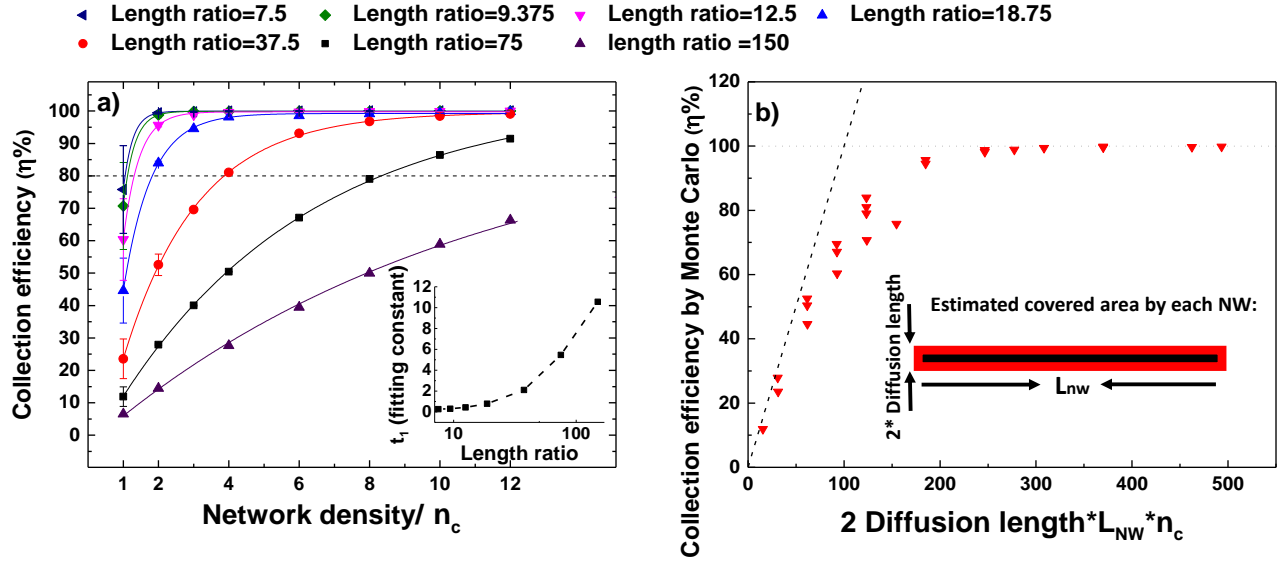


Figure 4-13 a) Collection efficiency versus normalized network density for networks from  $n_c$  to  $12 n_c$  and Length ratios of 7.5, 9.375, 12.5, 18.75, 37.5, 75 and 150. b) Collection efficiency based on Monte Carlo simulations compared to the estimated coverage ratio. The dashed line indicates the slope of 1. (Dots closer to this line, indicate better accuracy of this estimation approach.)

#### 4.6.3. Estimation of collection efficiency based on the sum of areas method

Since simulations to obtain collection efficiency maps such as the ones shown in Figure 4-12 are time-consuming and limited in studied system size and *Diffusion length*, one might search for other approaches to estimate the expected collection ratio values. A simple and straightforward approach to study the collection efficiency would be to estimate an approximate area around each NW which we assume all the photo-generated carriers can be collected. Let's consider the Gonzalez-Vazquez and Bisquet model [93] and the integral of exponential decay from zero to infinite distance:

$$\int_0^{\infty} e^{\frac{-x}{\text{Diffusion length}}} dx = \text{Diffusion length} \quad (4-15)$$

Such an integral provides a constant, *Diffusion length*. Therefore, one can define an area corresponding to the width of  $2 \times \text{Diffusion length}$  around each NW and consider that as a covered area for every single stick. Then by adding up the sum of these areas and dividing the sum values to the overall area of the system, one could obtain the estimated average area covered by NW network. In a first consideration, we expect that this approach would lead to an overestimation of collection probability since this method does not consider the intersection area around the junctions. At the beginning of Figure 4-13.b, for low  $n_c$  values, the calculated values are quite close to simulated data. The reason behind is that for low  $n_c$  values, the intersection areas are rather limited, therefore do not imply a big impact on the estimated

average area covered by NW network. While as the network density and overall number of NWs increases, the estimated values surpass 100%. Therefore, this simplified technique cannot provide reliable values for estimation of collection efficiency for large  $n_c$  values.

#### 4.6.4. A new definition for the Figure of Merit (*FoM*)

As discussed in section 1.3.3 of Chapter 1, Haacke's Figure of Merit is a widely used parameter to evaluate the performance of TEs. However, this parameter only considers electrical resistance and optical transparency of transparent electrodes and is expressed by the following relation:

$$Haacke's\ FoM = \frac{T^{10}}{R_{sh}} \quad (4-16)$$

In solar cell devices, the efficiency of collecting photo-generated carriers is another critical factor that affects the performance of the final device. Figure 4-14.a shows quite a good agreement with experimental results for AgNWs (Average diameter 117 nm and average length 42.5  $\mu$ m) with the values predicted by Equation 1-7, 1-8.a and 1-8.b, obtained by Lagrange et al.[3]

Since we have developed a model to estimate the collection efficiency of charge carrier for MNW networks, as well as theoretical tools to predict electrical and optical properties of such networks, one might use these models to propose a new definition for *FoM* by multiplying *FoM* values by  $\eta\%$ ,

$$modified\_FoM = Haacke's\_FoM \times \eta\% = \frac{T^{10}}{R_{sh}} \times \eta\% \quad (4-17)$$

Figure 4-14.b represents conventional and *modified\_FoM*, versus *amd* values from  $amd_c$  to  $20\ amd_c$ . As we see around  $7amd_c$ , the Haacke's *FoM* value is maximized, meaning electro-optical properties are in their best trade-off. Then for different *Length ratios* the collection efficiency values are simulated and *modified\_FoM* values are plotted. As the *Length ratio* increases, slight differences between *modified\_FoM* plots compared to Haacke's *FoM* are observed. When the *Length ratio* is 7.5 there is almost no change in *FoM* values, while for *Length ratio* of 150 (which represents smaller *Diffusion length* for unique *NW length*), *modified\_FoM* values show two important changes: first, since the  $\eta\%$  values are limited especially in low-density networks, the maximum of *modified\_FoM* would decrease compared to its original values. Second, the density where the maximum of *FoM* occurs would shift slightly to the right, from  $7\ amd_c$  for Haacke's *FoM* to  $9\ amd_c$  for *modified\_FoM*. The reason behind this change is that for small *Diffusion lengths* as we discussed in 4.7, high-density MNWs networks are required to reach acceptable efficiency in the collection.

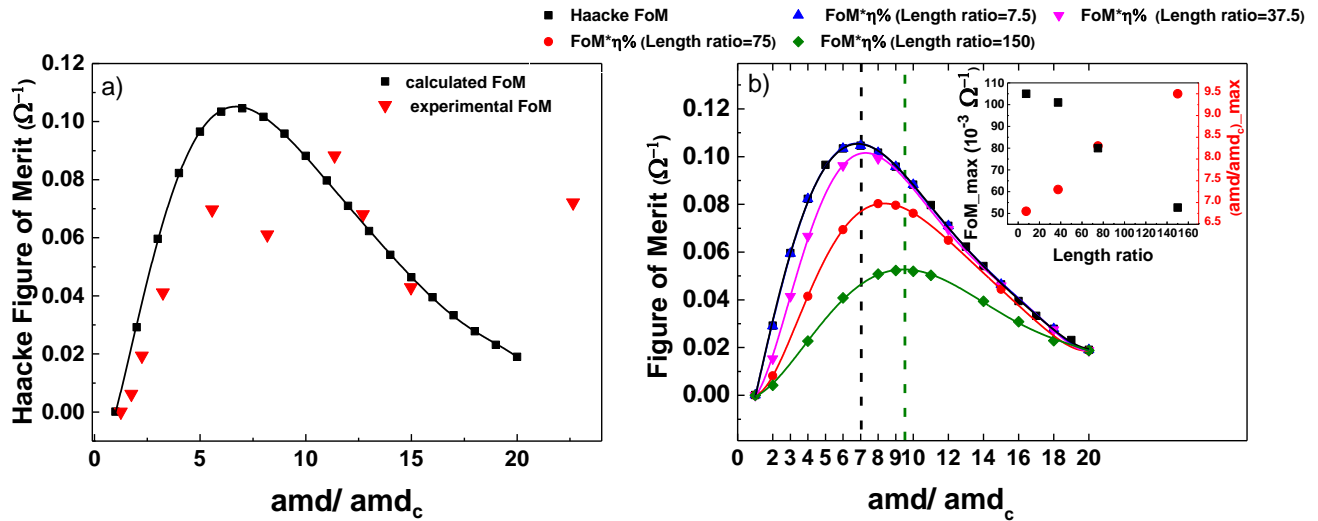


Figure 4-14 a) FoM value versus normalized amd for NWs of average length  $37.5 \mu\text{m}$  and diameter of  $117 \text{ nm}$ . Reproduced from reference [3]. b) Haack's figure of Merit (black) and modified\_FoM values for networks from  $amd_c$  to  $20 amd_c$  where Diffusion length is changed from  $5, 1, 0.5$  and  $0.25 \mu\text{m}$  associated respectively to Length ratio of  $7.5, 37.5, 75$  and  $150$ . (for NWs of  $37.5 \mu\text{m}$  length)

#### 4.6.5. Conclusion over collection efficiency of MNW based TEs in solar cells applications

In this part, we have presented a Monte Carlo based modeling approach to assess the collection efficiency of solar cells based on random MNWs. The *Diffusion length* of photo-generated carriers, the density of the MNW network and the length of MNWs were the main parameters that have been considered to affect collection efficiency. As expected intuitively, increasing the *Diffusion length* and the network density leads to higher chances of collection for generated charge carriers before recombination. Decreasing the *NW length*, on the other hand, leads to the formation of smaller voids between NWs in the network, and increases collection efficiency. However, using shorter NWs or higher density in the MNW network means a higher loss in the optical transparency due to the shadowing effect, therefore a trade-off should be considered. We suggested a modified value for *FoM* which includes, electrical resistance, optical transmittance and collection efficiency of MNW based TEs. This *modified\_FoM* indicates for each type of solar cells and *NW length*, what would be the ideal network density to optimize the performance of electrodes.

## References:

- [1] D. P. Langley, M. Lagrange, N. D. Nguyen, and D. Bellet, “Percolation in networks of 1-dimensional objects: comparison between Monte Carlo simulations and experimental observations,” *Nanoscale Horizons*, vol. 3, no. 5, pp. 545–550, 2018, doi: 10.1039/C8NH00066B.
- [2] D. Langley, “Silver nanowire networks: Effects of percolation and thermal annealing on physical properties,” PhD thesis, University of Grenoble Alpes (France), University of Liège (Belgium), 2014.
- [3] M. Lagrange, D. P. Langley, G. Giusti, C. Jiménez, Y. Bréchet, and D. Bellet, “Optimization of Silver Nanowire-Based Transparent Electrodes: Effects of Density, Size and Thermal Annealing,” *Nanoscale*, vol. 7, no. 41, pp. 17410–17423, Oct. 2015, doi: 10.1039/C5NR04084A.
- [4] “Applications Of Percolation Theory - M Sahini, M Sahimi - CRC Press. ISBN 978-0-203-22153-2.” .
- [5] M. F. Sykes and M. Glen, “Percolation processes in two dimensions. I. Low-density series expansions,” *J. Phys. A: Math. Gen.*, vol. 9, no. 1, p. 87, 1976, doi: 10.1088/0305-4470/9/1/014.
- [6] S. R. Broadbent and J. M. Hammersley, “Percolation processes. 1,” *Crystals and mazes. Mathematical Proceedings of the Cambridge Philosophical Society*, vol. 53, no. 3, pp. 629–641, Jul. 1957, doi: doi:10.1017/S0305004100032680.
- [7] H. E. Unalan *et al.*, “Zinc oxide nanowire networks for macroelectronic devices,” *Applied Physics Letters*, vol. 94, no. 16, p. 163501, Apr. 2009, doi: 10.1063/1.3120561.
- [8] R. M. Mutiso, M. C. Sherrott, A. R. Rathmell, B. J. Wiley, and K. I. Winey, “Integrating Simulations and Experiments To Predict Sheet Resistance and Optical Transmittance in Nanowire Films for Transparent Conductors,” *ACS Nano*, vol. 7, no. 9, pp. 7654–7663, Sep. 2013, doi: 10.1021/nm403324t.
- [9] Y. Jin *et al.*, “Long-term stable silver nanowire transparent composite as bottom electrode for perovskite solar cells,” *Nano Res.*, vol. 11, no. 4, pp. 1998–2011, Apr. 2018, doi: 10.1007/s12274-017-1816-8.
- [10] R. Zhang and M. Engholm, “Recent Progress on the Fabrication and Properties of Silver Nanowire-Based Transparent Electrodes,” *Nanomaterials*, vol. 8, no. 8, p. 628, Aug. 2018, doi: 10.3390/nano8080628.
- [11] S. De, P. J. King, P. E. Lyons, U. Khan, and J. N. Coleman, “Size Effects and the Problem with Percolation in Nanostructured Transparent Conductors,” *ACS Nano*, vol. 4, no. 12, pp. 7064–7072, 2010, doi: 10.1021/nm1025803.
- [12] I. Jeon *et al.*, “Polymeric acid-doped transparent carbon nanotube electrodes for organic solar cells with the longest doping durability,” *J. Mater. Chem. A*, vol. 6, no. 30, pp. 14553–14559, Jul. 2018, doi: 10.1039/C8TA03383H.

- [13] B. Che, D. Zhou, H. Li, C. He, E. Liu, and X. Lu, “A highly bendable transparent electrode for organic electrochromic devices,” *Organic Electronics*, vol. 66, pp. 86–93, Mar. 2019, doi: 10.1016/j.orgel.2018.12.015.
- [14] B. V. R. S. Subramanyam *et al.*, “Improved stability and performance of organic photovoltaic cells by application of carbon nanostructures and PEDOT:PSS composites as additional transparent electrodes,” *Solar Energy*, vol. 186, pp. 146–155, Jul. 2019, doi: 10.1016/j.solener.2019.04.097.
- [15] I. Jeon *et al.*, “High-Performance Solution-Processed Double-Walled Carbon Nanotube Transparent Electrode for Perovskite Solar Cells,” *Adv. Energy Mater.*, vol. 9, no. 27, p. 1901204, Jul. 2019, doi: 10.1002/aenm.201901204.
- [16] Q. Huang and Y. Zhu, “Printing Conductive Nanomaterials for Flexible and Stretchable Electronics: A Review of Materials, Processes, and Applications,” *Adv. Mater. Technol.*, vol. 4, no. 5, p. 1800546, May 2019, doi: 10.1002/admt.201800546.
- [17] X. Ni, C. Hui, N. Su, W. Jiang, and F. Liu, “Monte Carlo simulations of electrical percolation in multicomponent thin films with nanofillers,” *Nanotechnology*, vol. 29, no. 7, p. 075401, Feb. 2018, doi: 10.1088/1361-6528/aaa0be.
- [18] Y. Yu. Tarasevich and A. V. Eserkepov, “Percolation of sticks: Effect of stick alignment and length dispersity,” *Phys. Rev. E*, vol. 98, no. 6, p. 062142, Dec. 2018, doi: 10.1103/PhysRevE.98.062142.
- [19] Y.-B. Yi and A. Sastry, “Analytical approximation of the two-dimensional percolation threshold for fields of overlapping ellipses,” *Physical Review E*, vol. 66, no. 6, Dec. 2002, doi: 10.1103/PhysRevE.66.066130.
- [20] S. M. Bergin, Y.-H. Chen, A. R. Rathmell, P. Charbonneau, Z.-Y. Li, and B. J. Wiley, “The effect of nanowire length and diameter on the properties of transparent, conducting nanowire films,” *Nanoscale*, vol. 4, no. 6, p. 1996, 2012, doi: 10.1039/c2nr30126a.
- [21] R. M. Mutiso and K. I. Winey, “Electrical percolation in quasi-two-dimensional metal nanowire networks for transparent conductors,” *Physical Review E*, vol. 88, no. 3, Sep. 2013, doi: 10.1103/PhysRevE.88.032134.
- [22] J. Hicks, J. Li, C. Ying, and A. Ural, “Effect of nanowire curviness on the percolation resistivity of transparent, conductive metal nanowire networks,” *Journal of Applied Physics*, vol. 123, no. 20, p. 204309, May 2018, doi: 10.1063/1.5029896.
- [23] L.-P. Simoneau, J. Villeneuve, C. M. Aguirre, R. Martel, P. Desjardins, and A. Rochefort, “Influence of statistical distributions on the electrical properties of disordered and aligned carbon nanotube networks,” *Journal of Applied Physics*, vol. 114, no. 11, p. 114312, Sep. 2013, doi: 10.1063/1.4821885.
- [24] F. Du, J. E. Fischer, and K. I. Winey, “Effect of nanotube alignment on percolation conductivity in carbon nanotube/polymer composites,” *Physical Review B*, vol. 72, no. 12, Sep. 2005, doi: 10.1103/PhysRevB.72.121404.
- [25] W. Bauhofer and J. Z. Kovacs, “A review and analysis of electrical percolation in carbon nanotube polymer composites,” *Compos. Sci. Technol.*, vol. 69, no. 10, pp. 1486–1498, Aug. 2009, doi: 10.1016/j.compscitech.2008.06.018.

- [26] S. De *et al.*, “Silver Nanowire Networks as Flexible, Transparent, Conducting Films: Extremely High DC to Optical Conductivity Ratios,” *ACS Nano*, vol. 3, no. 7, pp. 1767–1774, 2009, doi: 10.1021/nn900348c.
- [27] T. K. Sau and C. J. Murphy, “Room Temperature, High-Yield Synthesis of Multiple Shapes of Gold Nanoparticles in Aqueous Solution,” *Journal of the American Chemical Society*, vol. 126, no. 28, pp. 8648–8649, Jul. 2004, doi: 10.1021/ja047846d.
- [28] E. Hao, R. C. Bailey, G. C. Schatz, J. T. Hupp, and S. Li, “Synthesis and Optical Properties of ‘Branched’ Gold Nanocrystals,” *Nano Letters*, vol. 4, no. 2, pp. 327–330, Feb. 2004, doi: 10.1021/nl0351542.
- [29] A. Garcia-Leis, I. Rivera-Arreba, and S. Sanchez-Cortes, “Morphological tuning of plasmonic silver nanostars by controlling the nanoparticle growth mechanism: Application in the SERS detection of the amyloid marker Congo Red,” *Colloids and Surfaces A: Physicochemical and Engineering Aspects*, vol. 535, pp. 49–60, Dec. 2017, doi: 10.1016/j.colsurfa.2017.09.013.
- [30] Y. Sun and Y. Xia, “Large-Scale Synthesis of Uniform Silver Nanowires Through a Soft, Self-Seeding, Polyol Process,” *Advanced Materials*, vol. 14, no. 11, pp. 833–837, 2002, doi: 10.1002/1521-4095(20020605)14:11<833::AID-ADMA833>3.0.CO;2-K.
- [31] J. Fang *et al.*, “Silver nanowires growth via branch fragmentation of electrochemically grown silver dendrites,” *Chem. Commun.*, no. 9, pp. 1130–1132, Feb. 2009, doi: 10.1039/B819003H.
- [32] A. Madeira, “Amélioration des performances d’électrodes conductrices et transparentes en modifiant le design de nanofils d’argent,” PhD thesis, university of Bordeaux, 2018.
- [33] I. Seshadri, G. L. Esquenazi, T. Cardinal, T. Borca-Tasciuc, and G. Ramanath, “Microwave synthesis of branched silver nanowires and their use as fillers for high thermal conductivity polymer composites,” *Nanotechnology*, vol. 27, no. 17, p. 175601, Mar. 2016, doi: 10.1088/0957-4484/27/17/175601.
- [34] P. Pallavicini *et al.*, “Triton X-100 for three-plasmon gold nanostars with two photothermally active NIR (near IR) and SWIR (short-wavelength IR) channels,” *Chem. Commun.*, vol. 49, no. 56, pp. 6265–6267, Jun. 2013, doi: 10.1039/C3CC42999G.
- [35] S. Mertens and C. Moore, “Series expansion of the percolation threshold on hypercubic lattices,” *J. Phys. A: Math. Theor.*, vol. 51, no. 47, p. 475001, Oct. 2018, doi: 10.1088/1751-8121/aae65c.
- [36] M. E. Fisher, “Critical Probabilities for Cluster Size and Percolation Problems,” *Journal of Mathematical Physics*, vol. 2, no. 4, pp. 620–627, Jul. 1961, doi: 10.1063/1.1703746.
- [37] M. F. Sykes and J. W. Essam, “Critical Percolation Probabilities by Series Methods,” *Phys. Rev.*, vol. 133, no. 1A, pp. A310–A315, Jan. 1964, doi: 10.1103/PhysRev.133.A310.
- [38] A. Drory, “Exact solution of a one-dimensional continuum percolation model,” *Physical Review E*, vol. 55, no. 4, pp. 3878–3885, Apr. 1997, doi: 10.1103/PhysRevE.55.3878.
- [39] J. N. Coleman *et al.*, “Percolation-dominated conductivity in a conjugated-polymer-carbon-nanotube composite,” *Physical Review B*, vol. 58, no. 12, p. R7492, 1998.

- [40] R. M. Ziff, “Spanning probability in 2D percolation,” *Phys. Rev. Lett.*, vol. 69, no. 18, pp. 2670–2673, Nov. 1992, doi: 10.1103/PhysRevLett.69.2670.
- [41] P. J. Reynolds, H. E. Stanley, and W. Klein, “Percolation by position-space renormalisation group with large cells,” *J. Phys. A: Math. Gen.*, vol. 11, no. 8, p. L199, Aug. 1978, doi: 10.1088/0305-4470/11/8/006.
- [42] M. E. J. Newman and R. M. Ziff, “Efficient Monte Carlo Algorithm and High-Precision Results for Percolation,” *Phys. Rev. Lett.*, vol. 85, no. 19, pp. 4104–4107, Nov. 2000, doi: 10.1103/PhysRevLett.85.4104.
- [43] M. E. J. Newman and R. M. Ziff, “Fast Monte Carlo algorithm for site or bond percolation,” *Phys. Rev. E*, vol. 64, no. 1, pp. 016706–016706–16, Jun. 2001, doi: 10.1103/PhysRevE.64.016706.
- [44] I. Balberg and N. Binenbaum, “Computer Study of the Percolation Threshold in a Two-Dimensional Anisotropic System of Conducting Sticks,” *Phys. Rev. B*, vol. 28, no. 7, pp. 3799–3812, Oct. 1983, doi: 10.1103/PhysRevB.28.3799.
- [45] G. E. Pike and C. H. Seager, “Percolation and conductivity: A computer study. I,” *Phys. Rev. B*, vol. 10, no. 4, pp. 1421–1434, 1974, doi: 10.1103/PhysRevB.10.1421.
- [46] J. Li and S.-L. Zhang, “Finite-size scaling in stick percolation,” *Phys. Rev. E*, vol. 80, no. 4, pp. 040104–040104–4, Oct. 2009, doi: 10.1103/PhysRevE.80.040104.
- [47] M. E. J. Newman and D. J. Watts, “Scaling and percolation in the small-world network model,” *Phys. Rev. E*, vol. 60, no. 6, pp. 7332–7342, Dec. 1999, doi: 10.1103/PhysRevE.60.7332.
- [48] P. J. Reynolds, H. E. Stanley, and W. Klein, “Large-cell Monte Carlo renormalization group for percolation,” *Phys. Rev. B*, vol. 21, no. 3, pp. 1223–1245, Feb. 1980, doi: 10.1103/PhysRevB.21.1223.
- [49] S. Mertens and C. Moore, “Continuum Percolation Thresholds in Two Dimensions,” *Physical Review E*, vol. 86, no. 6, Dec. 2012, doi: 10.1103/PhysRevE.86.061109.
- [50] C. H. Seager and G. E. Pike, “Percolation and conductivity: A computer study. II,” *Phys. Rev. B*, vol. 10, no. 4, pp. 1435–1446, 1974, doi: 10.1103/PhysRevB.10.1435.
- [51] M. Žeželj, I. Stanković, and A. Belić, “Finite-size scaling in asymmetric systems of percolating sticks,” *Phys. Rev. E*, vol. 85, no. 2, pp. 021101–021106, Feb. 2012, doi: 10.1103/PhysRevE.85.021101.
- [52] D. R. Baker, G. Paul, S. Sreenivasan, and H. E. Stanley, “Continuum percolation threshold for interpenetrating squares and cubes,” *Phys. Rev. E*, vol. 66, no. 4, p. 046136, Oct. 2002, doi: 10.1103/PhysRevE.66.046136.
- [53] I. Balberg, C. H. Anderson, S. Alexander, and N. Wagner, “Excluded volume and its relation to the onset of percolation,” *Phys. Rev. B*, vol. 30, no. 7, pp. 3933–3943, Oct. 1984, doi: 10.1103/PhysRevB.30.3933.
- [54] Y. Sun, B. Gates, B. Mayers, and Y. Xia, “Crystalline Silver Nanowires by Soft Solution Processing,” *Nano Lett.*, vol. 2, no. 2, pp. 165–168, Feb. 2002, doi: 10.1021/nl010093y.



- [55] Y. Sun, B. Mayers, T. Herricks, and Y. Xia, "Polyol Synthesis of Uniform Silver Nanowires: A Plausible Growth Mechanism and the Supporting Evidence," *Nano Lett.*, vol. 3, no. 7, pp. 955–960, Jul. 2003, doi: 10.1021/nl034312m.
- [56] A. S. De Silva Indrasekara, S. F. Johnson, R. A. Odion, and T. Vo-Dinh, "Manipulation of the Geometry and Modulation of the Optical Response of Surfactant-Free Gold Nanostars: A Systematic Bottom-Up Synthesis," *ACS Omega*, vol. 3, no. 2, pp. 2202–2210, Feb. 2018, doi: 10.1021/acsomega.7b01700.
- [57] J. Zhu, X.-H. Chen, J.-J. Li, and J.-W. Zhao, "The synthesis of Ag-coated tetrapod gold nanostars and the improvement of surface-enhanced Raman scattering," *Spectrochimica Acta Part A: Molecular and Biomolecular Spectroscopy*, vol. 211, pp. 154–165, Mar. 2019, doi: 10.1016/j.saa.2018.12.001.
- [58] M. Safdari and M. S. Al-Haik, "Synergistic electrical and thermal transport properties of hybrid polymeric nanocomposites based on carbon nanotubes and graphite nanoplatelets," *Carbon*, vol. 64, pp. 111–121, Nov. 2013, doi: 10.1016/j.carbon.2013.07.042.
- [59] Y. Sun, H.-D. Bao, Z.-X. Guo, and J. Yu, "Modeling of the Electrical Percolation of Mixed Carbon Fillers in Polymer-Based Composites," *Macromolecules*, vol. 42, no. 1, pp. 459–463, Jan. 2009, doi: 10.1021/ma8023188.
- [60] J. Hicks, A. Behnam, and A. Ural, "Resistivity in percolation networks of one-dimensional elements with a length distribution," *Physical Review E*, vol. 79, no. 1, Jan. 2009, doi: 10.1103/PhysRevE.79.012102.
- [61] Y. Y. Tarasevich, I. V. Vodolazskaya, A. V. Eserkepov, V. A. Goltseva, P. G. Selin, and N. I. Lebovka, "Simulation of the electrical conductivity of two-dimensional films with aligned rod-like conductive fillers: effect of the filler length dispersity," *Journal of Applied Physics*, vol. 124, no. 14, p. 145106, Oct. 2018, doi: 10.1063/1.5051090.
- [62] S. He, X. Xu, X. Qiu, Y. He, and C. Zhou, "Conductivity of two-dimensional disordered nanowire networks: Dependence on length-ratio of conducting paths to all nanowires," *Journal of Applied Physics*, vol. 124, no. 5, p. 054302, Aug. 2018, doi: 10.1063/1.5045176.
- [63] D.-J. Kim, H.-I. Shin, E.-H. Ko, K.-H. Kim, T.-W. Kim, and H.-K. Kim, "Roll-to-roll slot-die coating of 400 mm wide, flexible, transparent Ag nanowire films for flexible touch screen panels," *Scientific Reports*, vol. 6, no. 1, Dec. 2016, doi: 10.1038/srep34322.
- [64] E. Jung, C. Kim, M. Kim, H. Chae, J. H. Cho, and S. M. Cho, "Roll-to-roll preparation of silver-nanowire transparent electrode and its application to large-area organic light-emitting diodes," *Organic Electronics*, vol. 41, pp. 190–197, Feb. 2017, doi: 10.1016/j.orgel.2016.11.003.
- [65] A. K. Bentley, J. S. Trethewey, A. B. Ellis, and W. C. Crone, "Magnetic Manipulation of Copper–Tin Nanowires Capped with Nickel Ends," *Nano Lett.*, vol. 4, no. 3, pp. 487–490, Mar. 2004, doi: 10.1021/nl035086j.
- [66] C. M. Hangarter and N. V. Myung, "Magnetic Alignment of Nanowires," *Chem. Mater.*, vol. 17, no. 6, pp. 1320–1324, Mar. 2005, doi: 10.1021/cm047955r.

- [67] H. Hu, S. Wang, S. Wang, G. Liu, T. Cao, and Y. Long, "Aligned Silver Nanowires Enabled Highly Stretchable and Transparent Electrodes with Unusual Conductive Property," *Advanced Functional Materials*, p. 1902922, Jun. 2019, doi: 10.1002/adfm.201902922.
- [68] K. Ellmer, "Past achievements and future challenges in the development of optically transparent electrodes," *Nature Photonics*, vol. 6, no. 12, pp. 809–817, 2012, doi: 10.1038/nphoton.2012.282.
- [69] T. Minami, "Transparent conducting oxide semiconductors for transparent electrodes," *Semicond. Sci. Technol.*, vol. 20, no. 4, p. S35, Apr. 2005, doi: 10.1088/0268-1242/20/4/004.
- [70] R. G. Gordon, "Criteria for choosing transparent conductors," *MRS Bulletin*, vol. 25, no. 08, pp. 52–57, Aug. 2000, doi: 10.1557/mrs2000.151.
- [71] E. Fortunato, D. Ginley, H. Hosono, and D. C. Paine, "Transparent conducting oxides for photovoltaics," *MRS Bulletin*, vol. 32, no. 03, pp. 242–247, 2007, doi: 10.1557/mrs2007.29.
- [72] A. Klein, "Transparent Conducting Oxides: Electronic Structure–Property Relationship from Photoelectron Spectroscopy with in situ Sample Preparation," *J. Am. Ceram. Soc.*, vol. 96, no. 2, pp. 331–345, Feb. 2013, doi: 10.1111/jace.12143.
- [73] D. Bellet *et al.*, "Transparent Electrodes Based on Silver Nanowire Networks: From Physical Considerations towards Device Integration," *Materials*, vol. 10, no. 6, p. 570, May 2017, doi: 10.3390/ma10060570.
- [74] M. C. Larciprete, M. Centini, R. L. Voti, M. Bertolotti, and C. Sibilia, "Metallic oriented nanowires films for infrared radiation manipulation," *Appl. Phys. A*, vol. 122, no. 4, p. 343, Mar. 2016, doi: 10.1007/s00339-016-9901-5.
- [75] J. Graubmann *et al.*, "Silver nanowires: a new nanomaterial with advances for electrical, optical and IR systems," in *Electro-Optical and Infrared Systems: Technology and Applications XVI*, Oct. 2019, vol. 11159, p. 1115903, doi: 10.1117/12.2532245.
- [76] M. Song *et al.*, "Highly Efficient and Bendable Organic Solar Cells with Solution-Processed Silver Nanowire Electrodes," *Adv. Funct. Mater.*, vol. 23, no. 34, pp. 4177–4184, Sep. 2013, doi: 10.1002/adfm.201202646.
- [77] J.-W. Lim, D.-Y. Cho, Jihoon-Kim, S.-I. Na, and H.-K. Kim, "Simple brush-painting of flexible and transparent Ag nanowire network electrodes as an alternative ITO anode for cost-efficient flexible organic solar cells," *Solar Energy Materials and Solar Cells*, vol. 107, pp. 348–354, Dec. 2012, doi: 10.1016/j.solmat.2012.07.012.
- [78] G. Zeng, J. Zhang, X. Chen, H. Gu, Y. Li, and Y. Li, "Breaking 12% efficiency in flexible organic solar cells by using a composite electrode," *Sci. China Chem.*, vol. 62, no. 7, pp. 851–858, Jul. 2019, doi: 10.1007/s11426-018-9430-8.
- [79] T. Lei *et al.*, "Bendable and foldable flexible organic solar cells based on Ag nanowire films with 10.30% efficiency," *J. Mater. Chem. A*, vol. 7, no. 8, pp. 3737–3744, Feb. 2019, doi: 10.1039/C8TA11293B.
- [80] G. Y. Margulis *et al.*, "Spray Deposition of Silver Nanowire Electrodes for Semitransparent Solid-State Dye-Sensitized Solar Cells," *Adv. Energy Mater.*, vol. 3, no. 12, pp. 1657–1663, Dec. 2013, doi: 10.1002/aenm.201300660.

- [81] M. G. C. M. Kumari, C. S. Perera, B. S. Dassanayake, M. A. K. L. Dissanayake, and G. K. R. Senadeera, "Highly efficient plasmonic dye-sensitized solar cells with silver nanowires and TiO<sub>2</sub> nanofibres incorporated multi-layered photoanode," *Electrochimica Acta*, vol. 298, pp. 330–338, Mar. 2019, doi: 10.1016/j.electacta.2018.12.079.
- [82] Q. Nguyen and J. W. Kwon, "Silver nanowire-based transparent electrode as FTO replacement for dye-sensitized solar cell," *Int Nano Lett*, vol. 9, no. 1, pp. 83–87, Mar. 2019, doi: 10.1007/s40089-018-0258-y.
- [83] A. Kim, Y. Won, K. Woo, S. Jeong, and J. Moon, "All-Solution-Processed Indium-Free Transparent Composite Electrodes based on Ag Nanowire and Metal Oxide for Thin-Film Solar Cells," *Adv. Funct. Mater.*, vol. 24, no. 17, pp. 2462–2471, May 2014, doi: 10.1002/adfm.201303518.
- [84] S. Lee *et al.*, "Determination of the lateral collection length of charge carriers for silver-nanowire-electrode-based Cu(In,Ga)Se<sub>2</sub> thin-film solar cells," *Solar Energy*, vol. 180, pp. 519–523, Mar. 2019, doi: 10.1016/j.solener.2019.01.059.
- [85] S. Lee *et al.*, "Fabrication of Robust Nanoscale Contact between a Silver Nanowire Electrode and CdS Buffer Layer in Cu(In,Ga)Se<sub>2</sub> Thin-film Solar Cells," *JoVE (Journal of Visualized Experiments)*, no. 149, p. e59909, Jul. 2019, doi: 10.3791/59909.
- [86] S. Lee *et al.*, "Electrodeposited Silver Nanowire Transparent Conducting Electrodes for Thin-Film Solar Cells," *ACS Appl. Mater. Interfaces*, vol. 12, no. 5, pp. 6169–6175, Feb. 2020, doi: 10.1021/acsami.9b17168.
- [87] J.-S. Yu *et al.*, "Silver front electrode grids for ITO-free all printed polymer solar cells with embedded and raised topographies, prepared by thermal imprint, flexographic and inkjet roll-to-roll processes," *Nanoscale*, vol. 4, no. 19, pp. 6032–6040, Sep. 2012, doi: 10.1039/C2NR31508D.
- [88] A. Kim, Y. Won, K. Woo, C.-H. Kim, and J. Moon, "Highly Transparent Low Resistance ZnO/Ag Nanowire/ZnO Composite Electrode for Thin Film Solar Cells," *ACS Nano*, vol. 7, no. 2, pp. 1081–1091, Feb. 2013, doi: 10.1021/nn305491x.
- [89] K. Han *et al.*, "Fully solution processed semi-transparent perovskite solar cells with spray-coated silver nanowires/ZnO composite top electrode," *Solar Energy Materials and Solar Cells*, vol. 185, pp. 399–405, Oct. 2018, doi: 10.1016/j.solmat.2018.05.048.
- [90] R. Liu *et al.*, "Solution-processed composite electrodes composed of silver nanowires and aluminum-doped zinc oxide nanoparticles for thin-film solar cells applications," *Solar Energy Materials and Solar Cells*, vol. 174, pp. 584–592, Jan. 2018, doi: 10.1016/j.solmat.2017.09.042.
- [91] M. N. Gueye *et al.*, "Structure and Dopant Engineering in PEDOT Thin Films: Practical Tools for a Dramatic Conductivity Enhancement," *Chemistry of Materials*, vol. 28, no. 10, pp. 3462–3468, May 2016, doi: 10.1021/acs.chemmater.6b01035.
- [92] A. Kumar, "Predicting efficiency of solar cells based on transparent conducting electrodes," *Journal of Applied Physics*, vol. , no. , pp.014502.1-7. 2017-01-03 121AD, doi: 10.1063/1.4973117.
- [93] J. P. Gonzalez-Vazquez, J. A. Anta, and J. Bisquert, "Determination of the electron diffusion length in dye-sensitized solar cells by random walk simulation: Compensation effects and voltage

- dependence,” *The Journal of Physical Chemistry C*, vol. 114, no. 18, pp. 8552–8558, 2010, doi: 10.1021/jp100874e.
- [94] J. Bisquert, “Theory of the Impedance of Electron Diffusion and Recombination in a Thin Layer,” *J. Phys. Chem. B*, vol. 106, no. 2, pp. 325–333, Jan. 2002, doi: 10.1021/jp011941g.
- [95] T. Fuyuki, H. Kondo, T. Yamazaki, Y. Takahashi, and Y. Uraoka, “Photographic surveying of minority carrier diffusion length in polycrystalline silicon solar cells by electroluminescence,” *Appl. Phys. Lett.*, vol. 86, no. 26, p. 262108, Jun. 2005, doi: 10.1063/1.1978979.
- [96] H. Hoppe and N. S. Sariciftci, “Organic solar cells: An overview,” *Journal of Materials Research*, vol. 19, no. 7, pp. 1924–1945, Jul. 2004, doi: 10.1557/JMR.2004.0252.
- [97] J. You *et al.*, “A polymer tandem solar cell with 10.6% power conversion efficiency,” *Nat Commun*, vol. 4, p. 1446, Feb. 2013, doi: 10.1038/ncomms2411.
- [98] S. D. Stranks *et al.*, “Electron-Hole Diffusion Lengths Exceeding 1 Micrometer in an Organometal Trihalide Perovskite Absorber,” *Science*, vol. 342, no. 6156, pp. 341–344, Oct. 2013, doi: 10.1126/science.1243982.
- [99] S. Yanagida, Y. Yu, and K. Manseki, “Iodine/Iodide-Free Dye-Sensitized Solar Cells,” *Acc. Chem Res.*, vol. 42, no. 11, pp. 1827–1838, Nov. 2009, doi: 10.1021/ar900069p.
- [100] Y. S. Lee *et al.*, “ $\text{Cu}_2\text{ZnSnSe}_4$  Thin-Film Solar Cells by Thermal Co-evaporation with 11.6% Efficiency and Improved Minority Carrier Diffusion Length,” *Advanced Energy Materials*, vol. 5, no. 7, p. 1401372, 2015, doi: 10.1002/aenm.201401372.
- [101] T. Dullweber *et al.*, “Back surface band gap gradings in  $\text{Cu}(\text{In,Ga})\text{Se}_2$  solar cells,” *Thin Solid Films*, vol. 387, no. 1, pp. 11–13, May 2001, doi: 10.1016/S0040-6090(00)01726-0.
- [102] J. Toušek, D. Kindl, J. Toušková, S. Dolhov, and A. Poruba, “Diffusion length in CdTe by measurement of photovoltage spectra in CdS/CdTe solar cells,” *Journal of Applied Physics*, vol. 89, no. 1, pp. 460–465, Dec. 2000, doi: 10.1063/1.1332418.
- [103] J. Britt and C. Ferekides, “Thin-film CdS/CdTe solar cell with 15.8% efficiency,” *Applied Physics Letters*, vol. 62, no. 22, p. 2851, Jun. 1998, doi: 10.1063/1.109629.
- [104] J. H. Lee, P. Lee, D. Lee, S. S. Lee, and S. H. Ko, “Large-Scale Synthesis and Characterization of Very Long Silver Nanowires via Successive Multistep Growth,” *Crystal Growth & Design*, vol. 12, no. 11, pp. 5598–5605, Nov. 2012, doi: 10.1021/cg301119d.
- [105] Y. Li, X. Yuan, H. Yang, Y. Chao, S. Guo, and C. Wang, “One-Step Synthesis of Silver Nanowires with Ultra-Long Length and Thin Diameter to Make Flexible Transparent Conductive Films,” *Materials*, vol. 12, no. 3, p. 401, Jan. 2019, doi: 10.3390/ma12030401.

## **Conclusions and future work**



AgNW based transparent electrodes have been the subject of major studies both in research and industry in last few years. Large-scale fabrication of cheap and flexible (even stretchable) electrodes with high electro-optical properties and long-term sustainability has been the major objective of these studies. Today, there is a comprehensive understanding of the electro-optical properties of AgNW-based TEs, which offers a strategic approach to exploring the potential applications of these materials.[1]–[5] TEs based on MNWs with optical transmittance above 90% and sheet resistance of less than  $10 \Omega\text{sq}^{-1}$  have been reported by many research groups so far.[6] Using procedures described in section 2.2.1 and 2.2.2 of **Chapter 2**, spin-coated and air-brush spray-coated AgNW networks were deposited, with sheet resistance values of  $9.2 \Omega\text{sq}^{-1}$  and  $5.9 \Omega\text{sq}^{-1}$  and optical transmittance at 500 nm (without subtracting the substrate contribution) of 84% and 84.3%, respectively. However, there are several drawbacks which have caused setbacks in the commercialization stage of MNW based TEs for many years and even a cost in the reputation of these materials to date.[7, p. 656] Lack of chemical, thermal and electrical stability,[8], [9] high tendency of MNWs to oxidation or sulphidation,[10]–[12] high surface roughness and poor adhesion of MNWs to the beneath substrates,[8] are among major drawbacks associated with these TEs.[13] Addressing the lack of efficient stability in the morphology and electrical properties of AgNW networks under high electrical/thermal stress or long term storage in environmental conditions, was the main focus of experimental studies in the scope of this thesis.

Reviewing the literature confirms that improving the stability of AgNW networks is only feasible through passivation of them by thin and transparent coatings such as graphene, [12], [12], [14], [15] amorphous carbon films,[16] small organic molecules of 11-mercaptoundecanoic acid (MUA) [17] or polymer coatings of PDMS and PMMA. [18] We have chosen to coat AgNWs with thin (a few tens of nanometers in thickness) conformal and homogeneous layers of metal oxides. The reason behind this choice was that the efficiency of metal oxide coatings on the stability enhancement of AgNWs had already been proven by several research teams. Coating of oxides like Zinc Oxide (ZnO),[8], [19]–[21] Aluminum doped Zinc Oxide (AlZnO),[22]–[24] Titanium dioxide ( $\text{TiO}_2$ )[25], [26] or Aluminum oxide ( $\text{Al}_2\text{O}_3$ )[20], [27] have been shown to provide a clear enhancement of the stability of AgNW networks. So far sol-gel,[25], [28] sputtering,[19], [23] spin-coating,[29], [30] and atomic layer deposition (ALD) [31] have been used to deposit metal oxide coatings over AgNW networks. The composite layers fabricated using these methods showed much enhanced stability as compared to the un-coated AgNW networks. However, these deposition methods, have some characteristics such as the requirement of vacuum, low deposition rate or the low scalability. Such characteristics counterbalance one of the main advantages of AgNW-based TEs, which is low-cost and high-throughput scalable fabrication. We have shown that AP-SALD is a very appealing technique to engineer stable AgNW electrodes,[8] since it shares the main advantages of ALD (conformal and homogeneous oxide films with precise control of the thickness deposited), while being up to two orders of magnitude faster than conventional ALD and more suitable for scaling up.[32], [33] High-quality coatings of ZnO and  $\text{Al}_2\text{O}_3$  were

deposited using AP-SALD while electrical, thermal and ageing stability of composite films were compared to uncoated AgNW networks.

We have observed that the coating of ZnO and Al<sub>2</sub>O<sub>3</sub> (sections 3.4.6 and 3.5.2 of **Chapter 3**, respectively), can dramatically improve the thermal stability of AgNW networks. *In-situ* electrical measurements were performed on both uncoated and metal oxide-coated AgNWs during thermal ramps of 2 °C min<sup>-1</sup> in air. Such measurements showed that bare AgNW networks with an average diameter of 90 nm were degraded and lost their electrical conductivity above 300 °C. In contrast, a 50 nm of ZnO coating was enough to provide an efficient barrier against diffusion of Ag atoms and keep the network conductive after heating up to 450 °C followed by cooling down to room temperature. Similarly, coating of 12 nm Al<sub>2</sub>O<sub>3</sub> on AgNWs protected them from degradation and the electrical resistance remained unchanged after a thermal ramp up to 380 °C. We have formulated the dependence of the failure voltage of metal oxide-coated AgNW networks, with thickness of coating using a diffusion model for Ag atoms and proposed a simple physical model explaining the dependence of the failure voltage versus oxide thickness: the failure voltage varies with the square of the oxide layer thickness, leading to a clear stability enhancement.[8] However, such a gain in stability comes along with a loss in the optical transmittance of metal oxide-coated AgNW networks. A 50 nm thick ZnO coating reduces the average total transmittance in the visible range (from 380 to 700 nm) from 85% for bare AgNWs to 73% due to the rather low band gap of ZnO coating (3.3 eV).[33] Al<sub>2</sub>O<sub>3</sub> coating causes a milder effect on the total transmittance compared to ZnO coating, due to its higher band gap with respect to ZnO (8 instead of 3.3 eV). A 50 nm thick Al<sub>2</sub>O<sub>3</sub> coating reduces the average total transmittance in the visible range from 85% for bare AgNWs to 80%. [9]

However, despite superior optical properties for Al<sub>2</sub>O<sub>3</sub>-coated AgNW, we have observed some local damage and delamination in some of the Al<sub>2</sub>O<sub>3</sub>-coated samples at temperatures above 400 °C. The reason behind, might be the mismatch in the thermal expansion coefficient between Al<sub>2</sub>O<sub>3</sub> coating and glass substrate. So unlike ZnO coatings, Al<sub>2</sub>O<sub>3</sub> films are not able to follow the thermal expansion of glass substrates at elevated temperatures. To find a trade-off between the reproducibility of ZnO-coated AgNW networks and high optical performance of Al<sub>2</sub>O<sub>3</sub>-coated ones, bilayer coatings of ZnO/ Al<sub>2</sub>O<sub>3</sub> have been proposed and tested as an alternative to AgNW networks with a single coating of ZnO or Al<sub>2</sub>O<sub>3</sub>. Al<sub>2</sub>O<sub>3</sub> coating has been used due to its anti-reflective coating effect on ZnO films, which leads to an overall improvement in optical transmittance of bilayer-coated AgNW network compared to ZnO-coated ones. While a 70 nm thick ZnO coating on AgNW networks showed an average transmittance in the visible range of 64.9%, bilayer coatings consisting of 70 nm ZnO/ 70 nm Al<sub>2</sub>O<sub>3</sub> on similar networks showed a transmittance up to 73.5%. The improvement in the optical transmittance comes along with the superior thermal stability of bilayer-coated AgNW networks compared to solely ZnO-coated ones. Samples of AgNWs/ 70 nm ZnO/ 70 nm Al<sub>2</sub>O<sub>3</sub> showed excellent stability after 6 cycles of annealing in the air from room temperature to 450 °C.



Finally, the mechanical flexibility of bare ZnO and bilayer ZnO/Al<sub>2</sub>O<sub>3</sub>-coated AgNW networks was compared to reference ITO values. ZnO-coated AgNW networks show the best mechanical stability, with only a 4.7% increase in the electrical resistance after 10,000 bending cycles with a radius of 5 mm. The addition of Al<sub>2</sub>O<sub>3</sub> coating leads to an increase in the total oxide thickness and partially limits the bending stability of bilayer composites. However, 60 nm ZnO/ 60 nm Al<sub>2</sub>O<sub>3</sub>-coated AgNW-based transparent electrodes still show superior mechanical flexibility compared to ITO electrodes. Bilayer coated AgNWs show thoroughly less change in the electrical resistance (150 times less) compared to ITO electrode after bending for the same number of cycles (100 cycles). Therefore a compromise in terms of ZnO and Al<sub>2</sub>O<sub>3</sub> thicknesses between enhanced thermal/electrical stability and flexibility, as well as optical and electrical properties, has to be considered. Such a compromise depends drastically on the envisaged application.

Finding a trade-off between enhancements of thermal, electrical, and environmental stability of AgNW networks and the loss in the optical transmittance values, seems to be a future challenge of AgNW network research. So far we have only studied the effect of ZnO, Al<sub>2</sub>O<sub>3</sub> and composites of ZnO/ Al<sub>2</sub>O<sub>3</sub> coatings on stability of AgNW networks and loss in the optical transmittance values. However, a wide range of other metal oxides can be also deposited by AP-SALD and their stability enhancement performance along with optical properties can be studied. Titanium dioxide (TiO<sub>2</sub>), Silicon dioxide (SiO<sub>2</sub>), Molybdenum trioxide (MoO<sub>3</sub>), are among the few candidates which can be used as coating layers on AgNWs.

One way to minimize the effect of additional coating on the total transmittance is to selectively coat only AgNWs with the coating film, rather than the case of conformal AP-SALD coating in our study which coats both AgNWs and the substrate. Bai et al.[34] showed an example of silica nanoparticle-coated AgNW networks where nanoparticles are mainly decorated around the AgNWs, as this configuration minimizes their free energy. The composite films of AgNWs/ silica nanoparticles (average diameter of 50 nm) had sheet resistance of 28 Ωsq<sup>-1</sup> and total transmittance around 97% (without substrate contribution). These outstanding electro-optical properties come along with mechanical flexibility after 1000 cycles of bending and no change in the electrical resistance. Composite layers of AgNWs and metallic meshes are alternative candidates which exhibit excellent electro-optical properties. Shinde et al. have reported TEs based on metallic mesh/AgNW with a sheet resistance of 0.745 Ωsq<sup>-1</sup> and total transmittance of 90.3% (without substrate contribution).[35] Furthermore, metallic mesh/ AgNW composites showed better stability in electrical resistance compared to TEs with solely AgNWs or metal mesh on PET under various environmental conditions, including light, temperature, and humidity.[35]

Taken together, it seems that major steps have been taken in order to overcome the stability issue associated with TEs based on AgNWs. TEs based on AgNW networks finally have the potential to enter the global market of TEs. Market studies predict that AgNW based TEs are in the growth phase and will keep growing. A study performed

by IDtechEx predicted that in 2028 TEs based on AgNWs will be comparable in the market share to the TEs based on ITO. [7] However, there is a common agreement between research communities that there is no single formula to fabricate a TE which can meet the requirements of all different applications. Features like high electro-optical properties, flexibility, stretchability, tactility, energy efficiency, environmental stability, abundance of required materials and ease of fabrication cannot be achieved by one single material. Wide range of hybrid approaches have been used to integrate the properties of different TEs into a single functional electrode. Multi compound metal oxides (e.g. IGZO, IZO, ZTO), hybrid electrodes of AgNWs and PEDOT:PSS,[36] AgNWs and graphene,[37], [38] AgNWs and metal oxides,[39], [40] hybrids of graphene and PEDOT:PSS,[41] graphene and metal oxides are used to meet properties required for different applications.[13]

So far, we have focused on TEs based on AgNW networks and discussed the electro-optical properties of these TEs along with the main challenges which these materials have faced so far following by suggested strategies to overcome those challenges. However, there is yet the question of whether or not NWs are the most optimum nano-shape to form percolative random networks. Moving on to the theoretical part of the study, presented in **Chapter 4**, we have used Monte Carlo simulations to investigate the percolation behaviour of networks composed of random nano-objects with different orders of symmetry. The algorithm was originally developed by Daniel Langley in his thesis and adapted for the present study.[42] The goal of the latter is to find the elemental shape with the lowest possible percolation threshold since a lower percolation threshold leads to a lower total length of material at the percolation threshold for different nano-objects. This, in turn, leads to lower material areal density and more transparent, more economic devices. Our algorithm, based on a super-fast method proposed by Newman and Ziff, enabled us to study a wide range of elemental shapes with acceptable accuracy. We observed that considering an optimum order of symmetry to nano-objects can lead to a decrease in material areal density down to 50% compared to similar networks composed of sticks. Symmetry in nano-objects can be in the form of m-fold periodic stick arrangements, or polygonal shapes, or finite-size regular grids. The decrement in the total length of the material density is observed even if there is angular and length distribution of symmetric shapes. The main conclusion from this section of the work is that MNW are not necessarily the most optimum shape to form TEs based on randomly deposited metallic nano particles. We concluded that TEs based on branched silver NWs and shapes like nano-stars have the potential to offer even better electro-optical properties compared to MNW based ones. The moment of inertia is another feature that has been used in this study as a general tool to evaluate different nano-objects in the terms of the required material to reach percolation. Our initial study confirmed that there is a strong correlation between the moment of inertia and the total length of material density. However, there is yet a lack of systematic study to see whether it's possible to formulate such a correlation or not? To study such correlation it is better to study sets of geometrical shapes with continuous changes in the moment of inertia. For instance ellipses with changing semi-major to semi-minor axes ratio is an example of shapes with a continuous moment of inertia. One

might expect that the total length of material density will be highest for the circular shapes and decrease while elongating ellipses. However, ellipses were not studied during this thesis and can be the subject of a further step in understanding the association between the percolation threshold and moment of inertia.

Finally, in the last part of the theoretical studies, we focused on the collection efficiency of MNW based TEs for solar cells. We have studied the collection efficiency of charge carriers ( $\eta$  in %), versus MNW network density, NW length, and diffusion lengths of photo-generated charge carriers in the active material. Our simulations predict that increasing the density of MNW networks increases  $\eta$ %, while increasing the *ratio* of NW length to Diffusion lengths decreases  $\eta$ %. In the study of the collection efficiency of MNW based TEs for solar cells, several simplifications have been made. A careful examination of any of them would lead to more reliable and precise results. The first major assumption was to assume that all the photo-generated charge carriers can reach the interface of the active layer and front electrode (MNW based TE). However, in reality, a fraction of charge carriers will recombine before arriving at this interface. Therefore one might define a more comprehensive model considering the active layer, the TE, and the interface between these layers to obtain a better estimation of the collection efficiency. Secondly, an additional thin layer of conducting metal oxide (e.g. Al:ZnO) can be used to cover MNWs to enhance the collection efficiency of the final device. This additional layer is not modelled in our simulations but can be studied in a comprehensive model as well. We believe that improving this model can provide a reliable guideline to design a TE for a targeted solar cell application from the NW geometry to network properties level.



## References:

- [1] H. G. Manning, C. G. da Rocha, C. O. Callaghan, M. S. Ferreira, and J. J. Boland, “The Electro-Optical Performance of Silver Nanowire Networks,” *Sci. Rep.*, vol. 9, no. 1, pp. 1–9, Aug. 2019, doi: 10.1038/s41598-019-47777-2.
- [2] D. Tan, C. Jiang, Q. Li, S. Bi, and J. Song, “Silver nanowire networks with preparations and applications: a review,” *J. Mater. Sci. Mater. Electron.*, vol. 31, no. 18, pp. 15669–15696, Sep. 2020, doi: 10.1007/s10854-020-04131-x.
- [3] Y. Zhang, S.-W. Ng, X. Lu, and Z. Zheng, “Solution-Processed Transparent Electrodes for Emerging Thin-Film Solar Cells,” *Chem. Rev.*, vol. 120, no. 4, pp. 2049–2122, Feb. 2020, doi: 10.1021/acs.chemrev.9b00483.
- [4] D. Bellet *et al.*, *Smart Nanosystems for Biomedicine, Optoelectronics and Catalysis*. intechopen. 2019. doi: 10.5772/intechopen.89281.
- [5] H. Sohn, C. Park, J.-M. Oh, S. W. Kang, and M.-J. Kim, “Silver Nanowire Networks: Mechano-Electric Properties and Applications,” *Materials*, vol. 12, no. 16, p. 2526, Aug. 2019, doi: 10.3390/ma12162526.
- [6] T. Sannicolo, “Transparent Electrodes based on Silver Nanowire Networks: Electrical Percolation, Physical Properties, and Applications,” PhD thesis, University of Grenoble Alpes (France), 2017.
- [7] “<https://www.idtechex.com/en/research-report/transparent-conductive-films-and-materials-2019-2029-forecasts-technologies-players/656>.”
- [8] A. Khan *et al.*, “Stability Enhancement of Silver Nanowire Networks with Conformal ZnO Coatings Deposited by Atmospheric Pressure Spatial Atomic Layer Deposition,” *ACS Appl. Mater. Interfaces*, vol. 10, no. 22, pp. 19208–19217, Jun. 2018, doi: 10.1021/acsami.8b03079.
- [9] S. Aghazadehchors *et al.*, “Versatility of bilayer metal oxide coatings on silver nanowire networks for enhanced stability with minimal transparency loss,” *Nanoscale*, vol. 11, no. 42, pp. 19969–19979, 2019, doi: 10.1039/C9NR05658K.
- [10] J. Jiu *et al.*, “The effect of light and humidity on the stability of silver nanowire transparent electrodes,” *RSC Adv.*, vol. 5, no. 35, pp. 27657–27664, Mar. 2015, doi: 10.1039/C5RA02722E.
- [11] Y. Ahn, Y. Jeong, and Y. Lee, “Improved Thermal Oxidation Stability of Solution-Processable Silver Nanowire Transparent Electrode by Reduced Graphene Oxide,” *ACS Appl. Mater. Interfaces*, vol. 4, no. 12, pp. 6410–6414, Dec. 2012, doi: 10.1021/am301913w.
- [12] W. H. Chae, T. Sannicolo, and J. C. Grossman, “Double-Sided Graphene Oxide Encapsulated Silver Nanowire Transparent Electrode with Improved Chemical and Electrical Stability,” *ACS Appl. Mater. Interfaces*, vol. 12, no. 15, pp. 17909–17920, Apr. 2020, doi: 10.1021/acsami.0c03587.
- [13] M. Morales-Masis, S. De Wolf, R. Woods-Robinson, J. W. Ager, and C. Ballif, “Transparent Electrodes for Efficient Optoelectronics,” *Adv. Electron. Mater.*, vol. 3, no. 5, p. 1600529, May 2017, doi: 10.1002/aelm.201600529.
- [14] Y. C. G. Kwan, Q. L. Le, and C. H. A. Huan, “Time to failure modeling of silver nanowire transparent conducting electrodes and effects of a reduced graphene oxide over layer,” *Sol. Energy Mater. Sol. Cells*, vol. 144, pp. 102–108, Jan. 2016, doi: 10.1016/j.solmat.2015.08.005.

- [15] S. R. Das *et al.*, “Single-Layer Graphene as a Barrier Layer for Intense UV Laser-Induced Damages for Silver Nanowire Network,” *ACS Nano*, vol. 9, no. 11, pp. 11121–11133, Nov. 2015, doi: 10.1021/acsnano.5b04628.
- [16] H.-J. Seok, J.-K. Kim, and H.-K. Kim, “Effective passivation of Ag nanowire network by transparent tetrahedral amorphous carbon film for flexible and transparent thin film heaters,” *Sci. Rep.*, vol. 8, no. 1, pp. 1–12, Sep. 2018, doi: 10.1038/s41598-018-31927-z.
- [17] A. Madeira, M. Plissonneau, L. Servant, I. A. Goldthorpe, and M. Tréguer-Delapierre, “Increasing Silver Nanowire Network Stability through Small Molecule Passivation,” *Nanomater. Basel Switz.*, vol. 9, no. 6, Jun. 2019, doi: 10.3390/nano9060899.
- [18] J. Mock *et al.*, “Aqueous Synthesis, Degradation, and Encapsulation of Copper Nanowires for Transparent Electrodes,” *Nanomaterials*, vol. 8, no. 10, p. 767, Sep. 2018, doi: 10.3390/nano8100767.
- [19] A. Kim, Y. Won, K. Woo, C.-H. Kim, and J. Moon, “Highly Transparent Low Resistance ZnO/Ag Nanowire/ZnO Composite Electrode for Thin Film Solar Cells,” *ACS Nano*, vol. 7, no. 2, pp. 1081–1091, Feb. 2013, doi: 10.1021/nn305491x.
- [20] A.-T. Pham, X.-Q. Nguyen, D.-H. Tran, V. Ngoc Phan, T.-T. Duong, and D.-C. Nguyen, “Enhancement of the electrical properties of silver nanowire transparent conductive electrodes by atomic layer deposition coating with zinc oxide,” *Nanotechnology*, vol. 27, no. 33, p. 335202, Aug. 2016, doi: 10.1088/0957-4484/27/33/335202.
- [21] H. Yu *et al.*, “Use of solution-processed zinc oxide to prevent the breakdown in silver nanowire networks,” *Nanotechnology*, vol. 31, no. 18, p. 18LT01, Feb. 2020, doi: 10.1088/1361-6528/ab6fe4.
- [22] X. Yan, J. Ma, H. Xu, C. Wang, and Y. Liu, “Fabrication of silver nanowires and metal oxide composite transparent electrodes and their application in UV light-emitting diodes,” *J. Phys. Appl. Phys.*, vol. 49, no. 32, p. 325103, Aug. 2016, doi: 10.1088/0022-3727/49/32/325103.
- [23] Q. Huang *et al.*, “Highly Thermostable, Flexible, Transparent, and Conductive Films on Polyimide Substrate with an AZO/AgNW/AZO Structure,” *ACS Appl. Mater. Interfaces*, vol. 7, no. 7, pp. 4299–4305, Feb. 2015, doi: 10.1021/am508704u.
- [24] V. H. Nguyen *et al.*, “Low-cost fabrication of flexible transparent electrodes based on Al doped ZnO and silver nanowire nanocomposites: impact of the network density,” *Nanoscale*, vol. 11, no. 25, pp. 12097–12107, 2019, doi: 10.1039/C9NR02664A.
- [25] T.-B. Song *et al.*, “Highly Robust Silver Nanowire Network for Transparent Electrode,” *ACS Appl. Mater. Interfaces*, vol. 7, no. 44, pp. 24601–24607, Nov. 2015, doi: 10.1021/acsam.5b06540.
- [26] Y. Huang *et al.*, “TiO<sub>2</sub>-Coated Core–Shell Ag Nanowire Networks for Robust and Washable Flexible Transparent Electrodes,” *ACS Appl. Nano Mater.*, vol. 2, no. 4, pp. 2456–2466, Apr. 2019, doi: 10.1021/acsanm.9b00337.
- [27] B. Hwang *et al.*, “Highly Flexible and Transparent Ag Nanowire Electrode Encapsulated with Ultra-Thin Al<sub>2</sub>O<sub>3</sub>: Thermal, Ambient, and Mechanical Stabilities,” *Sci. Rep.*, vol. 7, p. 41336, Jan. 2017, doi: 10.1038/srep41336.

- [28] W. Shin, W. Cho, and S. J. Baik, “Silver nanowires network encapsulated by low temperature sol–gel ZnO for transparent flexible electrodes with ambient stability,” *Mater. Res. Express*, vol. 5, no. 1, p. 015050, Jan. 2018, doi: 10.1088/2053-1591/aaa67a.
- [29] R. Liu *et al.*, “Solution-processed composite electrodes composed of silver nanowires and aluminum-doped zinc oxide nanoparticles for thin-film solar cells applications,” *Sol. Energy Mater. Sol. Cells*, vol. 174, pp. 584–592, Jan. 2018, doi: 10.1016/j.solmat.2017.09.042.
- [30] W. Lan *et al.*, “Novel transparent high-performance AgNWs/ZnO electrodes prepared on unconventional substrates with 3D structured surfaces,” *Appl. Surf. Sci.*, vol. 433, pp. 821–828, Mar. 2018, doi: 10.1016/j.apsusc.2017.10.054.
- [31] M. Göbelt *et al.*, “Encapsulation of silver nanowire networks by atomic layer deposition for indium-free transparent electrodes,” *Nano Energy*, vol. 16, pp. 196–206, Sep. 2015, doi: 10.1016/j.nanoen.2015.06.027.
- [32] D. Muñoz-Rojas and J. MacManus-Driscoll, “Spatial atmospheric atomic layer deposition: a new laboratory and industrial tool for low-cost photovoltaics,” *Mater. Horiz.*, vol. 1, no. 3, p. 314, 2014, doi: 10.1039/c3mh00136a.
- [33] D. Muñoz-Rojas, V. H. Nguyen, C. Masse de la Huerta, S. Aghazadehchors, C. Jiménez, and D. Bellet, “Spatial Atomic Layer Deposition (SALD), an emerging tool for energy materials. Application to new-generation photovoltaic devices and transparent conductive materials,” *Comptes Rendus Phys.*, vol. 18, no. 7, pp. 391–400, Sep. 2017, doi: 10.1016/j.crhy.2017.09.004.
- [34] S. Bai, H. Wang, H. Yang, H. Zhang, T. Chen, and X. Guo, “Fused silver nanowires with silica sol nanoparticles for smooth, flexible, electrically conductive and highly stable transparent electrodes,” *RSC Adv.*, vol. 8, no. 24, pp. 13466–13473, 2018, doi: 10.1039/C8RA01569D.
- [35] M. A. Shinde, K. Mallikarjuna, J. Noh, and H. Kim, “Highly stable silver nanowires based bilayered flexible transparent conductive electrode,” *Thin Solid Films*, vol. 660, pp. 447–454, Aug. 2018, doi: 10.1016/j.tsf.2018.06.054.
- [36] T. Lei *et al.*, “Bendable and foldable flexible organic solar cells based on Ag nanowire films with 10.30% efficiency,” *J. Mater. Chem. A*, vol. 7, no. 8, pp. 3737–3744, Feb. 2019, doi: 10.1039/C8TA11293B.
- [37] A. G. Ricciardulli, S. Yang, G.-J. A. H. Wetzelaer, X. Feng, and P. W. M. Blom, “Hybrid Silver Nanowire and Graphene-Based Solution-Processed Transparent Electrode for Organic Optoelectronics,” *Adv. Funct. Mater.*, vol. 28, no. 14, p. 1706010, Apr. 2018, doi: 10.1002/adfm.201706010.
- [38] A. R. bin M. Yusoff, S. J. Lee, F. K. Shneider, W. J. da Silva, and J. Jang, “High-Performance Semitransparent Tandem Solar Cell of 8.02% Conversion Efficiency with Solution-Processed Graphene Mesh and Laminated Ag Nanowire Top Electrodes,” *Adv. Energy Mater.*, vol. 4, no. 12, p. 1301989, 2014, doi: 10.1002/aenm.201301989.
- [39] A. Kim, Y. Won, K. Woo, S. Jeong, and J. Moon, “All-Solution-Processed Indium-Free Transparent Composite Electrodes based on Ag Nanowire and Metal Oxide for Thin-Film Solar Cells,” *Adv. Funct. Mater.*, vol. 24, no. 17, pp. 2462–2471, May 2014, doi: 10.1002/adfm.201303518.
- [40] X. Zhang, J. Wu, J. Wang, Q. Yang, B. Zhang, and Z. Xie, “Low-Temperature All-Solution-Processed Transparent Silver Nanowire-Polymer/AZO Nanoparticles Composite Electrodes for Efficient ITO-Free

Polymer Solar Cells,” *ACS Appl. Mater. Interfaces*, vol. 8, no. 50, pp. 34630–34637, Dec. 2016, doi: 10.1021/acsami.6b11978.

[41] K. S. Lee, Y. Lee, J. Y. Lee, J.-H. Ahn, and J. H. Park, “Flexible and Platinum-Free Dye-Sensitized Solar Cells with Conducting-Polymer-Coated Graphene Counter Electrodes,” *ChemSusChem*, vol. 5, no. 2, pp. 379–382, 2012, doi: 10.1002/cssc.201100430.

[42] D. Langley, “Silver nanowire networks: Effects of percolation and thermal annealing on physical properties,” PhD thesis, University of Grenoble Alpes (France), University of Liège (Belgium), 2014.